# INTERNATIONAL INNOVATIVE APPROACHES IN EGINEERING & TECHNOLOGY



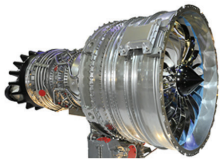
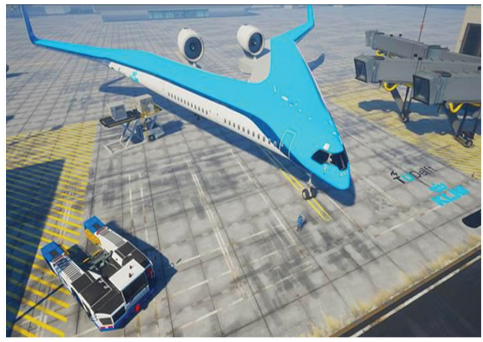

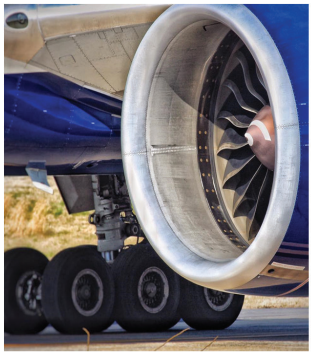

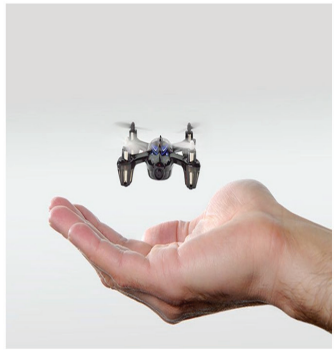

**EDITORS**
**Prof. Dr. Yusuf ŞAHİN**
**Assist. Prof. Senai YALÇINKAYA**

# INTERNATIONAL INNOVATIVE APPROACHES IN EGINEERING & TECHNOLOGY

**EDITORS**
Prof. Dr. Yusuf ŞAHİN
Assist. Prof. Senai YALÇINKAYA

**INTERNATIONAL INNOVATIVE APPROACHES IN EGINEERING & TECHNOLOGY**

**EDITORS**
**Prof. Dr. Yusuf ŞAHİN**
**Assist. Prof. Senai YALÇINKAYA**

**Güven Plus Group Inc. Publications: 46/2021**
**15 DECEMBER 2021**

**Publisher Certificate No: 52866**
**E-ISBN: 978-625-7367-02-8**
**Güven Plus Group Inc. Publications**



**Text and Language Editors**
Assoc. Prof. Gökşen ARAS (Turkish – English)
Assist. Prof. L. Santhosh KUMAR (English)

**Cover and Graphic Design**
Prof. Dr. Pelin AVŞAR KARABAŞ
Lec. Ozan KARABAŞ
Ozan DÜZ

**Page Layout**
Burhan MADEN

**Print-Binding**
GÜVEN PLUS GROUP CONSULTANCY INC. CO. PUBLICATIONS®
Kayaşehir Neighborhood Evliya Çelebi Street Emlakkonut Başakşehir Houses 1/A D Block Floor 4 Number 29
Başakşehir İstanbul - Turkey Phone: +902128014061- 62 Fax: +902128014063 Mobile: +9053331447861

**BOOK LICENSEE**
**GÜVEN PLUS GROUP CONSULTANCY INC. CO. PUBLICATIONS®**
Kayaşehir Neighborhood Evliya Çelebi Street Emlakkonut Başakşehir Houses 1/A D Block Floor 4 Number 29
Başakşehir İstanbul - Turkey Phone: +902128014061- 62 Fax: +902128014063 info@guvenplus.com.tr, www.guvenplus.com.tr

# TABLE OF CONTENTS

# PREFACE

***International Innovative Approaches in Engineering & Technology***

*Technological improvements in engineering and science have been developed very fast. For Guven Plus Group Limited Company, most important part of the publication comes from academic books that have gained quite good prejtice due to doing national or international scale of job. The book printed out by Guven Plus Group Lt. called ".International Innovative Approaches in Engineering & Technology "consist of 10 Chapters with manys scientific articles covering experimental, theoretical, analysis and evaluations. They have discussed their results with participants people.*

They have included many interesting topics/titles such as "bor minerals from sources to end use", "effect of carbon nano tubes on mechanical properties of polymeric composites"," surface completeness for ostenite stainless steel as an implant material", "improvements of heat-treatment process for Al7075 alloys"and,"prediction of tribological behaviour on some polymeric materials" etc. many other important topics also will be found out in this book. Each of this section in the book, academicions/researchers have prepared with own contributions and consists of original study.

Many interesting topics and subjects regarding Enginnering Technologies have been discussed in this book, which will be light for academicians and researchers. In addition, it will also replace for catalogue of Higher Education Institute (HEI), other institution's libraries and individual's archieves.

We wish to express our thanks to our authors, rewievers of these papers for making them available, technical teams for assisting me in making ready for printing the book.

**Prof. Dr. Yusuf ŞAHİN**
**Assist. Prof. Senai YALÇINKAYA**
**December, 2021**

# THE USAGE OF BIOACTIVE GLASSES IN BONE TISSUE ENGINEERING: REVIEW

*Cem ÖZEL[1], Pelda KIZIL[2], Ceren EMİR[1], Sevil YÜCEL[3]*

**Abstract:** The skeletal system is the most important component of our body that gives shape to our body, keeps it alive, and protects our internal organs against external impacts. When skeletal system is damaged, it can regenerate itself, but if the damage is big and severe, it cannot be regenerated by normal physiological processes. Therefore, bone damage requires scaffolds to improve healing process. The purpose of bone tissue engineering is to restore, regenerate, improve and maintain the function of damaged bone tissue through a combination of cells, biomolecules, and scaffolds. In order to repair and functionalize the bone tissue, scaffolds that mimic the structure of bone mineral and adapt to the cell are prepared. Metals, ceramics, polymers, and composite materials are used as biomaterials in the production of scaffolds. Among these, bioactive glasses, which are in the class of biologically used ceramics (bioceramics), draw attention. Various biomaterials and manufacturing techniques for scaffold provide achievable advances in bone tissue regeneration. Bioactive glass (BG) can form a strong bond with bone by forming a layer of apatite on its surface. They have important properties such as bone conduction, bone inducibility, biocompatibility, and bioactivity. BG can stimulate gene expression that regulates bone formation by releasing ions from its surface. They are mainly composed of silicon, sodium, calcium and phosphate components. When transplanted into the human body, it binds to bone

1 Yıldız Technical University, Faculty of Chemical and Metallurgical Engineering, Department of Bioengineering, İstanbul / Turkey, cemozel@yildiz.edu.tr, Orcid No:0000-0002-6288-2091

2 Yıldız Technical University, Faculty of Chemical and Metallurgical Engineering, Department of Bioengineering, İstanbul / Turkey, ckececi@yildiz.edu.tr, Orcid No:0000-0001-9015-3104

3 Yıldız Technical University, Faculty of Chemical and Metallurgical Engineering, Department of Bioengineering, İstanbul / Turkey, syucel@yildiz.edu.tr, Orcid No:0000-0002-9495-9321

through the hydroxyapatite layer formed on the surface and reacts with surrounding tissues to form a strong mechanical interface bond between the host tissue and the implant. These properties make BG an important potential material in bone tissue regeneration. BG has been widely used to process skeletal structures with or without one or more biopolymers to proper scaffold. Bioactive glass nanoparticles (BGNP) have also grown significantly in bone tissue engineering applications due to important properties such as very large specific surface area, small size, and high surface area to volume ratio. BGNP can be mainly obtained by conventional melt quenching or sol-gel methods. BGNP has applications for soft tissue regeneration/repair and other biomedical applications as well as being particularly interesting biomaterials for bone-related applications.

***Keywords*:** Bone Regeneration, Bone Tissue Engineering, Scaffolds, Bioactive Glasses, Bioactive Glass Nanoparticles

## INTRODUCTION

Bone is a type of connective tissue that is a vascularized, functionalized solid organ that plays an important role in the human body. It is not uniformly rigid but consists of living cells located in a biomineral matrix. In fact, bone tissue is formed as this matrix around living bone cells hardens (Behzadi et al. 2017). The hierarchy and components of the bone are shown in Figure 1.

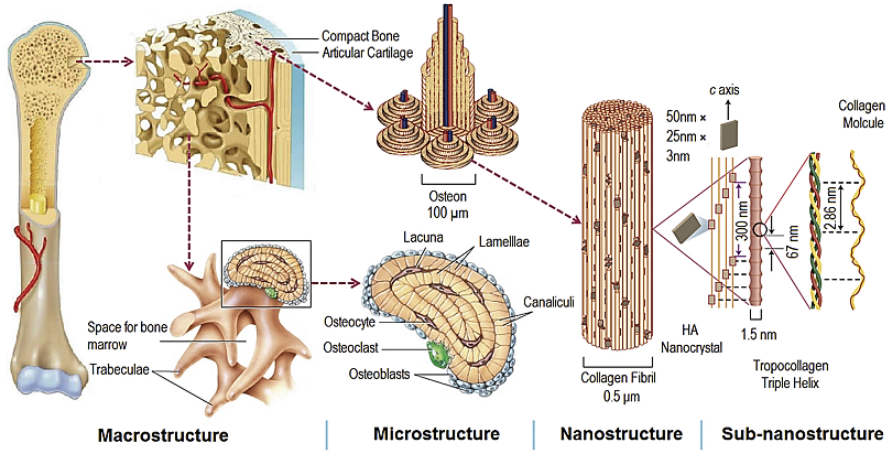


**Figure 1. Hierarchical Structure of Bone from Macroscale to Nanoscale (Wang et al., 2016)**

**Bone Structure and Bone Components**

Bone tissue has a hierarchical structure based on length scales varying from macrostructure to nanostructure level, including the Extracellular matrix (ECM). Basically, the tissue structure of bones can be divided into four scales.

- The macroscopic structure of bone (> 0.5 mm) forms the overall shape of the bone and consists of cancellous bone, also called cancellous or spongy bone and cortical bone (compact bone)
- Microscale structure (10-500 μm) with Haversian canal and osteons.
- Nanoscale structures (hundreds of nanometers to 1 micron) consist of collagen fibrils surrounded by minerals.
- Ultrafine structures sub-hundreds of nanometers contain collagen, non-collagen proteins and minerals (Chocholata, Kulda, and Babuska 2019; Qu et al. 2019).

Bone structure is divided into two main types: trabecular bone, which forms the outer shell, and cortical bone, which forms a porous inner core. They differ in porosity, metabolic activity and structure. Both types of bone are formed by collagen fibers (Qu et al. 2019). Cortical bone is almost rigid except for 3-5% of the area with canaliculi and osteocytes. These are the bones that provide strength to the cortical layer of the bone. Lamella is the name of the bone layer and is located around the Haversian canal. These layers in the cortical layer of bone have a cylindrical regular shape. Cortical bone is formed by inorganic crystalline minerals and a small number of osteocytes and blood vessels found in the Haversian canal. Cortical bone provides resistance to torsion and bending and compressive strength (Qu et al. 2019). The trabecular bone has an interconnected porous network of 50-90% porosity and a large inner area containing the bone marrow. It has a greater bone surface/volume ratio than cortical bone (Chocholata, Kulda, and Babuska 2019; Elalmış et al. 2019). The high porosity of cancellous bone allows the diffusion of nutrients and growth factors over a large surface area. Trabecular bone remodels more frequently than cortical bone because access to nutrients can activate cancellous bone more (Polo-Corrales, Latorre-Esteves, and Ramirez-Vick 2014). The trabecular bone has irregular semi-

circular plates, unlike the plates of the cortical bone. The advantage of this property of lamellae is that they provide deformation and absorption of loads applied to the cancellous bone (Keaveny 1998).

Bone contains various elements such as hydroxyapatite (HAp) minerals located in lamellae, bone, fiber bundles and collagen fibrils. Osteoprogens, osteoblasts, osteoclasts, and osteocytes are cells found in bones. Collagen crystals and calcium phosphate apatite (CaP) are major components of bone tissue. Apatite crystals are embedded in collagen fibrils. The bone marrow is located within the cancellous bone. It has various hierarchically arranged units of nano size, from lamellae to collagen fibrils. The crystal of HAp, a bone mineral, has a nanostructure with a size of several hundred nanometers. Bone cells work together to maintain bone integrity and regeneration. In critical-sized defects, bone graft is required to promote regeneration of these lesions because the bone does not repair itself and the recovery process is impossible itself (Saravanan, Leena, and Selvamurugan 2016).

**Bone Properties**

Bone is an anisotropic tissue because its mechanical, chemical, and biological properties depend on its structure. The bone structure is non-uniform, heterogeneous and irregular (Qu et al. 2019). Bones are a major part of the human skeletal system (Chocholata, Kulda, and Babuska 2019) and perform a variety of functions that play important roles in the body, including mechanical functions such as defense, movement, and shaping (Kular et al. 2012; Tal et al. 2012). It can be seen as an organ that connects ligaments, muscles, and tendons; therefore, it provides mechanical support. It is defined as the integument that protects the other organs of the body so that the skeleton can withstand stress. In addition to structural functions, it has some metabolic functions such as it regulates some bioactive ions such as Ca, P and fat deposition. It helps to increase the concentration of electrolytes in the blood. Bone also plays a synthetic role that promotes the synthesis of blood cells and plays an important role in the body's acid-base balance. Also hematopoietic, blood cells, bone marrow (Ansari 2019).

**Table 1. The Mechanical Properties of Bone (Filippi et al., 2020)**

| Bone type | Porosity % | Pore size (μm) | Elastic modulus (GPa) | Tensile Strength (MPa) | Compressive Strength (MPa) |
|---|---|---|---|---|---|
| Cortical bone | 5-10 | 10-50 | 11.5-18.9 | 50-170 | 130-180 |
| Trabecular bone | 30-90 | 300-600 | 0.05-0.1 | 8-20 | 4-12 |

It is very important to know the physicochemical structure and mechanical properties of bone in order to select the most suitable material for bone tissue engineering. These properties of bones depend on their sex, age, bone quality, and the location of the bones in the body. Table 1 shows the mechanical properties of bones (Wang et al. 2016). Stiffness and compressive strength are enhanced by the rigid structure of the cortical bone, mainly associated with the dense arrangement of HAp crystals. T The most important mechanical properties of the bone are elasticity and strength. Longitudinal compact bones are stiffer than transverse bones. Young's modulus of elasticity, tensile strength, and compressive strength are significantly different in the longitudinal and transverse directions. The porosity and structure of cancellous bone determine its mechanical properties (Qu et al. 2019).

**Biomaterials for Bone Scaffolds**

Various types of materials are used to create bone regeneration scaffolds, including ceramics, synthetic or natural polymers, bioactive glass, composites, and metals. Table 2 shows the types of biomaterials and their advantages and disadvantages. Each material has specific properties such as biocompatibility, osteoinductivity and osteoconductivity, making it a candidate for bone tissue scaffolds. Depending on the application, there may be some limitations and advantages. For example, bioactive glass and hydroxyapatite are very similar in content to bone minerals, but their fragility is a serious problem that limits their use to correct load-bearing defects. Unfortunately, there is no ideal substitute for autologous bone in clinical practice (Basaran Elalmis et al. 2021; Huang, Xie, and Li 2020).

The mechanical properties of the scaffolds are strongly influenced by the material composition. The modulus of elasticity for compressive strength of human bones versus some biomaterials used in bone engineering is shown in Figure 2. High-density ceramics such as Tricalcium phosphate (TCP) and HAp have the same compressive strength and modulus of elasticity of human cortical bone, but they have a slower rate of decomposition and brittleness. Metal scaffolds, including screws and plates, are thermal insulators, durable and biocompatible.

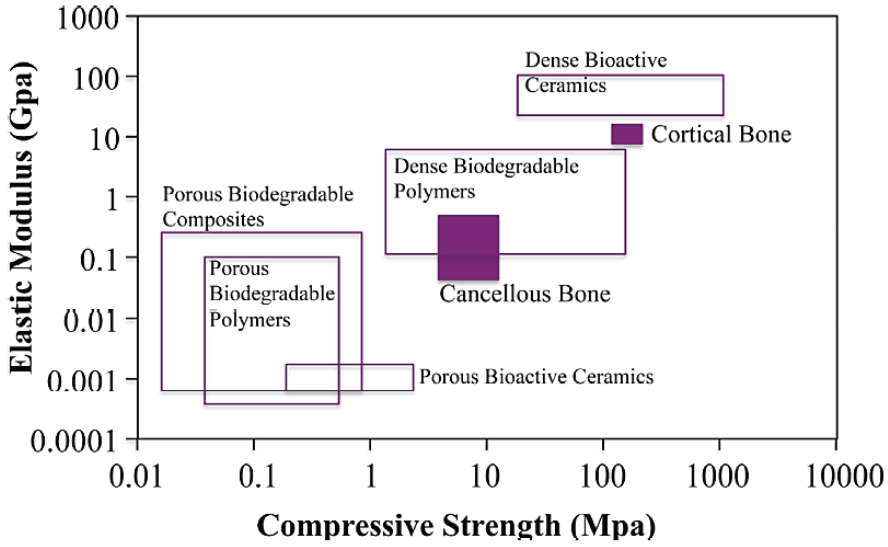


**Figure 2. Elastic Modulus Versus Compressive Strength of Some Biomaterials Used Bone Tissue Engineering Compared to Human Bone**

**Table 2. Type of Biomaterials with Their Disadvantages and Advantages (Chocholata, Kulda, and Babuska 2019; Filippi et al. 2020).**

| Type of Biomaterial | Advantages | Disadvantages |
|---|---|---|
| Metals | -biocompatibility<br>-corrosion resistance<br>-non-toxicity | -non-biodegradability |

| | | |
|---|---|---|
| Bioactive ceramics | -biocompatibility<br>-non-toxicity<br>-bioactivity<br>-osteo-conductivity and non-inflammatory | -low strength<br>-brittleness |
| Bioactive glasses | -biocompatibility<br>-osteo-conductivity<br>-non-toxicity and non-inflammatory<br>-bioactivity<br>-enhance differentiation and osteogenesis | -low strength<br>-brittleness |
| Natural polymers | - natural origin<br>- owning cell adhesion and recognition sites<br>- similar nature with native ECM<br>- not need harsh chemicals in production process<br>- bioactivity<br>- biodegradability<br>- biocompatibility | -properties dependence on manufacturing procedures and extraction<br>- insufficient mechanical properties<br>- expensive processing<br>- susceptibility to cross-contamination<br>- difficult production<br>- low stability |
| Synthetic polymers | - great purity<br>- low immune response<br>-reproducible mechanical and chemical properties<br>- good mechanical properties<br>- low costs for the production<br>- manufacturing in large quantities<br>- possibility of fixing material properties during production | -poor biocompatibility<br>-biodegradation side effects can be risky (nanotoxicity, inflammation, etc.)<br>-difficult 3D printing<br>- low ductility<br>- doubtable cell-matrix interaction<br>- non-degradable polymers can have long-term retention in the body<br>-biodegradable polymers can have low mechanical strength after degradation |

Therefore, they have been used to mechanically support long bones because of their high compressive strength. However, the disadvan-

tage is that they are biologically inert. They have some limitations that make them insufficient for bone repair applications (Boyan, Cohen, and Schwartz 2017; Huang, Xie, and Li 2020). There are two types of polymers used for bone regeneration: natural polymers and synthetic polymers. Polymers are physically similar to fibrous proteins in connective tissue. Polymer-based scaffolds can be gel, fibrous and rigid. Although there are several polymers for bone regeneration, one biodegradable polymer cannot provide all the desired properties in bone tissue engineering (Filippi et al. 2020).

**Bioactive Glasses**

BGs were discovered in 1969 by Larry L. Hench, professor at the University of Florida in the Department of Materials Science and Engineering (Hench and West 2002). The BG produced is named 45S5 with components 45% $SiO_2$–24.5% $Na_2O$–24.5% CaO–6% $P_2O_5$ (weight %). The first 45S5 was initially deposited with Bioglass®. It is a silicate glass having a $SiO_2$ tetrahedron as the oxide forming network. For bone tissue regeneration, BG in various preparations has been produced since 45S5. From 1969 to 1971, three types of glass with different compositions based on the the $Na_2O$–CaO–$SiO_2$ ternary state diagram were evaluated as shown in Figure 4 to create a viable biomaterial. In the human body without scarring around it (Fiume et al. 2018).

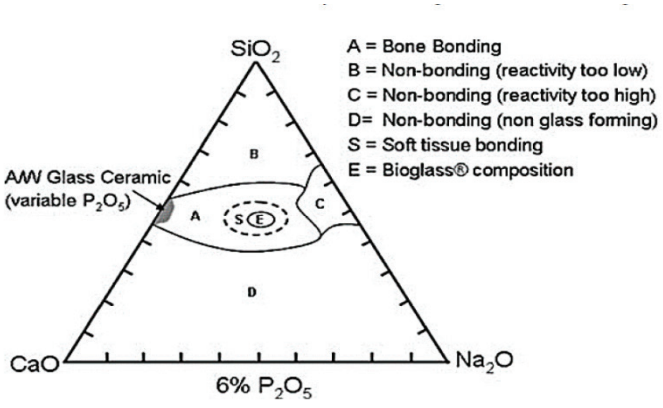


**Figure 4. Diagram For Bone-Bonding. S Region is Defined as the Region Where BG Bond Soft Tissues and Bone (Fiume et al., 2018).**

Bioactive glass consists of $SiO_2$, $Na_2O$, CaO and $P_2O_5$ of various compositions. Compared to conventional soda-lime glass, BG has a lower amount of silica, a higher amount of CaO and $Na_2O$, and a higher calcium to phosphorus ratio. Table 4 shows the composition of different types of bioactive glasses. The high calcium/phosphate ratio stimulates the formation of apatite crystals and makes the surface highly reactive under physiological conditions when silicon and calcium ions act as nuclei for crystallization. There are four BG classes.

**1.** 35-60 wt% $SiO_2$, 10-50 wt% CaO, 5-40 wt% $Na_2O$: BGs are bioactive and can attach to bone and soft tissues with some formulations.

**2.** <35wt% $SiO_2$: non-glass forming

**3.** >50wt% $SiO_2$, <10 wt% CaO, <35 wt% $Na_2O$: Resorption of BGs in 10-30 days.

**4.** >65wt% $SiO_2$. BGs are not bioactive, and nearly inert (Nicholson and Connor 2002).

**Table 4. The Compositions of Various Types of Bioactive Glasses (Rahaman et al., 2011).**

| Composition (wt.%) | 45S5 | 13-93 | 6P53B | 58S | 70S30C | 13-93B1 | 13-93B3 | P50C35N15 |
|---|---|---|---|---|---|---|---|---|
| $Na_2O$ | 24..5 | 6.0 | 10.3 | 0 | 0 | 5.8 | 5.5 | 9.3 |
| $K_2O$ | 0 | 12.0 | 2.8 | 0 | 0 | 11.7 | 11.1 | 0 |
| MgO | 0 | 5.0 | 10.2 | 0 | 0 | 4.9 | 4.6 | 0 |
| CaO | 24.5 | 20.0 | 18.0 | 32.6 | 28.6 | 19.5 | 18.5 | 19.7 |
| $SiO_2$ | 45.0 | 53 | 52.7 | 58.2 | 71.4 | 34.4 | 0 | 0 |
| $P_2O_5$ | 6.0 | 4.0 | 6.0 | 9.2 | 0 | 3.8 | 3.7 | 71.0 |
| $B_2O_3$ | 0 | 0 | 0 | 0 | 0 | 19.9 | 56.6 | 0 |

BG can also be doped with cations other than $Na^+$ and $Ca^{2+}$ to provide additional adavanatages. These doping elements might be $Al^{3+}$,

$Mg^{2+}$, $Ag^{+}$, $K^{+}$, $Zn^{2+}$, etc. The ions added to the bioactive glass and their effects are shown in Figure 5

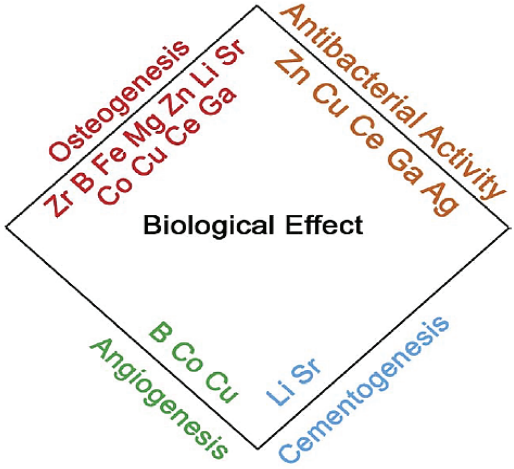


**Figure 5. The Ions Added to Bioactive Glasses and Their Effects (Kaya, Cresswell, and Boccaccini 2018)**

When BG is immersed in body fluids, it can produce bioactive HAp and bind to target bone tissues. Bioactive glass enhances osteogenic and cellular differentiation as it delivers silicon ions that activate the genetic transfer pathway (Miguez-Pacheco, Hench, and Boccaccini 2015; Wu, Zhu, and Tao 2013). They have the ability to bind to bones and have good biocompatibility. From 45S5, different compositions of BG have been developed for bone tissue regeneration. They have many advantages, such as controlled biodegradation and good bone bonding ability, making them excellent biomaterials for bone repair. It also releases ions with bone-forming potential (Huang, Xie, and Li 2020). The BG morphology is shown in Figure 3.

BG creates a calcium carbonated HAp layer on its surface when exposed to body fluids. This formed by BG layer promotes adhesion to adjacent bone tissue. Therefore, it can be said that BG has bioactivity (Ojansivu et al. 2015). The rate of disintegration can be controlled by changing the composition and manufacturing method. Therefore, it can be designed with a specific degradation rate to meet the requirements

of bone tissue. The two main manufacturing methods of BG are sol-gel and melt quenching method. It is as brittle like TCP. BG bones are not suitable for bearing load restoration because of their low fracture toughness and weak mechanical properties. However, the composite material can solve this problem by combining BG with a certain polymer with good mechanical properties (Huang, Xie, and Li 2020). BG can support angiogenesis, enzymatic activity and promote osteoblast adhesion, differentiation and growth. The biodegradation rate (biodegradability) and chemical properties can be changed by alternating the chemical and molecular structure of BG (Tariverdian et al. 2019).

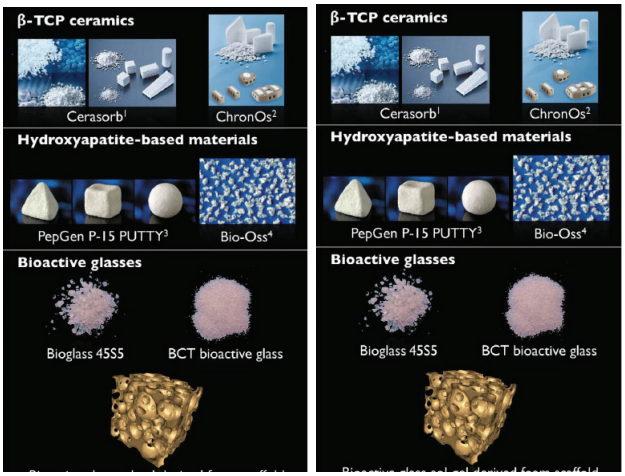


**Figure 3. The Morphology of Some Different Bone Scaffold Materials (Wu, Zhu, and Tao 2013)**

BG has been fabricated in a variety of sizes from a few millimeters to submicron powders and in a variety of shapes, such as rods, discs, porous scaffolds, fibers, spheres. They are used in various types of applications including nerve repair, periodontal defect repair, implant components for bone scaffolds, dental applications such a toothpaste ingredient, bioactive coating of metals plastics and ceramics, fiber recruitment for composites, vascular regeneration, etc. (Karasu et al. 2017). Table 3 shows the mechanical properties of the cortex and trabecular bone compared with 45S5 BG. Furthermore, by varying the components and their production methods, the degradation kinetics can be controlled.

Therefore, they can be engineered with high degradation rates to meet the needs of bone tissue (Huang, Xie, and Li 2020).

**Table 3. Mechanical Properties of Cortical and Trabecular Bone in Comparison with 45S5 BG (Filippi et al., 2020; Fiume et al., 2018)**

| Property | Trabecular bone | Cortical bone | 45S5 BG |
|---|---|---|---|
| Elastic modulus (GPa) | 0.05-0.1 | 11.5-18.9 | 35 |
| Tensile Strength (MPa) | 8-20 | 50-170 | 42 |
| Compressive Strength (MPa) | 4-12 | 130-180 | 500 |

### Bioactivity Mechanism of BGs

The bioactivity mechanism of BG occurs with formation of chemical bond between biomaterial and host tissue material. The bioactive mechanism of BG is mainly divided into two steps.

**1.** Formation of a carbonate-substituted hydroxyapatite (HCA) layer; It proceeds in five steps and leads to the crystallization of amorphous calcium phosphate.

**2.** Dissolution of ions in bioactive glass and bone formation; It causes mineralization of the ECM (Jones 2013).

### The HCA Layer Formation

This is the initial step in creating a bond between material and host tissue on the surface of the material. BG which dissolves in host tissue accumulate in the environment and change the physiological pH and chemical composition of body fluids. The HCA layer is formed in five steps (Fiume et al. 2018; Rahaman et al. 2011).

**1.** Ion exchange occurs between $H_3O^+$ and $H^+$ ions in the environment and $Na^+$ and $Ca^{2+}$ in substances as shown in the chemical reaction below. Si-OH (silanol bonds) are formed on the surface of the material, and the pH of the solution increases due to the release of alkali ions. This will form a silica-rich layer on the glass surface. If the composition contains these ions, $(PO_4)^{3-}$ ions are also released.

$$Si{-}O{-}Na^{+} + H^{+} \rightarrow Si{-}OH^{+} + Na^{+}(aq) \quad (1)$$

This reaction is very rapid and occurs in a few minutes after the bioactive glass is exposed to body fluids

**2.** Consumption of $H^{+}$ ions increase the $OH^{-}$ concentration and, consequently, it results in increasing the pH of the solution. This causes the silica to dissolve and form Si-OH groups on the bioactive glass surface.

$$Si{-}O{-}Si + H_2O \rightarrow Si{-}OH + OH{-}Si \quad (2)$$

**3.** Condensation of silanol groups and re-polymerization of an amorphous layer rich in $SiO_2$ occurs. This layer is lack of $Ca^{2+}$ and $Na^{+}$ ions. The layer thickness is 1-2 μm.

4. $Ca^{2+}$ and $(PO_4)^{3-}$ migrate out of solution due to the $SiO_2$-rich glass layer and further glass dissolution. This allows the formation of an amorphous calcium phosphate (ACP) layer on the $SiO_2$-rich layer.

$OH^{-}$ and $(CO_3)^{2-}$ are released from solution while the glass dissolves. The amorphous layer then becomes a crystallized HCA layer. The figure 6 shows the Scanning Electron Microscopy (SEM) image of the HCA layer on the BG surface after immersion in simulated body fluid (SBF) for 14 days.

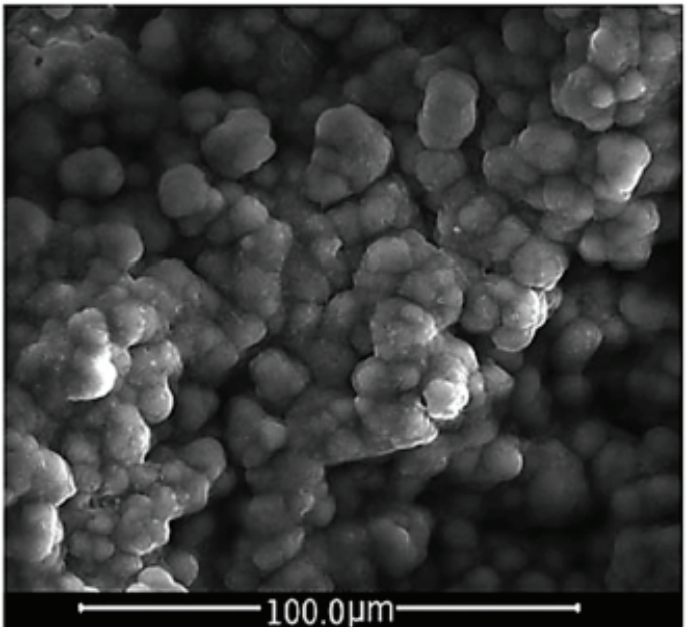


**Figure 6. SEM Image of Layer of HCA on the BG Surface After Soaking in SBF for 14 Days (Sola et al., 2011)**

**Ionic Dissolution and Osteogenesis**

The mechanism of glass-to-bone binding includes growth factor adsorption and the attachment, differentiation, and proliferation of bone progenitor cells. Bone-forming cells (osteoblasts) produce ECM, mainly collagen. During the glass transition and degredation, ECM mineralizes to form collagen and nanocrystalline minerals (Rahaman et al. 2011). The reaction steps for 45S5 bioactive glass are summarized in Table 5.

**Table 5. The Reaction Stages of 45S5 Bioactive Glass (Fiume et al., 2018)**

| Stage | Reaction event |
|---|---|
| 0 | Initial glass surface |
| 1 | Ion exchange |
| 2-3 | Silica dissolution and repolymerization |
| 4 | Precipitation of ACP |
| 5 | Crystallization of calcium phosphate to HCA |
| 6 | Adsorption of biological moieties |
| 7 | Action of macrophages |
| 8-9 | Stem cells attachment and differentiation |
| 10 | Cellular attachment |
| 11 | Crystallization of the matrix |

**Production of Bioactive Glasses**

Bioactive glass is produced through two processes: melt-quenching and sol-gel processes. These methods are used to obtain various BGs with different mechanical properties, bioactivity, porosity and distribution (Vichery and Nedelec 2016).

**Melt-derived Bioactive Glasses**

It is the first bioactive glass produced with melting method by Larry Hench. The method for synthesizing BG from the melt-derived is similar to the process for producing soda–lime–silica glass. The oxide and raw material (silica) are combined together at high temperature and then allowed to melt, followed by a quenching step (Vichery and Nedelec 2016). High purity reagents must be used to eliminate the risk of contamination. The melting process takes place at high temperatures between about 1200 °C and 1550 °C using an electrical furnace (oven). The mixture is then poured into a molding mold and dried to obtain a powder. Process parameters are adjusted to ensure a uniform melting without air bubbles. During processing, the melt viscosity should be less than a 100

Poise to avoid bubble formation. Melting times should be ranged from 1 h to 24 h depending on batch size and method of testing. Melting can be performed more than once to ensure high uniformity (Fiume et al. 2018).

**Sol-gel Derived Bioactive Glasses**

Nanoporous bioactive glass can be synthesized by the sol-gel method having a large surface area of 50 $m^2/g$ or more, therefore, sol-gel-BG exhibits higher levels of bioactivity and higher degradation rates than BG obtained from the melt. The surface area of BG produced by the melt quenching process is less than 1 $m^2/g$ (Fiume et al. 2018). Sol-gel bioactive glasses are synthesized by hydrolysis and polycondensation of alkoxide precursors. Tetramethylorthosilicate (TMOS) and tetraethylorthosilicate (TEOS) are often used as precursors. It is then subjected to aging and drying processes in the ambient atmosphere. Firstly, the reagents are blended at room temperature to build covalent bonds among the elements. Then hydrolysis and polycondensation take place until a homogeneous solution is obtained. The second step is the gelation step, which creates a three-dimensional mesh to increase the viscosity of the solution. In the third stage, aging takes place at a temperature of about 60°C. At this stage, the mechanical strength increases and the porosity decreases. The fourth step is to remove the liquid phase by heat treatment, usually at a temperature between 120°C and 140°C. After obtaining the dried gel in the last step, the material is stabilized at a high temperature of about 700 °C (Fiume et al. 2018).

**Bioactive Glass Combined Composite Scaffolds for Bone Tissue Engineering**

Composite scaffolds made of biodegradable polymers and bioactive glass were attractive for bone regeneration. Various amounts of polymers such as PLGA (poly(lactic-co-glycolide)), PLA (poly (lactic acid)), PGA (poly (glycolic acid)), chitosan, and collagen can be combined with BG to make composite scaffolds (Misra and Boccaccini 2007). A schematic diagram of the production of a composite frame combining polymer and bioactive glass is shown in Figure 7. In combination with biopoly-

mer matrices, fillers of various shapes can be used in the production of composites. These fillers can be nanoparticles, nanofibers and particles. (Verrier, Gough, and Boccaccini 2011).

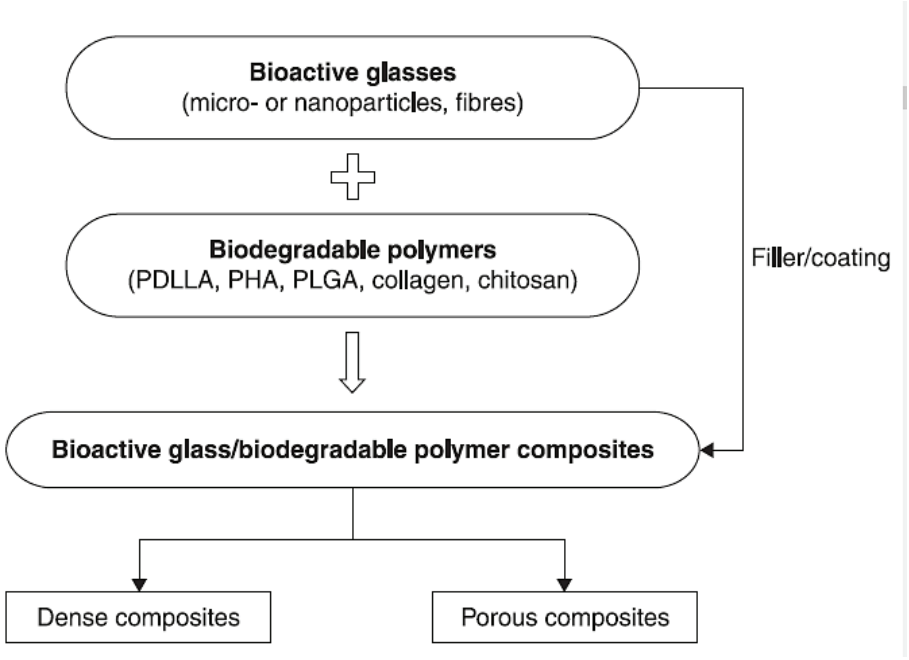


**Figure 7. Schematic illustration of Production of Composite Scaffolds Combining Polymers and Bioactive Glass (Verrier, Gough, and Boccaccini 2011)**

There are many reasons to combine polymers and BG for bone tissue regeneration. The polymers exhibit relatively low stiffness and compressive strength while being flexible. Therefore, they might not meet the mechanical requirements of a scaffold. On the other hand, BG are brittle and hard unlike bones. Furthermore, the ability to create efficient porous structures can be improved by the addition of bioactive glasses. BG also improve water absorption for scaffolds as they increase the number of internal contact surfaces between the hydrophilic glass beads and the polymer. The combination of BG with the polymer provides a scaffold to interact with adjacent bone tissue because a layer of hydroxyapatite carbonate forms on the surface of the BG and promotes the creation of a strong bond with the bone. Therefore, composite scaffolds are a signifi-

cant alternative for the treatment of the bone skeleton since their properties can be tailored to the physiological and mechanical nature of bone tissue by glass incorporation bioactive with polymeric substrates (Lu et al. 2003).

Studies have shown that bioactive glass nanoparticles can be combined with polymers to increase their volume fraction and higher surface area-to-volume ratio to promote bioactivity (Rezwan et al. 2006). In addition, BG can enhance cell growth and differentiation, growth factor synthesis according to BG content (Verrier, Gough, and Boccaccini 2011). Figure 8 shows the biological response to bioactive glass.

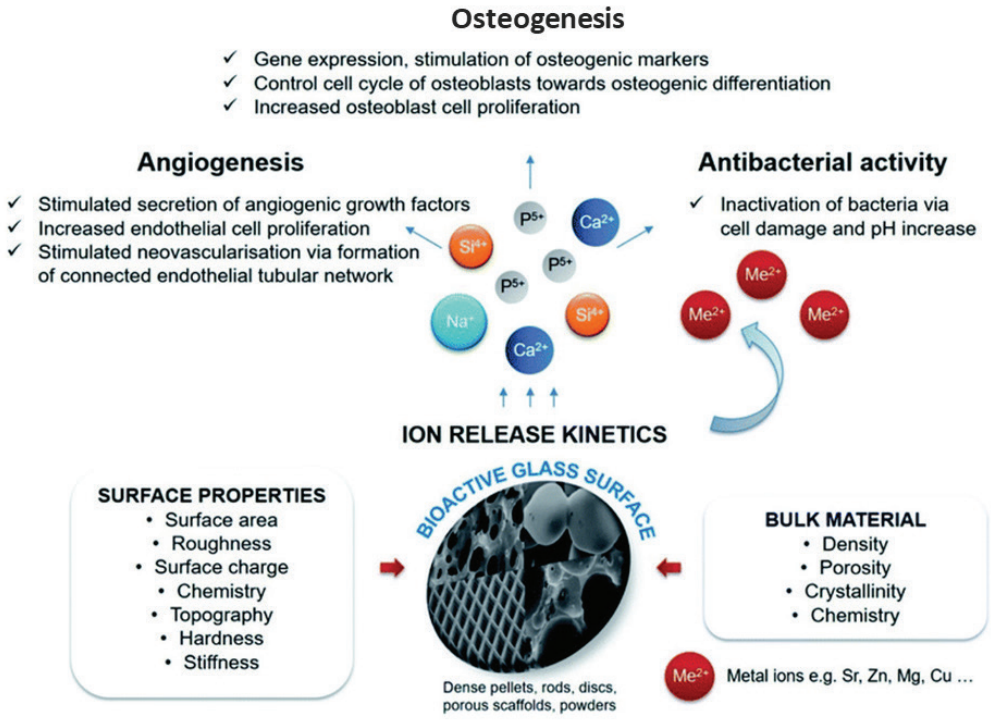


**Figure 8. Biological Response Against Bioactive Glasses (Deshmukh et al., 2020)**

### Sol-Gel Derived Bioactive Glass Nanoparticles

Bioactive glass nanoparticles (BGNPs) have been synthesized through conventional fusion strategy or sol-gel methods. Compared

with the fusion-derived BG, the sol-gel-derived BG was synthesized at a lower temperature (Treccani et al. 2013). In the melt-quenching method, it is difficult to control the properties of BG. In addition, fusion-derived BG exhibit non-uniform size distribution and irregular shape. This method requires complex equipment. On the other hand, the sol-gel method produces BG of more controllable size and shape because the precursor solutions are stirred and reacted under liquid conditions in a controlled manner. In addition, this method reduces equipment complexity and stabilization of the resulting BG is performed at lower temperatures than melt-quenching. Thus, the sol-gel route is very versatile and practical for the production of bioactive glass by providing chemically pure and homogeneous biomaterials (Baikousi et al. 2008; Zheng and Boccaccini 2017).

The sol-gel method produces nanoscale BG with high specific surface area. Most studies indicate that BGNPs are larger than 100 nm in size with submicron scale, although the nanoparticles range in size from 1 to 100 nm (Vichery and Nedelec 2016). F Figure 9 illustrates the sol-gel protocol for BGNP production. The sol-gel method is a process for synthesizing bioactive glasses from metal ions and silicate tetrahedral. This method includes condensation and hydrolysis of precursors, drying and stabilization. The morphology and composition of the material can be adjusted by varying the factors of the process. TEOS is the most commonly used silicate precursor for sol-gel-derived BGs. Ethanol and water were used as solvents (Hench and West 2002). This method occurs under basic or acidic conditions that affect the properties of the material. Different morphologies of BG can be obtained by varying the pH.

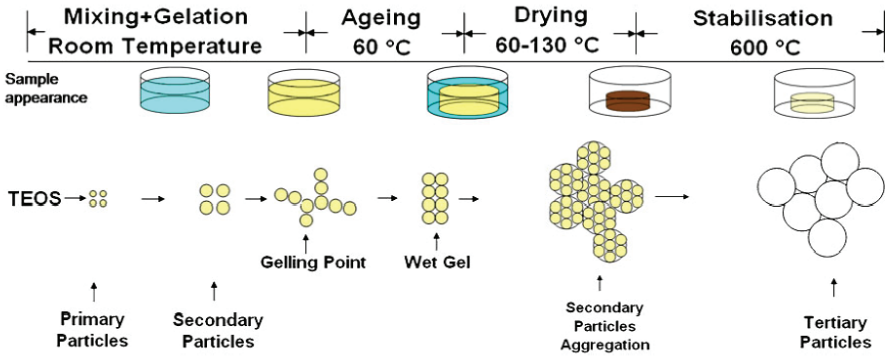


**Figure 9. Sol-Gel Protocol of BGNPS Production (Baikousi et al., 2008)**

First, TEOS undergoes hydrolysis and condensation under the action of a catalyst to form $SiO_2$ nanoparticles. Metal ion precursors such as nitrates can be added after synthesis of $SiO_2$ nanoparticles or during hydrolysis and condensation of TEOS. The nanoparticles are then dried and calcined to produce BGNPs. Organic substances can be added during synthesis to improve the dispersion and shape of the bioactive glass nanoparticles. Table 6 summarizes some studies on BGNP production by the sol-gel method.

**Table 6. BGNPs by The Sol-Gel Method with Sizes, Surface Area and Pore Sizes**

| Composition (Si:Ca:P) | Size (nm) | Surface Area ($m^2/g$) | Pore Size (nm) | Reference |
|---|---|---|---|---|
| 0.80:0.15:0.05 | 250 | 949 | 2.6 | (Li et al. 2015) |
| 0.82:0.09:0.09 | 400 | 275-484 | 3.5-3.9 | (Arcos et al. 2009) |
| 0.77:0.15:0.08 | 187-294 | 444-972 | 4.6-8.8 | (Hu et al. 2014) |
| 0.77:0.15:0.08 | 150 | 318-455 | 3.7 | (Li et al. 2015) |
| 0.79:0.17:0.04 | 30 | 1040 | 2.2 | (Yun et al. 2010) |
| 0.58:0.35:0.08 | 28-254 | 151-684 | 5.1-14 | (Liang et al. 2015) |

Characteristics of BG derived from sol-gel:

- BG derived from the sol-gel method has a mesoporous structure with a pore diameter of 2 to 50 nm.
- The sol-gel process provides the surface of the material with functional silanol groups that are important for site formation in the HAp and HCA layers.
- These BGs have a large surface area, which improves solubility, reactivity, and cellular response.
- Nanoporous particles can be obtained by adjusting the pH.
- They have a uniform size distribution.
- BG derived from the sol-gel method has chemically pure properties.
- The manufacturing process is relatively moderate temperatures
- BGNP rapidly promotes the formation of apatite when exposed to body fluids.
- The large surface area-to-volume ratio of BGNP improves its incorporation into the polymer matrix.
- Due to its nanoporous structure, it has advantages when used in drugs and biomolecules.
- The smaller the size, the easier it is to be taken up by cells.
- BG from sol-gel exhibits higher bioactivity and decomposition rate than BG obtained from melt. The number of small-diameter pores is increasing (Baino et al. 2018; Karakuzu-Ikizler et al. 2020; Zheng and Boccaccini 2017).

Sol-gel methods used to form BGNP include base-catalyzed (Stöber), acid / base co-catalyzed methods, post-modification sol-gel-derived NP, microemulsion, and aerosol-assisted sol-gel method. Figure 10 shows BGNP synthesized in various ways**.**

The base-catalyzed sol-gel method is a method in which TEOS is added to a solution containing alcohol, ammonium hydroxide and water. By varying the TEOS/$H_2O$ ratio and pH, the morphology and size of the particles can be altered. The repulsion occurs due to the $OH^-$ groups, which causes the monodisperse BGNPs to form spheres. In this method, pore-forming agents (PFAs) such as cetrimonium bromide cationic surfactant (CTAB), a cationic surfactant, is commonly used to generate mes-

oporous BGNP (Stöber, Fink, and Bohn 1968). The shape of BGNPs by base catalysis can be spherical, ellipsoid, hollow or rod-shaped (Zheng and Boccaccini 2017)

The acid/base co-catalyzed sol-gel method is a method in which metal ions and TEOS precursors are mixed under acidic conditions. Then, concentrated base catalysts are added to form the nanoparticles. Monodisperse BGNP can be produced using a weak organic acid such as citric acid. PEG can be used as a non-ionic surfactant to improve BGNPs' size and dispersion (Zheng and Boccaccini 2017).

Post-modification can be applied to simplify BGNP synthesis. There are two modification strategies for BG. The first is to immerse the beads in a salt solution or to create metal nanoparticles on top of $SiO_2$–CaO particles or $SiO_2$ particles. This method allows metal ions to be incorporated into BGNPs (Zheng and Boccaccini 2017).

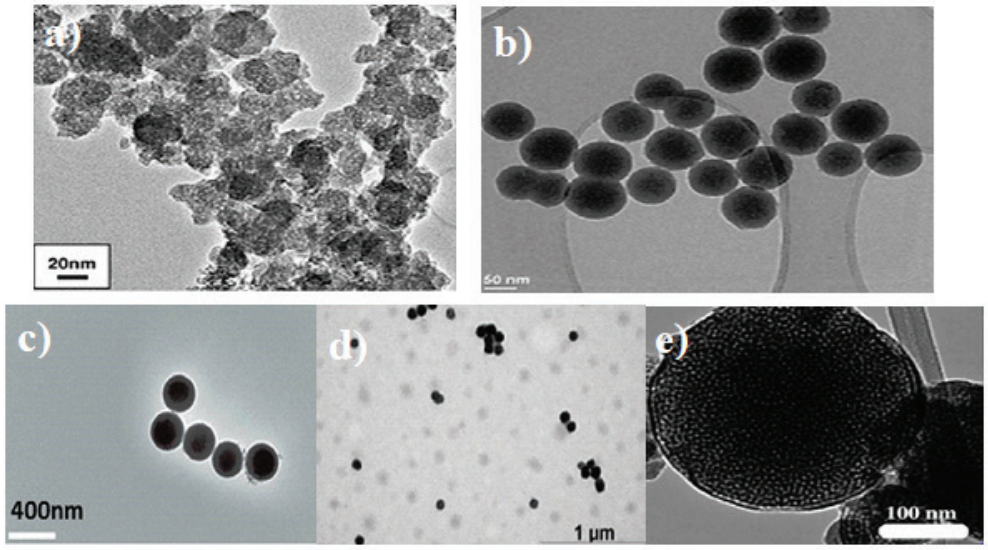


**Figure 10. BGNPs Structures Synthesized by a) Acid/Base Co-Catalyzed Method, b) Post-Modification Method, c) Base-Catalyzed Method, d) Microemulsion-Assisted Sol-Gel Method and e) Aerosol-Assisted Sol-Gel Method (Zheng and Boccaccini 2017)**

Another method for generating BGNPs is the microemulsion-assisted sol-gel method. Microemulsions are liquid mixtures containing water

phase, oil phase and surfactants and they are thermodynamically stable. BGNPs are formed by reverse microemulsion (water dispersed in oil) method. The aqueous phase consists of metal ion precursors, catalysts, and silicate precursors. Condensation and hydrolysis of silicate precursors occurs in water droplets. These droplets act like a reactor and they randomly collide and combine to create larger droplets. The oil phase functions as a barrier preventing the agglomeration of nanoparticles and the surfactants stabilize these droplets. Therefore, the obtained nanoparticles have a uniform composition. The oil phase and surfactants such as CTAB are removed by washing before drying and heating. Using this method, it is possible to generate neutral BGNPs with sizes ranging from 28-250 nm and conifer or spherical shapes (Zheng and Boccaccini 2017).

The aerosol-assisted solgel method was used to make 45S5 bioactive glass using a flame. Mesh-like BGNPs with specific structures were synthesized using an aerosol technique with sol-gel treatment. In this process, an aerosol dispersion is formed by dissolving the precursor and surfactant in the solvent. This dispersion was then used to produce BGNP by warping (Zheng and Boccaccini 2017).

## RESULTS

Because of their high biocompatibility, bioactivity, non-toxicity, osteoconductivity, and non-inflammatory properties, bioactive glasses have proven to be viable biomaterials for hard and soft tissue regeneration. They also promote osteogenesis and differentiation (Vichery and Nedelec 2016). BG can help osteoblasts adhere, differentiate, and develop by promoting vascularization, enzyme activity, and adhesion, differentiation, and growth. They have the ability to build a strong, quick, and stable connection with tissues. Bioactive glass is the first example of third-generation biomaterials since it has a biological role through its products via ionic dissolution, may be released under physiological conditions, and forms a strong link with the host bone tissue through the creation of calcium phosphate layers. BG are calcium and phosphate-based silica glasses. They create bioactive HAp after being exposed to human fluids and can bind to target tissues. Bioactive glass-based medicinal products are frequently utilized in dentistry and ortho-

pedics for the restoration of calcified tissues, including bone. As a result, they are referred to as bioactive materials. Bioactive glass is also used for soft tissue regeneration due to its potential for nerve regeneration, neochondral formation, and angiogenesis (Basaran Elalmis et al. 2021; Fiume et al. 2018).

Bioactive glass nanoparticles are proliferating significantly in a variety of tissue engineering applications due to their important properties. BGNP is an excellent biomaterial with a large specific surface area, small size, and high surface area-to-volume ratio. BGNP has these excellent morphological properties and can deliver biomolecules such as growth factors and drugs, which is a great advantage over other micrometer-sized particles.

BGNP has morphological properties that are uniformly incorporated into the polymer matrix. The use of BGNP as a filler in the polymer phase is aimed at improving the biological and mechanical performance of the scaffold through proper in vivo interaction with bone and supporting bone integration through the formation of a calcium phosphate layer. Therefore, it can be said that BGNP promises building blocks for the manufacture of composite scaffold.

The sol-gel process increases the surface area and porosity of bioactive glass nanoparticles, thereby increasing the ability of BG to act as a carrier for controlled release of biomolecules. BG derived from the sol-gel method has a mesoporous structure with a pore size of 2 to 50 nm and provides a functional silanol group on the material surface that is important for site formation of HAp and HCA layers. The large surface area of these BGs improves their solubility, reactivity, and cell responsiveness. They have a uniform size distribution, and the manufacturing process is relatively cold. BGNP rapidly promotes the formation of apatite when exposed to body fluids. The large surface area-to-volume ratio of BGNP improves its incorporation into the polymer matrix.

## REFERENCES

Ansari, Mojtaba. 2019. "Bone Tissue Regeneration: Biology, Strategies and Interface Studies." *Progress in biomaterials* 8(4): 223–37.

Arcos, D. et al. 2009. "Ordered Mesoporous Microspheres for Bone Grafting and Drug Delivery." *Chemistry of Materials* 21(6): 1000–1009.

Baikousi, M. et al. 2008. "Synthesis and Characterization of Sol-Gel Derived Bioactive CaO-SiO 2-P2O5 Glasses Containing Magnetic Nanoparticles." *Journal of Sol-Gel Science and Technology* 47(1): 95–101.

Baino, Francesco, Elisa Fiume, Marta Miola, and Enrica Verné. 2018. "Bioactive Sol-Gel Glasses: Processing, Properties, and Applications." *International Journal of Applied Ceramic Technology* 15(4): 841–60.

Basaran Elalmis, Yeliz et al. 2021. "Investigation of Alumina Doped 45S5 Glass as a Bioactive Filler for Experimental Dental Composites." *International Journal of Applied Glass Science* 12(3): 313–27.

Behzadi, Shahed et al. 2017. "Nanomedicine for Safe Healing of Bone Trauma: Opportunities and Challenges." *Biomaterials* 146: 168–82.

Boyan, B. D., D. J. Cohen, and Z. Schwartz. 2017. "Bone Tissue Grafting and Tissue Engineering Concepts." *Comprehensive Biomaterials II*: 298–313.

Chocholata, Petra, Vlastimil Kulda, and Vaclav Babuska. 2019. "Fabrication of Scaffolds for Bone-Tissue Regeneration." *Materials* 12(4).

Deshmukh, Kalim et al. 2020. "Recent Advances and Future Perspectives of Sol–Gel Derived Porous Bioactive Glasses: A Review." *RSC Advances* 10(56): 33782–835.

Elalmış, Yeliz et al. 2019. "The Role of Matrix Metalloproteinases in Bone Tissue." In *A Closer Look at Metalloproteinases*, ed. Lena Goodwin. New York, NY, USA: Nova Science Publishers, Inc., 153–249.

Filippi, Miriam, Gordian Born, Mansoor Chaaban, and Arnaud Scherberich. 2020. "Natural Polymeric Scaffolds in Bone Regeneration." *Frontiers in Bioengineering and Biotechnology* 8: 474.

Fiume, Elisa, Jacopo Barberi, Enrica Verné, and Francesco Baino. 2018. "Bioactive Glasses: From Parent 45S5 Composition to Scaffold-Assisted Tissue-Healing Therapies." *Journal of functional biomaterials* 9(1).

Hench, Larry L., and Jon K. West. 2002. "The Sol-Gel Process." *Chemical Reviews* 90(1): 33–72.

Hu, Qing et al. 2014. "Facile Synthesis of Hollow Mesoporous Bioactive Glass Sub-Micron Spheres with a Tunable Cavity Size." *Materials Letters* C(134): 130–33.

Huang, Yi-Zhou, Hui-Qi Xie, and Xiaoming Li. 2020. "Scaffolds in Bone Tissue Engineering: Research Progress and Current Applications." In *Encyclopedia of Bone Biology*, Elsevier, 204–15.

Jones, Julian R. 2013. "Review of Bioactive Glass: From Hench to Hybrids." *Acta Biomaterialia* 9(1): 4457–86.

Karakuzu-Ikizler, Burcu et al. 2020. "Role of Magnesium and Aluminum Substitution on the Structural Properties and Bioactivity of Bioglasses Synthesized from Biogenic Silica." *Bioactive Materials* 5(1): 66–73.

Karasu, B et al. 2017. "Bioactive Glasses." *El-Cezerî Journal of Science and Engineering* 4(3): 436–71.

Kaya, Seray, Mark Cresswell, and Aldo R. Boccaccini. 2018. "Mesoporous Silica-Based Bioactive Glasses for Antibiotic-Free Antibacterial Applications." *Materials Science and Engineering: C* 83: 99–107.

Keaveny, T. M. 1998. "Cancellous Bone." *Handbook of Biomaterial Properties*: 15–23.

Kular, Jasreen, Jennifer Tickner, Shek Man Chim, and Jiake Xu. 2012. "An Overview of the Regulation of Bone Remodelling at the Cellular Level." *Clinical biochemistry* 45(12): 863–73.

Li, Yuli et al. 2015. "Facile Synthesis of Mesoporous Bioactive Glasses with Controlled Shapes." *Materials Letters* 161: 605–8.

Li, Yunqi, Bishnu Prasad Bastakoti, and Yusuke Yamauchi. 2015. "Smart Soft-Templating Synthesis of Hollow Mesoporous Bioactive Glass Spheres." *Chemistry – A European Journal* 21(22): 8038–42.

Liang, Qiming et al. 2015. "A Facile Synthesis of Novel Mesoporous Bioactive Glass Nanoparticles with Various Morphologies and Tunable Mesostructure by Sacrificial Liquid Template Method." *Materials Letters* 148: 45–49.

Lu, Helen H., Saadiq F. El-Amin, Kimberli D. Scott, and Cato T. Laurencin. 2003. "Three-Dimensional, Bioactive, Biodegradable, Polymer–Bioactive Glass Composite Scaffolds with Improved Mechanical Prop-

erties Support Collagen Synthesis and Mineralization of Human Osteoblast-like Cells in Vitro." *Journal of Biomedical Materials Research Part A* 64A(3): 465–74.

Miguez-Pacheco, Valentina, Larry L. Hench, and Aldo R. Boccaccini. 2015. "Bioactive Glasses beyond Bone and Teeth: Emerging Applications in Contact with Soft Tissues." *Acta Biomaterialia* 13: 1–15.

Misra, S. K., and A. R. Boccaccini. 2007. "Biodegradable and Bioactive Polymer/Ceramic Composite Scaffolds." *Tissue Engineering Using Ceramics and Polymers*: 72–92.

Nicholson, John W., and J. A. Connor. 2002. "Ceramics." In *The Chemistry of Medical and Dental Materials (RSC Materials Monographs)*, ed. John W. Nicholson. Royal Society of Chemistry, 63–106.

Ojansivu, Miina et al. 2015. "Bioactive Glass Ions as Strong Enhancers of Osteogenic Differentiation in Human Adipose Stem Cells." *Acta Biomaterialia* 21: 190–203.

Polo-Corrales, Liliana, Magda Latorre-Esteves, and Jaime E. Ramirez-Vick. 2014. "Scaffold Design for Bone Regeneration." *Journal of nanoscience and nanotechnology* 14(1): 15–56.

Qu, Huawei, Hongya Fu, Zhenyu Han, and Yang Sun. 2019. "Biomaterials for Bone Tissue Engineering Scaffolds: A Review." *RSC Advances* 9(45): 26252–62.

Rahaman, Mohamed N. et al. 2011. "Bioactive Glass in Tissue Engineering." *Acta biomaterialia* 7(6): 2355–73.

Rezwan, K., Q. Z. Chen, J. J. Blaker, and Aldo Roberto Boccaccini. 2006. "Biodegradable and Bioactive Porous Polymer/Inorganic Composite Scaffolds for Bone Tissue Engineering." *Biomaterials* 27(18): 3413–31.

Saravanan, S., R. S. Leena, and N. Selvamurugan. 2016. "Chitosan Based Biocomposite Scaffolds for Bone Tissue Engineering." *International Journal of Biological Macromolecules* 93: 1354–65.

Sola, A., D. Bellucci, V. Cannillo, and A. Cattini. 2011. "Bioactive Glass Coatings: A Review." *Surface Engineering* 27(8): 560–72.

Stöber, Werner, Arthur Fink, and Ernst Bohn. 1968. "Controlled Growth of Monodisperse Silica Spheres in the Micron Size Range." *Journal of Colloid and Interface Science* 26(1): 62–69.

Tal, Haim, Ofer Moses, Avital Kozlovsky, and Carlos Nemcovsky. 2012. "Bioresorbable Collagen Membranes for Guided Bone Regeneration." In *Bone Regeneration*, IntechOpen, 111–38.

Tariverdian, Tara, Farshid Sefat, Michael Gelinsky, and Masoud Mozafari. 2019. "Scaffold for Bone Tissue Engineering." *Handbook of Tissue Engineering Scaffolds: Volume One*: 189–209.

Treccani, Laura et al. 2013. "Functionalized Ceramics for Biomedical, Biotechnological and Environmental Applications." *Acta Biomaterialia* 9(7): 7115–50.

Verrier, S., J. E. Gough, and A. R. Boccaccini. 2011. "Bioactive Glass Containing Composites for Bone and Musculoskeletal Tissue Engineering Scaffolds." *Bioactive Glasses: Materials, Properties and Applications*: 162–88.

Vichery, Charlotte, and Jean-Marie Nedelec. 2016. "Bioactive Glass Nanoparticles: From Synthesis to Materials Design for Biomedical Applications." *Materials* 9(4).

Wang, Xiaojian et al. 2016. "Topological Design and Additive Manufacturing of Porous Metals for Bone Scaffolds and Orthopaedic Implants: A Review." *Biomaterials* 83: 127–41.

Wu, Li, Fufan Zhu, and Guangshi Tao. 2013. "In-Vitro Biocompatibility Evaluation of Collagen-Hyaluronic Acid/Bioactive Glass Nanocomposite Scaffold." *Journal of Macromolecular Science, Part A* 50(11): 1121–25.

Yun, Hui suk, Sang hyun Kim, Soyoung Lee, and In hyuck Song. 2010. "Synthesis of High Surface Area Mesoporous Bioactive Glass Nanospheres." *Materials Letters* 64(16): 1850–53.

Zheng, Kai, and Aldo R. Boccaccini. 2017. "Sol-Gel Processing of Bioactive Glass Nanoparticles: A Review." *Advances in Colloid and Interface Science* 249: 363–73.

# IDEOLOGY DETECTION USING TRANSFORMER-BASED MACHINE LEARNING MODELS

*Oktay ÖZTÜRK[1], Alper ÖZCAN[2]*

**Abstract:** Ideology detection has been a challenging but essential problem that has been studied for a long time. Certain groups and organizations, such as politicians, rely on people's political views to make wise or forward-looking decisions. In the previous days, intensive survey studies were needed to collect the opinions of the people, and it was a very laborious and challenging process to analyze the political tendencies of the citizens. For example, it was observed that the answers given to the questions asked when people were not anonymous while participating in the surveys were biased or abstained. For this reason, the results of classical survey methods are open to discussion. Today, many users on social media have become accessible data sources and are used extensively in political research. On social media platforms such as Twitter, people reflect their political views with the comments they share. Inspired by recent studies that have successfully modeled sentiment analysis, we use a dataset called the Ideological Books Corpus (IBC) to identify emerging political opinion in a sentence. By using natural language processing methods, we delete unnecessary words, punctuation marks and apply Bidirectional Encoder Representations from Transformers (BERT), Long Short Term Memory (LSTM), Support Vector Machine, Decision Trees (Decision Trees), and Naive Bayes Classifier methods. As a result, it has been observed that the ELECTRA outperforms the other approaches we have used in terms of the F1-score performance metric.

1 Nişantaşı University, Computer Engineering, İstanbul / Türkiye, oktay.ozturk010@gmail.com, Orcid No: 0000-0001-5260-7312

2 Nişantaşı University, Computer Engineering, İstanbul / Türkiye, alper.ozcan@nisantasi.edu.tr, Orcid No: 0000-0002-5999-1203

***Keywords:*** Transformer-Based Models, Deep Learning, Ideology Detection, BERT, ELECTRA

## INTRODUCTION

In this modern era, where we are surrounded by the internet and media, the world has become a global village. The news travels fast from the past decades because of the advancement such as live telecasting and lives streaming these days. However, the writing medium of the news and content is still available at every platform, either in the libraries where books are occupying the large surface area or the internet where a person can find digital libraries, social media platforms where a person can share his/her ideology. Different sort of issues is being discussed at the internet especially at the social media platforms such as Twitter, Facebook, Reddit, etc. However, the political debate becomes controversial on such platforms when a politician discusses his/her ideology on such platforms. The media agencies are called biased as there might be a political affiliation of any news agency with political groups (Groseclose and Milyo, 2005). It is vital to analyze the thoughts and statements given by such entities to provide the appropriate answer to the public or users without any biases.

In the past, analyzing the biases of the ideology of a politician was determined manually. Some experts used to analyze and crack the biases of any statement given by the politician. In this era of big data, where multiple statements in the form of text, audio, and video are generated by such entities, it is costly to analyze each text document manually. Most of the time, the biased term or statement is present in a tiny portion of the whole document, and it would be a wastage of time to read and crack the whole document and look for such a portion. Moreover, it is challenging to pick the bias term from the document, even for humans. It requires sufficient knowledge to crack specific information as the semantics of political statements can be very tricky.

In past studies, different techniques have been used to detect bias statements. Initially, the techniques such as Bag of Words in (Gentzkow and Shapiro, 2010) have been used by this study. These techniques used some of the pre-defined words present in the dictionary and searched the

document-based of those specific words. For such studies, there should be a large number of vocabulary present in your dictionary. Moreover, these kinds of studies only fetch the overall perspective of the document that may lead to false assumptions. Multiple studies are using machine learning techniques to detect political, sentimental analysis. In this study (Schwarz, 2019), the author applied three classifiers of SVR to classify the political texts from multiple datasets.

Deep learning has shown promising results in the field of computer sciences. The robustness of deep learning models is being anticipated by every researcher, and it is being used in every field of research. It is showing promising results in the field of natural language processing. Multiple deep learning models have been used in the sentiment analysis and to detect political bias analysis in political documents. In this study, we classify political sentences with traditional machine learning and deep learning models. To our knowledge, we are the first study that applies transformer-based models to ideology detection. We also shared benchmarking of transformer-based models, including BERT and ELECTRA, with various prevalent machine-learning and deep learning methods such as support vector machines, random forest, Naïvebayes, Long Short term Memory (LSTM) (Hochreiter & Schmidhuber, 1997), and BiLSTM. For this purpose, Ideological Book Corpus (IBC) (Sim et al., 2013) dataset has been used in training and testing phases, which political sentences that labeled as liberal, conservative, and neutral.

The rest of the paper is organized as follows. After discussing related ideology detection studies in Related Works, we explain the dataset that is used in the Dataset section. In the method section, we provide brief knowledge about various ideology detection methods that are used in this research. In the Evaluation section, we describe our experimental setup, and we shared the results of the experiments in the Experimental Results section. Finally, we conclude our study in the Conclusion section.

## RELATED WORK

Iyyer et al. applied the tree structure recurrent neural networks because it captures the systematic composition of the text in a document

(Iyyer et al., 2014). This study achieved better results from the previous ones as it is using recurrent neural networks and achieved better performance as it includes the sentimental analysis, paraphrase detection, and parsing of the document. Moreover, in this study, the words were represented as a feature vector from a phrase. As the paragraph contains multiple phrases and each phrase is a combination of multiple words, so, merging these phrases provides the overall contextual meaning of the paragraph. The model was applied on the modified version of the Congressional debates dataset in which the data was annotated for ideological biases. By using this data set, the political position was determined by the sentence analysis.

Hojoon and Minbyul found that RNN's was suffering from gradient vanishing problems for the long sentences (Hojoon and Minbyul, 2017). To overcome the mentioned problem, the proposed study used LSTM's. Moreover, to enhance the performance of the model, this study used convolutional neural networks. For the evaluation of their model, this study used an Ideological book Corpus data set (IBC) that contains the magazine articles and books from the year 2008 to 2012. As each sentence contains various lengths of words, so this model uses 300-dimensional vectors for each word. Moreover, to match the input size of each sentence, it uses the same scale padding as Google word2vec. This study achieved an accuracy of 71% by using different models, but the best performance was achieved from LSTM's.

Juliana Schwarz proposed three different SVM classifiers for three different datasets (Schwarz, 2019). The first classifier was applied to the YouTube data set. In this data set, 500 comments were scrapped from YouTube and were manually labeled on the topic of the Mueller report. The second classifier was applied on the Twitter dataset that consists of tweets between specific time frames from presidential candidates. Finally, the third classifier was applied to the party manifesto dataset gathered from party electoral manifestos. The accuracy of 79%, 60%, and 54% was achieved in the case of YouTube comments, Twitter dataset, and electoral manifestos, respectively.

Kulkarni et al. proposed a new model called MVDAM that is different from other traditional models (Kulkarni et al., 2018). The tradi-

tional models only focus on the textual information, but this model also emphasizes the link structure such as hyperlinks on the digital sources as well as homophily between the news sources that share the same political ideology. This model estimates the political ideology present in a document and ranks them according to the ideology. The dataset was collected from 59 U.S. sources, and the results are 10% better in the case of F1 scores.

Xi et al. proposed a deep learning-based study that detects the affiliation of the specific politician from the party and his ideology (Xi et al., 2019). There are many images present on social media platforms that represent the ideological information of any politician and his party. In this study, the author predicted the affiliation of the U.S politician to their respective parties as well as the sentiment analysis that can be obtained from the images that politicians publish on social media platforms. This method achieved an accuracy of 59.28% when a single image is used to determine the class and 82.35% after aggregating the result from multiple photographs.

Misra and Basak used a deep learning-based methodology to detect the biases of an individual politician belong either to a liberal or conservative point on the issue of environment and socioeconomics (Misra and Basak, 2015). This study focuses on the individual statements given by politicians and analyzes the biases by using deep learning models such as LSTMs. As RNNs based studies predict the next word for the sentence, but in this methodology, LSTMs are used as a classifier that predicts the label at the end of a sequence. The dataset used for this research is IBC, and it achieved an F1 score of 0.718.

Lazaridou and Krestel presented research motivated by the power of journalism as the media outlets contain different mediums of publishing the news, e.g., Television, Newspapers, articles to inform the public. The statements given by each person on such mediums can be represented as accidental or deliberate bias. This study reveals the different patterns that a newspaper can follow for publishing their stories by applying *ElasticSearch*. The dataset used in this research comprised of the collection of articles from newspaper agencies such as the Guardian,

Telegram and the third dataset is speeches used in the U.K. parliament (Lazaridou and Krestel, 2016).

Gangula et al. presented another method to detect the political bias in news articles by using headline attention (Gangula et al., 2019). This study contains two distinct characteristics 1) it uses such a structure that mirrors the reading style of the person 2) the attention mechanism is applied to the headline of the newspaper/article. The attention mechanism enables the bias on the critical content of the article by using the bidirectional LSTMs. The dataset includes 1329 news articles from a specific Indian state. This model achieved an accuracy of 89.54 that is much better than other studies in this research area.

Sandeepa Kannangara proposed a model called JEST that classify the three aspects of the ideology. 1) Fine-Grained Political Opinion Polarity Classification in which the model tries to find and extract multiple targets such as different candidates of political parties, different topics discussed in the cabinet meetings such as problems of refugees, and sentiment analysis either positive, negative, or neutral. 2) Political Orientation Detection is detected by using the Twitter information of the users. The user's opinion is taken from the different tweets about the political candidates and identifies the sentiments. 3) Sarcasm Detection in Political Tweets is detected using both famous techniques present in the literature that is linguistic and contextual. By using both techniques and features, the model detects sarcastic tweets (Kannangara, 2018).

(Dinkov et al.) proposed a new deep learning model to predict political ideology. All the previous studies focused on extracting sentimental and contextual information from the text. This study generated a new data set that comprised of YouTube videos. To find the affiliated videos with the political parties, this study searched their political channels and downloaded a sample of videos. The model is comprised of multiple techniques to achieve the highest efficiency possible. The study used previous models such as NELA, i-vectors, and BERT for different purposes. This study produced multimodal data and developed a multimodal deep learning architecture for this specific task. The acoustic signal is used to achieve the politicians' bias, and the achieved results

indicate that this model produces better results than the traditional text-based models (Dinkov et al., 2019).

## METHOD

In this study, as a result of BERT's superior success over other language techniques, we fine-tune the transformer-based models that detect different ideologies from English sentences. BERT and ELECTRA have been used as transformer-based deep learning models for ideology detection. In addition to transformer-based models, we also classify the IBC dataset with Recurrent Neural Networks (RNN), which are LSTM, BiLSTM. As mentioned, different types of methods applied in political ideology detection before. In line with this, various machine learning and deep learning-based approaches, which are explained below, are compared with transformer-based BERT and ELECTRA models. Also, the dataset that used in the training and testing phases is investigated below.

### Dataset

We performed initial experiments on a dataset of Ideology Book Corpus (IBC) (Sim et al., 2013). The Ideological Books Corpus (IBC) comprises 4,062 sentences annotated for political ideology at the sub-sentential level. There are 2025 liberal sentences, 1701 conservative sentences, and 600 neutral sentences in this collection.

### Machine Learning

Machine learning is considered a part of artificial intelligence that deals with the electronic data. The general flow of machine learning methods is it takes an input and deals with that data in a specific manner or using human instructions. The data could be labeled or unlabeled, but it depends on the nature of the problem and the data availability. Based on the data the machine learning algorithms are divided into three categories 1) Supervised Learning 2) Unsupervised Learning 3) Semi supervised learning. However, for a machine learning algorithm the data gathered has greater importance. The quality and size of the

data is crucial for the machine learning model to predict the accurate and meaningful outcomes. The common example of such method could be the learning and predicting the documents-based data that comprises of finite collection of unseen documents labelled with respect to individual topics. Generally, the larger the sample size of the data, the easier is to predict accurate label. But it is not always the case, the labels in the document may not be accurate which effects the efficiency of the model. In the field of computer sciences, the quality and efficiency of the algorithm is generally measured by the time and space complexity. However, in machine learning algorithms we need to add a sample complexity as well that evaluates the sample size for the algorithm. As mentioned earlier in this field the success of the algorithm is generally dependent on the sample of the data so, many analysts consider it as a part of data analysis and statistics. (Mohri et al., 2018, pp. 1-2).

**Supervised Machine Learning**

In supervised machine learning training data, the learner is given a collection of labeled examples and can predict all unseen points. This is the most prevalent case encountered while dealing with classification, regression, and ranking tasks. Support Vector Machines (SVM), Decision Trees, and Naive Bayes can be defined as examples of supervised learning algorithms.

A training set is used in supervised learning to train models to produce the desired output. This training dataset contains both right and incorrect outputs, allowing the model to improve over time. The loss function is used to assess the algorithm's correctness, and it is adjusted until the error is suitably minimized. In Figure 1. the supervised machine learning workflow can be seen.

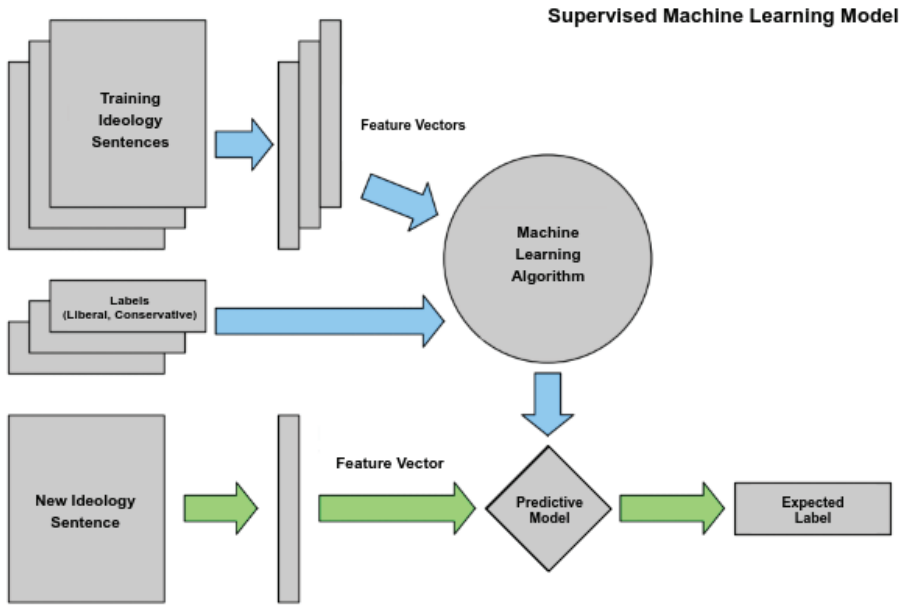


**Figure 1. Supervised Machine Learning Algorithm Workflow for Ideology Detection**

### Unsupervised Machine Learning

In unsupervised machine learning, the learner is only given unlabeled training data and must generate predictions for all unknown points. Unsupervised learning models are utilized for three main tasks—clustering, association, and dimensionality reduction. Because there are usually no labeled examples accessible in such situations, it might be difficult to quantify a learner's performance. K-means, k-nearest neighbors, principal component analysis can be defined as examples of supervised learning algorithms. In Figure 2. the supervised machine learning workflow can be seen.

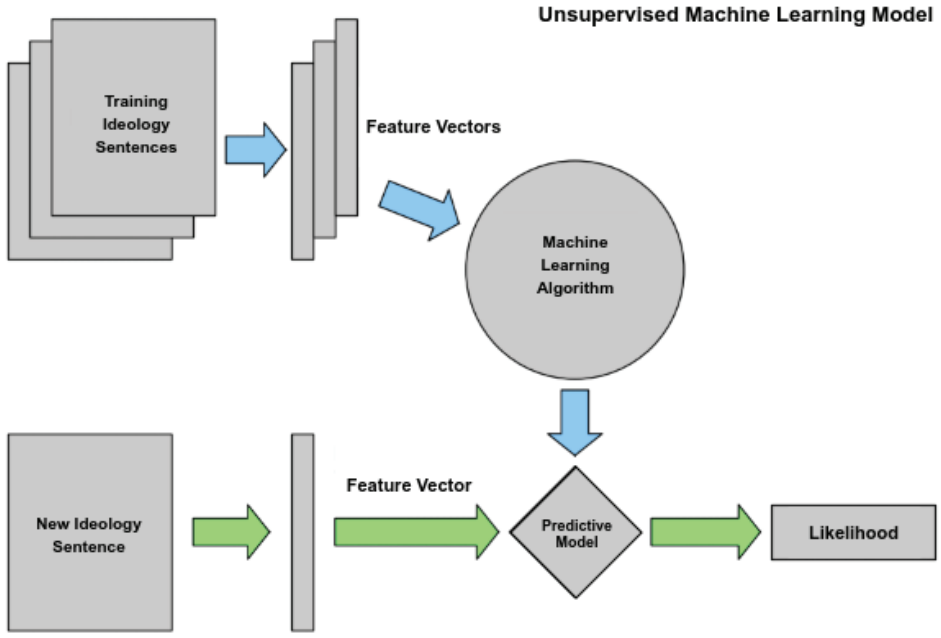


**Figure 2. Unsupervised Machine Learning Algorithm Workflow For Ideology Detection**

### Deep Learning

Deep learning is an artificial intelligence (A.I.) function that mimics the workings of the human brain in terms of data processing and pattern formation for use in decision making. Deep learning is a subtype of machine learning in artificial intelligence that involves networks that can learn unsupervised from unstructured or unlabeled input (Goodfellow et al., 2016).

### Artificial Neural Networks

Artificial neural networks (ANNs), sometimes known as neural networks (N.N.s), are computing systems that are loosely inspired by the biological neural networks that make up animal brains. An ANN is built from a network of linked units or nodes known as artificial neurons, which are roughly modeled after the neurons in the human brain.

The functioning of the ANNs is perceived similar to the working of human mind. It is designed on the similar concept in which each neuron is linked with each other and sends a signal to other neurons as the functioning of the human mind. In ANNs the signal to the neuron is given in the form of a real number and after analyzing it, the processed signal is passed to the next linked signal and the output generated by each neuron is some non-linear function generated by the sum of its inputs. The connections between each neuron are called an edge and normally each edge contains some weight that changes with the learning process.

Moreover, the ANNs contains many layers of neuron but that depends on the problem. Generally, different layers apply different modifications to the values that are being processed. The general flow of ANNs start with the inputs that are fed to the input layer, then it is further processed in multiple hidden layers. Finally, the processed data comes out from the output layer. In Figure 3. artificial neural network representation can be seen.

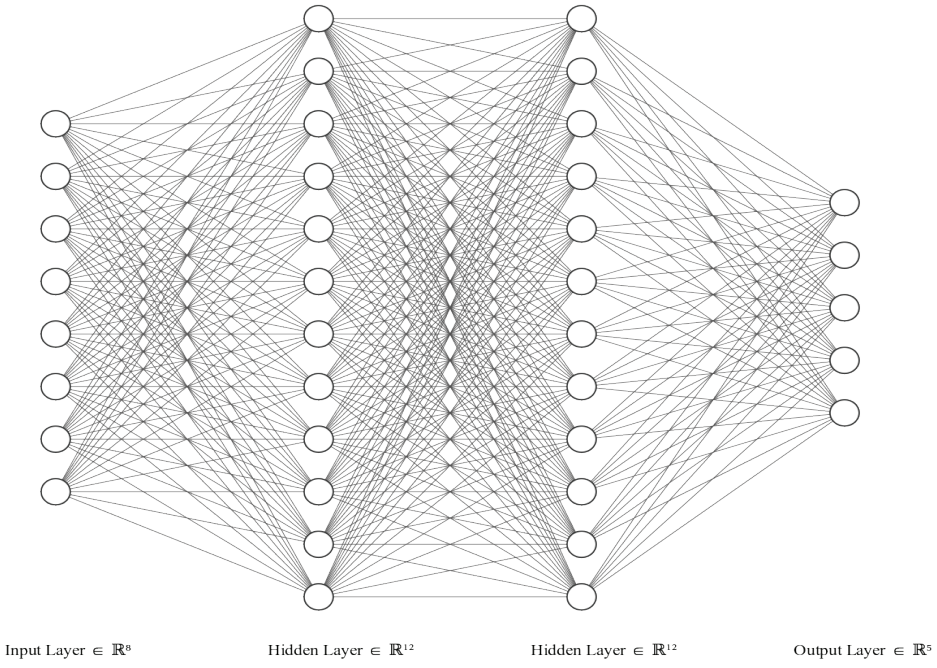


**Figure 3. Artificial Neural Network Representation**

Neural networks learn by analyzing samples that have a known "input" and "output," creating probability-weighted connections between the two, which are stored inside the net's data structure. Training a neural network from a given example is often accomplished by calculating the difference between the network's processed output (often a prediction) and target output. This is the mistake. The network then modifies its weighted associations based on a learning algorithm and this error value. With each change, the neural network will create output that is increasingly comparable to the goal output. Following a sufficient number of these modifications, the training might be ended depending on specific criteria. This is referred to as supervised learning.

**Transformer-Based Models**

A transformer is a deep learning model that uses the attention mechanism to weigh the impact of various sections of the incoming data. It is currently broadly has been used in the field of natural language processing (NLP).

Transformers, like recurrent neural networks (RNNs), are built to handle sequential input data like natural language for tasks like sentiment analysis, language translation, and text summarization. Transformers, unlike RNNs, do not require sequential input to be processed in sequence. The attention action, on the other hand, offers context for any point in the input stream. If the input data is a natural language sentence, for instance, the transformer does not need to process the first part of the phrase before the last. Instead, it detects the context that gives the word in a phrase meaning. The transformer, as opposed to RNNs, allows for significantly more parallelization, which decreases training durations. Transformers have quickly replaced previous RNN models, such as extended short-term memory as the model of choice for NLP issues LSTM. Because the transformer model allows for increased parallelization during training, it has made it feasible to train on much bigger datasets than before.

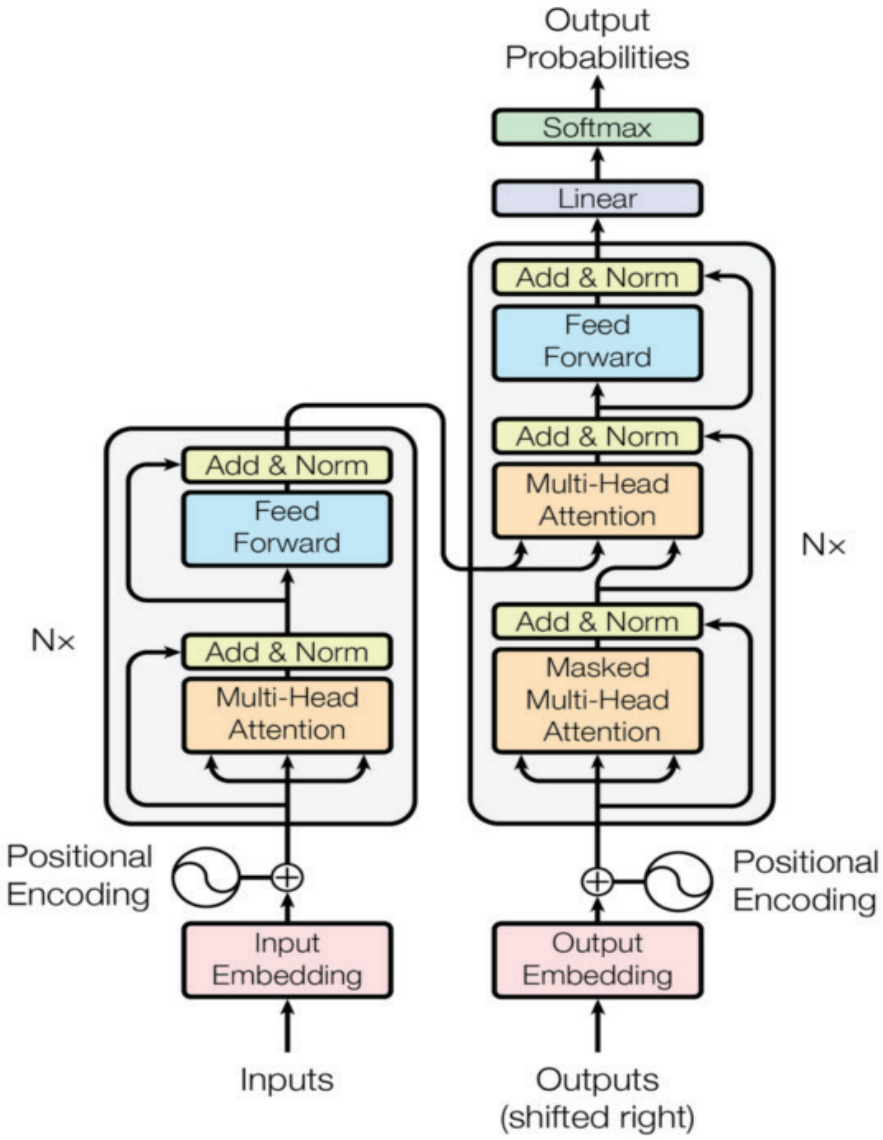


**Figure 4. Transformer Language Model Structure (Vaswani et al., 2017: 3)**

This resulted in the creation of pre-trained systems like BERT (Bidirectional Encoder Representations from Transformers) and Generative Pre-trained Transformer (GPT) (Brown et al., 2020), which have been

trained on substantial language datasets like Wikipedia Corpus[3] and Common Crawl and can be fine-tuned to particular applications.

**Bidirectional Encoder Representations From Transformers**

Bidirectional Encoder Representations from Transformers (BERT) is a machine learning technique for natural language processing (NLP). Simply BERT model looks in both directions, and it uses the full context of the sentence, both left, and right surroundings at the same time to do any given task (Devlin et al., 2019). After BERT was published, it outperformed other practices on General Language Understanding Evaluation (GLUE) task set, Stanford Question Answering Dataset (SQuAD) v1.1 and v2.0, and Situations With Adversarial Generations (SWAG). BERT can model semantic structure, which is the idea that a phrase's meaning is a variation of the meaning of the terms within that phrase and the grammar that connects those words. In BERT implementation, there are two steps which are pre-training and fine-tuning. The model is trained on unlabeled data in various pre-training tasks during pre-training. For fine-tuning, the model is fine-tuned by pre-trained parameters; after that, fine-tuning parameters using labeled data. BERT's unified architecture through tasks is one of its most distinguishing features. The pre-trained architecture and the existing downstream architecture are almost identical.

BERT has a multi-layer bidirectional Transformer encoder as its model architecture. As a part of BERT, transformers have an encoder that reads text input and a decoder that generates a prediction. Currently, there are two variants of architecture that exist, which are BERT Base and BERT Large. While BERT Base has 12 layers, 12 attention heads, and 110 million parameters, BERT Large has 24 layers, 16 attention heads, and 340 million parameters. In BERT, every input embedding is separated into three embeddings. These embeddings are position embeddings, segment embeddings, token embeddings. Positional embeddings are used by BERT to express the location of words in a sentence. With segment embeddings, BERT takes sentence pairs as input, and it learns

3 https://dumps.wikimedia.org/

an embedding for both sentences to help the model distinguish between them. Token embeddings are inserted at the beginning of the sentence called [CLS], and the end of the sentence called [SEP] by the BERT model. BERT's versatility stems from the preprocessing steps above.

BERT pre-train on two unsupervised tasks. These unsupervised tasks are Masked Language Modeling (MLM) and Next Sentence Prediction (NSP). The reason for the MLM task is standard conditional language models are trained left-to-right or right-to-left. In order to overcome it needs to train a deep bidirectional model. In the MLM task, randomly, some words of input tokens are masked, then the model predicts them. As a result of this, MLM allows obtaining a bidirectional pre-trained model, though it appears a downside. Masked tokens do not appear for fine-tuning, and this creates a divergence between pre-training and fine-tuning steps. To resolve this divergence between selected tokens, 80% of the tokens are replaced with the token mask, 10% of them are replaced with random tokens, and the last 10% of tokens are left unchanged. After the application of this solution, with cross-entropy loss, tokens can be used to estimate the original token.

BERT with Next Sentence Prediction (NSP) achieves an understanding of the relationship between two sentences since this relationship between two sentences cannot be understood with language modeling. To build a model that recognizes sentence relationships, The model takes pairs of sentences as feedback and learns to predict whether the second sentence is also the next in the original text. As we have mentioned earlier, the training model is fed two input sentences that are separated with a special token (SEP). 50% of these pair training inputs second sentence comes after the first one and the other half the sentence follows the first sentence is a random sentence comes from the corpus. The label of the second sentence is related to the first sentence is assigned using softmax. Fine-tuning in BERT uses the self-attention mechanism Transformer, which allows BERT to model many tasks. In this study, we aim to text classification with BERT. For this task, BERT is fed with input and outputs and fine-tune all the parameters end-to-end.

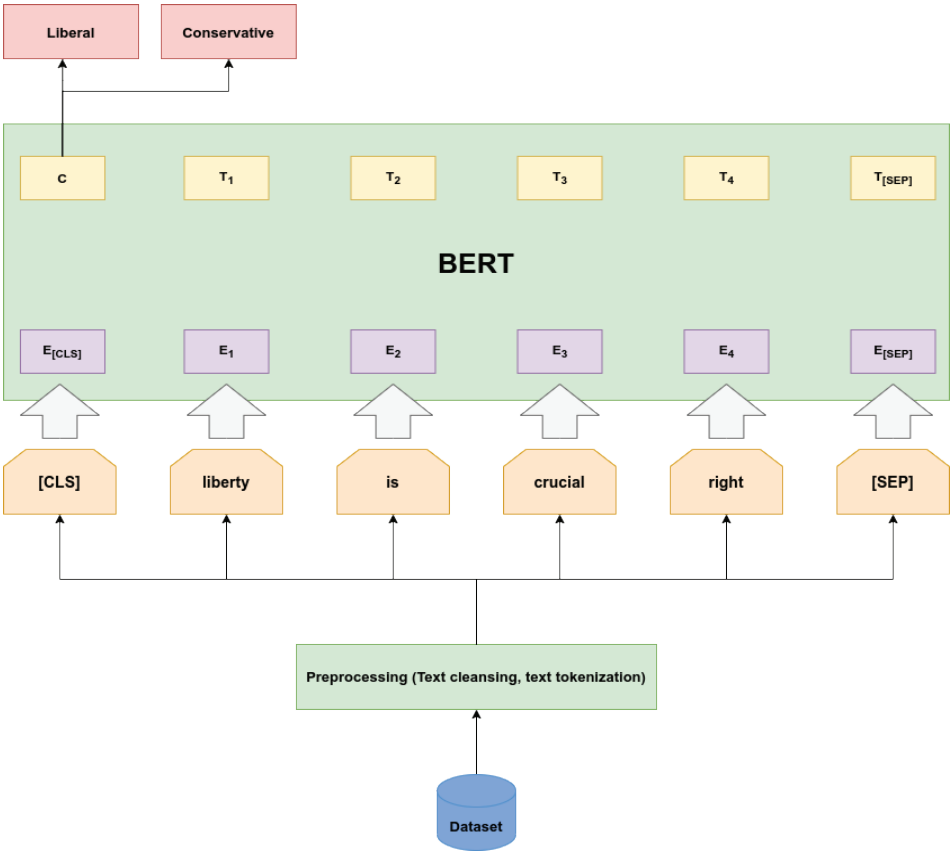


**Figure 5. BERT Model for the Political Ideology Detection Task**

### Electra

In ELECTRA, some random tokens of a sequence are replaced with the [MASK] token, and then the generator predicts the original of these [MASK] tokens. The output of the generator is given to the discriminator (ELECTRA) to decide if a token holds its original value or is replaced by the generator. The workflow of the ELECTRA can be seen in Figure. Base ELECTRA model contains the same hyper-parameters with $BERT_{BASE}$ while small and large models contain reduced and increased hyper-parameters relatively. Like BERT, there are some adaptations of ELECTRA too, for other languages rather than English, such as German

and Turkish. For ideology detection with ELECTRA, a released model which is trained with the same corpora as BERT has been used.

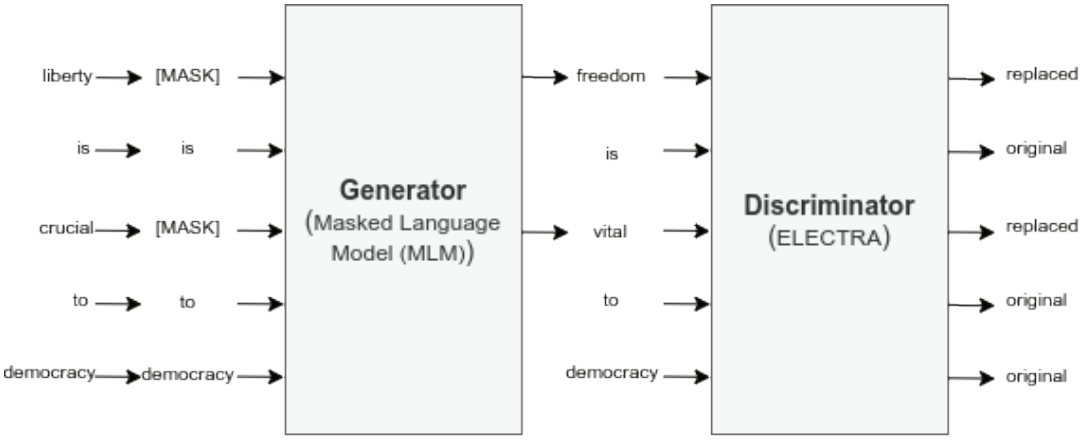


**Figure 6. ELECTRA Model for the Political Ideology Detection Task**

### Hyperparameters

A hyperparameter is a parameter in machine learning whose value is used to regulate the learning process. The values of additional parameters (usually node weights) are determined by training.

Different hyperparameters are required by different model training methods, although some basic algorithms (such as ordinary least squares regression) do not. The training algorithm learns the parameters from the data given these hyperparameters. The hyperparameter values of each method are shown in Table 1.

**Table 1. Hyperparameters for Each Method**

| Hyperparameter | LSTM | BiLSTM | BERT | ELECTRA |
|---|---|---|---|---|
| Batch size | 32 | 32 | 16 | 16 |
| Activation function | Sigmoid | Sigmoid | GELU | GELU |
| Optimizer | Adam | Adam | Adam | Adam |
| Learning rate | 1e-6 | 1e-6 | 5e-5 | 5e-5 |
| Epochs | 15 | 15 | 4 | 4 |
| Loss function | Cross entropy | Cross entropy | Softmax | Softmax |

## EVALUATION

Machine learning and deep learning methods have been run on Google Colab[4] in a GPU environment with Ubuntu 18.04 operating system. For training and testing parts, PyTorch, sci-kit-learn libraries, and Python programming language have been used. To validate the advantage of applying transformer-based models, BERT and ELECTRA, to ideology detection, we carried on the study on the real data sets of the ideology book corpus dataset. We contrast the proposed BERT and ELECTRA methods with traditional ideology detection methods (SVM, Decision Trees, Random Forest) with measuring their success in classifying ideology-based sentences into conservative and liberal. In training, for the transformer-based models, we fine-tune pre-trained BERT and ELECTRA models with sentences that are described in the Dataset section. After training models with split data set parts, testing performed with unseen parts of the dataset, separately for each of the data set. For performance criteria, accuracy, precision, recall, and F1 scores of these methods are calculated.

4 https://colab.research.google.com/

**Evaluation Metrics**

**Accuracy**

Accuracy is one statistical metric for evaluating classification models. One parameter for assessing classification models is accuracy. Accuracy is the ratio of the number of correct predictions to the total number of input samples. Accuracy can be defined as:

$$Accuracy = \frac{Number\ of\ correct\ predictions}{Total\ number\ of\ predictions} \quad (1)$$

For binary classification, accuracy can also be defined in terms of positives and negatives as follows:

$$Accuracy = \frac{TP + TF}{TP + TN + FP + FN} \quad (2)$$

Where TP = True Positives, TN = True Negatives, FP = False Positives, and FN = False Negatives.

**Precision**

The precision is determined as the ratio of positive samples categorized to the total number of positive samples classified. The precision metric assesses the model's ability to classify a sample as positive correctly. Precision can be defined as:

$$Precision = \frac{True_{positive}}{True_{positive} + False_{positive}} \quad (3)$$

**Recall**

The recall is determined by dividing the total number of Positive samples by the number of Positive samples accurately identified as Positive. The model's capacity to recognize Positive samples is measured by

the recall. The greater the recall, the more positive samples are discovered. Recall can be defined as:

$$Recall = \frac{True_{positive}}{True_{positive} + False_{negative}} \tag{4}$$

**F-Score**

The F-score, also known as the F1-score, is a metric for how accurate a model is on a given dataset. It is used to assess binary classification algorithms that classify samples as either "positive" or "negative." The F-score, which is defined as the harmonic mean of the model's accuracy and recall, is a means of combining the model's precision and recall. F-Score can be defined as:

$$F1 = \frac{2}{\frac{1}{recall} \times \frac{1}{precision}} = 2 \times \frac{precision \times recall}{precision + recall} \tag{5}$$

$$= \frac{tp}{tp + \frac{1}{2}(fp + fn)}$$

**EXPERIMENTAL RESULTS**

The quantitative results of each method are shown in Table 1. Accuracy, precision, recall, and F1 measure for each technique, scores are given. In general, transformer-based ideology detection methods of BERT and ELECTRA outperform other machine learning-based and deep learning-based approaches. However, other methods except decision trees do not perform poorly either. Another significant issue at this point is that the performance of SVM gets closer to BERT.

In conclusion, when various methods are tested with the IBC dataset, we observe that transformed-based methods have notable success for ideology detection.

**Table 2. Results of Models Trained With Ideology Dataset**

| Method | Accuracy | Precision | Recall | F1-Score |
|---|---|---|---|---|
| SVM | %68.27 | %68.19 | %68.41 | %68.14 |
| Naive Bayes | %66.91 | %66.90 | %66.90 | %66.90 |
| Decision Trees | %63.95 | %63.99 | %64.03 | %63.93 |
| LSTM | %63.82 | %63.70 | %63.70 | %63.71 |
| BiLSTM | %68.50 | %67.74 | %69.11 | %68.42 |
| BERT | %69.87 | %70.42 | %70.30 | %69.86 |
| ELECTRA | %70.24 | %70.30 | %70.20 | %70.19 |

## CONCLUSION

In this paper, we apply Bidirectional Encoder Representations from Transformers (BERT), ELECTRA, machine-learning, and deep-learning-based algorithms to classify the political ideology of a person from sentences. Our work focuses on the political ideology identification of a user, and we use two political classes. We compare the BERT, ELECTRA transformer-based models to SVM, Naive Bayes, Gradient Boosting, Decision Trees, Random Forest. As a result, we show that ELECTRA outperforms other methods on political ideology classification.

## REFERENCES

Brown, T. B., Mann, B., Ryder, N., Subbiah, M., Kaplan, J., Dhariwal, P., Neelakantan, A., Shyam, P., Sastry, G., Askell, A. & others (2020). Language models are few-shot learners. *arXiv preprint arXiv:2005.14165*,.

Devlin, J., Chang, M.-W., Lee, K., & Toutanova, K. (2019). BERT: Pre-training of Deep Bidirectional Transformers for Language Understanding. *arXiv*.

Dinkov, Y., Ali, A., Koychev, I. and Nakov, P. (2018). Predicting the Leading Political Ideology of YouTube Channels Using Acoustic, Textual, and Metadata Information, *INTERSPEECH*

Gangula, R. R., Duggenpudi, S. R. and Mamidi, R. (2019). Detecting Political Bias in News Articles Using Headline Attention. *Proceedings of the 2019 ACL Workshop BlackboxNLP: Analyzing and Interpreting Neural Networks for NLP,* 77-84. 10.18653/v1/W19-4809.

Gentzkow, M. and Shapiro, J. M. (2010). What drives media slant? evidence from us daily newspapers. *Econometrica*, *78*(1):35 -71.

Goodfellow, I., Bengio, Y., & Courville, A. (2016). *Deep Learning*. MIT Press.

Groseclose, T. and Milyo, J. (2005). A measure of media bias. *The Quarterly Journal of Economics, 120*(4):1191– 1237.

Hochreiter, S., & Schmidhuber, J. (1997, 11). Long Short-Term Memory. *Neural Computation*, *9*(8). 10.1162/neco.1997.9.8.1735

Hojoon, L. and Minbyul, J. (2017). Ideology Detection with using Deep Neural Network.

Iyyer, M., Enns, P., Boyd-Graber, J. and Resnik, P. (2014). Political Ideology Detection Using Recursive Neural Networks. *52nd Annual Meeting of the Association for Computational Linguistics, ACL 2014 - Proceedings of the Conference.* 1. 1113-1122. 10.3115/v1/P14-1105.

Kannangara, S. (2018). Mining Twitter for Fine-Grained Political Opinion Polarity Classification, Ideology Detection and Sarcasm Detection. *WSDM '18: Proceedings of the Eleventh ACM International Conference on Web Search and Data Mining,* 751–752

Kulkarni, V., Ye, J., Skiena, S. and Wang, W. Y. (2018). Multi-view Models for Political Ideology Detection of News Articles. *Proceedings of the 2018 Conference on Empirical Methods in Natural Language Processing Association for Computational Linguistics*, 3518--3527

Lazaridou, K. and Krestel, R. (2016). Identifying Political Bias in News Articles. *Bull. IEEE Tech. Comm. Digit. Libr.* vol. 12.

Misra, A. and Basak, S. (2015). *Political Bias Analysis*. Digital River Inc. Stanford University.

Mohri, M., Rostamizadeh, A., & Talwalkar, A. (2018). *Foundations of Machine Learning* (Second ed.). MIT Press. 10.5555/2371238

Schwarz, J. (2019). Detecting Political Ideology in Youtube Comments using Machine Learning. *Seminar Social Media and Business Analytics*

Sim, Y., Acree, B. D. L., Gross, J. H., & Smith, N. A. (2013). Measuring Ideological Proportions in Political Speeches. *Empirical Methods in Natural Language Processing*.

Vaswani, A., Shazeer, N., Parmar, N., Uszkoreit, J., Jones, L., Gomez, A. N., Kaiser, L., & Polosukhin, I. (2017). Attention Is All You Need. *Conference on Neural Information Processing Systems*, *31*, 3.

Xi, N., Ma, D., Liou, M., Steinert-Threlkeld, Z., Anastasopoulos, J. and Joo, J. (2019). Understanding the Political Ideology of Legislators from Social Media Images. *Proceedings of the International AAAI Conference on Web and Social Media*, *14*(1), 726-737.

# USAGE AREAS OF ACOUSTIC POLYURETHANE FOAM IN VEHICLES AND ITS CONTRIBUTION TO WEIGHT REDUCTION

*Alper ÖNER[1], Senai YALÇINKAYA[2]*

**Abstract:** One of the main reasons for the warming of our world is the fossil-based fuels used by vehicles. Fuel consumption of vehicles is directly proportional to the weight of the vehicles. Various applications exist to reduce fuel consumption or to use non-fossil fuels. Electric and hybrid vehicles are the most well-known of these. Some manufacturers have been producing hydrogen fueled vehicles. With the new regulations, serious limitations have come and will come, according to the carbon dioxide gas emissions of the vehicles, sound emissions inside and outside the vehicle, vehicle weights and classes. Compared to the engine noise of diesel and gasoline vehicles, those of hybrid and electric vehicles are much lower. These vehicles, on the other hand, are heavier than the others due to the heavy batteries they carry. In both cases, using light and acoustically advanced insulation materials is the best solution. These insulation materials are the patented or general products of companies that produce certain acoustic insulation materials. Among these, polyurethane-based foam with a density of approximately 14-15 Kg/m3 foamed up to 70 times, was discussed. This foam is a very light material with superior acoustic properties that can support itself, can be formed, contains all open and closed cells, and has pores of varying sizes. In the literature, the effects of density, porosity, air flow properties and thickness, which are the properties that affect the absorption of materials, have been studied in many studies. Here,

1 Marmara University, Institute of Pure and Applied Sciences, İstanbul / Turkey, muratalper308@hotmail.com,Orcid No: 0000-0003-3381-7474

2 Marmara University, Engineering Faculty, İstanbul / Turkey, : yalcinkaya2012@gmail.com, Orcid No: 0000-0001-7076-7766

the absorbing properties of this material in various thicknesses were examined and it was seen that it was compatible with the literature. With the use of impedance tube, acoustic performances of 10, 19 and 29 mm thick polyurethane foams at frequencies between 16 and 6300 Hertz were determined. Considering the obtained values, a comment has been developed on the possible uses of polyurethane foam in each thickness in vehicles. It has been shown that it can contribute to weight reduction compared to other materials by use as an sound absorbing material in a middle-upper class vehicle.

***Keywords:*** Acoustics, Sound Absorption, Polyurethane Foam, Weight Reduction, Absorption Thickness Effect

## INTRODUCTION

Sound is defined as the pressure change that can be noticed by the human ear. The cycle of the change that the ear can notice in pressure depending on time, we call frequency and its unit is Hertz. 1 Hz = 1 cycle / second. The sounds that are not pleasant to the human ear and disturb them, we call the noise. It is more subjective as the disturbance of a sound can vary from person to person. Sound mostly indicates the type of energy that can be noticed by the hearing sense of the listeners, and vibration indicates acoustic events that are determined by touch and cannot be heard (Dobie and Hemel, 2004). The unit used in the sound pressure is the Pascal (Pa - N / m2). A person with normal hearing can hear sounds with pressure between 2x10-5 and 2x10-20 Pascal. Figure 1 shows the sound pressure level and frequency hearing limit curves. Because this band is very wide, the sound is evaluated with a logarithmic expression called decibels (dB).

The algorithm of dividing a size by a reference value is called Bell (based on Graham Bell). 1 in 10 of this value is called decibels (dB). The lower limit indicated by the green line in Figure 1 corresponds to the lowest level at which the pure sound is heard. The red line indicates the pain threshold of the loudness. The boundaries for normal speech and music are also indicated in the Figure 1 as a dashed line and a blue area. Amplifiers are needed to reach higher level of sound (Peters at all, 2013).

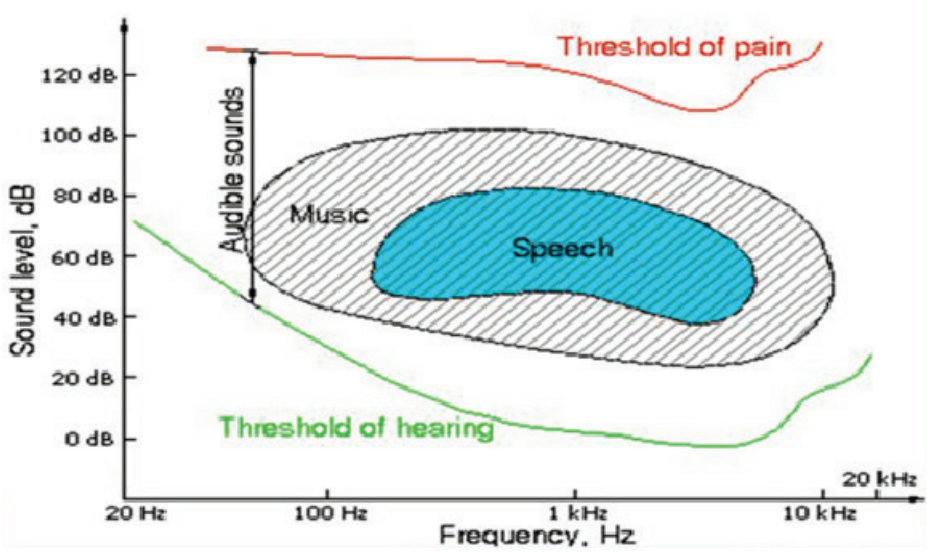


**Figure 1. Hearing Limits for Sound Pressure Level and Frequency**

Sound propagates in waves in air, water and in elastic and hard environments. The propagation of sound occurs at different speeds depending on the type, intensity and temperature of the place where it spreads. While the propagation speed of sound in a gas (like air) is 331 m/s at zero degrees, it is 346 m/s at 25°C.[3] The propagation speed of sound at $25^0$C temperature is 1531 m/s in liquid-like water and 5960 m/s in solid-like steel[4].

The sound levels of many environments that we may encounter in our lives have been examined and divided into various groups on average and given in Figure 2 as dB and micro Pascal (μPa)[5]. In cars, these limits depend on the class and NVH quality of the vehicle. Acceptable limits are 50-58 dB at idle running, 60-75 dB at normal speeds, 76-85 dB at high speeds.

3 C. R. Nave, "Wave Speeds," in Hyper Physics, Dept. of Phys. Astron. Georgia State University Atlanta-Georgia USA, http://hyperphysics.phy-astr.gsu.edu/hbase/Sound/souspe2.html

4 "How to calculate speed of sound in solids, liquids and gasses?" (2019, October 11), Physics About, https://physicsabout.com/speed-of-sound/

5 R. Malthus, "Basic noise terminology," Via Strada, https://viastrada.nz/pub/basic-noise-terminology

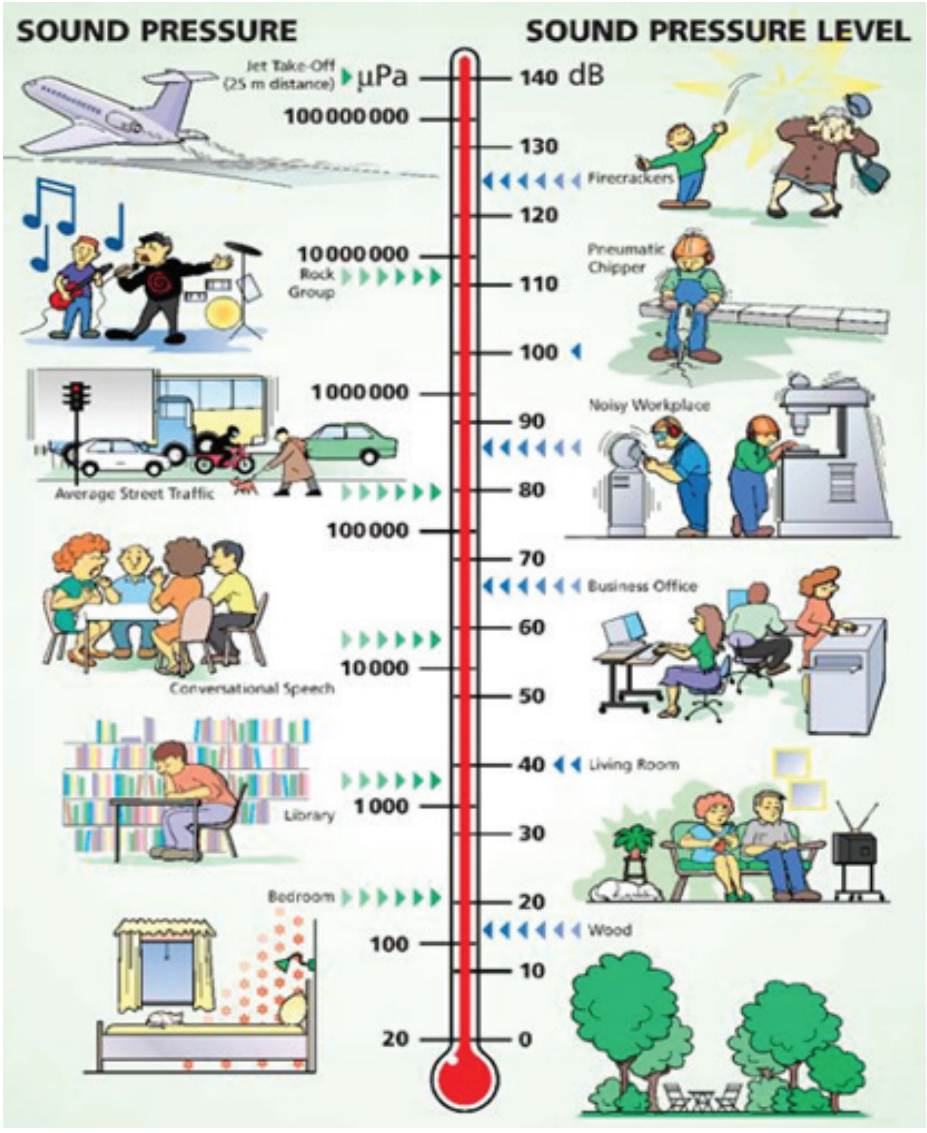


**Figure 2. Sound Pressure and Sound Pressure Levels**

## SOUND and VIBRATION in VEHICLES

The combination of the noise, vibration and harshness values of the vehicles (during vehicle use) gives the user a feeling about that vehicle, this feeling is very determining for vehicle users. If this feeling is good,

it will give the user the impression of a luxury, comfortable, quality and well-designed vehicle for that vehicle. Driving a car that vibrates and makes noise is tiring and uncomfortable. This vehicle evaluation phenomenon, which consists of noise, vibration and usage hardness, is called NVH. (Noise, Vibration & Harshness) On long journeys, a good NVH performance is one of the strongest brand differentiators as it greatly increases comfort. Therefore, good NVH performance is a necessity for luxury vehicles, while for others, it is an investment that will generously pay back every corner brand value and loyalty they can earn over competitors[6].

Vibration energy from a motor goes from the engine mounts to the sheet metal structure and eventually from the car seat and steering wheel to the driver. However, energy from the same source can follow a similar path through the metal structure to become acoustic noise when amplified by the cabinet. That's why optimizing these factors is extremely important. With the increasing competition in the automotive industry in recent years, automotive companies have been carrying out serious studies on this subject with their vehicle engineering teams in research and development departments. The most important source of sound and vibration of the vehicle is primarily the engine and power transmission organs. Tire / road noise has become more important to the overall perception of interior quietness, as the noise of the power, drivetrain and metal structure has been successfully reduced. Road noise usually begins to be noticeable at vehicle speeds above 50 km/h, but its contribution to total interior noise is usually between 50-100 km/h, and then its effect is reduced at higher speeds, as wind and aerodynamic noise is predominant. Road noise is caused by the interaction between the tire and the road surface, and the noise is carried into the vehicle both structurally and by air (Cerrato, 2009). At speeds above 80 km/h, wind noise becomes relatively more noticeable and noticeable for passengers. This affects the overall acoustic performance of the vehicle (Hiroyuki and Hiroyasu, 2002).

6 HBK Company "Applications: NVH - Noise, Vibration and Harshness," Brüel & Kjaer Denmark. https://www.bksv.com/en/Applications/vehicle-noise-vibration-and-harshness-development

The sounds affecting the interior of a moving vehicle and the sound and vibrations originating from the vehicle are given in Figure 3. What is striking here is that the noise of the vehicle's engine and powertrain can also enter the cabin through the windshield. For noise control, each of these sources should be examined and evaluated separately and together with their interactions (Rissler, 2011). For a person sitting in the front seat of the vehicle, the sounds coming from the engine and powertrain that generate more powerful noise are prioritized. Then, the sounds coming from the wheels and the exhaust system in a structural way are taken into account. At the same time, the sounds carried by the air from the engine and transmission organs, as well as the sounds of the road and wind carried by the air, are taken into consideration.

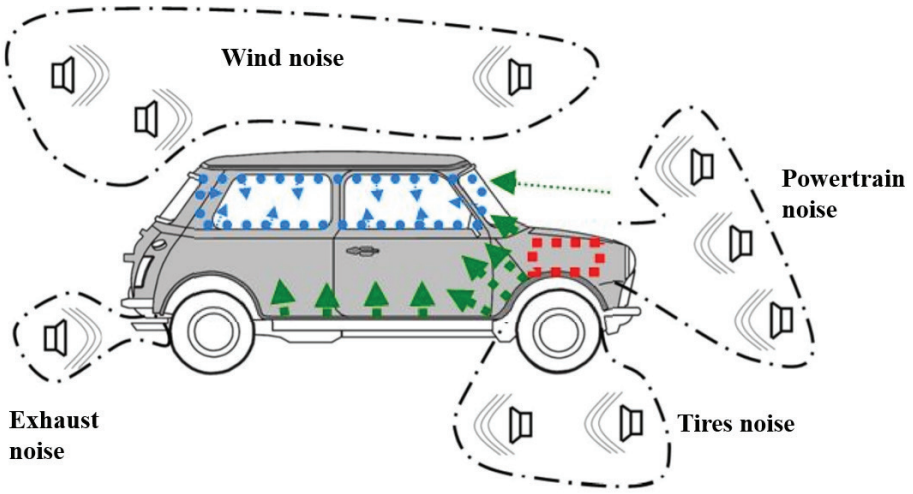


**Figure 3. Sounds Penetrating Inside of the Vehicle**

The sounds inside the vehicle are not just sources of vibration and sound. This sound can be differentiated with the effect of the medium that carries the sound between the source and the sound receiver (such as the driver and passengers). There are two ways that carry (transmit) the sound in the vehicle. The first of these is structurally conductive and the second is airborne. The mechanisms of the two paths carrying the sound for transporting the energy of the sound are very different from each other. In vehicles with internal combustion engines, the main noise

and vibration comes from the engine and the noise emission can be at the level of approximately 95 dB right next to the engine (Panza, 2015).

This 95 dB level of noise emission is reflected into the vehicle structurally over the body as can be seen in Figure 3, and diffuses into the vehicle with air over the dashboard, windshield and engine (Harkude and Malagi, 2015). The sources of noise are the engine and powertrain, road and tire noise, wind, exhaust sound, suspension system noise, and squeak-rattling. Noise is propagated from these sound sources into the vehicle as a transmission path, structurally (vibration and contact) and via air. The addressee, or receiver, of these noises is the driver and, if any, passengers. Interaction between source and receiver is shown in Figure 4 (Gelen, 2016).

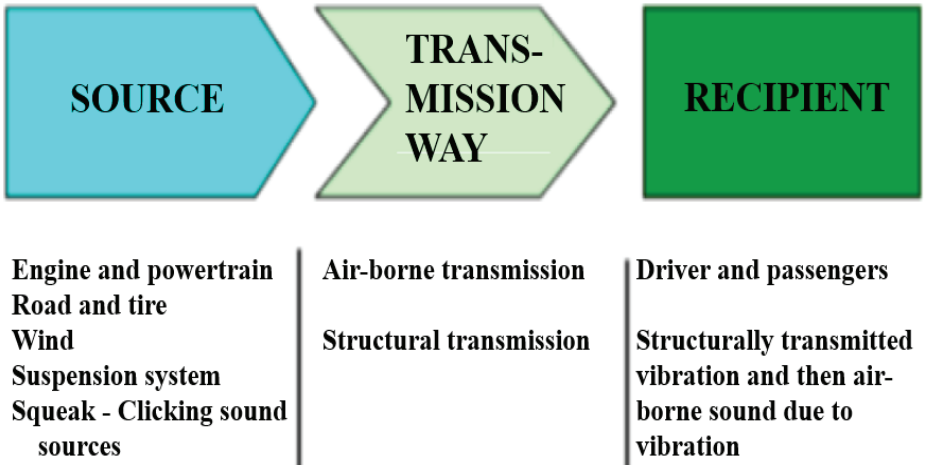


**Figure 4. Interaction Between Source and Recipient**

If the frequency ranges and percentages of the noise sources in the vehicles are examined; Road-borne noise; Vibration and impact created by the wheels, transmitted through a structure. It consists of structurally transmitted road noise and airborne tire sound. All these road-borne noise constitute 9-15% of the total noise level of the vehicle interior. Noises originating from power and transmission organs: Boom sound made up of an internal combustion engine and transmitted through a structural way. Noises transmitted by medium frequency structural means consisting of transmission organs and noises transmitted by air flow at

medium and high frequencies. All of these make up 39-60% of in-vehicle noise. Aerodynamic sounds are structural and airborne noises. It constitutes 5-30% of the total noise depending on the speed. Equipment-induced noises are structural and airborne sounds. The most important of these are exhaust, fan and compressor sounds. They make up 32-50% of the total noise. The factors causing in-vehicle noise transported by air and structural means and the frequency ranges in which they are effective are given in Figure 5 (Deulgaonkar at all, 2014).

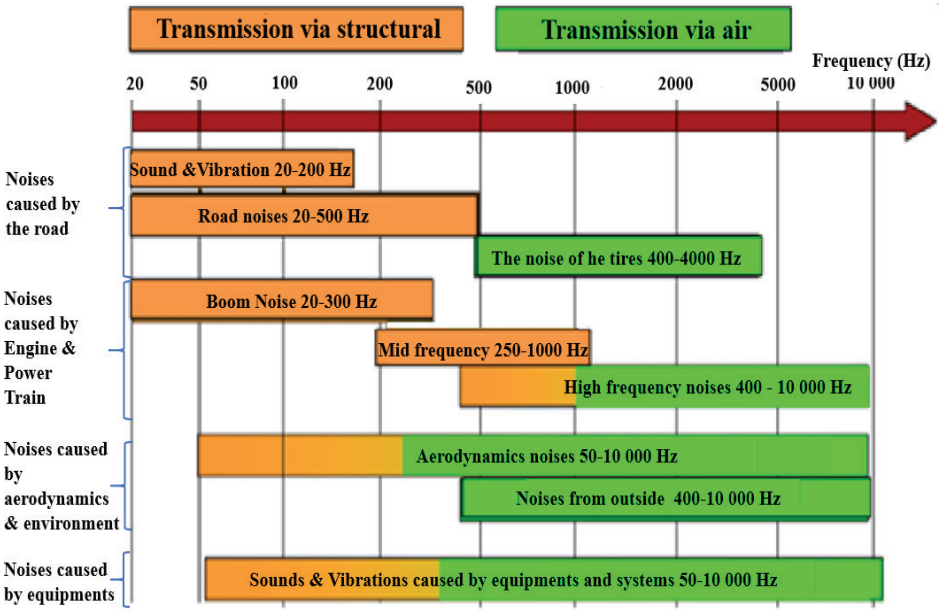


**Figure 5. Vehicle Sound and Vibration Source Frequency Analysis Sound and Vibration Control in Vehicles**

The sound is structurally transmitted into the vehicle, especially through sheet metal panels and steel reinforcements. It is transmitted by spreading into the cabin. The running engine is the biggest source of vibration in the vehicle, especially due to the vibration caused by the movements of the pistons and crankshaft. This situation is shown in Figure 6. The vibrations occurring in the motor are transmitted to the chassis or steel body to which the motor is connected, through the motor ears, despite all insulation measures taken. Vibrations occurring in the

chassis and body spread into the vehicle, especially thanks to the sheet metal panels and steel reinforcements. The vibration energy generated in the sheet metal panels reflects into the vehicle as sound and vibration[7]. Bitumen-based deadeners are placed on the sheet metal panels to insulate the structural spread of sound and vibration inside the vehicle. These are applied while the vehicle is in the paint oven and adheres to the sheet metal panel. In the case of holders such as motor mounts and brackets, the application of rubber and similar solid elastic materials between metals prevents direct contact of metals with each other and provides vibration insulation. Engine blocks that make less noise have been designed for diesel engines that are louder than other internal combustion engines, and it has been proven both experimentally and modelling that they emit 10% less noise (Mao, 2013).

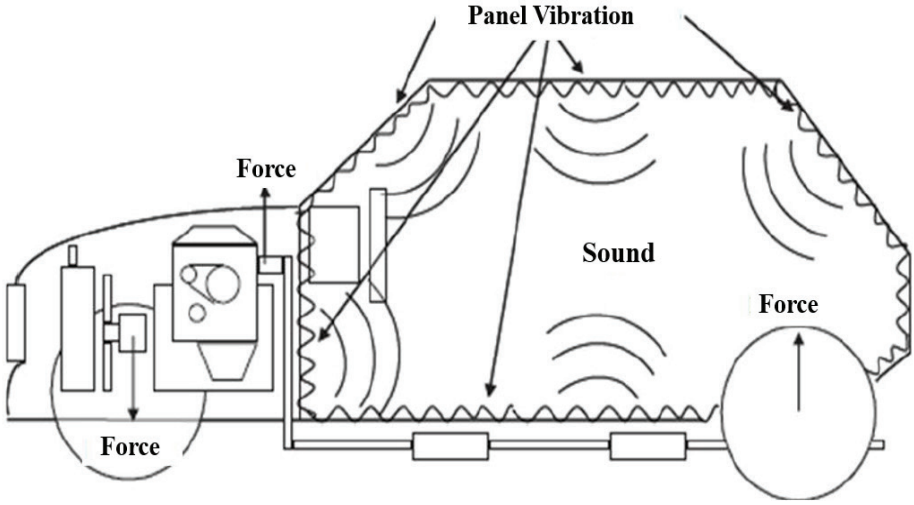


**Figure 6. Transmission of Sound and Vibration**

In a vehicle with an engine running, both the engine and the powertrain, as well as the components such as the exhaust and catalytic converter act as sound sources. Noise and vibrations from these sources will cause the sheet panels associated with the interior of the vehicle to

7 J. Pellettieri, (2019, September 3), Noise, Vibration & Harshness Challenges in Vehicle Lightweighting, http://lightweightingworld.com/noise-vibration-harshness-challenges-in-vehicle-lightweighting/

vibrate with the air-born as seen in Figure 7, and this will cause noise in the vehicle. The best insulation methods for the sound and noises transmitted acoustically to the interior of the vehicle is to cover the gaps, welding gaps of the holes in these sheet metal panels with mastic or other insulation materials to prevent sound and noise leaks.

Sources of squeaking and rattling: These unwanted noises are the noises (sounds) made by the door and wall coverings, dashboard, complete instrument panel and seats (etc.) used in the vehicle due to vibration and interaction occurring while the vehicle is running or driving. Creaking occurs as a result of the contact between the sheet metal panels in the body of the vehicle due to the stretches occurring in the body while the vehicle is in motion. In order to prevent creaking, mastic or sealers are applied to the parts of the sheet metal panels where they can come into contact with each other. The clicks consist of the interaction of surfaces that touch or are close to each other while the vehicle is in motion. Clicks appear in the medium-high frequency range (0.2-2kHz), while squeaks appear in the high frequency range (0.5-5kHz) (Matijević and Popović, 2017).

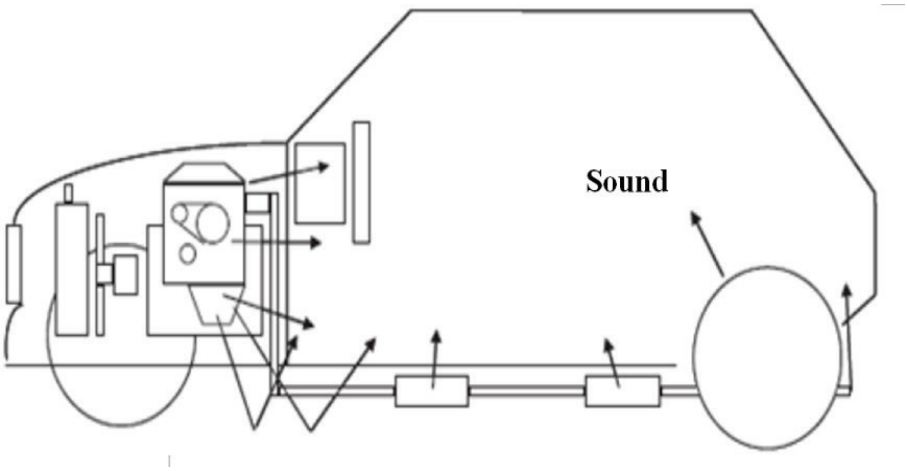


**Figure 7. Transmission of Sound and Vibration by Air**

Overall, noise and vibration control from the engine to the passenger compartment has improved significantly over the years; Therefore, the problem now is more with the quality of the engine sound rather

than its noise. Sound Quality engineering uses basic psycho-acoustic methods known to accurately describe the sensation of pleasantness or discomfort to achieve a desired balance of frequencies and sound levels in the vehicle interior (Siano and Panza, 2017).

### Sound Isolation and Development of Insulation and Absorption Materials in Vehicles

Although the investigation of the sound structures of vehicles goes back to ancient times, recent studies have a more important place in the rapidly developing and changing automotive industry. As the comfort expectations increase with the development of technology, the vehicles are also expected to be quieter (Aldhahebi at all, 2016). This silence is important not only inside the vehicle but also outside the vehicle. Since vehicle noise spreading to the environment creates environmental pollution, measures are taken in this regard and various regulations are issued by environmentally sensitive countries. With the first decision taken by the European Union on February 6, 1970 on "approximation of the laws of the Member States on the type approval of motor vehicles and trailers" the work started to ensure that the vehicles produced and used within the community meet a certain standard. Later, many other decisions were made, in which air pollution and noise pollution caused by fossil fuels were added. Finally, the European Union's parliament issued a regulation under the name of "Pass By Noise", taking into account vehicle engine power, weight and type for environmental noise pollution with its decision number 540/2014 in 2014. With this regulation, it restricted the sound propagation of vehicles in three stages, in 2016, 2023 and 2025[8] (Publications Office of the EU. Regulation, 2014).

As a result of regulations and comfort expectations, the use of insulation materials in vehicles has increased. Considering vehicle weights and costs, insulation materials that are lighter and with high acoustic performance are constantly being developed to meet these expectations. The bottoms of new model vehicles are now covered with lightweight,

8 Publications Office of the EU. Regulation (EU) No 540/2014 of the European Parliament and the Council, Official Journal of the European Union, vol. L158 pp. 131-195, 2014.

water and outdoor resistant textile-based materials. Some vehicles have started to use more durable types of the same textile material on the inside of the vehicle fenders instead of plastic fender interior covers. These insulation materials, which absorb the sound of the road and wheels, prevent these sounds from entering the vehicle, while absorbing the sound of the engine and powertrain coming from the vehicle, keeping the sound emission at the desired levels. The textile-based fender insulator absorbs the wheel-borne road noise and reduces its emission, bringing it below the limits of the new regulation.

Many studies have been carried out in the literature on the use of insulation parts in vehicles, material selection according to regions, acoustic properties and expectations according to regions. Sound insulation and absorption materials in electric vehicles also provide thermal insulation. Thermal insulation values have been taken into account, as it will save energy rather than increase the acoustic performance of a well-insulated electric vehicle. According to the assessment of air conditioning and heating, indoor temperature was lowered by 2.80C in summer in open parking conditions and by 3.90C during cooling compared to conventional insulation. In the case of heating during winter driving, the interior temperature was 7.70C higher than with conventional insulation, proving that the same amount of heating energy can be used to keep the cabin warm even in winter. Under the same conditions, the time required for air conditioning and heating decreases, and it means the available for driving energy is increases, especially as the electrical energy used for air conditioning decreases (Baek at all, 2019).

With our changing world, the demand for sound insulation materials has increased due to the increase in expectations for in-car comfort. Companies that produce insulation materials have tended to develop insulation materials with a lightened solution and increased acoustics. The effects of density and thickness, which are the main features that increase the sound absorption performance, are shown graphically in Chart 1, and the effects of porosity and air flow are graphically shown in Chart 2. The assimilation of the effects highlighted in the diagrams in Chart 1 and Chart 2 guides the studies to increase the sound absorption performance. (Bilova and Lumnitzer, 2011).

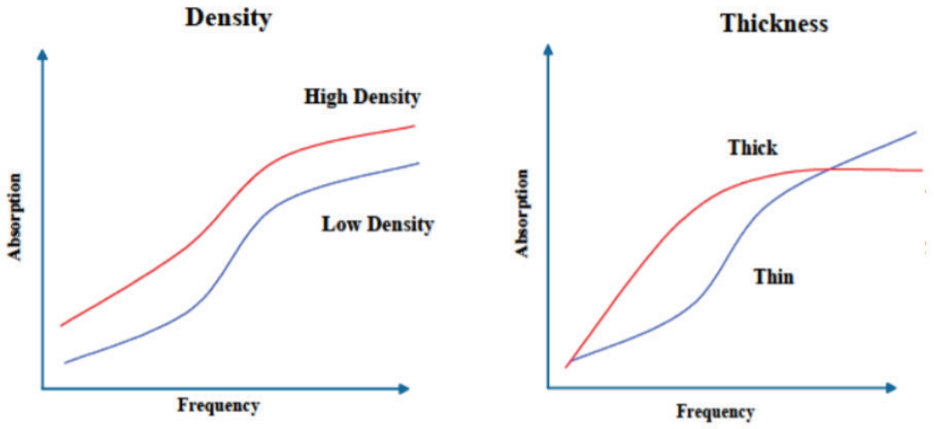


**Chart 1. The Effects of Density and Thickness to the Sound Absorption Performance**

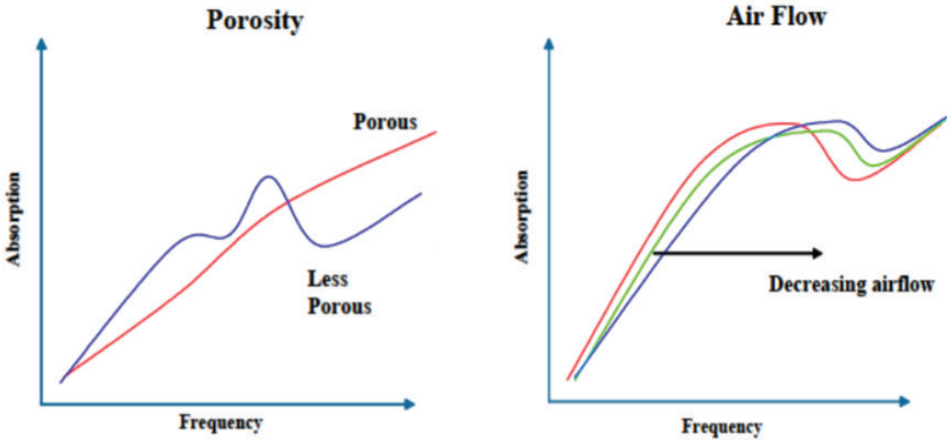


**Chart 2. The Effects of Porosity and Air Flow to the Sound Absorption Performance**

In recent years, instead of heavy old parts in automobiles, new lighter and more performance parts have been used (Çelikel and Babaarslan, 2017). The best examples of these are the lighter and more durable textile-based parts, instead of the heavy plastic materials used in the fend-

ers and under the vehicle. When the parts turned into textile-based parts from plastic materials, their acoustic performances also increased. With the use of these materials, the use of some of textile or polyurethane foam-based acoustic parts mounted on the back of the plastic parts has also been eliminated. The use of polyurethane foam parts with increased acoustics and thermal resistance in the engine area is becoming more common day by day.

Various experiments and studies have been carried out by testing many materials that can be used in under-hood insulation for the engine area in various weights and thicknesses (Siano at all, 2016). In these studies, high-quality polyurethane foams came to the fore because they are polymers that can withstand heat. In this way, polyurethane foams have been developed in the engine area, which can be very hot, resistant to fire and other external effects, very light, thermally shaped and with very high sound absorption values. Polyurethane Foams show much better acoustic performance than materials such as glass wool, rock wool and phenolic felt at least 3-7 times heavier than themselves. These sponge materials are used in the required thicknesses according to the needs and provide ease of use in terms of both weight and financial. Knowing the sound absorption coefficients for many thicknesses according to the frequencies ensures that the most appropriate thickness is selected for the place of use.

## SOUND ABSORPTION EXPERIMENT of POLYURETHANE FOAM (LEVECELL) by USING IMPEDANCE TUBES

The test device set used in the experimental study consists of a versatile, task-oriented "Pulse" system for noise and vibration analysis of Brüel & Kjaer, one of Europe's greatest and reliable brands in this regard. This system is consist of a FTT (Fast Fourier Analyser) signal analyser, signal boosting amplifier, microphones, impedance tubes (3 and 10 cm diameter combined), sound source (at the very end of the impedance tube), non-acoustic plug (at the other end of impedance tube) and a computer with LAN interface, PULSE software, Windows, Windows Vista, Microsoft Office hardware as shown in Figure 8. These system components;

- **Amplifier:** It is a Brüel & Kjaer brand 2716-C type 100 W stereo audio power amplifier. The amplifier with right and left channels volume settings and indicators is sensitive to sounds in the frequency range of 20 Hz – 20 kHz. It has the power to amplify the incoming sound, signal or noise up to 105dB. Its power can be up to 200 W, depending on the output resistance of 8, 4 and 2 Ohm (Ω). It amplifies the signals sent by the signal generator (FFT Analyser) and sends them to the sound source.
- **Microphones:** It detects the sound created at certain frequencies from the sound source and the sounds that transmitted into the tube and the sounds that hit the sample after it detects, it converts the sound to signals and transmit it to the FFT Analyser. Usually three microphones are used in the big tube and two microphones in the small tube. The microphones used in the experiment are the 4187 model of Brüel & Kjaer brand. In Figure 8, three attached to the big tube and two attached to the small tube are given

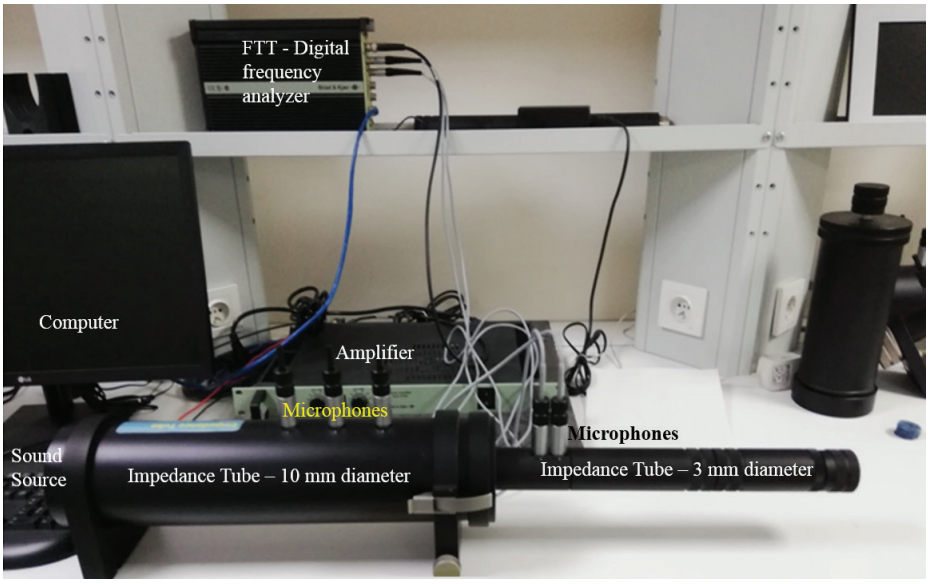


**Figure 8. Test Device Set Used in Experimental Study**

- **Large and small Impedance tubes:** The large tube with an inner diameter of 10 cm contains a sound source, a non-acoustic pis-

ton, three outlets for inserting a microphone and a slot suitable for placing the sample to be tested in front of the piston. Sound waves move inside this tube and are used for frequencies between 0-1600 Hz. Since the wavelengths of low frequency sounds are wide, the sensitivity is increased and the tolerance is reduced by using a 10cm large tube. The small tube, on the other hand, has a 3 cm inner diameter and is used for high frequencies between 1600-6300 Hz because the wavelengths of high frequency sounds are small. The big piston is lifted to allow the sound to pass from the big tube to the small tube. The small tube has an outlet for inserting three microphones and a slot at the end of the tube suitable for sample placement and a non-acoustic piston. This sound source and tubes are 4206 models of Brüel & Kjaer brand. As can be seen in Figure 8 in the experiment, 10 cm and 3 cm tubes were used as Combined EC.

- **FFT (Fast Fourier Transform) Digital Frequency Analyser (Signal Generator):** FTT used in the experiment is a 3560-B-130 model of Brüel & Kjaer brand. It can simply be called a compact data collection system. There are five microphone inputs and it has one output. Has a connection that provides all communication with the computer (The blue cable shown in the Figure 8). It can generate signals in the frequency range of 0-25.6 kHz (Signals between 0-6.3 kHz were used in the experiment). Its batteries work for 5 hours or with 10-32V DC current. The first is the task of signal generator, it creates analogue signals between 0 - 25.6 kHz and sends it to amplifier (values between 0-6.3 kHz were used in the experiment). The second task is to organize the analogue signals transmitted by microphones, convert them into digital signals, and associate them with the generated signal, and send them to the computer using the "LAN" interface.
- **Package Software and computer:** The "Pulse" package software is the whole of the software used in this impedance tube sound analysis system called "Pulse" by Brüel & Kjaer. While these devices are purchased, they can only be obtained from Brüel & Kjaer. It is extremely easy to use and usage training is also provided

upon purchase. Thanks to this software, digital data coming from the FFT (Fast Fourier Transform) Analyser are processed and the results are taken from the computer numerically.

The computer used in the experiment was a computer with a minimum Pentium processor, a standard video card and sound card with at least 80 GB hard disk. It includes Pulse software, Microsoft Windows Vista operating system, Microsoft Office 2003 program and "LAN" local area network connection for data transfer from FTT Analyser.

**MATERIALS USED in the EXPERIMENT**

In the experiment, polyurethane-based foams with a density of 15 kg / m3, commercially known as Levecell, were prepared in three different thicknesses and used. One of the biggest features of this polyurethane foam is that it shows semi-rigid viscoelastic properties and has a random cell structure. The diameters of the pores are not similar to each other, they are randomly large and small, which enables them to respond to many frequencies acoustically.

The polyurethane levecell foam used in the experiment were prepared in three different thicknesses: Figure 9 (a) 10 mm thick, Figure 9 (b) 19 mm thick and Figure 9 (c) 29 mm thick. Samples of 10 cm diameter were prepared from each to be used in an impedance tube of 10 cm diameter. The same process was done for samples of 3 cm diameter to use in 3 cm diameter impedance tube. As a result, a total of six samples were prepared in two different diameters and three different thicknesses. These materials used in the experimental study are shown in Figure 9 (a), (b) and (c) according to their thickness.

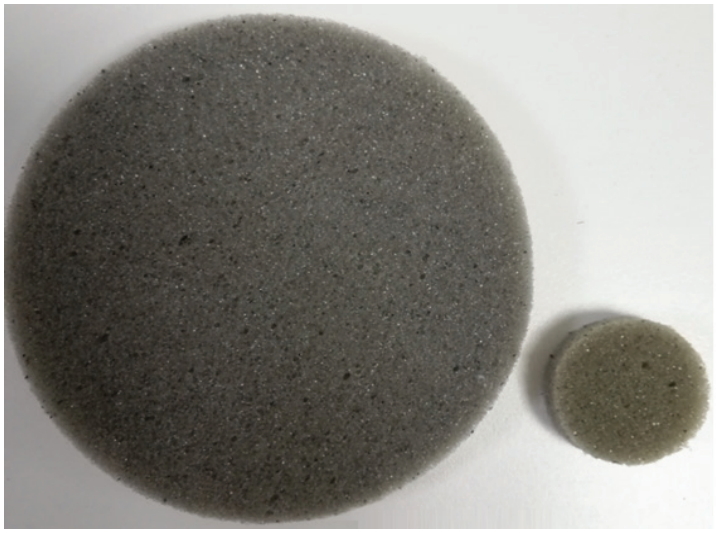

**Figure 9. (a) Levecell Foam 10 mm Thick**

**Figure 9. (b) Levecell Foam 19 mm Thick**

**Figure 9. (c) Levecell Foam 29 mm Thick**

## EXPERIMENT

The experiment was performed according to ASTM-E 1050-98, "Standard test method for impedance and sound absorption of acoustic materials using a tube, two microphones and a digital frequency analysis system". This standard test setup is explained in Figure 10. Since Combined EC used in the experiment is a combined version of 10 cm and 3 cm impedance tubes, the experiments were carried out in two stages. Since the wavelengths of low frequency (0-1600 Hz) sounds are wide, it is necessary to use a large diameter (10 mm) impedance tube and a small diameter (3 mm) impedance tube because the wavelengths of high frequency (1600-6300 Hz) sounds are small.

Two tubes are used to reduce the tolerance. In case the experiment of determining the absorption coefficient for all frequencies (between 0-6300 Hz) is performed in a large tube, it will not cause an error because it is more suitable for low frequency sounds between 0 and 1600 Hz for measurements. However, in the measurement of high frequency sounds between 1600-6300 Hz, it will cause errors because it will be wide for

narrow wavelengths. Likewise, if experiments are made to determine the absorption coefficient for all frequencies in a narrow 3 cm impedance tube, the narrow wavelengths of high frequency sounds

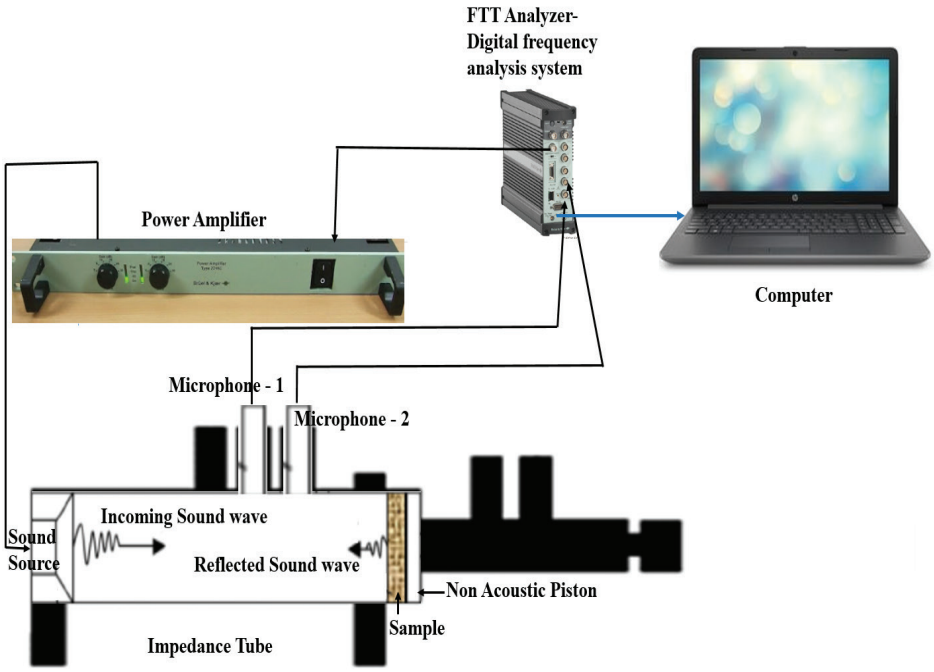


**Figure 10. Experiment Setup, Combined Impedance Tube (10 mm & 3 mm) and Working Principle**

will not cause errors to match the tube diameter. However, low frequency sounds with wide wavelengths will cause errors due to diameter mismatch. All these were evaluated and the mechanism indicated in Figure 8 was prepared.

In the first stage tests, a sample of 10 cm diameter and 29 mm thickness was placed on the 10 cm diameter part of the impedance tube as shown in Figure 9 (a). Signals starting from 16 Hz up to 1250 Hz were sent from the frequencies determined in 1/3 octave band to the amplifier from the FTT Analyser. The Amplifier amplified these signals and transmitted them to the speaker, which is the sound source, and the sound source transformed the sent frequency signal into sound and transmitted it to a 10 cm diameter impedance tube as random sound at

fixed frequency. These sound waves passed through the sample and hit the non-acoustic piston and went back through the sample. The microphones mounted on the tube detected these outgoing and return sounds, converted them into signals and sent them to the FTT Analyser.

FTT Analyser interpreted these signals as the equivalent of the frequency it sent, converting these two signals to digital data and sent them using the "LAN" local network interface. Pulse software on the computer recorded these data as 16-1250 Hz data of the 29 mm thick sample.

As a second step, the impedance tube was prepared for measurement between 1600 Hz and 6300 Hz. For this, the non-acoustic piston at the end of the 10 cm section of the impedance tube was removed and the 29 mm thick and 3 cm diameter sample was attached to the place shown in Figure 9 (b).

Two microphones are detached from the 10 cm tube and mounted on a 3 cm tube. Signals were sent again in the 1/3 octave band with frequencies between 1600 Hz and 6300 Hz. The amplifier amplified these signals and transmitted them to the speaker, which is the sound source, and the sound source transformed the sent frequency signal into sound and transmitted it to a 3 cm diameter impedance tube as random sound at a fixed frequency. These sound waves passed through the sample and hit the non-acoustic piston and returned through the sample again.

The microphones mounted on the tube perceived these outgoing and incoming sounds, converted them into signals and sent them to the FTT Analyser. The FTT Analyser interpreted these signals as the equivalent of the frequency it sent and converted these two signals into digital data and sent them to the computer using the LAN interface. Pulse software on the computer recorded these data as 1600-6300 Hz data of the 29 mm thick sample.

The same two-stage test was repeated for 19 mm and 10 mm thick samples, and the results were recorded in the computer and shown in Table 1 and graph in Chart 3.

**Table 1. Absorption Coefficients Against Frequency Obtained as a Result of the Experiment's It is made in Combined EC tube (10 cm and 3cm tubes are combined)**

| Frequency (Hz) | Absorption Coefficients | | |
|---|---|---|---|
| | 29 mm Foam | 19 mm Foam | 10 mm Foam |
| 16 | 0,02 | 0,02 | 0,02 |
| 20 | 0,03 | 0,03 | 0,03 |
| 25 | 0,03 | 0,03 | 0,03 |
| 31,5 | 0,03 | 0,03 | 0,03 |
| 40 | 0,03 | 0,03 | 0,03 |
| 50 | 0,03 | 0,03 | 0,03 |
| 63 | 0,04 | 0,04 | 0,03 |
| 80 | 0,04 | 0,04 | 0,04 |
| 100 | 0,05 | 0,04 | 0,04 |
| 125 | 0,06 | 0,05 | 0,04 |
| 160 | 0,08 | 0,06 | 0,05 |
| 200 | 0,1 | 0,06 | 0,05 |
| 250 | 0,12 | 0,06 | 0,05 |
| 315 | 0,15 | 0,07 | 0,05 |
| 400 | 0,19 | 0,09 | 0,05 |
| 500 | 0,26 | 0,14 | 0,06 |
| 630 | 0,45 | 0,23 | 0,08 |
| 800 | 0,68 | 0,35 | 0,12 |
| 1000 | 0,84 | 0,49 | 0,17 |
| 1250 | 0,9 | 0,63 | 0,21 |
| 1600 | 0,91 | 0,81 | 0,32 |
| 2000 | 0,97 | 0,9 | 0,47 |
| 2500 | 0,94 | 0,93 | 0,5 |
| 3150 | 0,9 | 0,98 | 0,7 |

| | | | |
|---|---|---|---|
| 4000 | 0,84 | 0,93 | 0,85 |
| 5000 | 0,88 | 0,79 | 1 |
| 6300 | 0,94 | 0,86 | 0,96 |

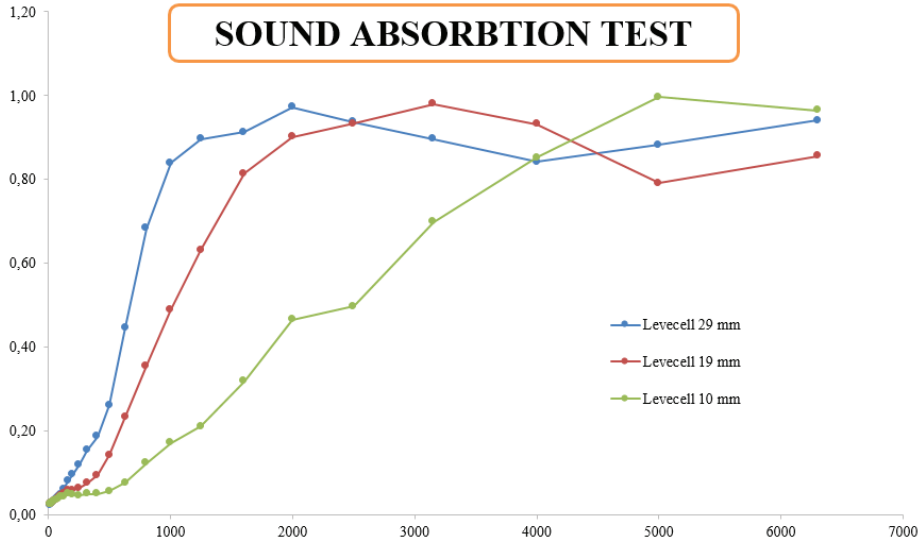


**Chart 3. Sound Absorption Graph According to the Foam Thicknesses of the Experimental Study Results**

## CONCLUSION

It is known that the acoustic performance of the vehicles is one of the most important factors in the comfort of the vehicle and the luxury of the vehicle. It has been stated how important lightness and weight reduction are in today's vehicles. According to the thickness of the polyurethane foam material, which is one of the most suitable materials for meeting these two criteria, its acoustic performance coincides with the literature.

The patented trademark Levecell foam with a thickness of 10 mm is more effective than the others at high frequency noises above 4200 Hz. This is effective in absorbing the high-frequency noises generated in the door and front fender areas, fender and trunk area, where the external noises transmitted by the air flow are present in the vehicles. In some vehicles, it can be used very comfortably against the interior of the instru-

ment panel and the tools and equipment that produce high-frequency sound. It is a cheaper one due to its thickness as 10mm.

19mm thick polyurethane foam is more effective at noises between 2000 and 4200 Hz. This is used by shaping to fit the engine hood sheet in order to absorb the internal noises and reduce the noise leaking out in the hood insulation of the vehicles. In addition, it is used as a low density absorber of inner dash insulators. This insulators types are called as "dual impedance" and "multi-layer laminated".

29 mm thick polyurethane Levecell foam absorbs the noise much more at low and medium frequencies (100-2600 Hz) than others. It is the most expensive because of its thickness. Despite this, it is used in places such as the engine side dashboard and engine tunnel, together with a regional high heat protective aluminium coating, in absorbing the noises (250-1000 Hz) transmitted by the engine and transmissions. It is used for road and tire noise and for absorbing aerodynamic noises, by shaping it in areas such as the top of the transmission, under the floor carpet and under the windshield.

An average of 0.25m3 of only this type of absorbent material is used in a middle-upper class vehicle. With Levecell foam its weight is 3,75 kg. It weighs 13 kg with a viscoelastic material, and about 18-22 kg with a material such as felt and glass wool. With the use of a very light, formable, self-supporting material such as Levecell foam with high mechanical properties and absorption coefficient, the acoustic performance can be increased. The weight of an average vehicle can be reduced between 3.5 - 5.5 times by using only in this type of absorption materials.

## REFERENCES

Aldhahebi, A. M., Junoh, H. J., Ahmed, A. (2016). A review on the major sources of the interior sound vibration and riding comfort in vehicles. *AIP Conference Proceedings* 1775, 030039.

Baek, S. W., Lee, S. W., Kim, C. S. (2019). Experimental verification of use of vacuum insulating material in electric vehicle headliner to reduce thermal load. Applied Sciences, 9, 4207; DOI:10.3390/app9204207

Bilova, M., Lumnitzer, E. (2011). Advanced techniques used for acoustical parameters determination of sound absorbers. Annals of faculty engineering Hunedoara – International Journal Of Engineering, Tome IX. Fascicule 1. P.39-42. ISSN 1584 – 2665. http://annals.fih.upt.ro/pdf-full/2011/ANNALS-2011-1-04.pdf

Çelikel, D. C., Babaarslan, O. (2017). Effect of Bicomponent Fibers on Sound Absorption Properties of Multilayer Nonwovens. Journal of Engineered Fibers and Fabrics V.12, Issue 4. Pg.15-25. DOI: https://doi.org/10.1177/155892501701200403

Cerrato, G. (2009). Automotive Sound Quality – Powertrain, Road and Wind Noise. *Sound & Vibration*. vol. 43, no. 4, pp.16-24,

Deulgaonkar, V.R., Kallurkar, S. P., Mattani, A. G. (2014). Review and Diagnostics of noise and vibrations in automobiles. International Journal of Modern Engineering Research (IJMER), Vol.1, no. 2, pp. 242-246, 2014, ISSN: 2249-6645.

Dobie, R. A., Hemel, S. V. (2004). *Basics of Sound, the Ear, and Hearing, in Hearing Loss: Determining Eligibility for Social Security Benefits*. Dobie, R. A., Hemel, S. V. Ed., National Academies Press Washington (DC),Chapter 2,ISBN-10: 0-309-09296-5.

Gelen, M. (2016). Investigation of the effects of acoustic materials and material properties used in the automotive industry on acoustic parameters. *M. S. thesis*, Institute of Science, Mechanical Engineering Department, Istanbul Technical University.

Harkude, M. N., Malagi, R. R. (2015). Automobile noise and vibration-sources, prediction, and control. *Indian Journal of Scientific Research*. vol.12, no. 1, pp. 0001-0006.

Hiroyuki, H., Hiroyasu, K. (2002). A new objective evaluation method of wind noise in a car based on human hearing properties. *Acoustical Science and Technology*. vol. 23, no. 1, pp. 17-24,

Mao, J., Hao, Z. Y., Jing, G. X., Zheng, X., Liu, C. (2013). Sound quality improvement for a four-cylinder diesel engine by the block structure optimization. *Applied Acoustics. vol*. 74, pp. 150-159.

Matijević, D. V., Popović, V. M. (2017). Overview of modern contributions in vehicle noise and vibration refinement with special emphasis on diagnostics. *FME Transactions*, vol. 45, no. 3, pp. 449-458.

Panza, M. A. (2015). A review of experimental techniques for NVH analysis on a commercial vehicle. *Energy Procedia*. vol. 82 pp. 1017-1023.

Peters, R. J., Smith, B.J., Hollins, M. (2013). *Human Response to noise, in Acoustics and Noise Control*. 3rd ed., New York, USA: Routledge, pp. 55-74. ISBN: 13:978-0-273-72468-1

Rissler, K. (2011). Applying the reciprocal transfer path analysis for the airborne sound of power train components. *M.S. thesis*, Department of Civil and Environmental Engineering Division of Applied Acoustics Vibroacoustics, Group Chalmers University of Technology, Göteborg, Sweden,

Siano, D., Panza, M. A. (2017) . sound quality analysis of the powertrain booming noise in a Diesel passenger car. *Energy Procedia*. vol. 126, pp. 971–978. DOI:10.1016/j.egypro.2017.08.189

Siano, D., Viscardi, M., Panza, M. A. (2016). Automotive materials: An experimental investigation of an engine bay acoustic performances. *Energy Procedia*, vol. 101 ss. 598-605,

**INTERNET REFERENCES**

HBK Company. (2021). *Applications: NVH - Noise, Vibration and Harshness*. Brüel&Kjaer Denmark. Accessed: October 12, 2021. [Online]. Available: https://www.bksv.com/en/Applications/vehicle-noise-vibration-and-harshness-development

*How to calculate speed of sound in solids, liquids and gasses*? (2019). October 11, *Physics About*, Accessed: October 17, 2021. [Online]. Available: https://physicsabout.com/speed-of-sound/

Malthus, R. (2021). *Basic noise terminology*. Via Strada, Accessed: October. 20, 2021. [Online]. Available: https://viastrada.nz/pub/basic-noise-terminology

Nave, C. R. (2021). *Wave Speeds, in Hyper Physics*. Dept. of Phys. Astron. Georgia State University Atlanta-Georgia USA, Accessed: Oc-

tober. 15, 2021. [Online]. Available: http://hyperphysics.phy-astr.gsu.edu/hbase/Sound/souspe2.html

Pellettieri, J. (2019). *Noise, Vibration & Harshness Challenges in Vehicle Lightweighting*, 2019 September 3) Accessed: October. 7, 2021, [Online]. Available: http://lightweightingworld.com/noise-vibration-harshness-challenges-in-vehicle-lightweighting/

Publications Office of the EU. Regulation (EU) No 540/2014 of the European Parliament and the Council, Official Journal of the European Union, vol. L158 pp. 131 195,2014.Available: https://eur-lex.europa.eu/legalcontent/EN/TXT/PDF/?uri=CELEX:32014R0540&rid=4

# ENERGY MODELING FOR BUILDING DESIGN

*Hamdi Levent KOÇALİOĞLU*[1], *Ayhan ONAT*[2]

**Abstract:** Buildings account for roughly 40% of primary energy use and 70% of overall electricity use and are frequently identified as a key target for reducing carbon emissions. New and existing buildings energy efficiency can be improved in a variety of ways, and energy models can be used to compare different strategies. Building energy modelling (BEM) is the process of analyzing a building's annual energy consumption using a computer-based simulation tool by enacting a numerical model of the building. A single building simulation can take seconds to hours to complete, depending on the level of detail and complexity of the analysis. BEM has several advantages for both new construction and retrofit projects. In new construction projects, BEM can be used to compare energy-efficiency options and assist in the finalization of design decisions for new construction buildings. In retrofit projects, it aids in optimizing the efficiency of existing buildings and evaluating retrofit options. The engine of any modeling software drives its performance and functionality. While many modeling programs use the same engine, each has its own interface, giving it a unique look and, in many cases, design and modeling options. The US Department of Energy's DOE-2 and EnergyPlus engines are the most widely used. While DOE-2 is more widely used and industry accepted, EnergyPlus is newer and has more features. The IES Virtual Environment uses Apache SIM, a newer entrant in the building energy use analysis field. The energy modelling output is generally as accurate as the input data used for the thermal model. Thus, simulation accuracy is dependent on dynamic input parameters like occupancy and weather data, which are difficult to model accurately, especially early

1 Marmara University, Faculty of Technology, Mechanical Engineering, İstanbul, Türkiye, leventkocalioglu@marmara.edu.tr, Orcid No: 0000-0002-5584-5938

2 Marmara University, Faculty of Technology, Mechanical Engineering, İstanbul, Türkiye, onattayhan@gmail.com, Orcid No: 0000-0001-9737-6300

in the design process. The weather data used in the simulation has a big impact on the outcome.

***Keywords:*** Building Energy Modeling, Building Performance Simulation, Building Energy Modeling Softwares

## INTRODUCTION

Buildings account for roughly 40% of primary energy use and 70% of overall electricity use and are frequently identified as a key target for reducing carbon emissions. Improving the efficiency of building design has become a significant strategic effort for the entire industry. Building energy modeling has been recognized as a critical tool for enhancing the design of energy-efficient buildings.

Building Energy Modeling (BEM) is the process of analyzing a building's energy use using computer-based simulation tool. The simulation tool operates through a numerical model that presents a building's thermal model. External weather conditions, orientation of the building, building's geometry, construction materials, user schedules, and HVAC system equipment will all be input into the building model by an energy modeler. The calculation engine solves thermodynamic and building science equations. Based on required complexity level of the analysis, simple energy simulation runtime can be a couple of seconds or even hours to complete. The building's zone heating and cooling loads, several systems energy use and costs breakdown, natural daylight mapping, and other significant energy and occupant comfort related parameters are typically reported for annual performance. Figure 1 shows an image of typical workflow of building energy modeling process.

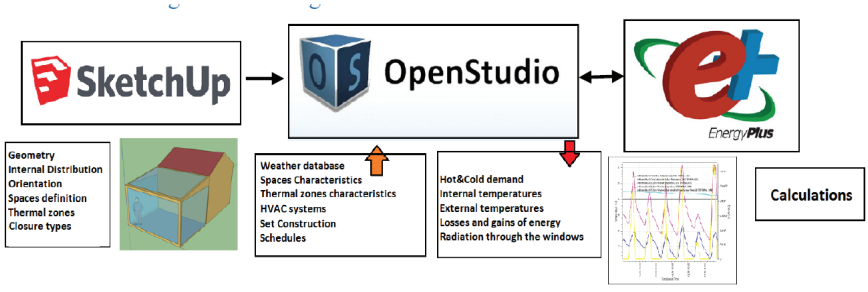


**Figure 1. Typical Building Energy Modeling Workflow**

Prior to construction, BEM can be utilized for comparing energy-efficient design options and help to finalize design decisions. It also assists existing buildings in maximizing their efficiency or evaluating retrofit options. BEM incorporates building performance simulation and comprehensive equipment study using specific tools for indoor air quality, daylighting, occupant comfort, and natural ventilation. Figure 2 illustrates an example of 3D representation of buildings' thermal model created in DesignBuilder software.

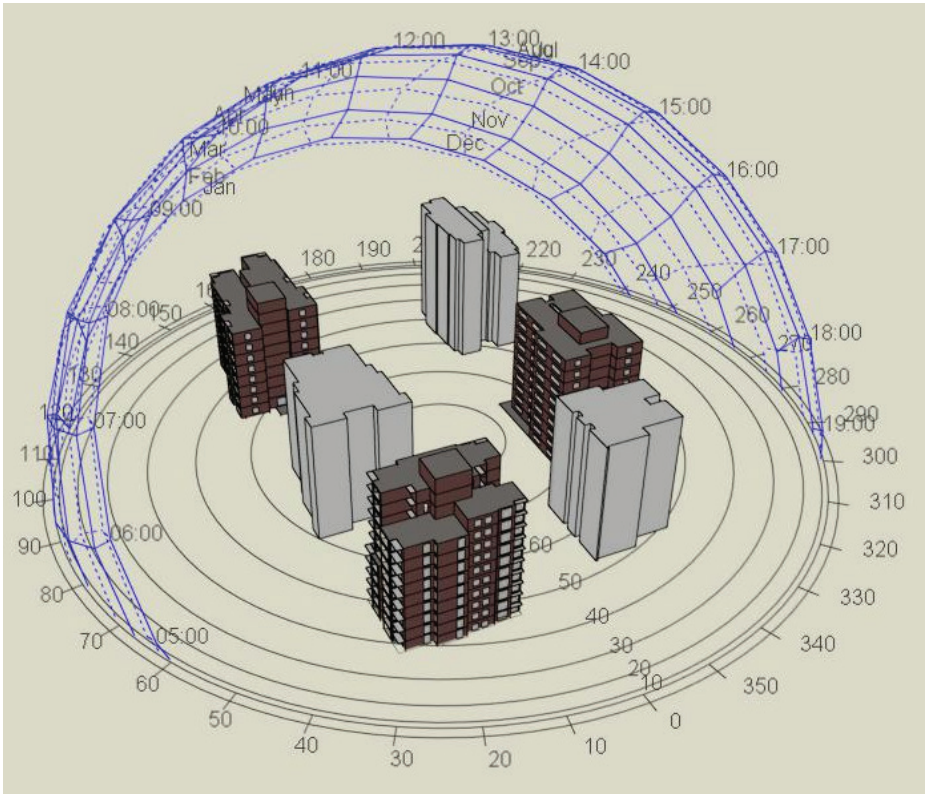


**Figure 2. Typical 3D Representation of Buildings**

The majority of whole-building simulations include:

- *The geometry of the building, the floor plan, the construction materials, elements, and systems*
- *Typical weather data for the location*

- *Heat transfer, both instantaneous and delayed*
- *Divided thermal zones for building*
- *Day, week, and season variations for occupants, interior and exterior lighting, receptacle equipment, thermostat setback and setpoints, and operation of HVAC systems*
- *End-use Breakdown of Each Energy System*
- *Cost Breakdown of Each Energy Type*

**What are the Benefits of BEM?**

BEM has several advantages for new design and existing building projects. BEM, for instance, aids in the development of an integrated design process (IDP). Project stakeholders establish and agree on outcome-based goals through IDP. BEM provides the team with the information they need to make critical, cost-effective design decisions which mostly includes both initial cost and total operation costs for a year. The cost of energy modeling is often a small additional increase in total budget, but it could result in effective cost savings. When it comes to energy efficient building design, system integration, and renewable energy, quantifying performance tradeoffs could help an owner maximize their return on investment.

In general, BEM can be useful for a project in three different purposes.

**Lower Initial Costs**

BEM can lower a building's initial cost by including effects of thermo-physical properties of of building materials and controlling systems holistically to optimize them and properly sizing zone, system, and plant equipment. Additionally, BEM can also significantly minimize project change orders. Moreover, BEM can be useful for providing the necessary evidence in order to apply for incentives programs.

**Lowering Operating Costs**

BEM can help to save money on building's annual operating costs by allowing to compare different operation and control alternatives

which are affecting energy use. In addition, BEM could aid life cycle assessment by selecting efficient materials/systems which might be costly up front yet reduce significant energy and maintenance costs in the long run.

**Improved Occupant Comfort**

BEM can assist in identifying ways to make employees more productive while reducing absenteeism. Improved occupant comfort has been linked to enhanced building envelope, appropriate fresh air rates, maximized use of daylighting, and personal equipment operation and control, according to research. BEM presents large sets of data to improve thermal comfort for occupants.

Another use of BEM is monitoring and informing existing buildings control and operation. Facility managers can identify performance gaps through comparison of BEM outputs with building actual utility bills. To ensure that everything is working properly, BEM can be used for benchmarking to make comparison for HVAC system energy use. Performance gaps can be resolved with revealing those gaps in optimum operational period to make adjustments for enhancement.

**What is the Purpose of BEM?**

Facility managers are increasingly recognizing the value of BEM through retrofit opportunities with guiding energy efficiency measures decisions, so it's becoming more common to include it in building energy efficient retrofit projects. Additionally, BEM might be necessary to show compliance with energy use improvement from baseline buildings in several certification rating systems.

BEM could help to achieve wide range of goals. The applications are divided into three categories based on their general modeling purpose: comparing, complying, and predicting. There are several parameters (purpose, complexity, scope) that can all be influenced by the underlying goal. Understanding the differences between efforts can assist defining the project modeling scope and securing the services required.

### Comparison Model

Most modeling efforts rely on BEM to compare energy efficient design options for zone, system, and plant level equipment. Performance comparisons are almost always included in the process.

Comparing performance allows the design team to compare and contrast different design concepts quickly. For example, simulating specific glazing types to see how they affect several key parameters such as heating and cooling load demand, lighting systems energy use. Energy efficient options may be combined to understand harmonious effects for reducing the need for air conditioning, using passive measures, and decrease initial costs.

The goal of creating baseline case for potential savings prediction can be guiding design decisions. As a result, a modeler may concentrate on characterizing important items in detail while relying on standard values for less-important items. Figure 3 shows a graph comparing actual annual energy use with simulated annual energy use.

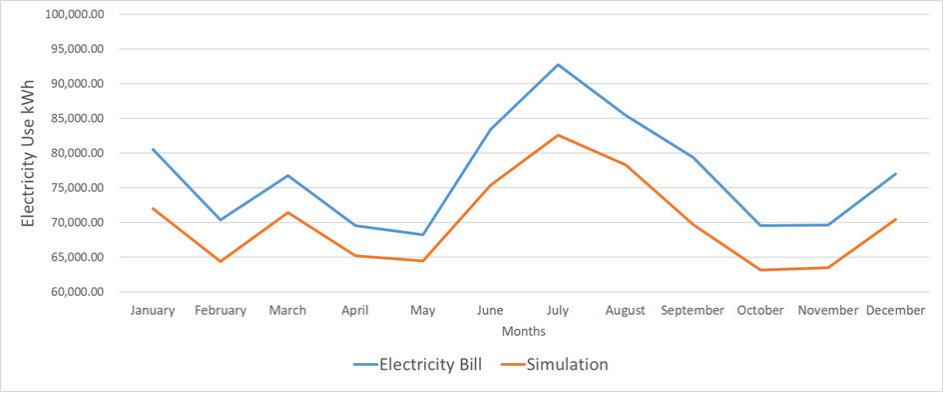


**Figure 3. Graph Comparing Actual Electricity Use with Simulated Electricity Use**

### Compliance Model

The proposed and baseline case models are two models to make a comparison analysis for energy performance as part of compliance modeling. The baseline case is a building that ensures code compliance program's reference standard.

For instance, the Leadership in Energy and Environmental Design (LEED) program of the United States Green Building Council (USGBC) awards performance credits over to a baseline case costs. The ASHRAE 90.1 Standard serves as the LEED reference baseline. The energy model must be in compliance ASHRAE 90.1 Appendix G to create the base case model. Many of the base case model input parameters, e.g., climatic region, building construction area, and building height are dependent on design model details; while other data inputs, e.g., zone, system, plant equipment minimum efficiency requirements, are documented in the 90.1 Standard Appendix G. Even if LEED modeling's ultimate goal is certification, it can also be used to compare design options. As a result, both comparison and compliance scope should be included in the certification modeling effort.

**Prediction Model**

Energy models that incorporate utility bills data sets can depict the building's current energy use and anticipate the renovated building's energy use. Developing a complex detailed model requires time and effort. Several building systems, such as lifts, escalators, and large exhaust fans, must be added in energy model, although those systems will remain constant throughout design variations. Additionally, the model must incorporate current occupant and HVAC system operation profiles, which might be challenging to get even while the building is operational. Furthermore, the model's weather data input must be relevant to its location.

The majority of building energy modelling inputs start with common occupancy patterns, and ideal operation of building HVAC systems. However, there might be unexpected problems during construction, such as improper installation or control sequence of HVAC system. Therefore, for parameters that are unknown during design, the latter must rely on assumed input values. However, after full occupancy completed and utility bills data gathered, building energy model calibration can be performed for those outputs.

Making direct connection between design and operation can give valuable feedback to project teams. This contributes to mutual understanding of energy efficient design and alternative solutions. Moreover, elements that are underperforming can be identified and corrected using the performance gap analysis between calibrated simulation model and final construction model.

**Building Energy Modeling Types and Uses**

The performance of a proposed model will be compared to baseline model in terms of annual energy use and costs. In both models, number of operational assumptions will be identical (e.g., climate zone file, occupancy schedules). When compared to the baseline model, the model results will be expressed as energy and cost reduction for proposed model. This method is best for determining energy reduction target prior to design development. Prediction of energy performance will provide numerous expected results to make energy efficient design decisions and through that sensitivity analysis can be performed. The level of model accuracy associated with the chosen inputs will ideally decrease in design deve progresses. The system methodology works well for establishing comparison levels when utility bill data collected, and full occupancy completed. The most unpredictable input to any building simulation is the use and behavior patterns of the occupants.

**The Energy Model as a Comparative Tool**

Throughout the design process, modeling can help the project team. Multiple design alternatives can be compared side by side for a quick and low-cost assessment for several alternatives. Design decisions have a wide range of consequences that aren't easy to predict. The cross effects between building thermal properties and HVAC systems control and operation can be analyzed and quantify with reliable building simulation modes. In general, a computer simulated analysis is required to complete a cost-effective analysis of a design decision.

### The Predictive Energy Model

The annual energy use and costs of the building will be estimated using a predictive energy model. This data can be helpful with cost assessment of life cycle and renewable energy systems. If the project team wishes to use modelling outputs, there should be an integrated discussion among project teams. Standard energy modelling comparative analysis frequently lack the details and cost schedules needed to accurately forecast future costs.

### Life Cycle Cost Analysis

Life Cycle Cost Analysis (LCCA) is a methodology for assessing building's economic performance over its whole life. Occasionally referred to as "whole cost accounting" or "total cost of ownership,". LCCA represents a compromise between the initial financial investment and long time period of building's operating costs. Initial investment cost, operating costs, short- and long-term maintenance costs are included in the analysis. Inflation and projected fuel cost adjustments are also taken into account by the LCCA. While the initial capital costs are significant, they are not able to reflect a complete image. Powerful energy modelling output will be useful to adjusting project's budget and performing fine-tuning of design decisions.

### Modeling Documentation for Building Rating Certification

Numerous green building rating systems involve building energy modelling documentation to receive points for reduced energy consumption over a baseline. Under the USGBC's Leadership in Energy and Environmental Design rating system (LEED) criteria, point allocation for the primary energy credit is based on a building energy use and cost comparison over a code-compliant reference building. LEED define reference model based on ASHRAE 90.1 guidelines. There is no necessitates for the use of any specialized software. However, ASHRAE 90.1 has some specific performance prerequisites for building modelling tools.

**Measurement and Verification**

The term "Measurement and Verification" (M&V) refers to the process of planning, measuring, collecting, and analyzing data in order to verify and report energy savings for an individual building. After full occupancy has been completed, energy models are constructed for measurement and verification. The model is built using actual equipment and building systems, and the energy use outputs are analyzed to actual utility data measurements. Because the true energy performance of the building is known, modelling for measurement and verification process typically involves calibrated energy model with adjusted several inputs, most notably for the building's actual operational conditions, until the modeled energy consumption matches the actual measured data. Once calibrated, the model can be used to estimate the cost savings associated with various measures and can normalize for the input data variation in HVAC system operation and climatic properties, for example. In case of the energy use isn't within the expected range, it's possible that the equipment isn't calibrated correctly or isn't working properly. If problems are discovered, additional tracking can be used to ensure that the problems have been resolved.

**Asset Evaluation**

An asset evaluation uses a building energy model to assess the physical attributes of the building based on the components specified in the design (such as mechanical systems, building envelope, orientation, etc.). A few states in the United States are requiring such an assessment at the time of sale or lease. There are programs in place in the United Kingdom and Europe that require an asset rating. The asset evaluation must be compared to some benchmark performance standard in order to obtain an asset rating. This benchmark could be the ASHRAE Standard 90.1 baseline model, or a standard prototypical building developed by the US Department of Energy's Commercial Building Benchmark Model project.

### Energy Modeling Throughout the Design Process

Energy modeling should be used to assist in integrating and optimizing the energy performance of a building during design process. Furthermore, it requires early evaluation of system solutions among different disciplines in order to develop the best-fit solutions for the developing design, thereby avoiding drastic design changes late in the design phase. Figure 4 shows an image of synthesis of several factors for integrated design.


**Figure 4. Integrated Design Synthesis**

Throughout the construction process, there will be several consultants using early/late design model to understand and analyze the constructed site conditions. Following stages explain the necessity of energy modeling and the measures that must be taken during each design phase.

- *Predesign*
- *Schematic Design*
- *Design Development*
- *Construction Documents*

Energy efficient design should be considered with every decision in order to construct high-performance buildings. Benefits in energy efficient design are rarely achieved through a single big idea; rather, they are achieved through the combination of a hundred small ideas to achieve high performing buildings. A room with a light color partition walls and ceilings, for example, can influence how well it receives natural light. Reflection of more light from those components can be combined with proper daylighting sensors, could support cutting down on required lighting energy use. Partition walls color decision generally chosen at the end of the design development phase and if not properly coordinated with the energy model, they can have unintended consequences.

**Pre-Design and Conceptual Design**

At the conceptual and schematic stages of design, energy modeling can be extremely useful. Most of the data gathered through energy modelling could be used to aid project's design team during the preliminary stages for little to no cost. Changes become increasingly costly and difficult to implement as the design progresses. The energy model outputs can ensure that everyone on the design team is on the same page.

Building energy modelling can be used for analysis of climatic and environmental factors during the pre-design and conceptual design stages. Those factors reviews are necessary for developing building position and type of space use which are compatible to surrounding boundaries. Large sets of climatic inputs can be transformed to single reference data file and extends using a variety of modeling software packages. A wind rose and dry bulb temperature floodplot weather study for an entire year for Antalya are shown in Figure 5 and Figure 6, respectively. Those data give quick overview for project's site weather properties.

Energy modelling facilitates the start of discussions among project teams to consider energy efficiency targets. Create energy use intensity targets and improvement goals using the energy model.

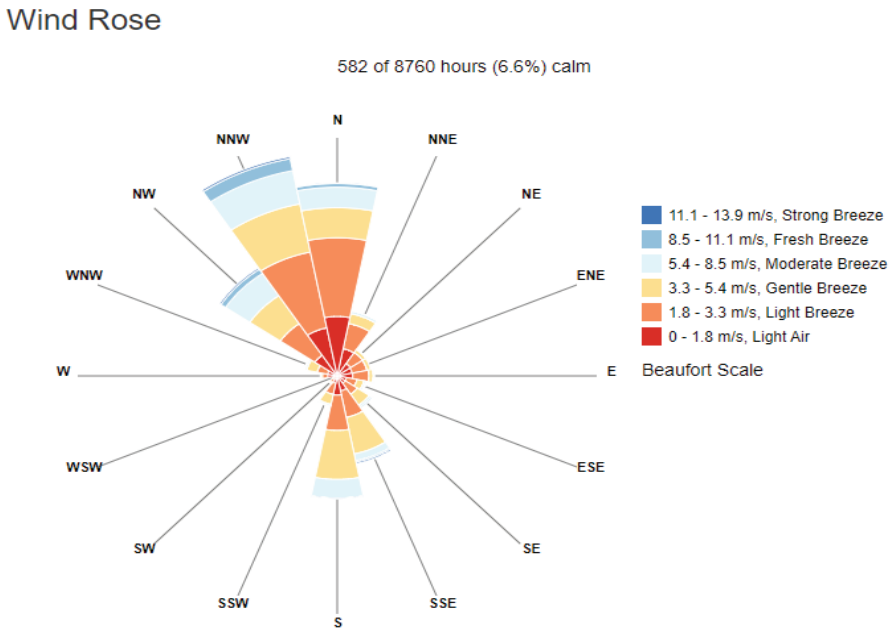


**Figure 5. Wind Rose- Annual Wind Speed Changes**

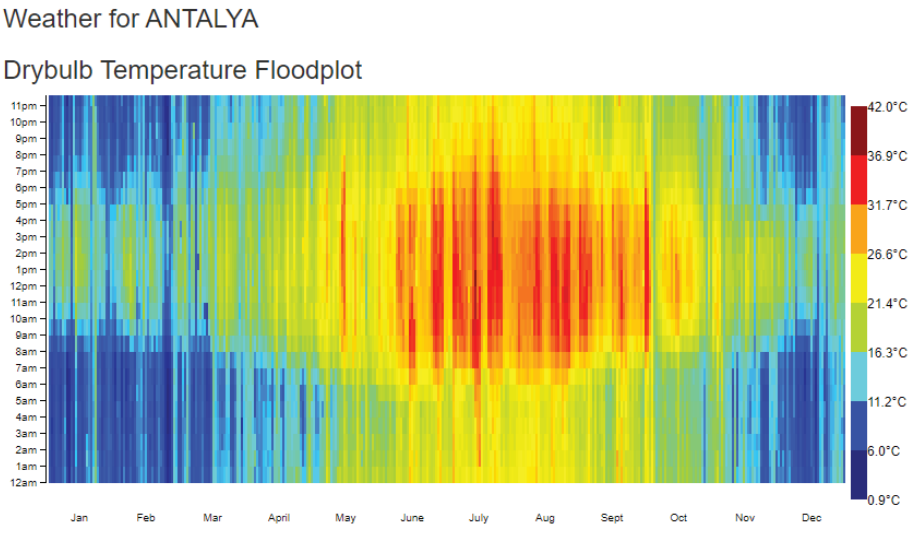


**Figure 6. Dry Bulb Temperature Floodplot Through the Year**

There are several ways that collected data can assist to design phase.

Climate Awareness:

- *Wind Direction*
- *Variations of Outdoor Temperature*
- *Analysis of Solar Radiation*

Occupant Comfort:

- *Space Temperatures*
- *Outdoor Air Rates*
- *Space Light Levels*

Operation Profiles

- *Assess Energy Efficient Design Alternatives*
- *Targets for Energy Use Intensity*

**Schematic Design**

At the schematic stages of design, energy modelling could help design team to evaluate several concept alternatives. Alternative room layout, window distribution, location of main heating and cooling plants can be designed and positioned. Even though those arrangements might develop to be mainly practical, they could all have an impact on the occupants' energy use and comfort on that modelling can aid to finalize. For the model outputs, for example, adding more insulation material might bring extra initial cost that results in lower operating costs year after year, also lower HVAC equipment costs might be cover additional costs of insulation. The design concepts of the selection of the equipment can be discussed in the latter stage. Choosing an energy efficient design option to use must be done at the early design stage and then, starting a discussion on energy efficient design ideas. Figure 7 illustrates an image of pedestrian comfort level analysis created for visualization of wind speed for a high-rise building.

Energy modeling during schematic design can optimize and analyze:

- *Building Envelope*
- *The Form of The Building and Orientation*
- *Selection of HVAC Alternatives*
- *Zoning Strategies*
- *Daylighting Analysis*
- *Natural Ventilation Possibilities (Figure 8 shows CFD Analysis for Natural Ventilation)*

Energy modeling during schematic design key findings:

- *Peak Energy Demand*
- *Energy Use*
- *Thermal Comfort*

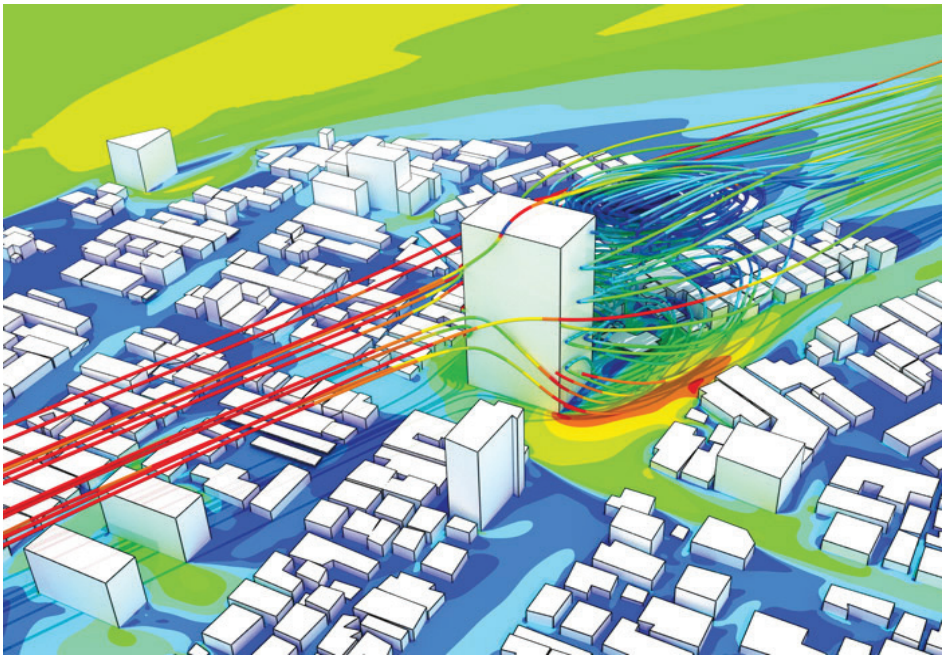

**Figure 7. Pedestrian Comfort Level Analysis**

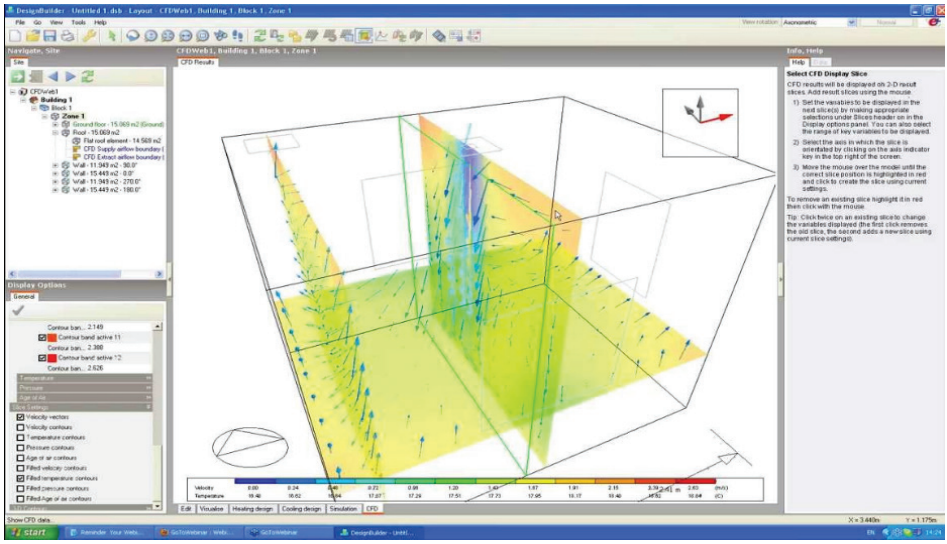

**Figure 8. Natural Ventilation Analysis**

### Design Development

The building configuration and systems are refined during the Design Development phase. During this phase, project members continue to discuss key performance necessities for building envelope and glazing, daylighting zones, and shading element devices. All of these decisions can be aided by a robust energy model.

Analysis of Design Development Stage

- *Optimization of Building Walls and Fenestration*
- *Integration of Lighting Automation with Daylighting Sensors*
- *Integration of Mechanical Controls Systems*
- *Selecting Optimum HVAC System*
- *Energy Recovery Identification*

### Construction Document

At the Construction Documents phase, energy modelling could help setting of heating and cooling design temperatures which directs zone level equipment sizing. Prior to construction, design team can optimize

HVAC system constant fan power, setback temperatures, and a variety of other settings. Parametric assessment can be performed by most of the modelling software that involves simulation runs for several parameters on minor changes to analyze project's targets like energy usage intensity, and load levelling strategies.

**Performance Documentation**

Simulate and compare methodology between proposed versus reference building models can be used to validate building performance. Hence, the project team is able to:

- *Evaluate the effects of construction changes*
- *Create documentation for LEED rating systems*
- *Support building recommissioning*
- *Verification of building performance as intended for below factors:*
  - *Air changes per Hour*
  - *Building Operation Profiles*
  - *Heating and Cooling Equipment Setpoint and Setback Temperatures*

**Modeling Results and Technical Reporting**

The Energy Simulation documentation provides a brief overview of the project's current energy effectiveness by key performance metrics. Each modeling report should include the following information:

- *Detailed Zone Level Equipment Summary*
- *Summary of Data Inputs*
- *Proposed List of Energy Efficient Design Parameters*

Designers can use the energy modelling data input summary and confirm that they are identical to project's system and equipment. A computer-based simulation can only work properly if its users input the correct data. Simple simulation reporting could present a parametric analysis to show cost effective design alternatives of adding one more layer to the external wall or upgrading current design heating system to highly efficient heat recovery equipment.

The simulation results report is perhaps the most important modeling summary. A quick review of the several building system's end-use breakdown of energy can be seen in this report. This information will be provided for both the proposed and existing designs, as well as any alternative designs that are being simulated. Most of the time, a baseline model generation is the first step for the preparation of a reference to compare design alternatives in order to find energy use or demand reduction. Building rating system certifications, and other documentation frequently require baseline models.

Most of the modelling report-based suggestions could include major changes to orientation of the building and methodology of construction early at the design process. Energy efficient design options must be concentrated on building envelope properties, passive and active measures for HVAC system, and system's sequence of operation in later design phases.

**Important Modeling Outputs**

- *Cost of Energy (Annually)*
  - *Electricity, Natural Gas, Chilled Water, etc.*
- *Use of Energy (Annually)*
  - *Heating, Cooling, Lighting, Pumps, Fans, DHW, etc*
- *Electricity and Natural Gas Demand*
- *Specific Energy Use (kWh/m$^2$)*

**Energy Modeling Software**

Building energy modeling program simulation engine is the most essential part of the software that solves mathematical models of the building elements, equipment, and so on 8760 times (one for every-hour), usually through a sequential process. Common results include annual energy consumption, annual energy cost, hourly profiles of cooling loads, and hourly energy consumption. Majority of software using similar simulation engines for modeling options. Both of DOE-2 and EnergyPlus, created by United States Department of Energy, are the most

widely used engines. DOE-2 has gained industrial recognition, while EnergyPlus has recent development with more features. Apache SIM, which is used in the IES Virtual Environment, is relatively new software product in the market. Apache SIM aims to provide a platform for evaluating all aspects of thermophysical properties of building envelope and HVAC systems control integration. On the other hand, Radiance can model daylighting potential and available for informing specific design considerations. Figure 9 illustrates an image of several energy modelling software programmes.

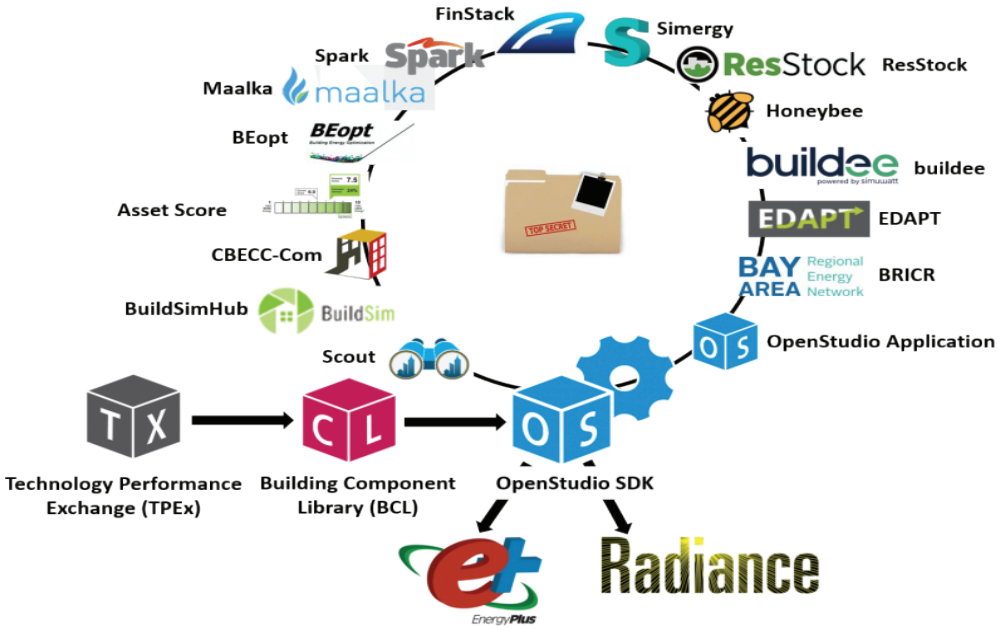


**Figure 9. Energy Modelling Software Programmes**

## CASE STUDY

The building energy modeling study has been completed for a 5200 $m^2$, 10-floor residential building in addition to one basement floor mainly for technical areas. The general building information is provided in Table 1 for case study. Additionally, the building has reinforced concrete building with filled in brick walls and without heat insulation. The fenestration of the building consists of aluminum frames without ther-

mal break and double-pane clear glass with U-value of 2,4 W/m$^2$K. The building includes residential units, corridors, and common associated areas.

The analysis tool chain is shown in the following Figure 10. Design-Builder is used to create full three-dimensional architectural models that are then exported to EnergyPlus (v9.4) as an input file, which is used for analysis of both the existing and proposed designs reported here.

3D Architectural Model

Preliminary modeling and anaylsis

Existing & Proposed Design energy modeling, parameter definition and detailed analysis


**Figure 10. Analysis Tool Chain**

**Table 1. Case Study Building Summary**

| | | |
|---|---|---|
| **General Information** | | |
| 1 | Building Area | 5,200 $m^2$ (Residential Units: 3,700 $m^2$ Core Areas and Corridors: 1500 $m^2$) |
| 2 | Building Type | Residential Building |
| 3 | Location | Antalya |
| 4 | Climate Zone | ASHRAE 3A |
| 5 | HVAC system | Heating System: Natural Gas Fired Condensing Boiler Cooling System: AC split units No mechanical ventilation |
| **Details of Energy Efficiency Measures** | | |
| 1 | Building envelope specific measure (solar control low-e glass and exterior wall and roof insulation) | |
| 2 | Highly efficient air conditioning units with SEER 5.6 | |
| 3 | Efficient LED lighting systems | |
| 4 | External shading element design for windows on south façade | |

Figure 11 shows typical building architectural floor plan for the case study building.

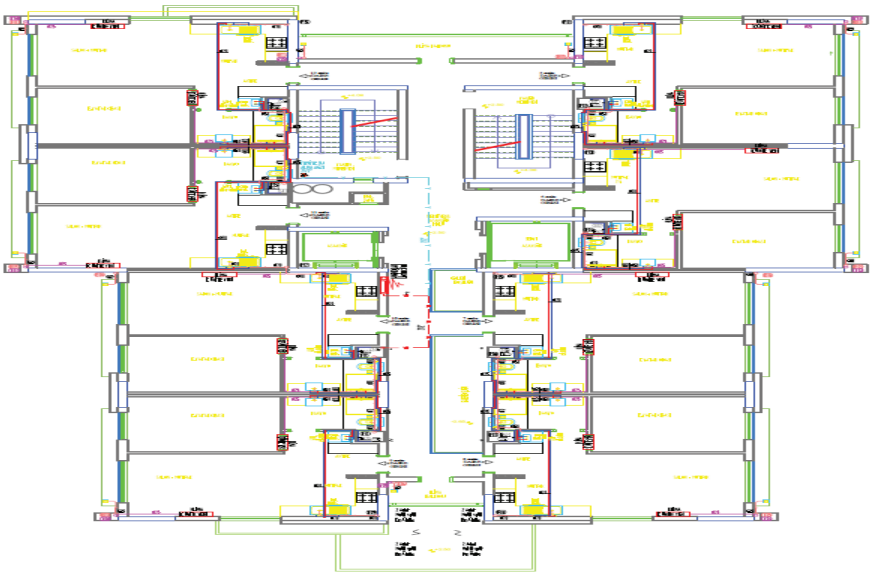

**Figure 11. Case Study Building Typical Floor Plan**

3D Thermal model is generated from building architectural drawings can be seen from Figure 12 and Figure 13, respectively.

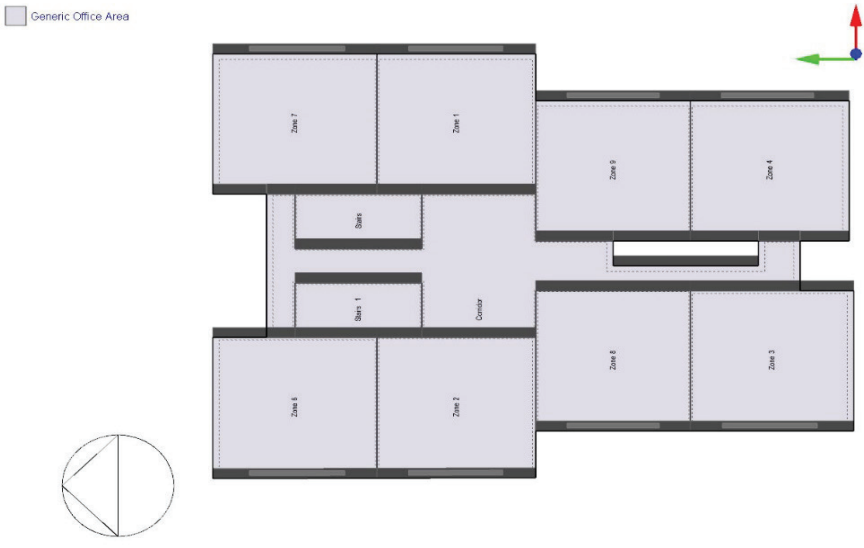


**Figure 12. Case Study Building Thermal Model Typical Floor Plan**

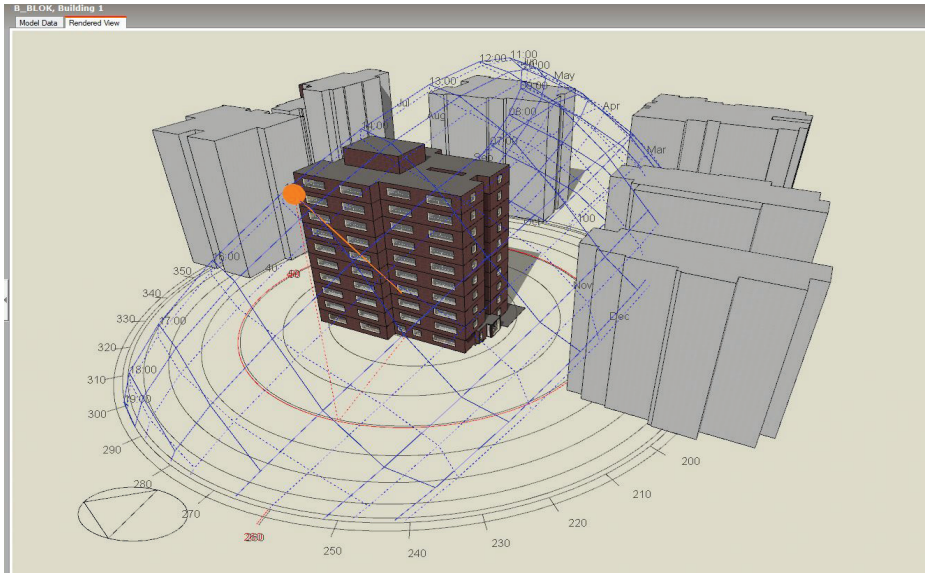


**Figure 13. Case Study Building Perspective View**

### Methodology

A whole building energy simulation has performed for showing annual energy performance improvement compared to the existing building performance through proposed energy efficiency design measures.

### Data Collection

The computer-aided design (CAD) drawings of the site, floor plans of the building and section details has provided for developing thermal model. MEP consultant has provided details of proposed design for lighting, envelope, and HVAC systems.

### General Building Model

By following the modelling guidelines and evaluating each simplification methodology carefully, in order to avoid any significant impact on simulation results, a representative thermal model of the proposed building has prepared as shown in Figure 14.

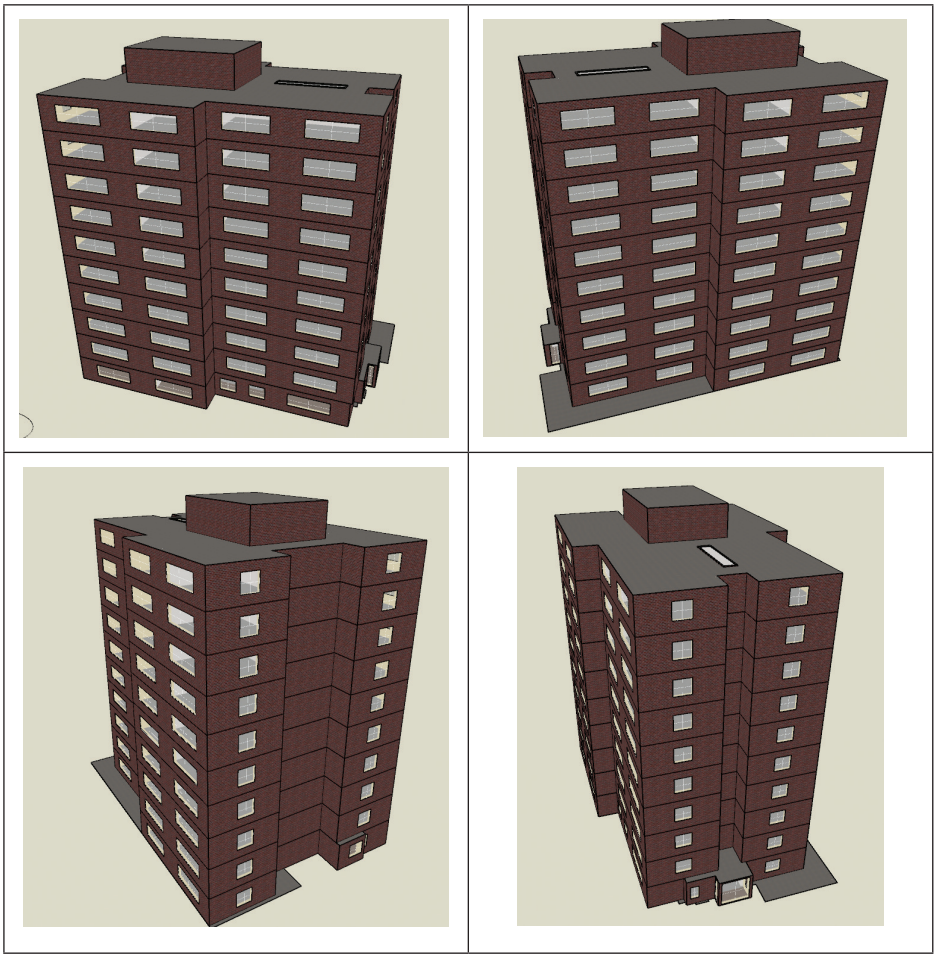

**Figure 14. 3D Views of Building Thermal Model**

The same methodology has applied for zoning while going through the floor plans. Briefly, both proposed and baseline models comprise of 79 conditioned and 37 unconditioned zones, simplified to enhance speed of the simulation runtime. Thermal model's basement floor and typical building floor can be seen in Figure 15.

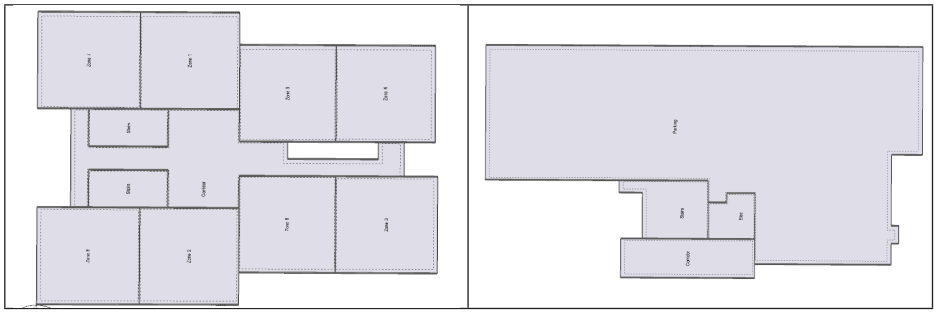

**Figure 15. Plan Views for the Thermal Model**

### Climate and Site Data

The project's location defined as Antalya with required geographical data and can be seen in Figure 16.

The project's climate zone is climate zone 3A. The weather data file used in the simulation is "ANTALYA - TUR IWEC2 WMO#=173000" weather data file. A plot of the dry bulb and wet bulb temperatures from the climate data is provided in Figure 17.

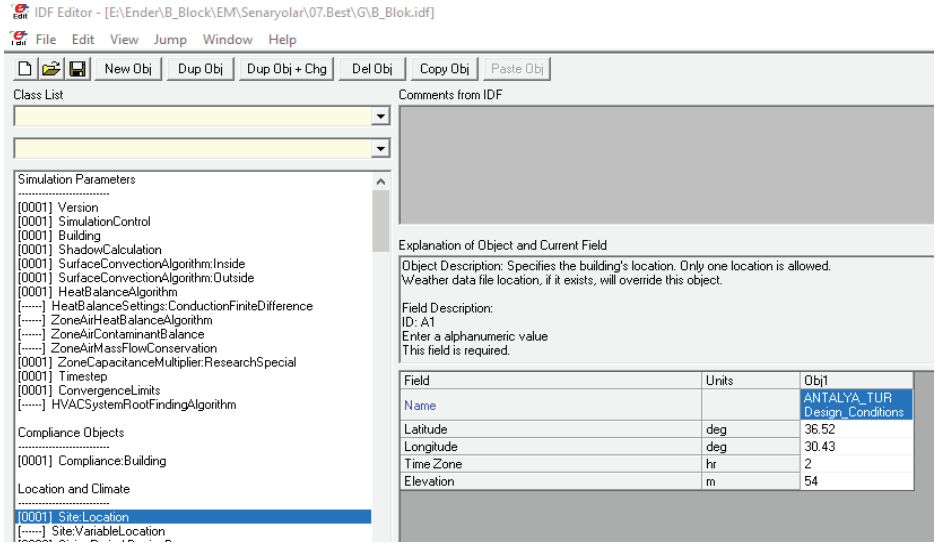


**Figure 16. Energyplus Input File Site Location**

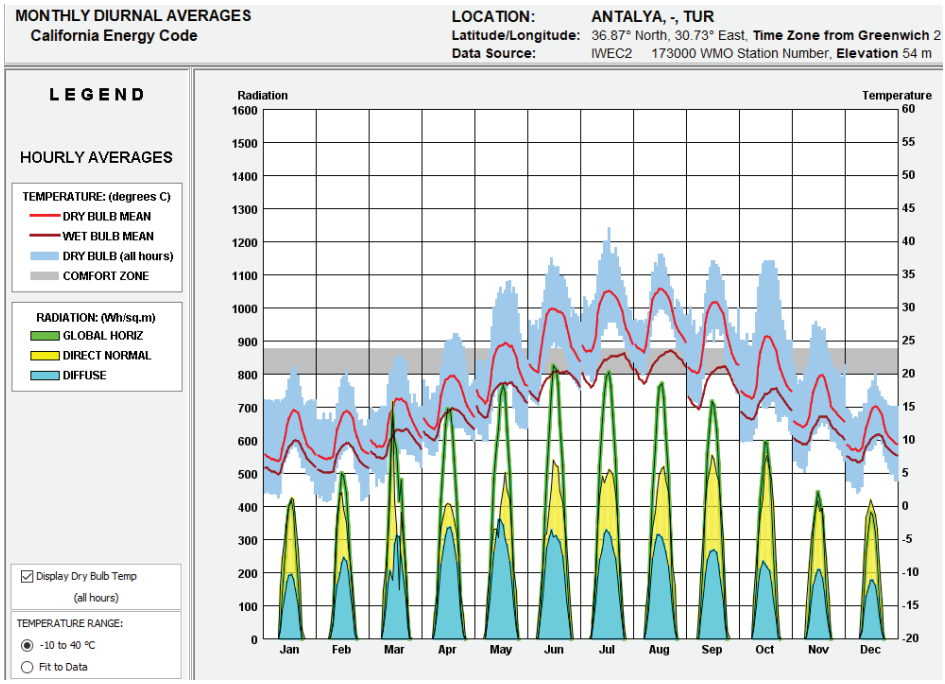


**Figure 17. Ambient Dry Bulb and Wet Bulb Temperatures**

## Schedules

In performing computer simulation of building, schedules/profiles need to be defined and assigned to parameters such as:

- *Occupancy / people*
- *HVAC plant operation*
- *Interior lighting*
- *Interior equipment*
- *Infiltration*
- *Thermostat Setpoints*

In defining these schedules, a usage percentage is allocated on hourly basis, covering all 24 hours of a day and accounting for every single day of the year. The schedules/profiles used in the computer simulations are based on project's specifications and the same schedules/profiles are used in all computer simulations. Information about HVAC sys-

tems, lighting systems and operation hours are received from building facility manager and have used for building energy modeling analysis.

### Existing Building Envelope

The existing building envelope and fenestration parameters are described in Table 2.

**Table 2. Existing Building Envelope Detail**

| | Building Component | Detailed Explanation |
|---|---|---|
| Building Envelope | Roof | U = 0.450 W/m$^2$K |
| | Slab-On Grade Floor | U = 0.620 W/m$^2$K |
| | Walls | U = 0.700 W/m$^2$K<br>U = 1.100 W/m$^2$K |
| | Glazing | U = 2.40 W/m$^2$K<br>Solar Heat Gain Coefficient= 0.50<br>Visible Light Transmittance= 81%<br>Shading – No shading device<br>Window to Wall Ratio of project =21.8% |

### Existing Building HVAC and Lighting System

The existing building HVAC system detailed explanation is described in Table 3.

**Table 3. Existing Building HVAC System Explanation**

| | System/Plant | Detailed Explanation |
|---|---|---|
| HVAC | HVAC System Description | The heating water is provided by one natural gas fired, wall type condensing boilers in the basement floor. Total heating capacity of boilers is 180 kW. Residential spaces are heated by baseboard heating system.<br>Cooling demand of residential units is provided by split AC units. Additionally, ACs are used for dehumidification mode for all seasons to achieve thermal comfort conditions. The cooling capacity of AC units' range between 3.5 kW to 7.1 kW. Windows are used for natural ventilation in residential units. |

The schematic view of modeled heating system of the existing building can be seen from Figure 18.

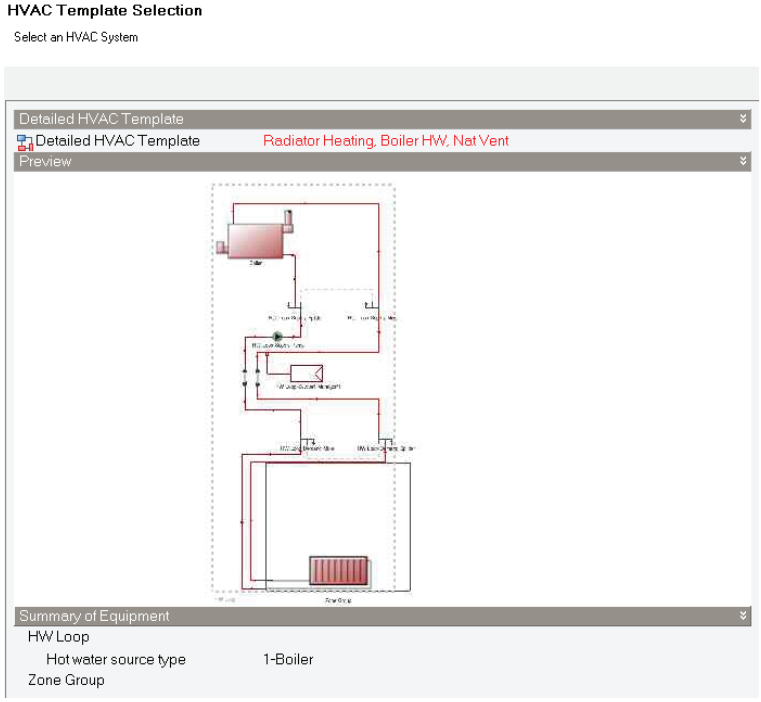


**Figure 18. Heating System Schematic View for Building**

The existing lighting power density is defined according to information that is provided from MEP Engineer and can be seen from Table 4.

**Table 4. Existing Building Lighting System Performance Specifications**

| | Space Type | Detailed Explanation |
|---|---|---|
| Lighting Power Density (W/m2) | Interior | Lighting power density of spaces in the building is identified as 6.33 W/m² based on lighting fixture quantities that can be seen below table.<br><br>Luminaire Type<br>Quantity<br>Power (Watt)<br>Total Power (kW)<br><br>Fluorescent Type Luminaire<br>60<br>50<br>3.0<br><br>LED Type Luminaire<br>225<br>24<br>5.4 |

**Existing Building Receptacle Loads**

Receptacle loads are defined as 6.0 W/m² for both existing and proposed building models and no energy efficiency measures are recommended for them. Therefore, they kept identical in simulations.

**Proposed Design Description**

The proposed building model envelope and fenestration parameters are described in Table 5.

**Table 5. Proposed Building Envelope Envelope Detail**

| | Building Component | Detailed Explanation |
|---|---|---|
| Building Envelope | Roof | U= 0.260 W/m²K |
| | Sla-b-On-Grade Floor | U= 0.500 W/m²K |
| | Walls | U= 0.300 W/m²K<br>U = 1.100 W/m²K |
| | Fenestration | $U_{windows}$ = 1.3 W/m²K<br>Solar Heat Gain Coefficient = 0.38<br>Visible Light Transmittance = 60%<br>Shading – External shading elements on South façade |

The proposed building model window performance parameters are defined with required thermophysical data and can be seen in Figure 19.

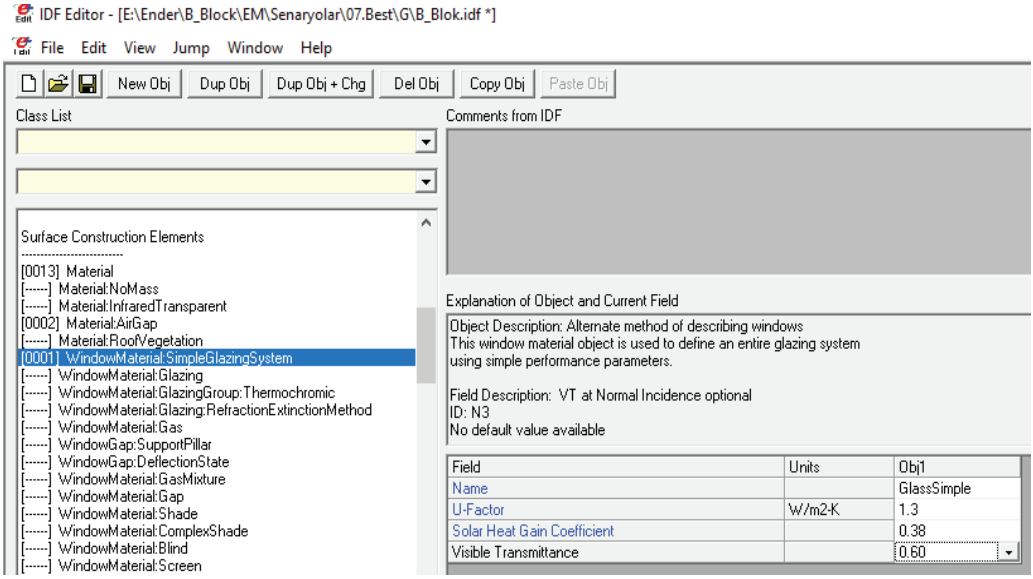


**Figure 19. Energyplus Input File Window Material**

The proposed building model HVAC system detailed explanation is described in Table 6.

**Table 6. Proposed Building HVAC System Performance Specifications**

| | Systems/Plants | Detailed Explanation |
|---|---|---|
| HVAC | HVAC System Description | High efficiency multi-split inverter heat pump AC with cooling capacity of 22.4 kW.<br><br>No energy efficiency measures proposed for the existing heating system. |

The schematic view of modeled cooling system interior units of the proposed building model can be seen from Figure 20.

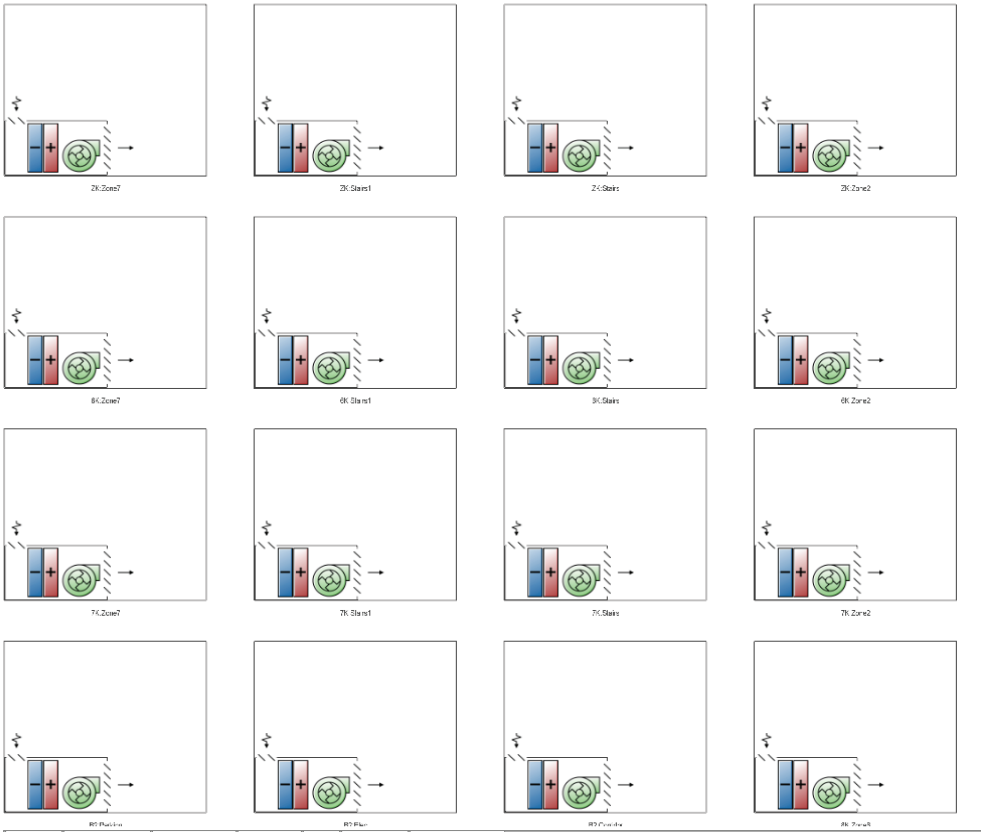

**Figure 20. Cooling System Interior Units Schematic View for Building**

The proposed design lighting power density is defined as space-by-space method in Table 7 below.

**Tablo 7. Proposed Building Lighting System Performance Specifications**

| | Space Type | Detailed Explanation |
|---|---|---|
| Lighting Power Density (W/m2) | Interior | The proposed building lighting power for overall interior spaces is 4.55 W/m².<br><br>**Space by Space LPD Value**<br><br>**Electrical/Mechanical Room:** 6.60 W/m²<br>**Corridor:** 4.65 W/m²<br>**Residential Unit:** 4.30 W/m² |

Proposed building model lighting system fixtures input can be seen from Figure 21.

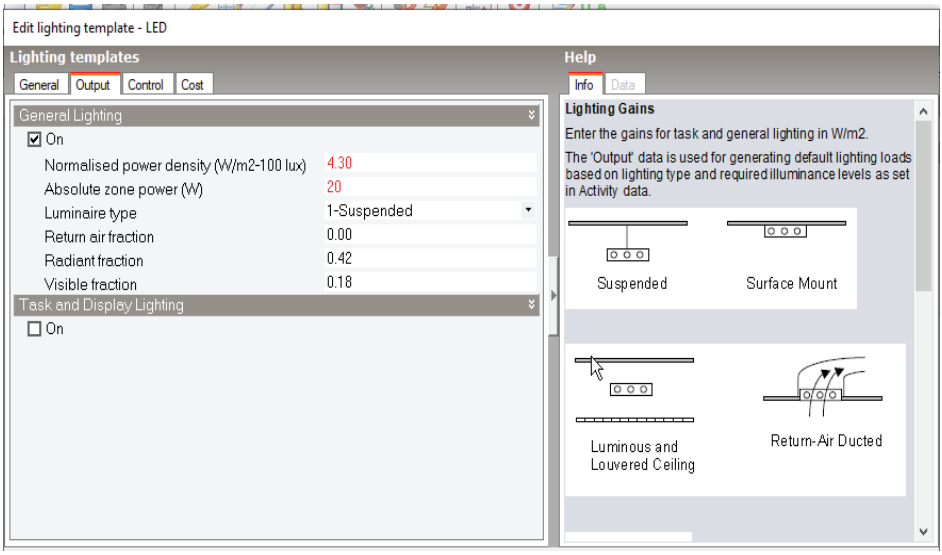


**Figure 21. Lighting System View for Data Input**

## RESULTS

The energy modeling case study performed to demonstrate energy savings and cost analysis of the existing building and proposed energy

efficiency measures such as external wall insulation, replacement of AC units with highly efficient air conditioning units, interior lighting power reduction and external shading device design on South façade. There are two energy model simulation results that include existing building design and proposed design annual energy use breakdown for HVAC, lighting, receptacle equipment, domestic hot water system.

In conclusion, when proposed energy efficiency measures are modeled through simulation software, the existing building design annual energy use calculated as 350.850 kWh, while proposed energy efficiency design annual energy use calculated as 226.420 kWh. As a result, proposed building annual energy use calculated 35,5% less energy use compared to existing building energy use.

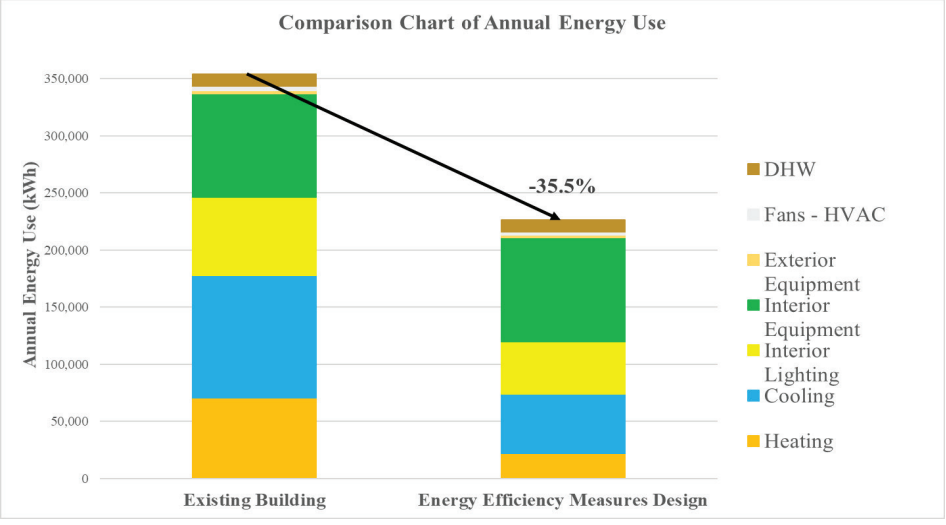


**Figure 22. Existing vs. Proposed Design Energy End Uses**

When proposed energy efficiency measures are modeled through simulation software, the existing building design annual energy cost calculated as 192.280 TRY, while proposed energy efficiency design annual energy cost calculated as 134.272 TRY. As a result, proposed building annual energy cost calculated 30,1% less energy cost compared to existing building energy use.

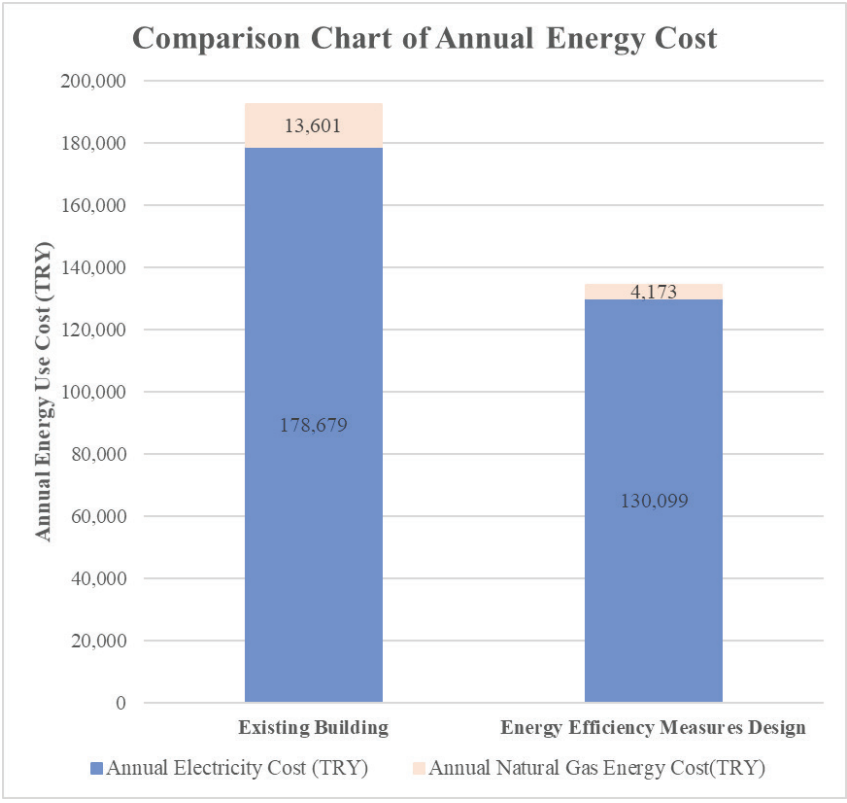


**Figure 23. Existing vs. Proposed Design Energy Costs**

Energy modeling is a complicated process that requires the integration of several disciplines in order to produce an accurate final product. The energy model's output will be used to make decisions about the current project as well as future ones. Energy modeling can be utilized as decision-making tool in complex facilities.

## REFERENCES

Waltz, J. P. (1999). Computerized Building Energy Simulation Handbook, Chap. 6. Lilburn, Ga.: Fairmont Press.

California Energy Commission. 2004. "Nonresidential Alternative Calculation Method (ACM) Approval Manual." http://tinyurl.

com/cmwtwsz.

Crawley, D. B., Hand, J. W., Kummert, M., Griffith, B. T. (2008). Contrasting the Capabilities of Building Energy Performance Simulation Programs. *Building and Environment*, 43(4), 661-673. https://doi.org/10.1016/j.buildenv.2006.10.027

COMNET. 2010. Commercial Buildings Energy Modeling Guidelines and Procedures.http://tinyurl.com/cphjluh.

Forrest, W., Kaplan, J., Kindler, N., (2008). Data Centers: How to Cut Carbon Emissions and Costs. *McKinsey on Business Technology*, 14, 4-13.

# PRODUCTION PROCESSING OF FABRIC REINFORCED COMPOSITES BY VACUUM-ASSISTED RESIN TRANSFER MOLDING

*Yusuf ŞAHİN [1], Mustafa ALSAYED[2], Mina Merve Nur GÜNTÜRK[3]*

**Abstract:** This paper describes the vacuum assisted resin infusion transfer molding method (VARTM) for manufacturing the polymer matrix composites using different fibers or fabrics. The manufacturing unit is basically composed of heating table made of from Al alloy, temperature control unit and touch screen and vacuum control unit. The heating table and the vacuum level can be controlled with this VARTM unit. The processes and systems are explained step by step to achieve the better composite samples. With the help of VARTM system, the polymeric composite laminates are manufactured with void free and high quality components. Finally, it is found that selected temperature, times and fabric types were significantly effective factors on the surface quality of composites

***Keywords:*** Polymer, Composite, VARTM Technique, Temperature Control, Time, Vacuum

## INTRODUCTION

Composite materials compose of the combination of two or more materials such as particle, whisker, fiber or fabrics reinforcement with

1 Department of Mechanical Engineering, Faculty of Engineering and Architecture, Nişantaşı University, Sarıyer, 34398 Istanbul, Turkey, yusuf.sahin@nisantasi.edu.tr. Orcıd No: 0000-0001-6495-5701

2 Department of Mechanical Engineering, Faculty of Engineering and Architecture, Nişantaşı University, Sarıyer, 34398 Istanbul, Turkey, moustafa.alsayed@nisantasi.edu.tr

3 Department of Mechanical Engineering, Faculty of Engineering and Architecture, Nişantaşı University, Sarıyer, 34398 Istanbul, Turkey, minamervemg@nisantasi.edu.tr

the selection of appropriate matrix. Due to their higher mechanical properties like stiffness, strength and higher load capacity associated with lighter weight, they are commonly used in aerospace, automobile and marine industries (Şahin, 2021). These are replaced to Aluminium, polymers, woods and even steel structures, especially for the country established near to sea. Polymer matrix composites become an attractive widely not only for the construction but also energy sectors since glass, carbon, graphite and aramid fibers are the most commonly used reinforcements for these types of composites.

For fiber reinforced polymer (FRP) composites, there have been wide range applications because of their orthotropic nature. The mechanical behaviours of these composites are various in different directions. Thus, more flexible design cannot be provided with homogenous engineering materials/particulate filled composites. FRPs are preferred for higher mechanical properties. There are considerable differences between unidirectional reinforced composites and woven textile composites in terms of mechanical properties and manufacturing point of view. Textile fabrics are more suitable in production methods. These types composites can be divided into three groups which are; woven, knitted and yarn/braided fabrics. Woven fabrics are widely preferred for applications of structural. Woven fabrics indicate good dimensional stability in both orientations whereas they have very low shear rigidity. These are composed of two sets of interlaced yarn elements that are called as warp and fill. Warp yarns run vertically, while weft yarns run horizontally (Naik et al.1991, Maskbay 2008).

On the other hand, the manufacturing method plays an important role on the mechanical properties of the composite. Some time, the quality of the products does not have the same quality. Thus there are different types of manufacturing processes for the fiber reinforced composites. These are basically hand lay-up, spray up, prepregs, liquid composite molding (LCM) and Vacuum-Assisted Resin Transfer Moulding (VaRTM). These first two methods are simple, cheap and donot requires many tools. However, voids become problem. For prepregs method, due to using autoclave for curing, it is expensive but widely used for aircraft structures (Afendi,.2005, Park et al.2019). High pressure can be em-

ployed to reduce the void rate (Bodaghi et al.2016). However, it needs to have high cost for investment, longer production period, poor efficiency and limited parts (Grunenfelder and Nutt, 2010). For LCM approach, prepregs are replaced by dry fiber preforms. This method became attractive for aeronautic applications due to reducing costs and cycle times (Maung et al., 2020). VARTM covers of fabric form and low viscous resin in producing lower cost parts but large aircraft structures with quality (Hashim et al., 2017, Park et al.2019, Maskbay 2008).

VARTM method differs from the prepreg method that fiber reinforcements and core materials are carried out in one-sided mold and vacuum bag. The epoxy then filled through placed in the warp direction of the material and drawn by vacuum through the reinforcements. Resin matrix composites are higher ranked in specific strength compared to aluminum alloys. This method requires neither high heat nor high pressure. It is comparatively economical tool that makes it possible to produce large and complex components. In VARTM, upper half of system is replaced by a vacuum bag, which is eliminated the need of making precisely matched metal mold as in RTM method. Recent studies have shown that it is feasible to produce aircraft-quality composite parts with this method (Sevkat and Brahimi, 2011). Moreover, it is easy to control the final fiber volume fraction and void content of the composite. The purpose of this study is to describes the overview of the VARTM method on epoxy based composites, their advantages and disadvantages, selection the elements used for the fabrication, preparation stages of the materials, control system of VARTM unit and how to build this closed system in order to manufacture of composites with free voids structural parts.

**VARTM Processing and Advantages**

The VARTM process has been developed for large ranges of industries in the past several years. This closed system technique produces high quality and variety of composites at very economical cost, which helps companies and factories extend to their ability of production (Sevkat and Brahimi, 2011). The main concept of the method involves putting the raw fibers and fabrics in a preform in the desired layout.

Often, the fiber and fabrics are gripped together by tapes and vacuumed to remove all the air inside the system. Then, the epoxy resin is filled by a tube into the system by the vacuum (Bolick,2000). In the next step, the laminate is pressurized and the system is completely stable and both injection and cure can be done at room temperature. In this process, we are capable of using a variety of fibers, and the sewed-up materials work in a perfect shape since the gaps allow for the faster movement of the epoxy resin (Wu et al., 2019). This is an intact process using affordable composite materials without prepregs and autoclaves compared with other prosses. The epoxy resin is typically open to room temperature involving a pressure differential between the input and output, causing the resin to be filled into the system.

The VARTM was applied to fabricate large-sized composite parts, such as marine and airplanes structures. This process is a low-cost process and was created for assembly-line production and the basic concept is to progress the pressure linked between the environment pressure and the vacuum to get the wanted condition. The advantages of the VARTM process are showed in Fig.1. The most important advantage of VARTM is the capability to work in low injection pressures, approx. 1 atm. At the stages of production, movement is not required for reinforcement, which has been obtained by the little pressure to achieve better quality composites (Chang, 2013). Because of the advantage and improving the acknowledgments of process physical properties, the VARTM method is involved in various transportations, marine and automotive parts with many variations of the method and more complicated composite parts with excellent strength, quality, and lower cast can be manufactured (Heider and Gillespie, 2008). Although there are huge advantages since the VARTM process is used widely for precise design, its main defects effect should be investigated alongside the formation of voids.

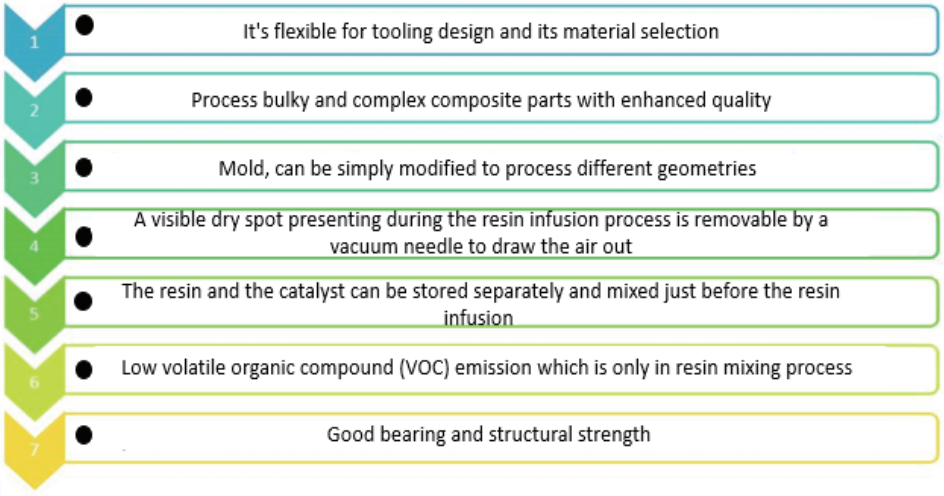


**Fig. 1. Advantages of VARTM Method**

## EXPERIMENTAL

### Epoxy Resin

The epoxy resin is one of the main material of the VARTM method. The resin provides chemical resistance, durability and strength to the composite. They submit high performance at higher temperature up to 121°C. Epoxies typically are cured by reaction with amines or anhydrides. The epoxies are not cured with a catalyst, a hardener used about 1/3 ratio. It's extremely important to calculate the mass of epoxy resin correctly because if we added more or less the amount to the system the fibers will not be joined correctly and the final product will not be clean as we expected.

### Takviye Elemanları / Warp and Weft direction

To produce any types of composites, reinforcement is the most important elements, which can be particle, powder, fiber, whiskers or fabric types because the most of loads are carried out by these components. However, in order to transfer the loads into the fibers, there should be

enough interface bonding between the fiber and matrix. In this study, both glass fiber/carbon fibers and hybrid fibers are used for making the epoxy based composites. This is 100% carbon fiber in the form of woven fabrics, which is used with resin matrix during the manufacturing of composites. The weight in mass is variable starting from 93 gr, 200 gr, 300 gr, 385 gr and finally reached to 420 gr. They are indicated as 200 gr/$m^2$ with plain or twill type. The carbon wowen fiber with areal weight of 300 g/$m^2$ is used as reinforcement. The average diameter of the fiber is 0.32 mm. E-glass fiber in the form of woven with areal density of 300 g/$m^2$ is used to as a reference. Besides, epoxy is used for this investigation.

The woven type of fiber in general compose of two sets of interlaced yarn components, warp and weft yarns, which is also called fill, according to the yarn orientation (Tan et al.1997). The warp one run lengthwise in woven fabrics while weft one run crosswise (Naik et al.1991). These fabrics generally indicates a good stability at dimensional size for both directions, they offer highest packing density. Whereas, the shear rigidity is lower for these fabrics, which is leading to have a good formability. Thus, these show anisotropic behaviour and poor in resisting in-plane shear. Two orientations are very important in production stage, which are warp fiber and weft fiber because most of the load was carried out with wrap direction while other is to bind the fibers by combining them together. The width is generally about 100 cm. Fig. 2 indicates the images of orthogonal fabric showing both warp and weft direction in addition to the weft to left direction for fiber reinforced composites that are very important step for selection to them because sometimes it is very difficult to differentiate between these orientated directions. Otherwise it is mixed each other and then to comment them becomes difficult.

(a)

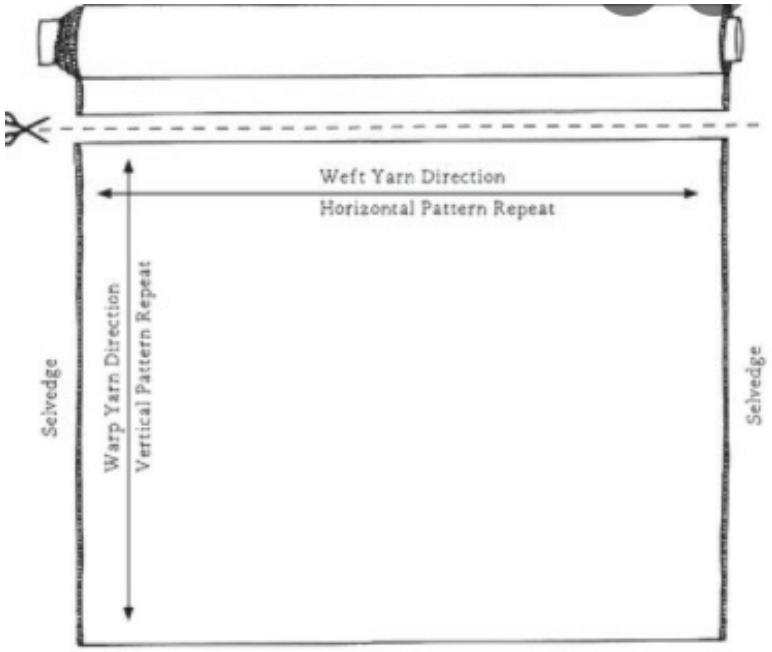


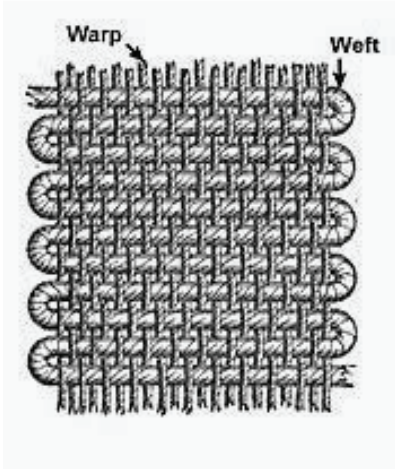


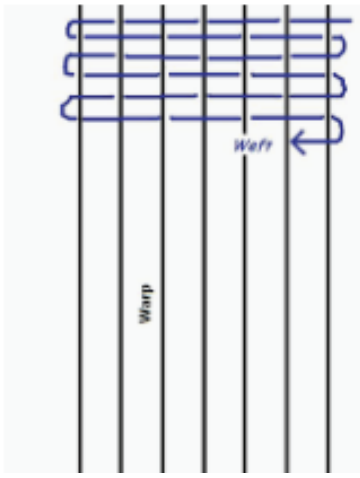


(b) Weft to left (c) Warp and Weft (Textile&fabrics/threads&needles

**Fig. 2. Images of Orthogonal Fabric Showing Warp and Weft Direction for Fiber Reinforced Composite**

## MATERIAL PREPARATION

### Experimental Setup

In VARTM method we usually use 5 different materials and sealant tape in our system, to prepare these materials perfectly we have a certain dimension, which is a 1200x1500x20 $mm^3$ on mould. First of all we need to prepare our fibers dimensions about 500mmx500 mm because all the other material dimensions are depend on the fiber dimensions. Then the release agent is applied on the top mould surface to improve the surface finish and not sticking to the surface. The main reason of using it is to protect the surface of the machine from the epoxy resin and make the composite components easy out since it is very hard to clean it up. The size of the release film is about 800x800 $mm^2$ size. The fabric fibers (carbon or glass) are prepared to the required sizes and preform is formed. After that we must insert our double faced sealant tape on the boundaries of the release film with one side kept closed, in the second layer we arranged our 6 layers fibers (Carbon fiber) sheets in the middle of the release film at the size of 500x500 $mm^2$. Then peel ply is placed on the top layer of the fiber preform at the size of 700x700 $mm^2$, but the peel ply should be adjusted 30 mm close to the vacuum system. To keep its location stable we use paper tapes to make sure that the sheet is not moving. After that we placed the mesh flow media above the peel ply at the size of 500x500 $mm^2$ for accelerating the resin flow. It can be realized that the peel ply surface finish determines the quality of surface. Again to make sure the sheet is stabilized using the paper tapes.

To let the epoxy spread in the right inside the system we use vacuum infusion spiral flow hose with a T connecter in the middle of the hose. Two spiral tubes are prepared and put on the both of cloth sides. One is connected with inlet tube while other is attached with outlet tube that are connected with the vacuum pump. It is where the vacuum pressure is applied during the production stage, see the Fig.3.

The final step we placed our final layer and the most important layer in the system which is the vacuum bag, the last layer that is responsible to remove out the air and fully close the system with the help of an air compressor, its size is about 1000x1000 $mm^2$. The vacuum bag sealed

tightly by tacky sealant tape that fixed on corners of the mold (Şahin, 2021). After this one, before the resin infusion it is checked whether or not any taking place of leakage. The vacuum bag is used to cover the whole top surface of the mold. Shrinkage factor should be considered deeply here because of possible air leakage problem. The mold was connected with a vacuum pumping and resin inlet on its side. By setting the pump, the resin infusion is started and 1 atm vacuum pressure is applied. Finally, the resin is moved inside the preform laminate to wet that will take several minutes, which is followed with closing off of the resin supply. The vacuum is allowed to persist until the resin has run out. Both inlet and outlet tubes are closed and they were set to cure at room temperature for a duration of 24 hours. This procedure is exhibited in Fig. 3.

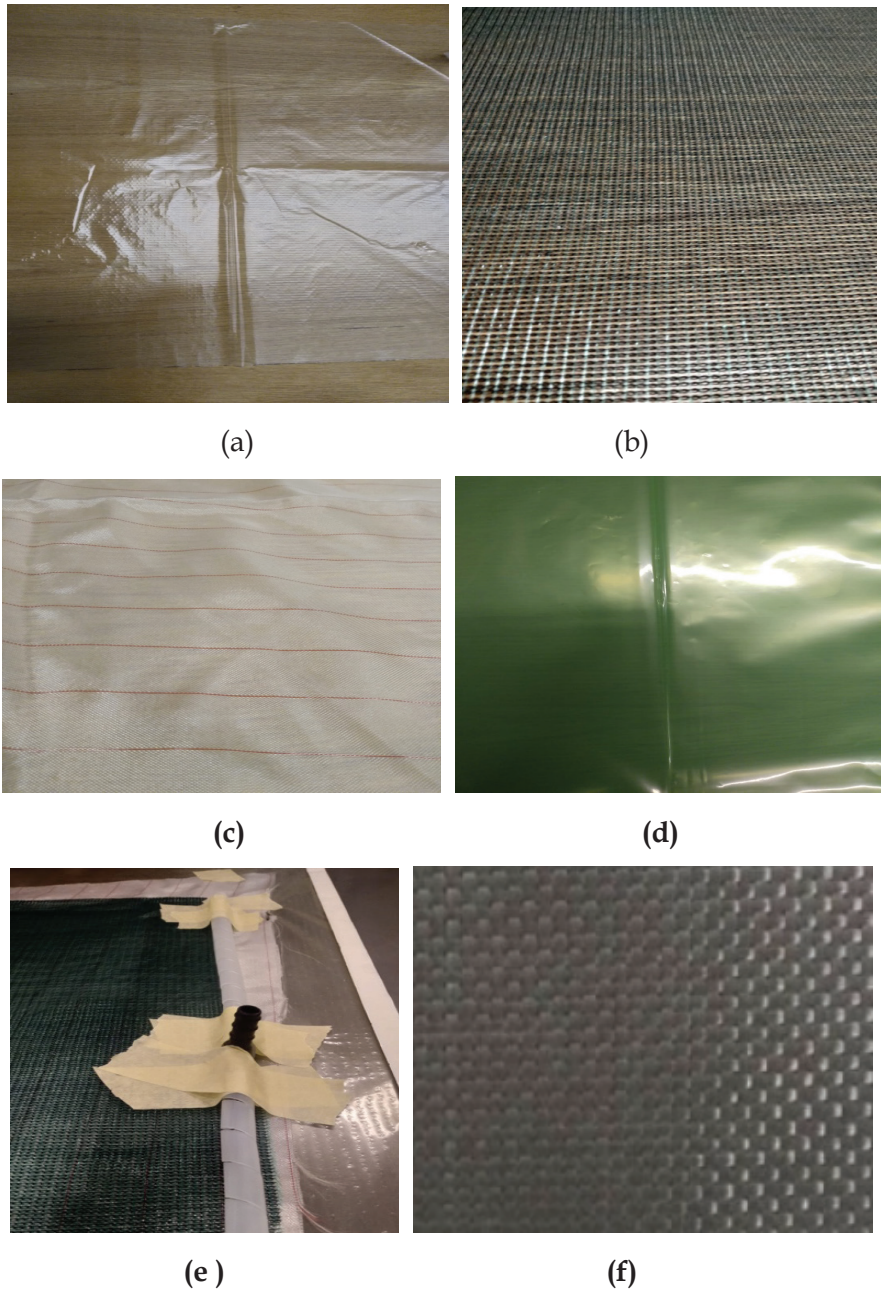


**Fig. 3. Preparation Stages of Polymer Based Composites. (A) Release Film, (B) Mesh ( C) Peel Ply, (D) Vacuum Bag, (E) Carbon Fabrics, (F) Vacuum Infusion Spiral Flow Hose and T Connecter**

**Application of VARTM Process**

In this method, vacuum has got two functions. First one; (a) the pressure difference created during the inlet and outlet is to provide the resin can be moved to introduce the fiber layers. (b) second one, is to bond fibers to each other and to performed the manufacturing more dense fiber reinforced composite structure. On the other hand, application of VARTM unit consists of 10 elements that are shown in Fig.4. These are: 1. Mould, 2. Release film, 3. Lamine by laying up fabrics or preform, 4. Peel ply, 5. Distribution medium from nylon, 6. Vacuum blanket, 7. Vacuum bag or nylon, 8. Vacuum pump, 9-10. Vacuum sealant tape sticking to both sides including some others such as spiral flow house and T connector. Fig.5 shows a schematic application of set up practically. Six plies of wowen fibres are stacked together on the release film of aluminium mold, and then vacuum processing was applied on the laminate composite and the whole cycles are completed. In this current work, carbon and glass fiber reinforced epoxy composites are manufactured using this methodology with the help of control unit of the machine. These composites are characterized carrying out some mechanical tests.

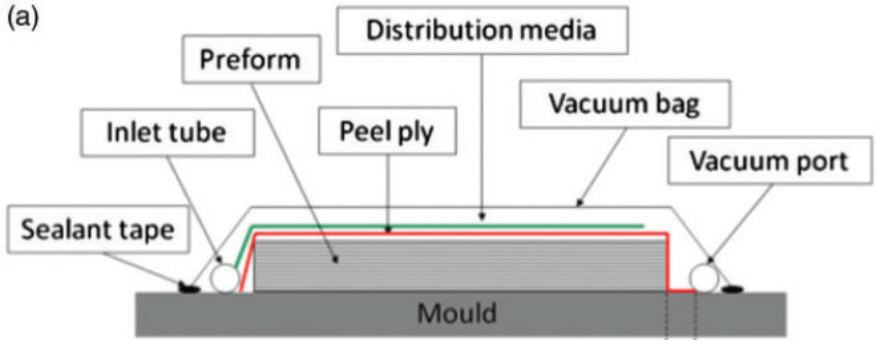


**Fig. 4. Schematic Application of VARTM Method Using Vacuum and Other Elements**

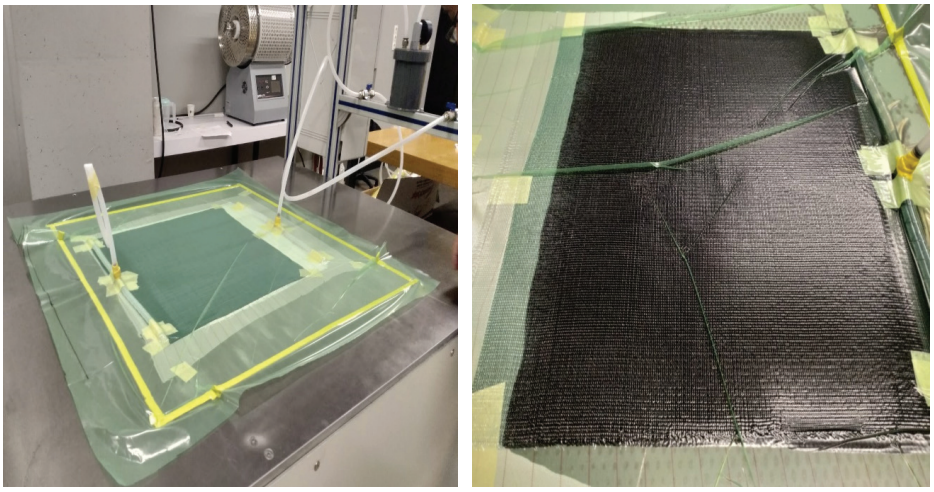

(a) Application of VARTM approach with some equipment, (b) completed vacuum processing on laminate composite

**Fig. 5. Practical Application of Set Up for VARTM Machine (A), and Completed Vacuum Processing on Laminate Composite (B)**

## CONTROL SYSTEM of MACHINE

To be able providing control of temperature and vacuum, the table dimensions are about 1500 mm x 1200 mm. To heat the table electrical heating resistances are used. The temperature is controlled with thermocouples, which is located beneath of the table surface. The system allowed you desired temperatures up to 200°C with PLC and a touch screen and curing cycles because curing is very important step for manufacturing composite components with optimum mechanical properties. Temperature distribution should be uniform through the heating table surface. In order to obtain constant temperature throughout tool surface, VARIM composed of eight regions, each has closed loop control. The cure cycle and temperatures can be programmed easily with an operator, as shown in Fig. 6. This figure diagram of the control system. This steps are related to the curing process on the composite quality.

The control panel enables to set three temperature steps in a cure cycle. Fig. 6 shows a schematic configuration of curing cycles with two

temperature steps and variations of vacuum versus time. In the first step we set the machine at room temperature of 25°C to 100°C within 50 min, after the first phase reaches the targeted temperature and time, we moved to step 2, which is the most important phase in the process, at this step the materials are getting cured and the fibers started to get fixed with each other after reaching to 100°C. We set the machine to keep the temperature stable at 100°C for 30 min to let the materials absorb the epoxy resin well. After the second step, we moved to the third phase set it to cool the machine from 100°C to 50°C for 10 min. After this step, the machine will be automatically stopped and try to return back to room temperature about 23°C. All these steps can be followed on the control screen of the machine. In other words, Fig. 6 indicates $T_o$, $T_1$, $T_2$ and $T_3$ stand for successive curing temperatures, which is corresponded to $t_o$, $t_1$ , $t_2$ and $t_3$ time intervals in curing process. This can be adjusted for different combinations of fibers and resin as well for making any fiber reinforced composites.

Apart from the temperature controls, the VARTM is equipped with a vacuum pump and a vacuum regulator associated with a vacuum gauge. The vacuum pump can be initialized and halted using a touch screen. Vacuum value can be adjusted by the operator before or during the production. The production quality depends upon the permeability of the reinforcement stack, the resin viscosity and inlet geometry. The resin flow is affected from these factors in moulding process. Thus, the vacuum regulation system includes PLC program as an open loop control. It enables to control vacuum manually during infusion moulding. Using this VARTM method, quality composite laminates with different thickness and stacking sequences can be manufactured successfully.

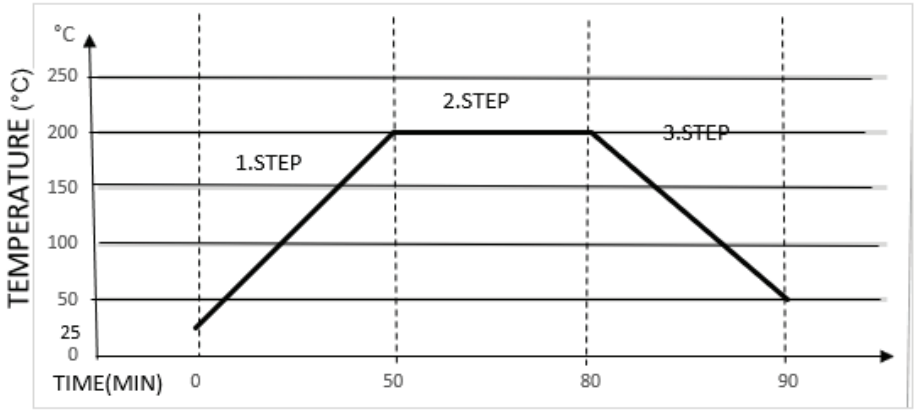


**Fig. 6. Temperature Versus Times for Composite Cooking Cycles**

## AIR LEAKAGE

To create high-quality composite parts with the VARTM method, it is important to avoid having any air leakages. Air leakages can cause the epoxy resin to leak under release film and cause damage to your machine surface, which is hard to clean up. Air leakage can be led to due to defect in release film or vacuum bag, an improper application of the sealant tape or an unsealed at the points where the hose meets the vacuum bag. Detecting the air leakages can be done with many techniques. The simplest 'leak isolation' method involves checking the vacuum pressure level to determine if there are any air leaks. If the vacuum pressure level does not decrease after the application of vacuum all air out of the mold, then it can be determined that there are no any air leakages. However, if there was a drop in the vacuum pressure level, it would be an indication that there was an air leakage in the system. Then it would be checked it again all around the connecting hose, T shape and sealant tape used there. When the pressure stopped and air bubbles are not removed from inside the laminae, it is finally appearing on the surface sample.

## CONCLUSION

In this study, A Vacuum Assisted Resin Transfer (VARTM) method and application of processes have been described to manufacture the

polymer based composites. This method allows you for controlling the vacuum level and the temperature of the table. The main steps of processes and function of each component used in the VARTM processes are explained. By using this system, laminate composites with high qualities and void-frees can be produced successfully. Further, the experimental result indicated that resin infuse, setting temperature and times, their steps and fabric types are found to be important parameters affecting the surface quality of the manufactured composite samples. Some mechanical and microstructural properties will be tested for characterization of these epoxy based composites.

**REFERENCES**

Afendi, M.; Banks,W.M.; Kirkwood, D.(2005). Bubble free resin for infusion process. Compos. Part A Appl. Sci. Manuf., 36, 739–746.

Bolick, R.(2000). Composite fabrication via the VARTM process; A&T State University: Greensboro, NC, USA.

Bodaghi, M., Cristóvão, C., Gomes, R., Correia, N.C.(2016). Experimental characterization of voids in high fibre volume fraction composites processed by high injection pressure RTM. Compos Part A. Appl. Sci. Manuf. 82, 88–99.

Chang, C.Y.(2013). Modeling and evaluation of the filling process of vacuum-assisted compression resin transfer molding. J. Polym. Eng., 33, 211–219.

Greco, A.; Lionetto, F.; Ma_ezzoli, A.(2015). Processing and characterization of amorphous polyethylene terephthalate fibers for the alignment of carbon nanofillers in thermosetting resins. Polym. Compos., 36, 1096–1103.

Grunenfelder, L.K., Nutt, S.R..(2010). Void formation in composite prepregs – effect of dissolved moisture. Compos. Sci. Technol. 70(16), 2304–2309.

Hashim,N., Majid,D.L:, Uda,N., Zahari,R.,and Yidris,N.(2017). Vacuum infusion method for woven carbon/Kevlar reinforced hybrid composite, IOP Conf. Series: Materials Science and Engineering 270. 012021. doi:10.1088/1757-899X/270/1/012021, AEROS Conference 2017.

Heider, D.; Gillespie, J.W.(2008). VARTM Variability and Substantiation Information; University of Delware Center for Composite Materials: Newark, DE, USA.

Maung, P.P.; Htet, T.L.; Malysheva, G.V.(2020). Simulation and optimization of vacuum assisted resin infusion process for large-sized structures made of carbon fiber-reinforced plastics. In Proceedings of the IOP Conference Series: Materials Science and Engineering; IOP Publishing: Bristol, UK; Volume 709, 22041-22047.

Mđskbay,A.O.(2008). Process characterization of composite structures manufactured using resin impregnation techniques,M.Sc Thesis, Mechanical Engineering in Middle East Technical University,Turkey.

Naik, N.K., Shembekar, P.S., and Hosur, M.V.(1991). Failure behavior of woven fabric composites. Journal of Composites Technology and Research, 13(2), 107-116.

Park, S.Y., Choi,C. H., Choi, J.C., Hwang,S.S.(2019). A comparison of the properties of carbon fiber epoxy composites produced by non-autoclave with vacuum bag only prepreg and autoclave process, Appl Compos Mater . 26:187–204. https://doi.org/10.1007/s10443-018-9688-y.

Şahin, Y.(2021). "Kompozit Malzemelere Giriş, 4.cü Baskı", Seçkin Yayın&Dağıtım Limited A.Ş, Ankara.

Sevkat, E.; Brahimi, M.(2011). The bearing strength of pin loaded woven composites manufactured by vacuum assisted resin transfer moulding and hand lay-up techniques. Procedia Eng., 10, 153–158.

Tan, P., Tong, L., and Steven, G.P.(1997). Modelling for predicting the mechanical properties of textile composites - A review. Composites Part A,28A, 903-922.

Wu, D.; Larsson, R.; Rouhi, M.S.(2019). Modeling and experimental validation of the VARTM process for thin-walled preforms. Polymers, 11, 2003-2008.

Yang,T., Hu,L., Xiong,X., Wang,Y., Wang,X., Petrů,M., Zhang,S., Mishra,R., Militký,J., A.(2021). comparison of fabric structures for carbon fiber reinforced composite: Laminated and orthogonal woven structures, Polymer composites, 42 (10), 5300-5309.

# NEW ANALYTICAL TECHNIQUE FOR IRRIGATION WATER DISTRIBUTION NETWORK SUBMAINS HYDRAULICS COMPUTATIONS-I: THE BEST EFFICIENT HYDRAULIC DESIGN CONCEPT[1]

*Gürol YILDIRIM*[1]

**Abstract:** Determining the actual energy (i.e., pressure head) profiles along the submain lines with a uniform slope is important for proper hydraulic design of water distribution systems. In practice, there are three general pressure head profiles (Type-I, Type-II, and Type-III) along the submain lines depending on different uniform line slope situations. Among all types of pressure profiles, the Type-II profile is considered as the optimal (or ideal) pressure profile which can produce the minimum pressure head difference for a given pipe length. This profile occurs when the total energy loss by friction is just balanced by the total energy gain due to uniform downslope. This paper presents a comprehensive analysis to identify the optimal pressure profile (Type II), to achive the minimal point of the relative maximum pressure variation, $\Phi_H$, which can be defined as the ratio of the maximum allowable pressure head difference ($\Delta H_{max}$) to the total friction drop ($h_{f(L)}$). This minimal point is regarded as "*the most efficient pressure profile*" or "*ideal hydraulic design*" in the literature. For this purpose, an illustrative figure is developed to compare values of the relative maximum pressure variation versus the dimensionless energy-gradient ratio ($K_S = S_0/S_f$) for all types of pressure profiles. The present $\phi_H$ curve versus $K_S$ values allows the design engineer to make a decision for the best alternative for selecting the $K_S$ value, where for a given pipe slope ($S_0$) the $K_S$ value can be selected to meet the minimum pres-

1 Giresun University Rectorate, Engineering Faculty, Civil Eng. Dept., Head of Hydraulics Division, Giresun / Turkey, gurol.yildirim@giresun.edu.tr, yildirimg3@itu.edu.tr, Orcıd No: 0000-0003-1899-5379

sure variation [$K_S = 1$, $(\phi_H)_{min} = 0.36$] or the range of pressure variation as close to the minimum point as possible. The implementation of the procedure based on the energy-gradient ratio (EGR) approach for all types of pressure profiles will be presented covering various design applications, in the companion paper (Yıldırım and Singh 2013b).

***Keywords:*** Water Distribution Systems; Energy Profiles; Pressure Head Distribution; Head Loss

## INTRODUCTION

In water distribution systems, a sub-main line with multiple outlets can be regarded as a typical hydraulic structure, whose design is limited by the operating inlet pressure head ($H_{0I}$), desired uniformity criterion for water application, total friction drop at the end of line ($h_{f(L)}$), field topography, as well as outlet hydraulic characteristics. Analysis of the hydraulic design of multi-outlet submain lines is important for the proper performance of these systems.

The main objective of this paper is to develop a procedure based an improved Energy Gradient Ratio (EGR) approach which is an improvement on the previous mathematical development (Yıldırım 2008) utilizing analytical approaches (Yıldırım 2006, 2007) and which covers different types of pressure head profiles (Type-I, Type-II.a, Type-II.b, Type- II.c and Type-III) (Gillespie et al. 1979, Wu et al. 1983, Barragan and Wu 2005) under different uniform line slope situations, while determining values of pressure parameters.

The energy-gradient ratio (EGR) approach is useful to identify first which type of pressure profile occurs for a given uniform design slope when other hydraulic variables are initially known, then comprehensively evaluate its hydraulic characteristics along the line. Knowledge of hydraulic properties for any type of pressure profile under consideration enables the design engineer to evaluate pressure parameters through the line sections in a simple way based on the proposed EGR approach. The EGR approach is essentially based on a simple ratio, defined as "the energy-gradient ratio ($K_S$)" which can be explained as "the ratio of uniform pipe slope ($S_0$) to the friction slope ($S_f$) [or the energy-gradient line (EGL) slope] ($K_S = S_0/S_f$)".

The design method, based on the EGR approach, was first presented by Gillespie et al. (1979), Wu and Gitlin (1979), and Wu et al. (1983), considering a single inlet submain line on uniform slopes. Gillespie et al. (1979) derived mathematical equations for pressure profiles resulting from the various possible combinations of friction drop and uniform slope situations. However, in their analysis a direct solution of most of the derived equations for determining the type of pressure profile is difficult. To simplify the implicit nature of their formulation, Barragan and Wu (2005) developed simple nomographs based on a trial-and-error procedure in which pipe ($S_0$) and friction ($S_f$) slopes can be estimated for different combinations of pipe diameter (D), total line length (L), and total inlet discharge (Q).

The most important difficulty, when recognizing the type of pressure profile, is the determination of energy-grade line slope (or friction slope) ($S_f$) which depends on the total inlet discharge (Q) and pipe diameter (D), since Q and D are unknown parameters in most design cases (Yitayew and Warrick 1988; Hathoot et al. 1993). Through the following analysis (Yıldırım and Singh 2013a), an improved EGR approach, based on the recent analytical development (Yıldırım 2006, 2007), encompassing different types of pressure head profiles (***Type-I***, ***Type-II.a***, ***Type-II.b***, ***Type-II.c*** and ***Type-III***) concerning different uniform line slope situations, is presented. In the companion paper (Yıldırım and Singh 2013b), several design examples covering various uniform line slope situations regarding different types of pressure profiles will be presented.

## Determination of Energy-Gradient Line (EGL) along Submain Line with Multiple Outlets

The energy-gradient line (EGL) in a multi-outlet submain line will not be a straight line but a curve of the exponential type. Fig. 1 sketches a horizontal multi-outlet submain line with a single inlet (single line size system) and shapes of hydraulic (piezometric) (HGL) and energy-gradient (EGL) curves along its length (Yıldırım 2007).

Flow in a submain line is considered to be steady, spatially varied flow with decreasing discharge along the direction of flow (from up-

stream inlet to dowmnstream closed end). Flow in a submain line is usually turbulent ($3{,}000<R<10^5$; R: Reynolds number). Sometimes fully turbulent flow ($10^5<R<10^7$) exists at the upstream end, and flow becomes laminar (R<2,000) at the downstream reach where the flow velocity decreases to zero. The transition flow approximately occurs in the interval $2{,}000<R\leq 3{,}000$, and the flow characteristics are indeterminate for the transition zone (Miller 1990).

The introduction of the Blasius friction factor [$f = aR^{b}$; a and b = empirically determined coefficients, a = 0.316 and b = -0.25 (von Bernuth and Wilson (1989), a = 0.302 and b = -0.25 (Provenzano et al. 2005); and R = Reynolds number] into the Darcy-Weisbach (DW) formula provides an accurate estimate of frictional losses produced by turbulent flow inside uniform pipes with low wall roughness and when Reynolds number changes within the range $3{,}000<R<10^5$ (Watters and Keller 1978; von Bernuth and Wilson1989; von Bernuth 1990; Bagarello et al. 1995). In most of the submain lines with plastic material, the flow regime rarely exceeds these flow conditions.

To determine the total amount of actual energy losses along a submain line, head losses through local singularities at the outlet connections must be additionally taken into account. These minor losses, $H_{s(L)}$, are usually calculated as if the pipe length were increased by the so-called equivalent length, $l_e$, i.e., a length of the same uniform pipe that would have the same head loss (Juana et al. 2002a). The total energy losses along the submain line, $H_{T(L)}$, includes friction ($h_{f(L)}$) and local ($h_{s(L)}$) head losses can be formulated as (Yıldırım 2006):

$$H_{T(L)} = h_{f(L)} + h_{s(L)} = F_S h_{f(L)} = \overline{F} F_S \left( K \frac{Q_I^{\,m}}{D^{m+3}} L \right) \qquad (1a)$$

where

$$F_S = \left( 1 + \frac{l_e}{s} \right) \qquad (1b)$$

in which $\overline{F}$ = 1/(m+1) = 1/2.75: the friction correction factor [m = flow or velocity exponent; for turbulent flow: m = 1.75 for the Darcy-Weisbach (DW) and m = 1.852 for the Hazen-Williams (HW) equations] taking into account continuous and uniform outflow along the submain line [for the $\overline{F}$ formulation based on uniform and discrete outflow from a finite number of operating outlets, see Eqs. (5a) and (5b) in Yıldırım (2006)]; $F_S$ = the amplification or enlargement factor to be applied to the friction losses in the uniform pipe sections, in order to take into account the effect of local losses [note that for the case of neglecting local head losses, $F_S$ is equal to one ($F_S$ = 1.0)]; $l_e$ = the equivalent length of a minor singularity (m) (Juana et al. 2002b, 2004); s = the distance between successive outlets along the submain line (m); $K$ = constant [ $K = a(4/\pi)^{(2+b)}/2g$ ]; the value of $K$ is equal to $2.458\times10^{-2}$ for the Blasius formula (von Bernuth 1990), and $2.35\times10^{-2}$ from Bagarello et al. (1995); $Q_I$ = the total inflow rate at the pipe inlet ($m^3s^{-1}$); D and L = the pipe internal diameter and length (m), respectively.

The slope of the energy-gradient line (EGL) or the friction slope, $S_f$, can be written as (for m = 1.75):

$$S_f = \frac{H_{T(L)}}{L} = 8.9 \times 10^{-3} \times F_S \times \frac{Q_I^{1.75}}{D^{4.75}} \qquad (2)$$

The pressure head change from the pipeline inlet to a given length, $l$, is a linear combination of the pressure head change due to friction and uniform slope along the pipeline. Applying the conservation of energy principle between pipe sections, $l$ = 0 ($i$ = 0) and $l$ = L ($i$ = 1), the pressure head profile along the line, H($l$), can be determined in terms of the operating inlet pressure head, $H_{0I}$, from the recent analytical development (Yıldırım 2006):

$$H(l) = H_{0I} + H_V\left[1-(1-i)^2\right] - F_S h_{f(L)}\left[1-(1-i)^{m_\beta+1}\right] - p\,\Delta S \qquad (3a)$$

As an alternative derivation, H($l$) in terms of the required pressure head, $\overline{H}$, can be written as (for the relationship between Eq. (3b) and Eq. (3a):

$$H(l) = \overline{H} + H_{VI}\,[1-(1-i)^2] + h_{f(L)}\left[F_S[\,1-i)^{m_\beta+1}-1] + \frac{m_\beta+1}{m_\beta+2}\right] - p\Delta S\left(i-\frac{1}{2}\right) \qquad (3b)$$

where

$$\mathbf{m_\beta =}\ \beta \times m\,, \quad \beta = 1-3.322x\log\left[1+\frac{H_{VI}}{\overline{H}}+\frac{h_{f(L)}}{\overline{H}}\left[\left(\frac{m+3-0.5^{m+1}}{m+2}\right)-F_S\right]+\frac{1}{4\overline{H}}(p\Delta S)\right] \quad \mathbf{(4)}$$

where H(l) = the pressure head at a given section of length l from the pipeline inlet (m); $\overline{H}$ = the required average pressure head for the entire pipeline (m); i = l/L: the dimensionless distance as the ratio of length (l) from inlet to the total length (L); HVI = the velocity head at the pipeline inlet (m); β = the nonuniform outflow exponent (Yıldırım 2006); mβ = the improved value of velocity exponent m from Eq. (4); $\Delta S = S_0 \times L$ = the total head loss or gain due to the change in elevation at the closed end of pipeline (m); and S0 = the line slope assuming to be uniform along the pipeline (m/m). In this procedure, the slope of a downhill pipeline is negative (p = -1), and the slope of an uphill pipeline is positive (p =1).

For determining the energy profile, H(l), Eq. (3b) has a greater practical importance than Eq. (3a), since Eq. (3a) requires computation of the operating inlet pressure head (H0I) in advance; whereas, Eq. (3b) can be directly used for the required average pressure head, $\overline{H}$, which is initially a known parameter in most usual design cases. In the proposed procedure, the pressure head distribution, H(l), can be determined in terms of H0I or $\overline{H}$ from Eq. (3a) or Eq. (3b), regarding two successive stages. In the first one, EGL can be evaluated from Eq. (3a) or Eq. (3b), assuming that the uniform outflow occurs along the line (mβ =m; β = 1.0); then in the second improved stage, EGL can be exactly determined, based on the nonuniform outflow distribution, by introducing the improved value of the velocity exponent (mβ = m × β, $\beta \neq 1.0$) [Eq. (4)] into Eq. (3a) or Eq. (3b). It should be noted that in most usual design cases, the first initial

approximation is sufficiently accurate with a little deviation; however, if a greater precision is required the second improved stage can then be implemented. For simplification of the derived procedure, the localized head loss along the pipe is regarded (FS $\neq$ 1.0), whereas the change in kinetic head is neglected ($H_V \cong 0$).

## TYPES of PRESSURE HEAD PROFILES for DIFFERENT UNIFORM LINE SLOPES

When a submain line with multiple outlets is designed using a single inlet system and laid on a uniform slope ($S_0$), the pressure head profile along the line resulting from the total energy drop by friction, $h_{f(L)}$ [ $h_{f(L)} = S_f \times L$ ; $S_f$: the slope of energy-gradient line or friction slope] and the total potential energy gain (or loss) due to uniform downslope (or upslope) at the end of the line, $\Delta S$ ( $\Delta S = S_0 \times L$ ), can be classified into three general types (Type- I, Type-II and Type-III). The classification can be based on a dimensionless energy gradient ratio, $K_S$ ($K_S = S_0/S_f$).

When the kinetic energy is considered to be small and neglected in a submain line, the shape of profile (pressure variation) will be simply a linear combination of the operating inlet pressure head ($H_{0I}$), total energy drop due to friction, and total potential energy change (gain or loss) due to uniform line slope, as suggested by Wu and Gitlin (1973,1974), Howell and Hiler (1974), and Gillespie et al. (1979).

A comprehensive description of the energy relations for all types of pressure profiles is synthesized in Table 1, and is also shown in Figs. 2 and 3. From this table, the effect of the dimensionless energy-gradient ratio, $K_S = S_0/S_f$, on the maximum and minimum pressure values with their positions, can be clearly analyzed. There are five typical pressure head profiles (Type-I, Type-II.a, Type-II.b, Type-II.c and Type-III) under three general types as shown in this figure, and can be expressed (Gillespie et al. 1979, Wu et al. 1983, Barragan and Wu 2005) in what follows:

### *I. Pressure Profile Type I (Minimum Pressure at the Downstream Closed End of the Line)*

As shown in Fig. 2(a), the pressure head decreases with respect to the submain length. This type occurs when the submain line is laid on

zero or uphill slopes. In this condition, the dimensionless energy-gradient ratio is $K_S = S_0 / S_f \leq 0$. The total energy is lost by both elevation change due to uniform upslope and by friction. The maximum pressure head, $H_{max}$, is at the inlet of line and is equal to the operating inlet pressure, $H_{0I}$ ($H_{0I} = H_{max}$); the minimum pressure head, $H_{min}$, is at the closed end of line, and is equal to the downstream pressure head ($H_d = H_{min}$).

***II. Pressure Profile Type II (Minimum Pressure along the Line):*** As shown in Fig. 2(b), (c) and 3(d), the pressure head decreases from the upstream end with respect to the pipeline length, reaches a minimum point ($i_{min}$) , and then increases with respect to the submain line.

The minimum pressure head is located somewhere along the line ($0 < i_{min} = l_{min}/L < 1$), depending on the large interval of $K_S$, $0 < K_S = S_0/S_f < 2.75$.

***a) Profile II-a:*** This type of pressure profile (Fig. 2b) occurs under the friction and slope situation, where $0 < K_S = S_0/S_f < 1.0$. In this type, the total energy gain due to uniform downslope at the end of line is smaller than the total energy drop due to friction; so the downstream end pressure head ($H_d$) is still less than the operating inlet pressure ($H_{0I}$). The maximum pressure head is at the inlet ($H_{max} = H_{0I}$); and the minimum pressure head is located somewhere along the line.

***b) Profile II-b (Optimal Pressure Profile):*** This is under the friction slope situation where the dimensionless energy-gradient ratio is $K_S = S_0/S_f = 1.0$. As shown in Fig. 2(c), this profile is similar to Profile II-a, but the profile is such that the downstream closed end pressure head is equal to the operating inlet pressure head ($H_{0I} = H_d$). The maximum pressure is at the inlet ($H_{max} = H_{0I}$) as well as at the closed end of line ($H_{max} = H_d$). The minimum pressure is located somewhere near the middle section of the line.

***c) Profile II-c:*** This is under the friction and slope situation where the dimensionless energy-gradient ratio is $1.0 < K_S < 2.75$ for the Darcy-Weisbach (DW) or $1.0 < K_S < 2.852$ for the Hazen-Williams (HW) equation. This occurs when the line slope is even steeper, so the pressure at the end of line is higher than the operating inlet pressure (Fig. 3.d). In this condition, the maximum pressure is at the downstream closed end of line

($H_{max} = H_d$), and the minimum pressure is located somewhere along the upstream segment of line.

***III. Pressure Profile Type III (Minimum Pressure at the Upstream Inlet of Line)***

This occurs when the submain line is on a steep downslope where the total energy gain by the uniform downslope is larger than the total energy drop due to friction for all sections along the line. As shown in Fig. 3(e), the pressure head increases with respect to the line length. This is caused by a steep downslope situation where the dimensionless energy-gradient ratio is $K_{S\geq} 2.75$ for the DW equation, or $K_{S\geq} 2.852$ for the HW equation. In this condition the maximum pressure is at the downstream closed end of line (($H_{max} = H_d$), and the minimum pressure head is at the pipe inlet and equal to the operating pressure head ($H_{min} = H_{0l}$).

Among all types of pressure profiles, the Type-II profile is considered as the optimal (or ideal) pressure profile which can produce the minimum pressure head difference for a given pipe length as discussed earlier (Wu and Gitlin 1980; Wu et al. 1983). This profile occurs when the total energy loss due to friction is just balanced by the total energy gain due to uniform downslope (Profile II-b) as shown in Fig. 2(b).

Percentage of Average Pressure Head ($\delta_H$) and Relative Pressure Variation ($\phi_H$)

The hydraulic design procedure for a submain line with multiple outlets usually establishes that the maximum difference in extreme outlet operating pressure heads along the pipeline is equal to the maximum allowable difference, ΔHmax. The uniformity criterion applied for the design of multiple outlet pipelines is that the maximum allowable difference in the outlet operating pressure head along the pipeline, ΔHmax, is less than a percentage of the average pressure head, δH:

$$\delta_H = \frac{\Delta H_{\max}}{\overline{H}} = \frac{(H_{\max} - H_{\min})}{\overline{H}} \qquad (5)$$

where δH = the percentage of the maximum allowable difference in the outlet operating pressure heads to the average outlet pressure head

(m/m); ΔHmax = the maximum allowable difference in the outlet operating pressure head along the pipeline (m); and Hmax - Hmin = the maximum difference in the extreme outlet operating pressure head along the pipeline (m). The usual criterion applied for the design of laterals is that the difference in outlet discharge along a single lateral is less than ± 10%. This corresponds to a maximum difference in the outlet operating pressure head of ± 20% (Cuenca 1989).

Another useful design criterion is defined as the relative maximum pressure variation, $\phi_H$, which is the ratio of the maximum allowable pressure head difference to the total head loss due to friction, and is given by the following expression (Barragan and Wu 2005):

$$\phi_H = \frac{\Delta H_{\max}}{h_{f(L)}} = \delta_H \times \frac{\overline{H}}{h_{f(L)}} \tag{6}$$

$\phi_H$ is an important indicator to practically determine the shape of pressure profile and evaluate the minimum pressure variation along the profile for different slope situations (Barragan and Wu.2005). In the following section, the extreme pressure heads (Hmax, Hmin) will be deduced for all types of pressure profiles to determine the maximum allowable difference in the outlet operating pressure, ΔHmax, the percentage of maximum allowable difference (δH), and the relative maximum pressure variation, $\phi_H$. Table 1 presents a systematic comparison between the relationships for the average and extreme pressures with their locations along the line, and for the relative maximum pressure variation, $\phi_H$, with the design case of considering ($F_S \neq 1$), and neglecting ($F_S = 1$) local head losses, for all types of pressure profiles in different slope situations, as discussed in the following section.

## COMPARATIVE ANALYSIS of PRESSURE HEAD PROFILES

Based on the procedure derived above for the design criterion, $\phi_H$, a systematic comparison between different types of pressure profiles for different slope patterns will be presented in this section. Note that for simplification, $F_S$ = 1 is considered in the related expressions for $\phi_H$. For this purpose, the relative maximum pressure variation [$\phi_H = \Delta H_{\max} / h_{f(L)}$

] [on the premier axis of y], and the minimum outflow (pressure head) point ($i_{min} = l_{min}/L$) [on the secondary axis of y] versus the dimensionless energy-gradient ratio ($K_S = S_0/S_f$) [on the x axis] were computed, as shown in Fig. 4.

In the present figure, there are different segments concerning five types of pressure profiles (***Type I, Type II.a, II.b, II.c*** and ***Type III***), concerning the related intervals of energy-gradient ratio, $K_S$. Each portion of this curve is individually determined based on the relationships for $\phi_H$, derived for each type of pressure profile. As shown in Figure 4, the shape of $\phi_H$ distribution is linear through the zero/upslope zone ($K_S \le 0$), whereas it has a curve form through the downslope zone [$0<K_S<1$, $1<K_S<2.75$ and $K_S \ge 2.75$ (for DW)]. This figure also illustrates the minimum outflow point ($i_{min}$) profile which starts decreasing from the downstream closed end ($i_{min} = 1$) to the upstream inlet ($i_{min} = 0$) as the $K_S$ value increases from 0 ($K_S = 0$: ***Type I***) to 2.75 ($K_S \ge 2.75$ : ***Type III***).

In the upslope zone (Type I: $K_S<0$, $i_{min} = 1$), the $\phi_H$ distribution linearly increases and yields values smaller than 1, which means the minimum pressure is at the downstream closed end, and the maximum pressure difference is smaller than the total friction drop [$\phi_H<1$; $\Delta H_{max}<h_{f(L)}$]. $\phi_H$ is finally equal to 1 [$\phi_H = 1$; $\Delta H_{max} = h_{f(L)}$], for the value of $K_S = 0$ (Type I, $i_{min} = 1$), which means the minimum pressure occurs at the downstream closed end, and the total friction drop is just balanced by the maximum pressure head difference [$\Delta H_{max} = h_{f(L)}$].

In the first portion of the downslope zone (Type II.a: $0<K_S<1$), the $\phi_H$ curve yields smaller values than 1 ($0.36<\phi_H<1$), then reaches a minimum value ($\phi_{H\,min} = 0.36$) for $K_S = 1$ (Type II.b). For this interval ($0<K_S<1$), $i_{min}$ occurs near the pipe downstream section, $0.44<i_{min}<1$, and finally reaches a critical value of 0.44, for ***Type II.b*** profile (for $K_S = 1$, $i_{min} = 0.44$, $\phi_{H\,min} = 0.36$). In the second portion of downslope zone (Type II.c: $1<K_S<2.75$), the $\phi_H$ profile increases again for the interval, $0.36<\phi_H<1.75$, with increasing values of $K_S$; and the $i_{min}$ profile occurs near the upstream section for the interval, $0<i_{min}<0.44$.

As a remarkable result from Fig. 4, $\phi_H$ is equal to 1 ($\phi_H = 1$) which means that the maximum pressure head difference is just balanced by

the total friction drop ($\Delta H_{\max} = h_{f(L)}$), for two different values of $K_S$. The first one is the Type I profile in which when $K_S = 0$, $\phi_H$ =1, $i_{min}$ = 1; and the second one is the Type II.c profile in which when $K_S \cong 1.9$, $\phi_H$ =1, and $i_{\min} \cong 0.2$. This practical consideration may give an idea to the design engineer when selecting the best alternative among these two slope conditions for the submain line design.

In the third portion of downslope zone (Type III: $K_S \geq 2.73$), the $\phi_H$ profile linearly increases with increasing values of $K_S$, for the interval $\phi_H \geq 1.73$ ; and $i_{\min}$ just occurs at the upstream inlet point ($i_{\min} = 0$), which means the operating inlet pressure is equal to the minimum pressure, and the maximum pressure head difference is much higher than the total friction drop ($\Delta H_{\max} \geq 1.73 \times h_{f(L)}$), for the steep downslope case (Type III).

## EVALUATION for IDEAL HYDRAULIC DESIGN

An ideal hydraulic design is to obtain the minimum pressure variation, or a range of pressure variation as close to the minimum point as possible, for a given total friction drop (Barragan and Wu 2005). As illustrated in Fig. 4, among of all five types of pressure profiles, the one (***Type II.b***), which can produce the minimum pressure variation ($\phi_{H\min}$ = 0.36), occurs when the energy-gradient ratio is equal to 1 ($K_S$ = 1), and $i_{min}$ = 0.44 ($l_{\min} = 0.4 \times L$). In this ideal design case, the ratio of the maximum pressure head difference, $\Delta H_{\max}$ to the total friction drop, $h_{f(L)}$ is a minimum point which is defined as "*the most efficient pressure profile*", or "*ideal hydraulic design*", however, it may not be feasible because of the restraints in the field. such as slope and layout of the submain unit (Barragan and Wu 2005).

The present $\phi_H$ curve versus $K_S$ values (Fig. 4) allows the design engineer to make a decision for the best alternative for selecting the $K_S$ value, in which for a given pipe slope ($S_0$) the $K_S$ value can be selected to meet the minimum pressure variation [$K_S$ = 1, $(\phi_H)_{\min}$ = 0.36], or the range of pressure variation as close to the minimum point (near $K_S$ =1) as possible, then finally the friction slope $S_f$ can be determined, depending on the $K_S$ value, assigned in advance.

## CONCLUDING REMARKS

In the present paper, a comprehensive hydraulic analysis for different types of pressure head profiles is carried out, based on the improved energy-gradient ratio (EGR) approach. Practically, five typical pressure head profiles are observed along the submain line for various line slope combinations. When a submain line is designed for a uniform slope, the dimensionless "energy-gradient ratio ($K_S = S_0/S_f$)" can be efficiently used to identify the type of pressure profile with the corresponding hydraulic characteristics, and determine the proper values of the main pressure parameters through the energy-gradient line.

Considering a single inlet in a submain line on a uniform slope, pressure profiles resulting from the various combinations of friction drop and slope situations are derived. For a given uniform pipe slope, first the type of pressure head profile is primarily assigned, based on the EGR approach; then certain values of the main pressure parameters along the energy-gradient line [operating inlet pressure ($H_{0l}$), downstream end pressure ($H_d$), extreme pressures ($H_{max}$, $H_{min}$) with their specific positions along the line ($i_{max}$, $i_{min}$), total friction drop ($h_{f(L)}$), maximum pressure head difference ($\Delta H_{max}$) and pressure variation ($\phi_H$)] are also evaluated. Hence, the operating inlet pressure head is reformulated by incorporating different uniformity patterns, by setting a multiplification factor, $\alpha$, for the required average outlet pressure head, and $\beta^*$ for the potential energy head change due to uniform line slope. The procedure is simplified by regarding the localized head loss along the pipe but neglecting the change in kinetic head.

The proposed procedure offers flexibility by directly computing values of the required hydraulic variables along the energy profile incorporating different uniformity patterns and without needing any additional hydraulic variables (pipe diameter, total inlet discharge, required average outflow, downstream end pressure head, total friction drop or outlet characteristics). The procedure performs better than the conventional procedures, and can be efficiently used for different types of pressure profiles in different line slope situations.

Further investigation on the current hydraulic analysis will be presented in a companion paper encompassing various design applications, comparative analysis and verification.

**Based on the present analysis, the following conclusions can be drawn:**

**1.** Among all types of pressure profiles, there is an "*ideal hydraulic design*" for downslope situation at which the dimensionless energy-gradient ratio is equal to 1 ($K_S = S_0/S_f = 1$), in which the ratio of maximum pressure difference to the total friction drop is a minimum [$(\phi_H)_{\min} = \Delta H_{\max} / h_{f(L)} = 0.5$], as shown in Fig. 4 (***Type II.b*** profile). The present $\phi_H$ curve versus $K_S$ values (Fig. 4) permits the design engineer to make a decision for the best alternative for selecting the $K_S$ value, in that for a given pipe slope ($S_0$) the $K_S$ value can be selected to meet the minimum pressure variation, or the range of pressure variation as close to the minimum point (near $K_S = 1$) as possible. Finally, the friction slope $S_f$ can be determined, depending on the $K_S$ value assigned in advance. For ***Type-II.b*** profile, the minimum outflow (or pressure head) occurs in the upstream pipe section, $i_{min} = 0.44$ ($l_{min} = 0.44 \times L$).

**2.** As a remarkable result from Fig. 4, $\phi_H$ is equal to 1 ($\phi_H = 1$) which means that the maximum pressure head difference is just balanced by the total friction drop ($\Delta H_{\max} = h_{f(L)}$), for two different values of $K_S$. The first one is the ***Type I*** profile in which when $K_S = 0$, $\phi_H = 1$, $i_{min} = 1$; and the second one is the ***Type II.c*** profile in which when $K_S \cong 1.9$, $\phi_H = 1$, and $i_{\min} \cong 0.2$. This practical consideration may give an idea to the design engineer to select the best alternative among these two slope conditions for submain line design. For ***Type II.b*** profile, the maximum, minimum and average pressure heads can be functionally expressed by simple relationships, in which when one of the extreme pressures or the average pressure head is required for design, the unknown pressure head can be directly determined, depending on the remaining two pressure heads initially known.

**REFERENCES**

Anyoji, H. and Wu, I.P. (1987). "Statistical approach for drip lateral design" Transactions of the ASAE, 31(1): 187-232.

Barragan, J. and Wu, I.P. (2005). "Simple pressure parameters for micro-irrigation design" Biosystem Eng. 90(4): 463-475.

Bralts, V. F., Wu, I. P., and Gitlin, H. M. (1981). "Manufacturing variation and drip irrigation uniformity." Trans. ASAE, 24(1), 1234-1240.

Bralts, V. F., Edwards, D. M., and Wu, I. P. (1987). "Drip irrigation design and evaluation based on the statistical uniformity concept." Advances in irrigation, Vol. 4. Academic, New York, 67-117.

Gillespie, V.A., Phillips, A.L.. and Wu, I.P. (1979). "Drip irrigation design equations. J. Irrig. Drain Division, ASCE, 105(IR3): 247-257.

Hathoot, H. M., Al-Amoud, A. I., and Mohammad, F. S. (1993). "Analysis and design of trickle irrigation laterals." J. Irrig. and Drain. Eng., 119(5), 756-767.

Howell, T.A., Hiler, E.A. (1974). "Trickle irrigation lateral design. Transactions of the ASAE, 17(5), 902-908.

Juana, L., Losada, A.., Rodriguez-Sinobas L., Sanchez, R. (2004). "Analytical relationships for designing rectangular drip irrigation units" J. Irrig. and Drain. Eng., ASCE, 130(1): 47-59.

Kang, Y., and Nishiyama, S. (1996). "Analysis and design of microirrigation laterals." J. Irrig. and Drain. Eng., 122(2), 75-82.

Kang, Y. (2000). "Effect of operating pressures on microirrigation uniformity." Irrig. Sci. 20: 23-27.

Keller, J., and Karmelli, D. (1974). "Trickle irrigation design parameters." Trans. ASAE, 17(4), 678-684.

Keller, J., and Bliesner, r. D. (1990). Sprinkler and trickle irrigation, Van Nostrand Reinhold, New York.

Mahar, P. S., and Singh, R. P. (2003). "Computing inlet pressure head of multioutlet pipeline." J. Irrig. and Drain. Eng., 129(6), 464-467.

Ravikumar, V., Ranganathan, C. R., and Santhana Bosu, S. (2003). "Analytical equation for variation of discharge in drip irrigation laterals." J. Irrig. and Drain. Eng., 129(4), 295-298.

von Bernuth, R. D. (1990). "Simple and accurate friction loss equation for plastic pipe." J. Irrig. and Drain. Eng., 116(2), 294-298.

von Bernuth, R. D., and Wilson, T. (1989). "Friction factors for small diameter plastic pipes." J. Hydraulic Eng., 115(2), 183-192.

Wu, I.P. Sarawatari, C.A. and Gitlin, H.M. (1983). "Design of drip irrigation lateral length on uniform slopes" Irrig. Science, 4, 117-135.

Wu, I. P. (1992). "Energy gradient line approach for direct hydraulic calculation in drip irrigation design." Irrig. Sci., 13, 21-29.

Wu, I. P. (1997). "An assessment of hydraulic design of micro-irrigation systems." Agric. Water Manage., 32, 275-284.

Wu, I.P. and Barragan, J. (2000). "Design criteria for microirrigation systems" Transactions of the ASAE, 43(5),B1145-1154.

Yıldırım, G., and Ağıralioğlu, N. (2004). "Comparative analysis of hydraulic calculation methods in design of micro-irrigation laterals." *J. Irrig. and Drain. Eng.,* 130(3), 201-217.

Yıldırım, G., and Ağıralioğlu, N. (2004a). "Linear solution for hydraulic analysis of tapered microirrigation laterals", *J. Irrig. and Drain. Eng.,* 130(1), 78-87.

Yıldırım, G. (2006). "Hydraulic analysis and direct design of multiple outlets pipelines laid on flat and sloping lands." *J. Irrig. Drain .Engrg., ASCE*, 132(6), 537-552.

Yıldırım, G. (2007a). "An Assessment of Hydraulic Design of Trickle Laterals Considering Effect of Minor Losses." *Irrig. and Drain. (ICID Journal)* 56(4), 399-421.

Yıldırım, G. (2007b). "Analytical Relationships for designing multiple outlets pipelines." *J. Irrig. Drain. Engrg., ASCE*, 133(2), 140-154.

Yıldırım, G. (2008a). "Determining inlet pressure head incorporating uniformity parameters for multioutlet plastic pipelines." *J. Irrig. Drain .Engrg., ASCE*, 134(3), 341-348.

Yıldırım, G. (2009b). "Simplified procedure for hydraulic design of small-diameter plastic pipes." *Irrig. Drain. (ICID J.)* 58(3):209-233.

Yıldırım, G. (2009c). "Total energy loss assessment for trickle lateral lines equipped with integrated in-line and on-line emitters" *Irrig. Science,* 28(4): 341-352.

Yıldırım, G. and Singh, V.P. (2013a). "Operating Pressure Assessment for Multi-outlets Submains: Ideal Hydraulic Design" 6th Congress on "International Perspective on Water Research and Environment" by ASCE & EWRI, İzmir, Turkey.

Yıldırım, G. and Singh, V.P. (2013b). "Operating Pressure Assessment for Multi-outlets Submains: Design Applications" 6th Congress on "International Perspective on Water Research and Environment" by ASCE & EWRI, İzmir, Turkey.

Yitayew, M., and Warrick, A. W. (1988). "Trickle lateral hydraulics. II: design and examples." J. Irrig. and Drain. Eng., 114(2), 289-300.

**Table 1. Relationships and Design Intervals for Pressure Parameters for Different Types of Pressure Profiles Concerning Various Line Slope Situations**

| Slope Definition | Type of Pressure Profile | Relationships for Average ($\overline{H}$) and Extreme Pressure Heads ($H_{0l}$, $H_d$, $H_{max}$, $H_{min}$) | Extreme Outflow Points ($i_{max}$ , $i_{min}$) (*also see Table 3*) | Energy Gradient Ratio $K_S = S_0 / S_f$ | Relationships for Relative Maximum Pressure Variation ($\Phi_H$): $\Phi_H = \Delta H_{max} / h_{f(L)}$ | |
|---|---|---|---|---|---|---|
| | | | | | ***Considering Local Losses*** [ $F_S \neq 1.0$ ] | ***Neglecting Local Losses*** [ $F_S = 1.0$ ] |
| Horizontal & Uphill | ***Type-I*** | $H_{0l} = H_{max} > \overline{H} > H_d = H_{min}$ | $i_{max} = 0$ (inlet)<br>$i_{min} = 1$ (downstream end) | $K_S \leq 0$<br>[ $S_0 = 0$ and $S_0 > 0$ , $S_f < 0$ ] | $K_S + F_S$ **(HW, DW)** | $K_S + 1.0$ **(HW, DW)** |
| Downhill (*Gentle*) | ***Type-II.a*** | $H_{0l} = H_{max} > \overline{H} > H_d > H_{min}$ | $i_{max} = 0$ (inlet)<br>$0.44 < i_{min} < 1$<br>(downstream segment) | $0 < K_S < 1$<br>[ $S_0 < 0$ ,<br>$S_0 < S_f$, $S_f < 0$ ] | $(F_S - K_S) + 0.357 \times F_S^{-0.57} K_S^{1.57}$ **(DW)**<br>$(F_S - K_S) + 0.368 \times F_S^{-0.54} K_S^{1.54}$ **(HW)** | $(1.0 - K_S) + 0.357 \times K_S^{1.57}$ **(DW)**<br>$(1.0 - K_S) + 0.368 \times K_S^{1.54}$ **(HW)** |
| Downhill (*Efficient*) | ***Type-II.b*** | $H_{0l} = H_d = H_{max} > \overline{H} > H_{min}$ | $i_{max} = 0$ (inlet) and/or<br>$i_{max} = 1$ (downstream end)<br>$i_{min} \cong 0.44$ **(DW)**<br>$i_{min} \cong 0.43$ **(HW)** | $K_S = 1.0$<br>[ $S_0 < 0$ ,<br>$S_0 = S_f$, $S_f < 0$ ] | $0.357 \times F_S^{-0.57}$ **(DW)**<br>$0.368 \times F_S^{-0.54}$ **(HW)** | $0.357 \cong 0.36$ **(DW)**<br>$0.368 \cong 0.37$ **(HW)** |
| Downhill (*Nearly-Steep*) | ***Type-II.c*** | $H_d = H_{max} > \overline{H} > H_{0l} > H_{min}$<br>and/or<br>$H_d = H_{max} > H_{0l} > \overline{H} > H_{min}$ | $i_{max} = 1$ (inlet)<br>$0 < i_{min} < 0.44$<br>(upstream segment) | $1 < K_S < 2.75$ **(DW)**<br>$[S_f < S_0 < 2.75 S_f]$<br>$1 < K_S < 2.852$ **(HW)**<br>$[S_f < S_0 < 2.852 S_f]$ | $0.357 \times F_S^{-0.57} K_S^{1.57}$ **(DW)**<br>$0.368 \times F_S^{-0.54} K_S^{1.54}$ **(HW)** | $0.357 \times K_S^{1.57}$ **(DW)**<br>$0.368 \times K_S^{1.54}$ **(HW)** |
| Downhill (*Steep*) | ***Type-III*** | $H_d = H_{max} > \overline{H} > H_{0l} = H_{min}$ | $i_{max} = 1$ (downstream end)<br>$i_{min} = 0$ (inlet) | $K_S \geq 2.75$ **(DW)**<br>$[S_0 \geq 2.75 S_f]$<br>$K_S \geq 2.852$ **(HW)**<br>$[S_0 \geq 2.852 S_f]$ | $K_S - F_S$ **(HW, DW)** | $K_S - 1.0$ **(HW, DW)** |

**Note:** ***HW*:** Hazen-Williams Equation and ***DW*:** Darcy-Weisbach Equation; ***F*S:** Amplification factor to be applied to friction losses to take into account the effect of local losses ($F_S = 1 + L_e/s$).

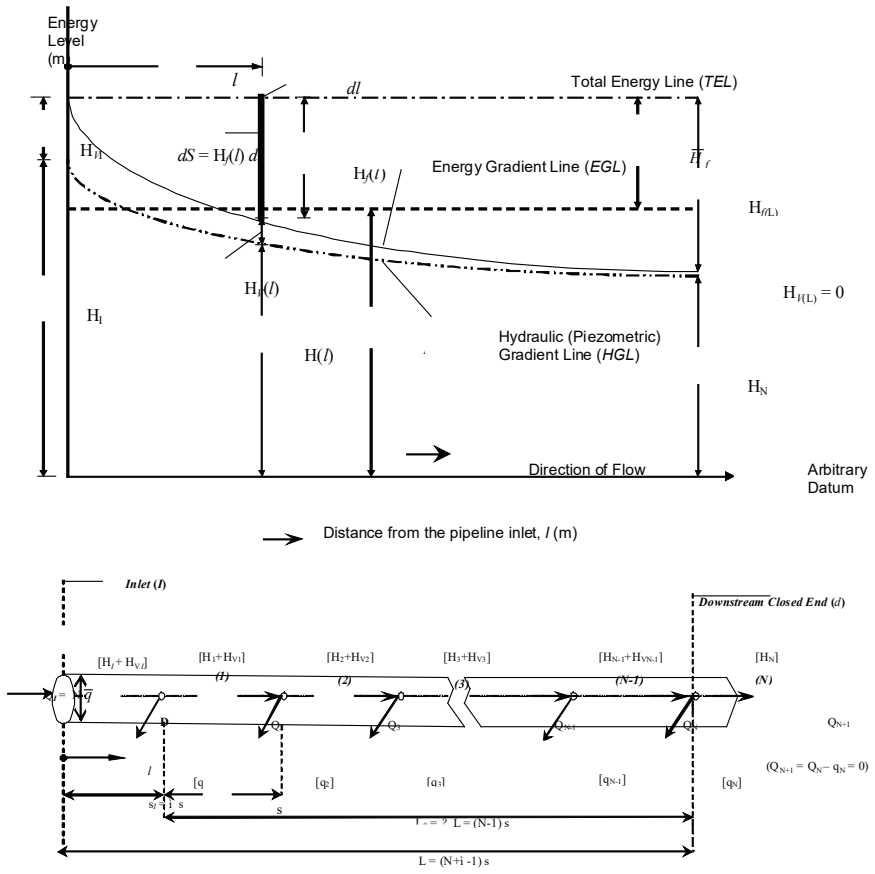


**Fig. 1. Shapes of hydraulic (piezometric) gradient line (HGL), and energy-gradient line (EGL) along horizontal submain line with multiple outlets (Yıldırım 2007)**

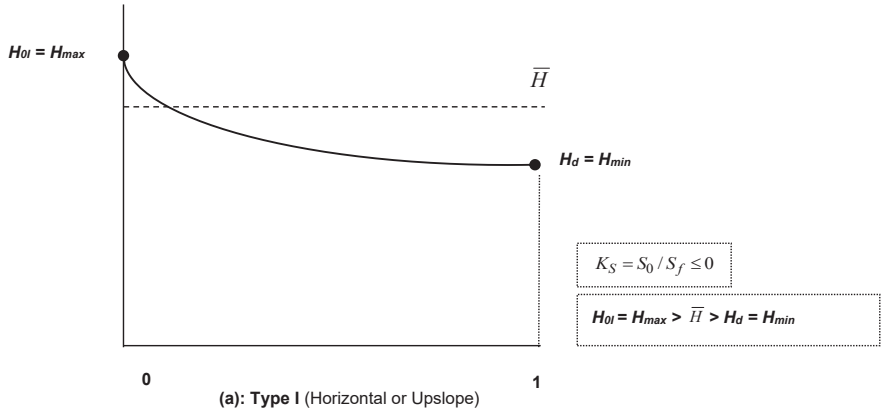


**(a): Type I** (Horizontal or Upslope)

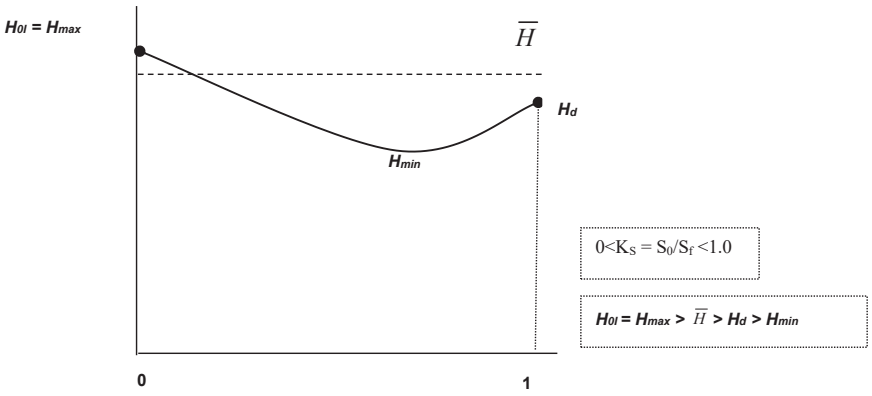


**(b): Type II-a** (Gentle Downslope)

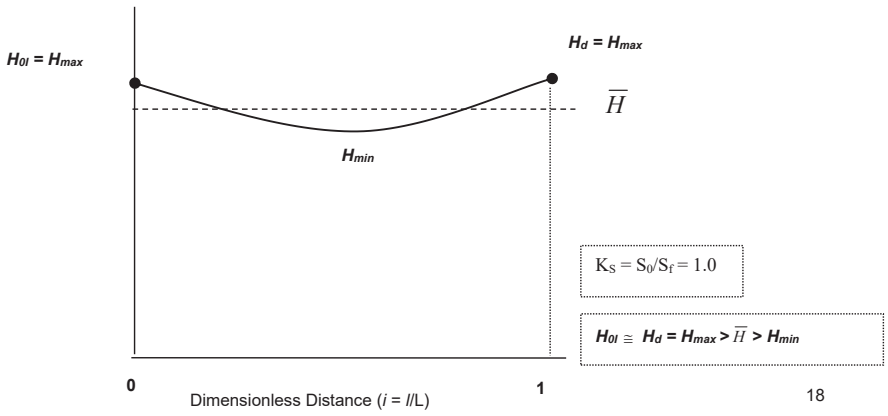


**(c): Type II-b** (Efficient Downslope)

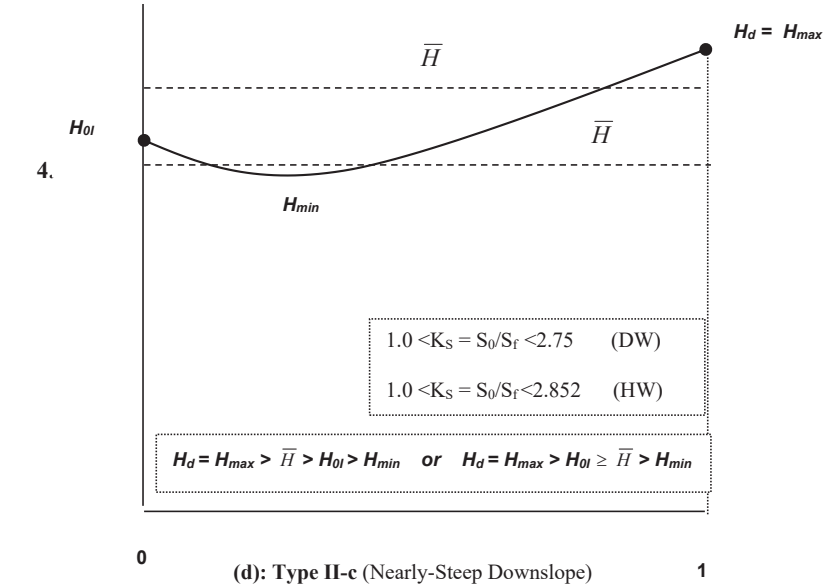


**(d): Type II-c** (Nearly-Steep Downslope)

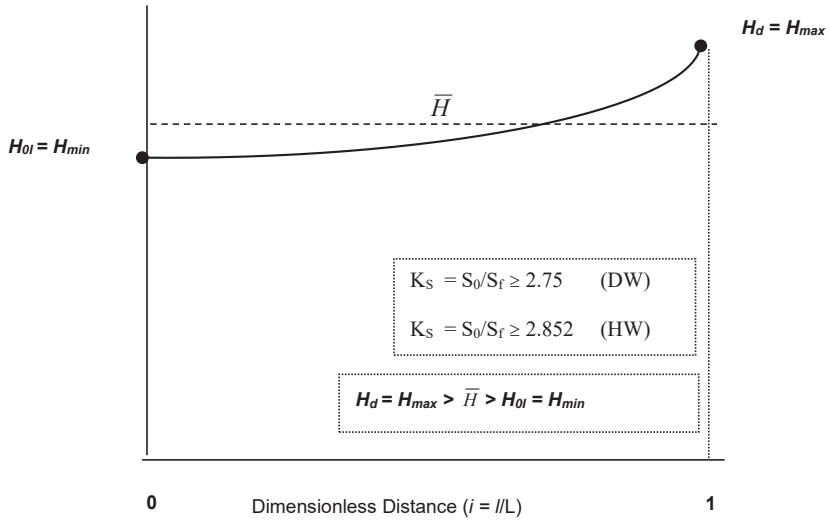


**(e): Type III** (Steep Downslope)

**Fig. 3.** Pressure Head Profiles in Downslope Situation for **(d):Type II.c** and **(e): Type**

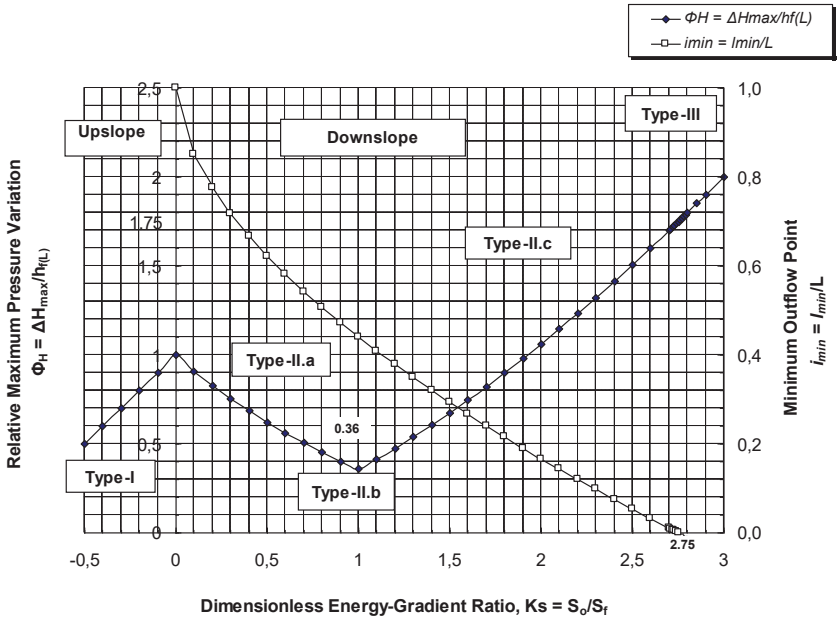


**Fig. 4.** Variation of Relative Maximum Pressure Variation [$\Phi_H = \Delta H_{max}/h_f$] and Minimum Outflow Point ($i_{min} = l_{min}/L$) Versus Dimensionless Energy-Gradient Ratio, $K_S = S_0/S_f$, for Three Types of Pressure Profiles.

# A LANE DETECTION ALGORITHM BASED ON IMAGE PROCESSING

*Tuğba Özge ONUR*[1]

**Abstract:** Traffic accidents are one of the major causes of traffic congestion on highways and require flexible traffic control methods. Lane control systems (LCS) are the traffic management technology used to manage lane usage on highways. Lane, on the other hand, is the part of the road that is wide enough for vehicles to move safely in a single line. For this reason, traffic accidents that occur with unwanted lane departures caused by the lack of attention of the relevant driver can cause death. In other words, a lane control system or lane-keeping assistance is useful as an active safety system to reduce unwanted lane departure. Lane-keeping assist systems and strategies can be divided into three parts such as the development of functions to detect the dangerous situation, driver warning system design, and intervention control strategies that assist the driver. In this study, an image processing-based algorithm is presented to detect lane lines with real-time images taken from the camera. The purpose of such systems is to provide safe driving without the need for human control and to help prevent accidents caused by human errors. In the proposed algorithm, a region of interest was created for the lane and lane detection was performed by filtering and edge detection algorithms. The results show that with the proposed algorithm, which provides an average of % 97.5 lane detection success, it will be easier for autonomous vehicles to follow the lane.

***Keywords:*** Lane Detection, Lane Tracking, Lane Keeping

1 Zonguldak Bülent Ecevit University, Dept. of Electrical-Electronics Engineering, Zonguldak / Turkey, tozge.ozdinc@beun.edu.tr, Orcid No: 0000-0002-8736-2615

## INTRODUCTION

According to the information compiled from the data of the General Directorate of Security, %97 of traffic accidents in our country are caused by driver errors, and according to statistics, the cause of the accidents that cause more than %50 of deaths in vehicles is the undesired departure from the lane caused by the lack of attention of the relevant driver (Sungur et al., 2014). A report presented by the European Commission's Directorate-General for Energy and Transport examined the use of lane departure warning systems. According to this report, it is predicted that with the use of lane departure warning systems, more than 5 thousand deaths and more than 30 thousand serious injuries can be prevented across Europe by 2020 (Cowi, 2006).

New sensor technologies (GPS, cameras, radar, etc.) have brought innovations to driver assistance systems beyond the concepts applied for vehicle control. For example, braking systems that operate when a collision hazard is detected are designed to reduce collisions. With the developing technology, it has become easier to make vehicles autonomous. Today, automatic systems called Driver Assistance System (DAS) have started to gain importance in reducing errors caused by drivers. For this purpose, many kinds of research have been carried out to detect traffic lanes using image processing and computer vision techniques (Vural et al., 2018; Kilikçıer and Yılmaz, 2018; Turan and Sancaktar, 2020).

Complex algorithms are used with the image processing techniques developed for the computer to detect lanes. Thanks to these algorithms, computers can see as a human and interpret the situation. Lane violations can be detected by interpreting the positions of lane lines. Therefore, successful detection of lane lines is required as the first step of this process. In this study, an image processing-based method was used to detect lane markings.

There are many different image processing-based lane detection methods using single or multiple cameras in the literature. When these methods are examined in general, they consist of three basic stages that are preprocessing, feature extraction, and post-processing. The pre-processing step aims to improve the input image so that the lane detection

process works robustly against possible disturbance effects (rain, fog, shadow, excessive luminosity, etc.) or that the next stages are not affected by these disturbances. In the lane detection step, candidate feature points that will enable the detection of lane lines are determined. In the last step, the lane lines are determined by eliminating the disruptive ones from the candidate lane line feature points. In addition, in this step, in some methods, the temporal relationship of the positions of the lane lines is also examined and it is aimed to prevent false detections.

Various types of systems have been created that are working on bird's eye view (Kim, 2008), perspective image (Wang et al., 2004), using distance transform (Jiang et al., 2009), stereo image processing (Nedevschi et al., 2004), monocular image processing (Lim et al., 2009), detecting stripes as straight lines (Grimmer and Lakshmanan, 1996; Kaliyaperumal et al., 2001), detecting lanes as parabolic curves (Kluge and Lakshmanan, 1995; Lakshmanan and Kluge, 1995). In the model created by Kim, a bird's eye view is studied and homogeneous matrix convolution is used for the transformation. By transforming the image to a gray level at a certain rate, it is ensured that the faint lines are clear. Artificial neural networks were used instead of image processing techniques while determining possible lane regions. Each pixel, together with the 3x9 frame around it, is given as an input to the neural network, and the information of whether that pixel belongs to the lane region or not is obtained. Then, by applying Gaussian smoothing filter and non-maxima suppression methods, the obtained points are diluted and unnecessary points are deleted. With this model proposed by Kim, %80 success was achieved. However, the method used produces unsuccessful results in bends and slope differences slightly above the standard. Therefore, unsuccessful results have been obtained in camera angle differences caused by changes in vehicle speed (Kim, 2008). Wang et al. worked on the perspective image and used the CHEVP (Canny / Hough Estimation of Vanishing Point) method to detect the points that may belong to the traffic lane in the grayscale image. In this approach, firstly, the Canny edge detection is used. The result obtained is divided vertically into 5 parts, and in each part, the Hough line detection method is applied separately. The angle between the resulting lines is based on their differences, reference points

are estimated. The reference points are clarified with the square of minimum mean error method that calculates the consistency of the obtained lanes and the original edge pixels and lanes are drawn. However, in this method, after the Canny edge detection is applied, a lot of noise has also occurred with the lane information (Wang et al., 2004). Gaikwad and Lokhande proposed a method based on PLSF (Piecewise Linear Stretching Function) to facilitate the detection of lane lines (Gaikwad & Lokhande, 2015). In this approach, Canny edge detection and then Hough transform (Duda and Hart, 1972) are applied on images enhanced by the PLSF method. The lines obtained after this process are interpreted and the final lane line positions are determined.

Finally, a lane departure warning situation is detected with a Euclidean distance-based approach. In this method, it has been seen that the detection of dashed lane lines is more difficult than continuous lane lines. In the study carried out by Borkar et al., it was aimed to turn the dashed road lines into continuous road lines in the average image obtained by averaging consecutive frames at certain intervals (for example, once in 3 frames) (Borkar et al., 2012). To benefit from the parallelism of the lane lines on this average image, IPM (Inverse Perspective Mapping) (Bertozzi & Broggi, 1998) transformation is used to work on the world plane instead of the camera plane. In the method, candidate lane points are obtained by the Hough transform during the feature extraction stage. To eliminate possible disturbance effects, a 1-dimensional correlation process is applied with the input image on the obtained candidate points. After the correlation process, RANSAC is worked on the post-determined candidate lane points (Fischler and Bolles, 1981) lane lines are detected. The method is aimed to prevent possible errors by establishing a temporal relationship between the detected status of the lane lines with the help of the Kalman filter. In the approach proposed by Espinoza and Torritti, the road area is determined first and the subsequent operations are carried out only on this area (Tapia-Espinoza and Torres-Torriti, 2013). Path area extraction is performed using Gabor textural features and mean-shift clustering. Lane lines are detected using a steerable filter, IPM, and Hough transform (Torr and Zisserman, 2000) methods, respectively. Lane line detection performance is improved by using the

extended Kalman filter. Illumination conditions are one of the most important factors affecting system performance in image processing-based methods. Yoo, et al. propose a gradient improvement approach based on linear discriminant analysis (LDA) that can work robustly against the lighting effect (Yoo et al., 2013). In this method, to separate the lane lines from the road surface, it is aimed to maximize the gradients on the lane lines. Maximum gradients are obtained by creating RGB color channel weights appropriately. Lane lines are obtained by LDA-based post-transformation Canny edge detection, Hough transform, and curve model fitting processes. It is generally more difficult to detect lane markings at night than during the daytime. The main reason for this situation is that the average luminance values of the images obtained from the camera are lower than the ones obtained during the daytime due to the low light level. The preprocessing step of the approach proposed by You et al. for lane detection in low light conditions includes average filtering, 8-way Sobel operator, and Otsu thresholding (You et al., 2013). By examining the pixel distributions on the thresholded image, the candidate lane points are detected. Within the scope of this examination, if a pixel's relationship with its neighbors is generally the same for different directions, this point is retained as a candidate lane point, while other pixels are evaluated and eliminated as noise. In the next step, lane lines are obtained by carrying out the Hough transform on the image containing only candidate lane points.

The method proposed by Küçükyıldız and Ocak serves on a Digital Signal Processor (Küçükyıldız & Ocak, 2012). In the preprocessing stage of this method, vertical 1-dimensional Sobel filter and thresholding are applied. Then, Hough transform is utilized to detect the lanes on the image. After the IPM transformation of only the starting and ending points of the detected lines, a metric elimination process based on lane width and parallelism is applied.

Most of the systems in the literature do not have a common database and a common success measurement method. It is also mentioned that there is no ground truth data prepared manually to measure the accuracy of the results obtained in many studies. Threshold values produced according to predictions and experimental results when measuring suc-

cess are used. Therefore, the success results in the studies become relative and can not be evaluated accordingly.

In this study, an image processing-based model that performs lane zone determination and lane tracking processes to find traffic lanes on the right and left of the vehicle by considering road video is proposed and implemented. The purpose of such systems is to provide safe driving without the need for human control and to help prevent accidents caused by human errors.

## THE IMAGE PROCESSING STEPS ın the LANE DETECTION ALGORITHM

Creating a new image by subjecting the received raw data to several pre-processing steps and obtaining more simplified or improved information constitute the Image Processing (IP) process. This process can also be characterized as a kind of digital signal processing.

In terms of image type; it is divided into three categories as a binary image, color image, and grayscale image.

*Binary images* are the group of images that are composed of only black and white pixels and take up the least amount of space. Binary images are represented by the values 0 and 1. Thanks to its small footprint and being in binary format, many operations can be applied to this image data more easily.

*In the color image* group, the RGB (Red-Green-Blue) color model is used. This model consists of three layers that are RGB like HSV (Hue-Saturation-Value), YUV (Luminance - Color Difference) samples. HSV color space uses the values of hue, saturation (color vividness), and brightness (color brightness). In YUV color space, black-white, blue-based colors, and red-based colors are represented in 3 vectors (Y, U, V), respectively. Red, green, and blue colors are used in RGB color space. The eight-bit allotment corresponding to a pixel in colors in RGB space is referred to as the color plane. In other words, the RGB color model contains 24 bits (8 bits red, 8 bits green, 8 bits blue), totally. Here, a value between 0 and 255 is assigned to the colors red, green, and blue, which are expressed as 8 bits.

*Grayscale images*, on the other hand, are a group of images consisting only of shades of gray.

It takes up more space than binary images. In this image group, 8 bits are allocated to a pixel. It is expressed notationally as [0, 255]. The clarity of the image differs according to the filters applied in the images.

In the lane detection algorithm proposed in this study, the steps applied are as follows:

**1-** *A snapshot is taken from the real-time view and the image is moved to grayscale.*

**2-** *Then, noise reduction is performed with the Median filter to remove the roughness that may occur due to noise in the image.*

**3-** *Canny Edge Detector is used for edge detection.*

**4-** *In the image taken, only the region with the lanes was taken and masked.*

**5-** *Later, the lane lines were thickened and the plane interiors were filled.*

Algorithm steps are given in Figure 1 with the flowchart.

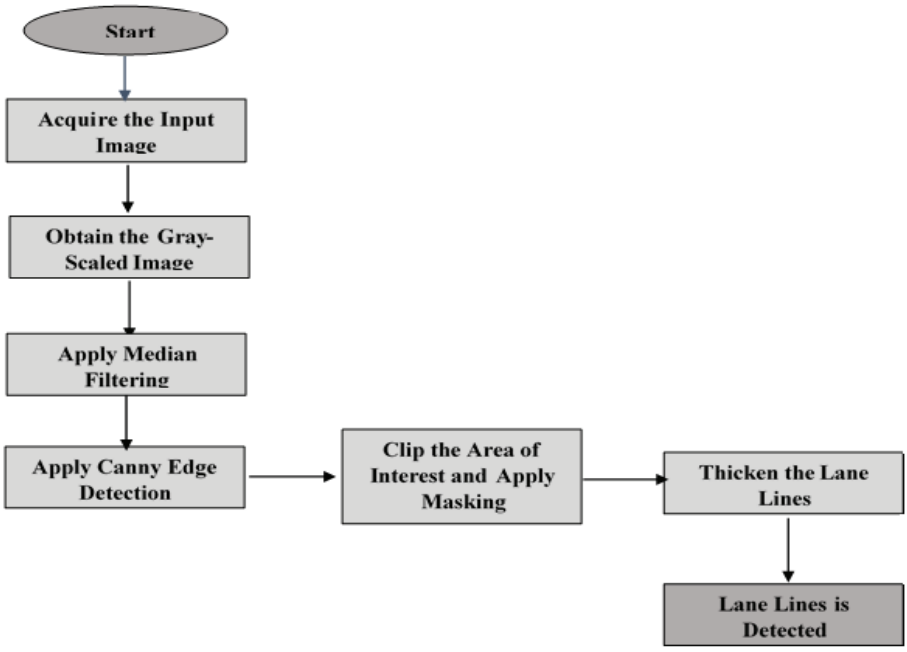


**Figure 1. Block Diagram of the Algorithm**

### Converting an Image to Grayscale

The dimensions of the image and the possible brightness value of each pixel should be determined in digitization process. The brightness value of each pixel corresponds to gray levels. The grayscale (monochromatic) images are coded between black and white which are the colors in the gray level range. In a grayscale image, there are $2^8$ = 256 different grayscale equivalent values in each pixel. Here, G={0, 1, 2, …, 255} corresponds to the gray value range where 0 and 255 gray levels correspond to black and white colors, respectively, and the rest values between these are the other gray tones. Equation (1) can be used to obtain these values,

$$Gray\ Value = 0.299xR + 0.587xG + 0.114xB \quad (1)$$

where R, G, and B represents the values of Red, Green, Blue, respectively. Figure 2 shows the original image and the grayscaled image examples of the obtained video.

**(a) Original Image (b) Grayscaled Image**

**Figure 2. Original and Grayscaled Image Examples**

### Noise Reduction with Median Filtering

The Median filter is generally used for noise cancellation or reduction in the image. Although there have been other filters used for this

purpose such as Mean filter, Median filter provides better results than the Mean filter in terms of not losing the details in the image. To calculate the value of each pixel, nearby neighbors are examined in Median filtering and the neighboring pixels are sorted and the middle value of the row is selected. In the case of an even number of pixels in the considered region, the median value is determined by averaging the two pixels that are in the middle. The smoothing effect of the filter increases as the size of the mask used increases. In Figure 3, the Median filtered version of the grayscale converted image in Figure 2(a) is given.

**Figure 3. Median Filtered Grayscaled Image**

**Edge Detection**

In this study, the Canny Edge Detection algorithm is used for the edge detection procedure. Gradient calculation, Non-maximum suppression, hysteresis thresholding operations are performed during the edge detection phase. Gradients are generally used in the solution of image processing problems and the derivatives of the image on the x and y axes are taken. Then, these derivatives are proportioned to each

other and an angle for the gradient direction is obtained. In Equation (2), the mathematical definitions of edge gradient and angle are presented.

$$Edge\ Gradient\ (G) = \sqrt{(G_x^2 + G_y^2)} \tag{2}$$

$$Angle(\emptyset) = tan^{-1}(\frac{G_y}{G_x})$$

In the non-maximum suppression method, the aim is to obtain the local maximum. When the local maximum is achieved, values below the maximum are ignored. Thus, thin edges can be obtained by applying non-maximum suppression. Then hysteresis thresholding is applied to clean up unnecessary edges. If the pixels on an edge are above the local maximum, they are considered as edges. In this case, the edge to which the pixels below the local minimum value are connected is not an edge. The connection is searched for the pixels between the minimum and maximum values. The parts connected with the points determined as strict edges can also be taken as edges. Other disconnected points are not considered as edges.

In the image of the road taken, borders are determined by edge detection, since the road is the same color and the lanes are white. Figure 4 shows the image with the edges determined from the Median filtered grayscale image given in Figure 3.

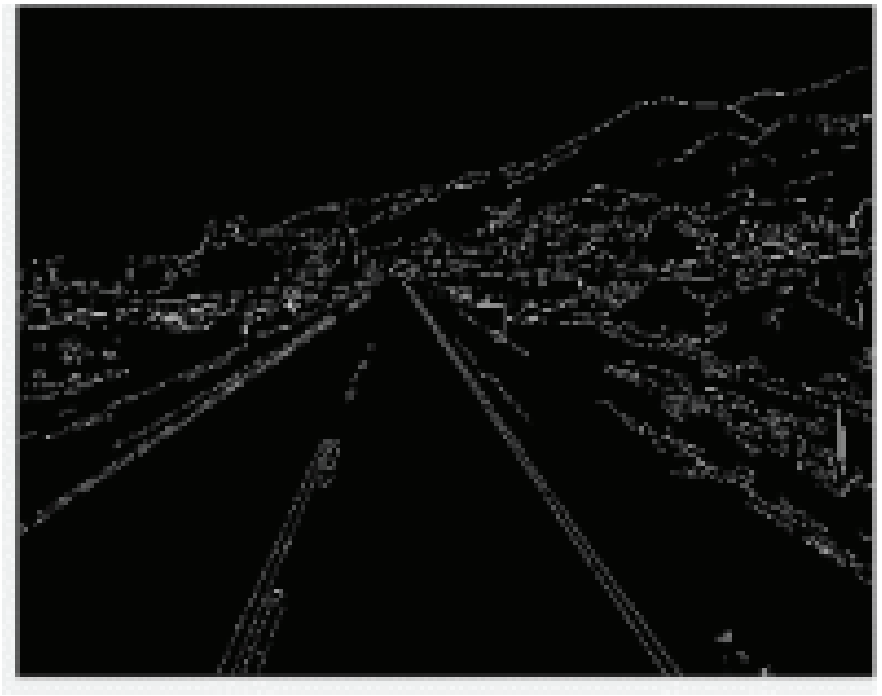

**Figure 4. Edge Detected Image**

**Masking**

To get only the desired pixels of the image, a suitable matrix is created and multiplied by the image. The pixels of the created matrix are made white (means as 1) according to the desired region. In this study, by taking only the region where the lanes are located in the image under consideration, the operations are greatly facilitated. For this, a region of interest belonging to the pixel locations of the desired region is determined and the outside parts of this region are taken as '0' and the pixel values in the region of interest are taken as '1' and multiplied by the image. Thus, the part with the lanes is separated from the image. Figure 5 shows the region of interest under consideration.

**Figure 5. Region of Interest**

### Lane Thickening

After the region of interest, the lane lines should be thickened to complete the missing pixels on the lane and to form a smooth line. The easiest way to do this is to find the white pixels of the lanes in the region of interest and then make the row, column, left diagonal pixels white. Figure 6 shows the thickened edges in the region of interest given in Figure 5.

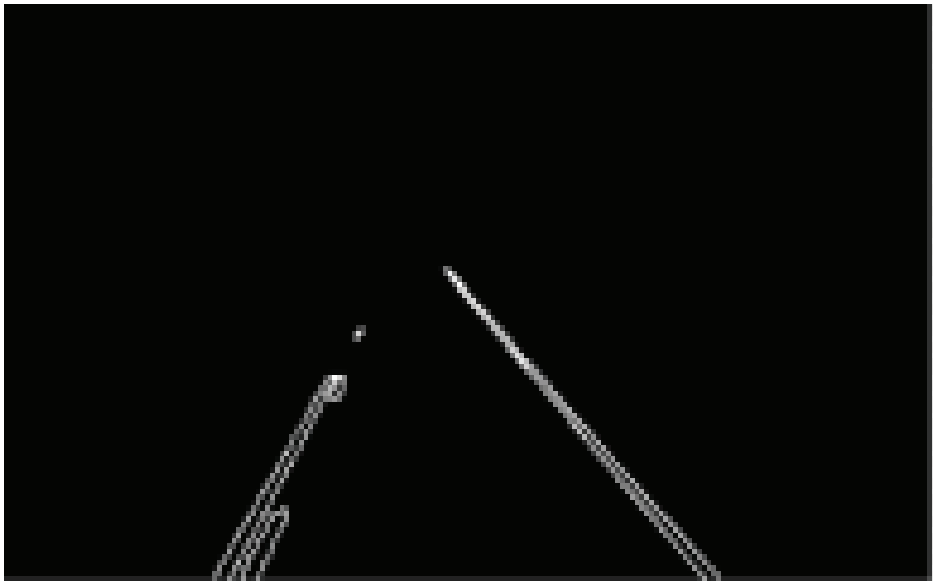

**Figure 6. Thickened Edges**

**Filling the Lanes**

In lanes with defined edges, they must be filled in according to the lines on the right and left. This ensures that the lanes fully come insight that makes it easier to control. Every row and column in the image is scanned and when a white pixel is found, white pixels are searched again in a certain range to the right. If there is a white pixel in that range, the pixels in the columns from the first found pixel to the next found pixel are given the value of white. Thus, the whitening process is performed by filling the lanes. Figure 7 shows the thickened version of the edges.

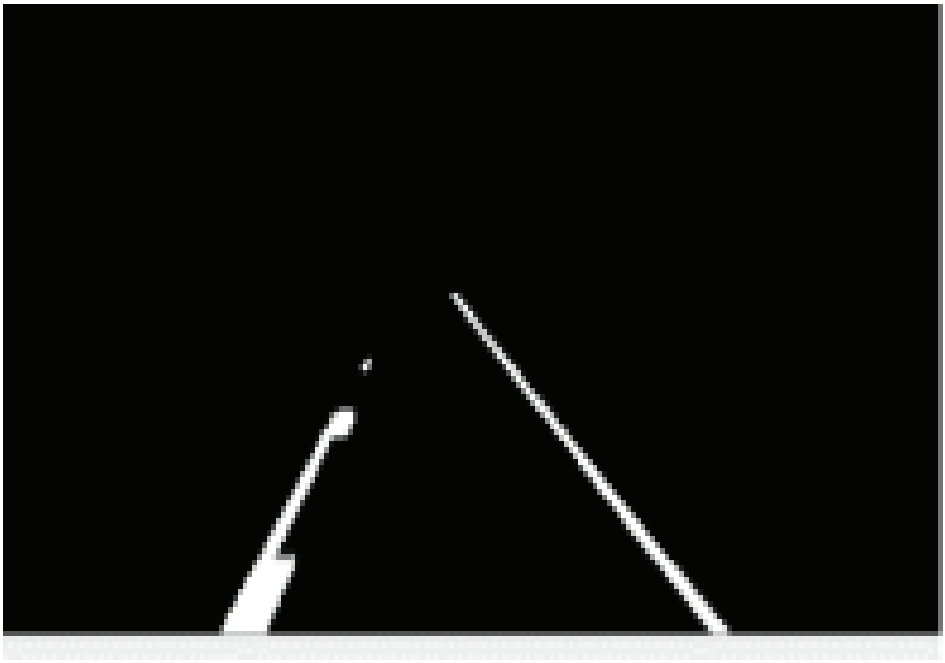

**Figure 7. The Image with Thickened Edges by Filling the Inside of the Lanes**

As a result, the lanes on a real-time image are shown as given in Figure 8 when the proposed algorithm is applied.

(a) Original Image (b) Lane Detected Image

**Figure 8. The Images of the Original and Lane Detected Road**

## RESULTS and DISCUSSION

In the context of this study, a lane detection algorithm that can be used in advanced driver support systems has been developed. In the

developed system, when a camera is set in front of the vehicle in flowing traffic, lane lines are determined by image processing methods and this provides preventing traffic accidents and makes it easier for autonomous vehicles to follow the lane. At the same time, a significant advantage is provided in terms of real-time operation with the proposed algorithm.

When the results in the test video and real-time video images used in the application were evaluated, it can be seen that an average of %97.5 success has been achieved. The images where the system fails are mostly images with long breaks between the lanes, that is, the bright pixels to which the curve model will be sampled are reduced or lost, and the images containing the negative effects caused by sudden slope differences on the road. In addition, according to the results obtained, the lanes are undetected rarely in the images that include camera angle differences caused by sudden speed changes, sharp bends, and vehicles within the viewing range.

In the proposed algorithm, the grayscale image generation phase spends a significant amount of time in the image acquisition phase, and it is aimed to reduce this time in future studies. In addition, the obtained results can be improved with machine learning techniques for autonomous driving for further studies. Besides that, the study can be considered in advanced dimensions by examining the direction of rotation with respect to the lane position. While designing DASs, it is thought that the number of negative lane detection results will be minimized by modeling the reflexes and behaviors of human drivers.

## REFERENCES

Bertozzi, M., and Broggi, A. (1998). GOLD: A parallel real-time stereo vision system for generic obstacle and lane detection. *IEEE Transactions on Image Processing*, 7(1), 62-81.

Borkar, A., Hayes, M., and Smith, M.T. (2012). A novel lane detection system with efficient ground truth generation. *IEEE Transactions on Intelligent Transportation Systems*, 13 (1), 365–374.

COWI, (2006). Cost-benefit assessment and prioritization of vehicle safety technologies (TREN-ECON2-002), Avrupa Komisyonu Enerji ve Taşımacılık Genel Müdürlüğü, Brüksel-Belçika.

Duda, R.O., and Hart, P.E. (1972). Use of the Hough transformation to detect lines and curves in pictures. *Communications of the ACM*, 15 (1), 11–15.

Fischler, M.A., and Bolles R.C. (1981). Random sample consensus: a paradigm for model fitting with applications to image analysis and automated cartography. *Communications of the ACM*, 24(6), 381–395.

Gaikwad, V., and Lokhande, S. (2015). Lane departure identification for advanced driver assistance. *IEEE Transactions on Intelligent Transportation Systems*, 16(2), 910-918.

Grimmer, D., and Lakshmanan, S. (1996). A deformable template approach to detecting straight edges in radar images. *IEEE Transactions on Pattern Analysis and Machine Intelligence*, 18, 438-443.

Jiang, R., Terauchi, M., Klette, R., Vaudrey, T., and Wang, S. (2009, 24-25 September). Low-level image processing for lane detection and tracking. First International Conference, ArtsIT 2009, Yi-Lan.

Kaliyaperumal, K., Lakshmanan, S., and Kluge, K. (2001). An algorithm for detecting roads and obstacles in radar images. *IEEE Transactions on Vehicular Technology*, 50, 170-182.

Kılıkçıer, Ç, and Yılmaz, E. (2018). Trafik ışığı tespiti yapan bir sürücü güvenlik destek sistemi. *Politeknik Dergisi*, 21(2), 419-426.

Kim, W. (2008). Robust lane detection and tracking in challenging scenarios. *IEEE Transactions on Intelligent Transportation Systems*, 9, 16-26.

Kluge, K., and Lakshmanan, S. (1995, 25-26 September). A deformable template approach to lane detection. IEEE Intelligent Vehicle Symposium, Detroit.

Küçükyıldız, G., and Ocak, H. (2012). Development and optimization of a DSP-based real-time lane detection algorithm on a mobile platform. *Turkish Journal of Electrical Engineering and Computer Sciences*, 22(6), 1484-1500.

Lim, K.H., Ang, L., Seng, K.P., and Chin, S.W. (2009, 18-20 March). Lane-vehicle detection and tracking. International MultiConference of Engineers and Computer Scientists, Hong Kong.

Nedevschi, S., Schmidt, R., Graf, T., Danescu, R., Frentiu, D., Marita, T., Oniga, F., and Pocol,

C. (2004, 3-6 October). 3D lane detection system based on stereovision. IEEE Intelligent Transportation Systems Conference, Washington.

Sancaktar, İ., and Turan, A. (2020). Araç ve sürücü kayıt kontrol sistemi uygulaması. *El-Cezerî Fen ve Mühendislik Dergisi*, 7(2), 346-357.

Sungur, İ., Akdur, R., and Piyal, B. (2014). Türkiye'deki trafik kazalarının analizi. *Ankara Med J*, 14(3), 114 – 124.

Tapia-Espinoza, R., and Torres-Torriti, M. (2013). Robust lane sensing and departure warning under shadows and occlusions. *Sensors*, 3(1), 3270-3298.

Torr, P.H.S., and Zisserman, A. (2000). MLESAC: A new robust estimator with application to estimating image geometry. *Computer and Vision Image Understanding*,78 (1), 138–156.

Vural, R.A., Sert, M.Y., and Karaköse, B. (2018). Gerçek zamanlı sürücü yorgunluk tespit sistemi. *Marmara Fen Bilimleri Dergisi*, 3, 249-259.

Wang, Y., Teoh, K.E., and Shen, D. (2004). Lane detection and tracking using B-snake. *Image and Vision Computing*, 22, 269-280.

Yoo, H., Yang, U., and Sohn, K. (2013). Gradient-enhancing conversion for illumination-robust lane detection. *IEEE Transactions on Intelligent Transportation Systems*, 14(3), 1083-1094.

# NEW ANALYTICAL TECHNIQUE FOR IRRIGATION WATER DISTRIBUTION NETWORK SUBMAINS HYDRAULICS COMPUTATIONS-II: DESIGN APPLICATIONS[1]

*Gürol YILDIRIM*

**Abstract:** This paper presents various design applications for multi-outlets submains based on an Energy-Gradient Ratio (EGR) approach presented in the companion paper (Yıldırım and Singh 2013a), mainly focusing on identifying the types of energy profiles for a given design slope and determining the required hydraulic variables through the energy-grade line. In this procedure, for a given pipe slope ($S_0$), the type of a pressure head profile is assigned, first; then proper values of the required hydraulic variables for energy profiles-the operating inlet pressure head ($H_{0l}$), downstream closed end pressure head ($H_d$), extreme pressure heads ($H_{max}$, $H_{min}$) with their positions along the line ($i_{max}$, $i_{min}$), and the total energy drop due to friction $h_{f(L)}$-are determined, ensuring the desired water application uniformity as well as the maximum allowable pressure head variation ($\Delta H_{\max}$). Hence, the operating inlet pressure head is reformulated by incorporating different uniformity patterns, and setting a multiplification factor, $\alpha$, and the required average outlet pressure head, and $\beta^*$, for the change in potential energy head due to the uniform line slope. The procedure is simplified by regarding the localized head loss along the pipe but neglecting the change in kinetic head. The proposed procedure is simple, direct, and sufficiently accurate for a wide range of water application uniformity, and can be efficiently used for different types of pressure profiles in different line slope situations, without requiring any ad-

1 Giresun University Rectorate, Engineering Faculty, Civil Eng. Dept., Head of Hydraulics Division, Giresun, Turkey. E-mail: gurol.yildirim@giresun.edu.tr; yildirimg3@itu.edu.tr, Orcid No: 0000-0003-1899-5379

ditional hydraulic variables (pipe diameter, total inlet discharge, required average outflow, downstream end pressure head, total friction drop or outlet characteristics). Analysis of results shows that the proposed procedure performs sufficiently accurately in comparison with the computer-aided step-by-step procedure.

***Keywords:*** Water Distribution Systems; Inlets; Waterways; Head Loss; Operating Pressure

## INTRODUCTION

Analysis of the hydraulic design of multi-outlet submain lines is important for the proper performance of water supply systems. Design engineers are often faced with three types of problems in most design cases. In the first problem type (energy profile determination), for the given design values of $S_0$ and $\overline{H}$, the required hydraulic variables concerning the pressure head profile [the operating inlet pressure head ($H_{0I}$), downstream closed end pressure head ($H_d$), extreme pressure heads ($H_{max}$ and $H_{min}$) with their locations along the line ($i_{max}$, $i_{min}$; *i:* percentage of length, *l* is a length from the inlet in m, and L is the total length of the submain line in m), and the total energy drop due to friction $h_{f(L)}$], can be determined ensuring the desired level of water application uniformity as well as the allowable pressure head variation along the line (Yıldırım 2007).

In the second problem type (water application uniformity evaluation), when $H_{0I}$ is given as an input parameter together with the required average outlet pressure head ($\overline{H}$) and for a given design slope ($S_0$), the proper values of required uniformity parameters ($U_C$, $D_U$, $CV_q$, $E_U$) can be directly approximated (Yıldırım 2008). In the third problem type (direct sizing procedure), the required parameters are the pipe diameter (D) or length (L) for a given design slope ($S_0$), the desired level of water application uniformity, and the required average outlet pressure head ($\overline{H}$), with the remaining variables as design variables (Yıldırım 2006).

In this classification of the design problems, determination of the actual pressure head (or outflow) profile along the line is greatest important concern for hydraulic design. The energy-gradient line (EGL) method is traditionally used for the determination of lateral pressure head and outflow profiles (Wu and Gitlin 1973, 1974, 1975). Application

of the analytical EGL or Revised Energy-Grade Line (REGL) (Wu 1992, 1997, Wu and Yue 1993) method is very easy; however, it has a limitation of the application region due to the constraints in the outlet flow regime and outflow variation along the line. Recently, an improved EGL method has been presented (Yıldırım 2006, 2007) to solve hydraulic design problems of various types of multi-outlet submain lines in different flow regimes and uniform line slope cases. In the analytical development, the improved energy-grade line is determined based on the average friction drop approach with a simple exponential function, to express the nonuniform outflow concept. The solution technique of this analytical procedure is simple and direct, and sufficiently accurate in comparison with the numerical stepwise procedures.

The operating inlet pressure head, $H_{0I}$, is a main hydraulic component for the proper design and evaluation of pressure head distribution along the line. This head can be achieved in a stepwise manner, either starting from the required pressure head at the downstream closed end, $H_d$, working back to the inlet upstream direction, by computing the friction head loss in each pipe segment between successive outlets (BSP: backward-step procedure) (Kang and Nishiyama 1996; Kang 2000); or starting from the inlet pressure head, $H_{0I}$, computing forward in the downstream direction (FSP: forward-step procedure) (Hathoot et al. 1993). In this procedure, $H_{0I}$ is determined by adding a reasonable head increment to the required average outlet pressure head, ensuring initial and boundary conditions to be based on the design algorithm discussed by Yıldırım and Ağıralioğlu (2004) and Yıldırım (2008).

In order to avoid the stepwise computer-aided design procedures (Kang and Nishiyama 1996; Kang 2000; Hathoot et al. 1993), Keller and Karmeli (1974) and Keller and Bliesner (1990) presented a graphical relationship among the required average outlet pressure head, pipe friction loss, and operating inlet pressure head for a sample design example, This procedure is efficient for the design of a multioutlet submain line with single-diameter and two-diameter, as well as multidiameter pipelines.

In conventional design procedures (Keller and Karmeli 1974; Perold 1977; Keller and Bliesner 1990; Mahar and Singh 2003), $H_{0I}$ is essentially

related to the main hydraulic variables of the energy profile, such as uniform pipe slope; $S_0$, downstream closed end pressure head, $H_d$; and/or total friction drop, $h_{f(L)}$, and required average outlet pressure head, $\overline{H}$. However, it may be hard to compute $H_{0I}$, directly, as $\overline{H}$ and $S_0$ are known a priori, whereas $H_d$ and/or $h_{f(L)}$ cannot be determined in advance, since the pipe diameter, D, is an additional unknown parameter for the required operating inlet pressure head, $H_{0I}$, in most usual design cases (Yitayew and Warrick 1988; Hathoot et al. 1993).

To overcome the implicity problem, Yıldırım (2008) proposed an alternative computing technique to directly determine $H_{0I}$ which incorporates different uniformity patterns for water application. In this analysis, first, simple mathematical expressions are deduced to relate uniformity parameters; then $H_{0I}$ is simply reformulated by setting a multiplification factor $\alpha$ for the required average outlet pressure head, and $\beta^*$ for the potential energy head change due to uniform line slope. This procedure is simple, direct, and sufficiently accurate to determine the required hydraulic variables along the pressure head profile.

However, the applicability of this procedure is only limited for the design case of a Type- I pressure profile for horizontal or uphill slope situation.

The main objective of this paper is to develop a procedure to solve the first and second types of design problems, based on improved Energy Gradient Ratio (EGR) approach which is an improvement on the previous mathematical development (Yıldırım 2008) utilizing analytical approaches (Yıldırım 2006, 2007) and which covers different types of pressure head profiles (Type-I, Type-II.a, Type-II.b, Type- II.c and Type-III) (Gillespie et al. 1979, Wu et al. 1983, Barragan and Wu 2005) under different uniform line slope situations, while determining values of pressure parameters ($H_{0I}$, $H_d$, $H_{max}$, $H_{min,}$ $h_{f(L)}$, $\Delta H_{max}$). The proposed procedure incorporates simple mathematical formulations encompassing different uniformity patterns for water application, such as Christiansen's uniformity ($U_C$), lower-quarter distribution uniformity ($D_U$), coefficient of variation of outflows ($CV_q$), emission uniformity ($E_U$), and fraction of the required average pressure head ($\delta_H$).

The procedure is simplified by regarding the localized head loss along the pipe line but neglecting the change in kinetic head. The proposed methodology is found to be simple, sufficiently accurate, and can be used efficiently for different types of pressure profiles in different line slope situations. It offers considerable flexibility by directly computing values of the required hydraulic variables along the energy profile, incorporating different uniformity patterns and without requiring any additional hydraulic variables, such as pipe diameter, total inlet discharge, required average outflow, downstream end pressure head, total friction drop or outlet characteristics.

## LITERATURE REVIEW

The energy-gradient ratio (EGR) approach is useful to identify first which type of pressure profile occurs for a given uniform design slope with other hydraulic variables initially known, then comprehensively evaluate its definite hydraulic characteristics along the line. Knowing the hydraulic properties for any type of pressure profile regarded enables the design engineer to evaluate pressure parameters through the line sections in a simple way based on the proposed EGR approach. The EGR approach is essentially based on a simple ratio, defined as "the energy-gradient ratio ($K_S$)" which can be explained as "the ratio of uniform pipe slope ($S_0$) to the friction slope ($S_f$) [or energy-gradient line (EGL) slope] ($K_S = S_0/S_f$)".

The design method, based on the EGR approach, was first presented by Gillespie et al. ( 1979), Wu and Gitlin (1979), and Wu et al. (1983), considering a single inlet submain line on uniform slopes. Gillespie et al. (1979) derived mathematical equations for pressure profiles resulting from the various possible combinations of friction drop and uniform slope situations. However, in their analysis, a direct solution of most of the derived equations for determining the type of pressure profile is difficult. To simplify the implicit nature of their formulations, Barragan and Wu (2005) developed simple nomographs based on a trial-and-error procedure in which pipe ($S_0$) and friction ($S_f$) slopes can be estimated for different combinations of pipe diameter (D), total line length (L) and total inlet discharge (Q).

The most important difficulty when recognizing the type of pressure profile is the determination of energy-grade line slope (or friction slope) ($S_f$), which depends on the total inlet discharge (Q) and pipe diameter (D), since Q and D are unknown parameters in most design cases (Yitayew and Warrick 1988; Hathoot et al. 1993). Through the following analysis, the implementation of the proposed EGR approach (Yıldırım and Singh 2013a), to cover different types of pressure head profiles (***Type-I***, ***Type-II.a***, ***Type-II.b***, ***Type-II.c*** and ***Type-III***) covering various design applications concerning different uniform line slope situations, will be presented.

**Relationships Between Uniformity Patterns ($U_C$, $CV_q$, $E_U$, $D_U$) for Pressure Profiles**

For a submain line system designed for high uniformity, all uniformity expressions can be related to each other. That means the design criterion made for any single uniformity expression can be converted and used for other uniformity expressions (Barragan et al. 2006). The Christiansen uniformity coefficient ($U_C$) (Christiansen 1942) which evaluates the mean deviation, and a statistical term, the coefficient of variation of discharge ($CV_q$), which evaluates the standard deviation, and is statistically defined as the standard deviation of discharge divided by the mean value and expressed in percent (Wu 1997), are the two most commonly used uniformity expressions. Both $U_C$ and $CV_q$ require a number of selected samples for calculation. Other frequently used uniformity measures are the distribution (or lower-quarter distribution) uniformity ($D_U$) (Merriam and Keller 1978), and emission uniformity ($E_U$) (Keller and Karmeli 1974), which express a ratio of minimum and mean discharge (Wu and Barragan 2000).

For normal distribution, $U_C$, is related to $CV_q$, as given by the following expression (Yitayew and Warrick 1988):

$$U_C = 1 - 0.798 \times CV_q \qquad (1a)$$

$U_C$ and $E_U$ can also be shown as follows (Keller and Bliesner 1990, Wu and Barragan 2000):

$$U_C = 1 - 0.6 \times (1 - E_U) \quad (1b)$$

For uniform distribution, $U_C$ is related to $D_U$ as follows (Warrick 1983, Warrick and Yitayew 1988):

$$U_C = 0.3 + 0.6 \times D_U \quad (1c)$$

For evaluating $U_C$, the following simple formulations incorporating the uniform pipe slope, $S_0$ and the friction slope, $S_f$, can be directly used for all types of pressure profiles (in different slope situations) are:

***Type I*:** Zero/Upslope (*p = 0* and *p = 1*):

$$U_C \cong 1 - 0.3 \frac{L}{H}(S_0 + S_f) \quad (2a)$$

***Types II.a:*** (Downslope, *p = -1*):

$$U_C \cong 1 - 0.3 \frac{L}{H}(S_f - S_0) \quad (2b)$$

***Type II.b*** ($K_S = 1$, $S_0 = S_f$)***:*** (Downslope, *p = -1*):

$$U_C \cong 1 - 0.6 \frac{L}{H} S_f = 1 - 0.6 \frac{L}{H} S_0 \quad (2c)$$

***Types II.c and Type III:*** (Downslope, *p = -1*):

$$U_C \cong 1 - 0.3 \frac{L}{H}(S_0 - S_f) \quad (2d)$$

**Interrelationships between Uniformity Patterns Using Dimensionless Physical Numbers**

In this section, mathematical relationships for each type of pressure profile will be deduced to evaluate the uniformity criteria ($U_C$, $CV_q$, $E_U$, $D_U$). Before starting the analysis, some dimensionless physical numbers for uniformity patterns are deduced as:

$$\lambda_1 = \frac{(1-U_C)}{x}, \quad \lambda_2 = \frac{CV_q}{x}, \quad \lambda_3 = \frac{(1-E_U)}{x}, \quad \lambda_4 = \frac{(1-D_U)}{x}, \quad \lambda_5 = \frac{\overline{H}}{L} \qquad (3)$$

***Type I Profile*** $(K_S \le 0)$***:***

From Eq. (2a), one can obtain the following simple transformation for this type of profile:

$$U_C \cong 1 - 0.3\,\frac{L}{\overline{H}}(S_0 + S_f) = 1 - 0.3\,x\delta_H \qquad (4)$$

The uniformity parameters ($CV_q$, $E_U$ and $D_U$) can be written in terms of the dimensionless physical numbers ( $\lambda_1, \lambda_2, \lambda_3, \lambda_4, \lambda_5$ ) as given by the following expression:

$$\delta_H = k_1 \times \lambda_1 = k_2 \times \lambda_2 = k_3 \times \lambda_3 = k_4 \times \lambda_4 \qquad (5)$$

where $k_1$, $k_2$, $k_3$, $k_4$ = design coefficients and are: $k_1$ = 4.357, $k_2$ = 3.477, $k_3$ = 2.745, and $k_4$ = 2.92.

***Type II.a Profile (0<$K_S$<1):***

As indicated in Table 1 (Yıldırım and Singh 2013a), there is no the relationship for $\delta_H$ in terms of $S_f$, since it is not possible to subtract $S_f$. For convenience, Eq. (2b) should be directly used to relate $S_f$ and $U_C$.

***Type II.b Profile ($K_S$ =1):***

Rearranging DW equation for the friction slope, $S_f$ ($F_S$ = 1), and substituting into Eq. (2c) for $U_C$, the following expression can be obtained:

$$U_C \cong 1-0.4\frac{L}{\overline{H}}S_f = 1-0.4\times\frac{L}{\overline{H}}\times\left(\frac{1}{0.357}\times\delta_H\times\frac{\overline{H}}{L}\right) = 1-1.286x\delta_H \qquad (6)$$

The uniformity parameters ($CV_q$, $E_U$ and $D_U$) can be written in terms of the dimensionless physical numbers ( $\lambda_1,\lambda_2,\lambda_3,\lambda_4,\lambda_5$ ) as given by the following expression:

$$\delta_H = k_1\times\lambda_1 = k_2\times\lambda_2 = k_3\times\lambda_3 = k_4\times\lambda_4 \qquad (7)$$

where $k_1$, $k_2$, $k_3$, $k_4$ = design coefficients and are: $k_1$ = 0.778, $k_2$ = 0.621, $k_3$ = 0.490, and $k_4$ = 0.521.

***Type II.c Profile ($1<K_S<2.75$):***

Rearranging DW equation for the $S_f$ ($F_S$ = 1), and substituting into Eq. (2d) for $U_C$:

$$U_C \cong 1-0.2\frac{L}{\overline{H}}(S_0-S_f) = 1-0.2\times\frac{L}{\overline{H}}\times\left\{S_0-\left[0.164\times S_0^{2.3}\times\left(\delta_H\frac{\overline{H}}{L}\right)^{-1.3}\right]\right\}$$

The above expression is reformulated for $\delta_H$ in terms of dimensionless physical numbers ( $\lambda_1,\lambda_2,\lambda_3,\lambda_4,\lambda_5$ ) as:

$$\delta_H = S_0\times\left(1-k_1\times\frac{\lambda_1\times\lambda_5}{S_0}\right)^{-1/1.3}\times\frac{k_5}{\lambda_5} \qquad (8a)$$

$$= S_0\times\left(1-k_2\times\frac{\lambda_2\times\lambda_5}{S_0}\right)^{-1/1.3}\times\frac{k_5}{\lambda_5} \qquad (8b)$$

$$= S_0\times\left(1-k_3\times\frac{\lambda_3\times\lambda_5}{S_0}\right)^{-1/1.3}\times\frac{k_5}{\lambda_5} \qquad (8c)$$

$$= S_0 \times \left(1 - k_4 \times \frac{\lambda_4 \times \lambda_5}{S_0}\right)^{-1/1.75} \times \frac{k_5}{\lambda_5} \qquad (8d)$$

where $k_1$, $k_2$, $k_3$, $k_4$, $k_5$ = design coefficients and are: $k_1$ = 4.357, $k_2$ = 3.477, $k_3$ = 2.745, $k_4$ = 2.92, $k_5$ = 0.356.

***Type III Profile*** $(K_S \geq 2.75)$**:**

Introducing the equation for $\delta_H$ ($F_S$ = 1) into Eq. (2d) for $U_C$, one can obtain the following simple transformation:

$$U_C \cong 1 - 0.25 \frac{L}{H}(S_0 - S_f) = 1 - 0.25 \, x\delta_H \qquad (9)$$

The uniformity parameters ($CV_q$, $E_U$ and $D_U$) can be written in terms of the dimensionless physical numbers ( $\lambda_1, \lambda_2, \lambda_3, \lambda_4, \lambda_5$ ) as given by the following expression:

$$\delta_H = k_1 \times \lambda_1 = k_2 \times \lambda_2 = k_3 \times \lambda_3 = k_4 \times \lambda_4 \qquad (10)$$

where $k_1$, $k_2$, $k_3$, $k_4$ = design coefficients and are: $k_1$ = 4.357, $k_2$ = 3.477, $k_3$ = 2.745, and $k_4$ = 2.92.

**Determining Friction Slope ($S_f$) and Operating Inlet Pressure Head ($H_{0I}$)**

To overcome the implicity in the procedure (Keller and Bliesner, 1990), Yıldırım (2008) recently proposed an improved direct computing technique to determine $H_{0I}$ for a single line size system which incorporates different uniformity patterns for water application. In this analysis, first, simple mathematical expressions are deduced to relate uniformity parameters; then $H_{0I}$ is simply reformulated by taking into account a multiplification factor $\alpha$ , for the required average outlet pressure head, and $\beta^*$, for the potential energy head change due to uniform line slope. However, the applicability of this procedure is only limited for the de-

sign case of a Type-I pressure profile for horizontal or uphill slope situation.

Eq. (11) can be transformed for a single line size system (k = 0.75), and suitable for the general slope situations (*p = 0* and *p = 1* for zero and upslope, *p = -1* for downslope) as follows:

$$H_{0I} = \overline{H} + L\left(\frac{3}{4}S_f + \frac{1}{2}(\beta_0)\right) \qquad (11)$$

In this section, the computing technique (Yıldırım 2008) based on the recent analytical development (Yıldırım 2006, 2007) which evaluates the operating inlet pressure head, $H_{0I}$ for a single line size system (k = 0.75), will be improved and extended to encmapss different types of pressure profiles concerning different uniform line slope situations, and various design combinations. In the analysis, first the friction slope ($S_f$) is formulated in terms of dimensionless physical mumbers (( $\lambda_1, \lambda_2, \lambda_3, \lambda_4, \lambda_5$ ), introduced into Eq. (11), and then $H_{0I}$ can be directly determined as follows.

***Type I Profile*** $(K_S \le 0)$***:***

The following expression for $H_{0I}$ can be reformulated in the following general form as:

$$H_{0I} = \alpha \times \overline{H} + \beta^* \times (S_0 \times L) \qquad (12)$$

where $k_1$, $k_2$, $k_3$, $k_4$ = coefficients and are: $k_1$ = 4.357, $k_2$ = 3.477, $k_3$ = 2.745, and $k_4$ = 2.92; $\alpha$ = multiplification factor for the required average pressure head, and $\beta^*$ = multiplification factor for the potential energy head ($S_{0 \times L}$ ) as:

$$\alpha = 1 + c_1 \times \delta_H = 1 + c_1 \times k_1 \times \lambda_1 = 1 + c_1 \times k_2 \times \lambda_2 = 1 + c_1 \times k_3 \times \lambda_3 = 1 + c_1 \times k_4 \times \lambda_4 \qquad (13)$$

$$c_1 = \frac{0.75}{F_S} \qquad [c_1 = 0.75 \text{ for } F_S = 1] \qquad (14a)$$

$$\beta^* = \frac{1}{2} - \frac{0.3}{F_S} \qquad [\beta^* = -0.3 \quad \text{for } F_S = 1] \qquad (14b)$$

***Type II.a Profile (0<$K_S$<1):***

Under a similar consideration, the following expression for $H_{0I}$ can be written as follows:

$$\alpha = = 1 + c_1 \times k_1 \times \lambda_1 = 1 + c_1 \times k_2 \times \lambda_2 = 1 + c_1 \times k_3 \times \lambda_3 = 1 + c_1 \times k_4 \times \lambda_4 \qquad (15)$$

$$c_1 = \frac{0.3}{F_S} \qquad [c_1 = 0.75 \text{ for } F_S = 1] \qquad (16a)$$

$$\beta^* = \frac{0.3}{F_S} - \frac{1}{2} \qquad [\beta^* = 0.3 \quad \text{for } F_S = 1] \qquad (16b)$$

***Type II.b Profile ($K_S$=$S_0$/$S_f$=1, $S_0$ = $S_f$):***

Under a similar consideration, the following expression for $H_{0I}$ can be deduced:

$$\alpha = 1 + c_1 \times \delta_H = 1 + c_1 \times k_1 \times \lambda_1 = 1 + c_1 \times k_2 \times \lambda_2 = 1 + c_1 \times k_3 \times \lambda_3 = 1 + c_1 \times k_4 \times \lambda_4 \qquad (17)$$

$$c_1 = \frac{0.0}{F_S^{-0.5}} \quad [c_1 = 0.70 \text{ for } F_S = 1] \qquad (18)$$

where $k_1$, $k_2$, $k_3$, $k_4$ = coefficients and are: $k_1$ = 0.778, $k_2$ = 0.621, $k_3$ = 0.490, and $k_4$ = 0.521. Note that for Type II.b profile, the multiplication factor, $\beta^*$ for the potential energy change is equal to zero ($\beta^* = 0$), by setting the equality of the friction slope, $S_f$ , to the uniform pipe slope, $S_0$ ($K_S$ = 1, $S_0$ = $S_f$).

***Type II.c (1<$K_S$<2.75) and Type III ($K_S \geq 2.3$ ) Profiles:***

Under a similar consideration, the following expression for $H_{0I}$ can be written:

$$\alpha = = 1 + c_1 \times k_1 \times \lambda_1 = 1 + c_1 \times k_2 \times \lambda_2 = 1 + c_1 \times k_3 \times \lambda_3 = 1 + c_1 \times k_4 \times \lambda_4 \quad (19)$$

$$c_1 = -\frac{0.75}{F_S} \qquad [c_1 = -0.75 \text{ for } F_S = 1] \quad (20a)$$

$$\beta^* = \frac{0.75}{F_S} - \frac{1}{2} \qquad [\beta^* = 0.25 \text{ for } F_S = 1] \quad (20b)$$

**Calculation Procedure for the Improved EGR Approach**

For the sake of comparison between the formulations derived for design parameters [the friction slope, $S_f$, fraction of the required average pressure head, $\delta_H$, and multiplication factors ($\alpha$ and $\beta^*$) for operating pressure], regarding the five types of pressure profiles (***Type I***, ***Types II.a, II.b, II.c*** and ***Type III***), all formulations are sythesized and are shown in Table 1. Before starting the present algorithm, the following input data for hydraulic variables are assigned in advance to finally evaluate the required pressure parameters along the profile.

***Input (initially known) parameters*:** $S_0$: pipe slope which is assumed to be uniform along the line (%), L: total length of the submain line (m), $\overline{H}$: required average pressure head (m), ($U_C$, $CV_q$, $E_U$ or $D_U$): uniformity parameters for the desired level of water application unformity (%), $l_e$: equivalent length (m) to determine the enlergement factor ($F_S$) (Yıldırım and Singh 2013a), s and x: outlet spacing (m) and outlet discharge exponent, respectively.

***Output (required) parameters:*** $S_f$: the friction slope (or the slope of *EGL*) (%), $K_S = S_0/S_f$: the dimensionless energy-gradient ratio, which primarily identifies the type of pressure profiles, $h_{f(L)} = S_f \times L$: the total friction drop at the end of line (m), $H_{max}$, $H_{min}$: the extreme pressure heads (m) with their locations ($i_{max}$, $i_{min}$), $\Delta H_{\max}$: the maximum allowable pressure head difference along the line (m), $\delta_H = \Delta H_{\max} / \overline{H}$: the fraction of the required average pressure head (%), $\phi_H = \Delta H_{\max} / h_{f(L)}$: the relative maximum pressure variation (%), $\alpha$ and $\beta^*$: the multiplification factors to the operating inlet pressure ($H_{0I}$), $H_{0I}$ and $H_d$: the operating inlet and downstream end pressure heads (m), respectively, and $\beta$: nonuniform

outflow exponent (Yıldırım and Singh 2013a) to evaluate the nonuniform outflow distribution along the line.

Based on the present improved EGR approach, the following calculation steps are implemented, respectively, using the related formulations for each type of pressure from Table 1 (Yıldırım and Singh 2013a):

***Step (a).*** For a desired value of the uniformity coefficient ($U_C$, $CV_q$, $E_U$ or $D_U$), and the outlet discharge exponent (x), the related dimensionless physical numbers ($\lambda_1$, $\lambda_2$, $\lambda_3$ or $\lambda_4$) are computed; and for a given value of required average pressure head ($\overline{H}$) and the total length of submain line (L), the dimensionless physical number, $\lambda_5$, are computed from the related expression.

***Step (b).*** Select the proper formulation for $S_f$ in accordance with the given design slope ($S_0$) condition [zero (*p = 0*), upslope (*p = 1), or downslope* (*p = -1)*]. Then $S_f$ is evaluated, depending on dimensionless physical numbers ($\lambda_1$, $\lambda_2$, $\lambda_3$, $\lambda_4$ and $\lambda_5$) and certain values of design coefficients ($k_1$, $k_2$, $k_3$, $k_4$ and $k_5$).

***Step (c).*** Compare the friction slope ($S_f$) to the uniform pipe slope ($S_0$) with respect to the design intervals of the energy-gradient ratio ($K_S = S_0/S_f$), and make a decision about the type of pressure profile depending on the $K_S$ value assigned in ***Step (b)***. It should be noted for downslope condition, as an initial computation, the $S_f$ formulation given for the pressure profiles Type II.c and Type III is first used; then if a negative value of $S_f$ is reached, this would indicate that $S_f$ is greater than the pipe slope, $S_0$; that means the formulation for $S_f$ deduced for Type II.a profile should be used (see, Table 1).

***Step (d).*** For the type of pressure profile assigned in ***Step (c)***, select the proper formulation to evaluate the percentage of the required average pressure head ($\delta_H$) from Table 1. Then, compute the total friction drop, $h_{f(L)}$.

***Step (e).*** For the type of pressure profile decided on above, compute multiplication factors ($\alpha$ and $\beta^*$) for the operating inlet pressure head ($H_{0l}$), depending on the dimensionless physical numbers ($\lambda_1$, $\lambda_2$, $\lambda_3$, $\lambda_4$ and $\lambda_5$) and certain values of design coefficients ($c_1$, $k_1$, $k_2$, $k_3$, and $k_4$) from

Table 1. Then, evaluate the operating inlet pressure head ($H_{0I}$) for both the design cases (considering or neglecting local losses).

***Step (f).*** For the above type of pressure profile, determine the extreme pressure heads ($H_{max}$, $H_{min}$) with their positions along the line ($i_{max}$, $i_{min}$), and evaluate the maximum allowable pressure head difference ($\Delta H_{\max}$) to check the value of $\delta_H$ computed from ***Step (d)***. Then, determine the relative pressure variation ($\phi_H = \Delta H_{\max} / h_{f(L)}$) from Table 1.

***Step (g).*** Compute the downstream end pressure head ($H_d$) from the conservation of energy principle or the related analytical equations derived for each type of profile. Then, set the order of operating inlet ($H_{0I}$), downstream end ($H_d$), extreme ($H_{max}$, $H_{min}$) and required average ($\overline{H}$) pressure heads to check the identity for the assigned type of pressure profile from ***Step (c)***.

***Step (h).*** Introduce the value of $S_f$ previously determined in ***Step (c)*** to reveal the certain form of the pressure head profile along the line. Then, check the identitiy of the specific hydraulic characteristics between the certain and assigned pressure profiles, with regard to Table 1. Note that if a higher precision is required, the nonumiform outflow distribution along the line should be taken into consideration. For this case the nonuniform outflow exponent, $\beta$ (Yıldırım and Singh 2013a) is evaluated depending on the values, $S_0$, x, L, $\overline{H}$, $F_S$, and $S_f$ [determined from ***Step (b)***]. Then, ***Steps (f)~(h)*** are repeated to evaluate the nonuniform outflow distribution.

***Step (ı).*** For water application uniformity evaluation, the proper values of required uniformity parameters ($U_C$, $D_U$, $CV_q$, $E_U$ or $\delta_H$), are computed respectively.

## DESIGN APPLICATIONS COVERING DIFFERENT TYPES of PRESSURE PROFILES and VARIOUS DESIGN CONFIGURATIONS

In the following design applications, the data (Hathoot et al. 1993) are originally selected herein, without needing further input data for the required hydraulic variables. To present a comprehensive comparative analysis (Table 2), covering various design configurations for a wide

range of water application uniformity, $U_C$, and for a large range of uniform line slope situations regarding three outlet discharge exponents (x = 0.2, 0.5 and 1.0), will be presented inTable 2 (please see "Results and Discussion").

**Application-I: Steep Downslope Situation (Type-III Pressure Profile)**

In order to demonstrate the applicability of the proposed improved EGR approach to compute the required pressure parameters along the energy-grade line (*EGL*), the original data given by Hathoot et al. (1993), are selected herein. The total length of the submain line is 151 m (L = 151 m), and the required average pressure head is 7.2 m ($\overline{H} = 7.2$ m), considering the turbulent flow condition through the pipeline (the velocity exponent, m = 1.75 for the DW equation). The steep-downslope situation, $S_0$ = 0.05, is considered and the desired level of water application uniformity is evaluated, $U_C$ = 90.5%, based on the nonuniform outflow concept ($m_\beta = \beta \times m$, $\beta \neq 1$), and the change in the kinetic energy head ($H_V \cong 0$) and local head losses ($F_S$ = 1) are neglected.

***Step a.*** For $U_C$ = 0.905, $\overline{H}$ =7.2 m, L = 151 m and x = 0.5, dimensionless physical numbers, $\lambda_1$ and $\lambda_5$ are already computed as follows: $\lambda_1 = 0.9$ and $\lambda_5 = 0.048$.

***Steps b. and c.*** The friction slope, $S_f$ is directly computed from ($k_1$ = 4.357):

$$S_f = S_0 - k_1 \times \lambda_1 \times \lambda_5 = 0.0 - 4.357 \times 0.9 \times 0.048 = 0.0105 \quad , \quad S_f = 1.05\%$$

The dimensionless energy-gradient ratio, $K_S = \frac{S_0}{S_f} = \frac{0.0}{0.0105} = 4.7$

$K_S = 4.7 > 2.7$ (Table 1), therefore ***Type-III*** profile is observed along the line.

**Total friction drop,** $h_{f(L)} = S_f \times L = 0.0105 \times 151 = 1.586 \cong 1.9$ **m.**

**Total energy gain due to steep-downslope situation,** $\Delta S = S_0 \times L = 0.0$ $\times 151 = 7.5$ **m.**

**For the nonuniform outflow distribution along the line, the non-uniform outflow exponent,** $\beta$ **is evaluated depending on the values of** $S_0$, **x, L,** $\overline{H}$, $F_S$, **and** $S_f$, **as follows:**

$$\beta = 1 - 3.322x\log\left[1 + \frac{H_V}{\overline{H}} + \frac{h_{f(L)}}{\overline{H}}\left[\left(\frac{m+3-0.5^{m+1}}{m+2}\right) - F_S\right] + \frac{1}{4\overline{H}}(p\Delta S)\right]$$

$$\beta = 1 - 3.322 \times 0.5 \times \log\left[1 + 0 + \frac{1.9}{7.2} \times \left[\left(\frac{4.3 - 0.5^{2.3}}{3.3}\right) - 1\right] + \frac{1}{4 \times 7.2} \times (-1) \times 7.5\right]$$

$\beta = 1.172$, **therefore the improved value of velocity exponent,** $m_\beta$ **:** $m_\beta = \beta \times m = 1.172 \times 1.3 = 2.0$

***Step d.*** For ***Type III*** profile, $\delta_H$ can be directly determined from ($k_1$ = 4.357):

$$\delta_H = k_1 \times \lambda_1 = 4.357 \times 0.1 = 0.828, \ \delta_H = 8 \ \%$$

***Step e.*** For ***Type III*** profile, multiplication factors ($\alpha$ and $\beta^*$) are computed from:

$k_1$ = 4.357, $c_1$ = -0.75 for $F_S$ = 1]:

$$\alpha = 1 + c_1 \times \delta_H = 1 - 0.3 \times 0.828 = 0.379$$

$\alpha = 1 + c_1 \times k_1 \times \lambda_1 = 1 - 0.3 \times 4.357 \times 0.1 = 0.379$, and $\beta^* = 0.3$ (for $F_S$ = 1).

The operating inlet pressure head ($H_{0l}$) is directly computed from:

$$H_{0I} = \alpha \times \overline{H} + \beta^* \times (S_0 \times L)$$

$$H_{0I} = 0.379 \times 7.2 + 0.3 \times (0.6 \times 151) = 4.617 \cong 4.6 \text{ m.}$$

Check the value of $H_{0I}$, for $i = 0$, for $S_f = 0.0105$ and $m_\beta = 2.6$ :

$$H_{0I} = H(l = 0, i = 0) = \overline{H} + H_V\,[1-(1-i)^2] + h_{f(L)}\left[F_S[1-i)^{m_\beta+1} - 1] + \frac{m_\beta + 1}{m_\beta + 2}\right] - p\Delta S\left(i - \frac{1}{2}\right)$$

$$= 7.2 + 0 + 1.9 \times \left[1 \times [1-0)^{2.6+1} - 1] + \frac{2.6+1}{2.6+2}\right] - (-1) \times 7.5 \times \left(0 - \frac{1}{2}\right) = 4.6 \text{ m.}$$

The downstream end pressure head, $H_d$, can be directly evaluated from the conservation of energy principle:

$$H_d = H_{0I} + L \times (S_0 - S_f) = 4.6 + 151 \times (0.6 - 0.0105) = 10.585 \cong 10.59 \text{ m.}$$

Check the value of $H_d$, for for $i = 1$, for $S_f = 0.0105$ and $m_\beta = 2.6$ :

$$H_d = H(l = L, i = 1) = 7.2 + 0 + 1.9 \times \left[1 \times [1-1)^{2.6+1} - 1] + \frac{2.6+1}{2.6+2}\right] - (-1) \times 7.5 \times \left(1 - \frac{1}{2}\right) = 10.582 \cong 10.58$$
m.

***Steps* f., g.** and **h.** The location of minimum pressure head ($i_{min}$) can be evaluated from:

$$i_{\min(M)} = \frac{l_{\min}}{L} = 1 - 0.561 \times \left(\frac{K_S}{F_S}\right)^{0.5} = 1 - 0.561 \times \left(\frac{4.3}{1}\right)^{0.5} = -0.6 \text{ ,}$$

Minus sign indicates the minimum outflow just occurs at the upstream pipe inlet point ($i_{min} = 0$), therefore the operating pressure head at the pipe inlet is just identical to the minimum pressure head along the line ($H_{0I} = H_{min} = 4.62$ m), and the maximum pressure head occurs at the downstream closed end ($H_{max} = H_d = 10.58$ m)

The maximum pressure head difference, $\Delta H_{\max} = H_{\max} - H_{\min} = 10.2 - 4.62 = 5.58$ m.

Check the value of $\delta_H$ from: $\delta_H = \frac{\Delta H_{\max}}{\overline{H}} = \frac{5.98}{7.2} = 0.828$, $(\delta_H = 83\%)$

Compute parameter, $\phi_H$, to evaluate the pressure variation:

$\phi_H = \frac{\Delta H_{\max}}{h_{f(L)}} = \frac{5.98}{1.99} = 3.37$ means the excessive level for the pressure variation along the line for a given steep downslope situation (for $K_S$ = 4.75>2.75)

Check the pressure orders for ***Type- III*** profile:

$H_d = H_{\max} = 10.6 > \overline{H} = 7.2 > H_{0I} = H_{\min} = 4.6$ m.

The distribution of pressure parameters evaluated based on the EGR approach is verified by the ***Type- III*** profile as demonstrated in Fig. 3 (e).

***Step* 1.** For water application uniformity, or ***Type III*** profile ($c_1$ = -0.75, $k_1$ = 4.357 and $\beta^*$ = 0.25), regarding the design value of operating pressure head, $H_{0I}$ = 4.62 m, and $\lambda_5 = \overline{H}/L = 7.2/151 = 0.048$, the uniformity parameters are evaluated as follows:

$$\theta = \frac{H_{0I}}{\overline{H}} - \beta^* \times \frac{S_0}{\lambda_5} - 1 = \frac{4.62}{7.2} - 0.25 \times \frac{0.06}{0.048} - 1 = -0.61875$$

$$\delta_H = \frac{\theta}{c_1} = -\frac{0.61875}{-0.75} = 0.825 \cong 83\% \qquad \lambda_1 = \frac{(1-U_C)}{x} = \frac{\theta}{c_1 \times k_1} = \frac{-0.61875}{-0.75 \times 4.357} = 0.1894$$

$$U_C = 1 - \lambda_1 \times x = 1 - 0.1894 \times 0.5 = 0.905 \cong 90.5\%$$

**Application-II: Efficient Downslope (Type II.b Profile) for "Ideal Hydraulic Design"**

To achieve "*the most efficient*" pressure profile or "*the ideal hydraulic design*" case, using the data in Application-I (L = 151 m, $\overline{H} = 7.2$ m), a sample solution is presented for the desired value of the water application uniformity, $U_C$ = 90.5%, based on the following calculation steps:

***Step a.*** Dimensionless physical numbers, $\lambda_1$ and $\lambda_5$ from:

$$\lambda_1 = \frac{(1-U_C)}{x} = \frac{(1-0.905)}{0.5} = 0.19 \quad \text{and} \quad \lambda_5 = \frac{\overline{H}}{L} = \frac{7.2}{151} = 0.048$$

***Steps b** and **c.*** The friction slope, $S_f$, which must be equal to the uniform pipe slope ($S_0$) for "*the most efficient*" design case (***Type II.b*** pressure profile: $K_S = S_0/S_f = 1$), is directly computed from (for ***Type II.b*** profile: $k_1 = 2.178$):

$$S_0 = S_f = k_1 \times \lambda_1 \times \lambda_5 = 2.178 \times 0.19 \times 0.048 = 0.0198 \cong 0.02 \text{ , } S_0 = S_f = 2\%$$

***Step d.*** For the desired ***Type II.b*** profile, $\delta_H$ can be determined by two alternative ways:

By neglecting local losses ($F_S = 1$):

$$\delta_H = 0.357 \times F_S^{-0.5} \times S_f \times \frac{L}{\overline{H}} \cong 0.36 \times S_f \times \frac{L}{\overline{H}} = 0.36 \times 0.02 \times \frac{151}{7.2} = 0.148 \quad (\delta_H \cong 15\,\%)$$

Alternatively, directy computed from ($k_1 = 0.778$):

$$\delta_H = k_1 \times \lambda_1 = 0.778 \times 0.19 = 0.148 \text{ , } \delta_H \cong 15\ \%$$

Total friction drop, $h_{f(L)} = S_f \times L = 0.02 \times 151 = 3.02$ m ($\Delta S = S_0 \times L = 0.02 \times 151 = 3.02$ m)

***Step e.*** For the desired ***Type II.b*** profile, multiplication factors ($\alpha$ and $\beta^*$) are computed from[$k_1$ = 0.778, $c_1$ = 0.70 for $F_S$ = 1]:

$$\alpha = 1 + c_1 \times \delta_H = 1 + 0.70 \times 0.148 = 1.104$$

$$\alpha = 1 + c_1 \times k_1 \times \lambda_1 = 1 + 0.70 \times 0.778 \times 0.99 = 1.104 \text{ and } \beta^* = 0$$

The operating inlet pressure head ($H_{0I}$) is directly computed from:

$$H_{0I} = \alpha \times \overline{H} + \beta^* \times (S_0 \times L)$$

$$H_{0I} = 1.104 \times 7.2 + 0 \times (0.02 \times 151) = 7.949 \cong 7.95 \text{ m.}$$

Check the value of $H_{0_I}$ ($H_{0I} = H_d$) for $S_f$ = 0.0197 [$\Delta S = h_{f(L)}$ = 3.02 m]:

$$H_{\max} = H_{0I} = H_{(l=0, i_{\max}=0)} = \overline{H} + \left(\frac{m+1}{m+2}\right) \times h_{f(L)} - \frac{\Delta S}{2} = 7.2 + \frac{2.73}{3.73} \times 3.02 - \frac{3.02}{2} = 7.905 \cong 7.91$$

**m;**

$$H_{\max} = H_d = H_{(l=L, i_{\max}=1)} = \overline{H} + \left(\frac{m+1}{m+2} - F_S\right) \times h_{f(L)} + \frac{\Delta S}{2} = 7.2 + \left(\frac{2.73}{3.73} - 1\right) \times 3.02 + \frac{3.02}{2} = 7.905 \cong 7.91$$

**m.**

***Steps* f., g.** and **h.** The location of minimum pressure head ($i_{min}$) can be evaluated from:

$$i_{\min(NV)} = \frac{l_{\min}}{L} = 1 - 0.561 \times \left(\frac{K_S}{F_S}\right)^{0.57} = 1 - 0.561 \times \left(\frac{1}{1}\right)^{0.57} \cong 0.44$$

The minimum pressure head ($H_{min}$) is directly computed for $i = i_{\min} = 0.44$ :

$$H_{\min} = H(i_{\min=0.44}) = \overline{H} + H_V\,[1 - (1 - i_{\min})^2] + h_{f(L)} \left[ F_S [1 - i_{\min})^{m_\beta + 1} - 1] + \frac{m_\beta + 1}{m_\beta + 2} \right] - p\Delta S \left( i_{\min} - \frac{1}{2} \right)$$

$$= 7.2 + 0 + 3.0 \times \left[1 \times [1 - 0.4^{2.5} - 1] + \frac{2.5}{3.5}\right] - (-1) \times 3.0 \times \left(0.4 - \frac{1}{2}\right) = 6.826 \cong 6.8$$

m.

Alternatively, for the Type-II.b profile, one can use the following simple relationships which evaluates $H_{min}$,

in terms of $H_{max}$ and $\overline{H}$ :

$$H_{\min} = f\left[H_{\max}, \overline{H}\right]: \qquad H_{\min} = \frac{1}{2} \times (3 \times \overline{H} - H_{\max}) = \frac{1}{2} \times (3 \times 7.2 - 7.9) = 6.825 \cong 6.8$$

m.

Therefore, the maximum pressure head difference, $\Delta H_{\max} = H_{\max} - H_{\min} = 7.9 - 6.8 = 1.2$ m.

Check the value of $\delta_H$ from: $\delta_H = \frac{\Delta H_{\max}}{\overline{H}} = \frac{1.2}{7.2} = 0.5$ , $(\delta_H = 15\%)$

Compute parameter, $\phi_H$ , to evaluate the pressure variation for "*ideal hydraulic design*" case:

$\phi_H = \frac{\Delta H_{\max}}{h_{f(L)}} = \frac{1.2}{2.9} \cong 0.3$ (acceptable critical level for the minimum pressure variation for ideal hydraulic design)

Check the pressure orders for ***Type- II. b*** profile:

$$H_{0I} = H_d = H_{\max} = 7.9 > \overline{H} = 7.2 > H_{\min} = 6.8 \quad \text{m.}$$

The distribution of pressure parameters, assigned based on the EGR approach, is verified by the ***Type- II. b*** profile, as shown in Fig. 2 (c).

***Step* 1.** For the pressure profile Type II.b ($c_1$ = 0.70, $k_1$ = 0.778 and $\beta^*$ = 0), regarding the design value of operating pressure head, $H_{0I}$ = 7.95 m, and $\lambda_5 = \overline{H}/L = 7.2/151 = 0.048$ , uniformity parameters are evaluated as follows:

$$\alpha_{(K_S=1,\beta^*=0)} = \frac{H_{0l}}{\overline{H}} = \frac{7.9}{7.2} = 1.104$$

Using Eq. (36b) for $\theta$ one can yield:

$$\theta_{(K_S=1,\beta^*=0)} = \alpha_{(K_S=1,\beta^*=0)} - 1 = \frac{H_{0l}}{\overline{H}} - 1 = 1.104 - 1 = 0.104$$

$$\delta_H = \frac{\theta}{c_1} = \frac{0.104}{0.70} = 0.149 \cong 15\ \% \qquad \lambda_1 = \frac{(1-U_C)}{x} = \frac{\theta}{c_1 \times k_1} = \frac{0.104}{0.70 \times 0.778} = 0.191$$

$$U_C = 1 - \lambda_1 \times x = 1 - 0.191 \times 0.5 = 0.905 \cong 90.5\%$$

**RESULTS and DISCUSSION**

For the sake of comparison, the results for the required design variables ( $S_f$, $K_S$, $H_{0l}$, $H_d$, $H_{max}$, $H_{min}$, $h_{f(L)}$, $\phi_H$ ) obtained from the proposed EGR approach are compared with those obtained from the previous analytical development (Yıldırım 2007), and the computer-aided step-by-step (SBS) procedure (Hathoot et al. 1993) and are synthesized in Table 2. For the solution of the SBS method, a computer program, *LATCAD* developed in *Visual Basic. 6.0* (Yıldırım and Ağıralioğlu 2004) based on the flowchart presented earlier (Hathoot et al. 1993), was conducted. The computational time was negligible, less than a few minutes for actual calculations, for *LATCAD* implementation.

As a useful reference, regarding three outlet discharge exponents (x = 0.2, 0.5, 1.0), various shapes of pressure head distributions [H(*l*)] versus the dimensionless distance ($i = l/L$) are observed for each type of pressure profiles, based on the results from the present EGR approach and the SBS procedure, and shown in Figs. 1, 2 and 3, respectively.

As shown in Fig. 1, three pressure head distributions for ***Type-I*** profile are demostrated for zero-slope case, $S_0 = 0$ from Fig. (1a), for uniform upslope case with $S_0 = 2\%$ from Fig. (1b), and for uniform steep-upslope case with $S_0 = 5\%$ by Fig. (1c), respectively. Fig. 1 reveals that typical hydraulic characteristics of ***Type-I*** profile are clearly observed in these three figures in which the pressure head exponentially decreases with

respect to the line starting from inlet, and reaches a minimum value at the downstream closed end ( $H_{0I} = H_{\max} > \overline{H} > H_d = H_{\min}$ ).

The maximum pressure head, $H_{max}$, is at the inlet of the line and is equal to the operating inlet pressure, $H_{0I}$ ($H_{0I} = H_{max}$); the minimum pressure head, $H_{min}$, is at the closed end of line, and is equal to the downstream pressure head ($H_d = H_{min}$). The value of the pressure head roughly intersects to the required average pressure head value in the middle section of the line. As shown in Fig. 1, ($S_0$ = 0, 2%, 5%), the pressure head is approximately equal to the average value ( $H = \overline{H} = 7.2m$ ) for the interval of dimensionless distance at about $i = 0.4$ ~ 0.45 through the upstream section.

As shown in Fig. (2a), the pressure distribution for ***Type-II.a*** profile is demonstrated for gentle-downslope case $S_0$ = 1%. As a typical hydraulic chaacteristic of ***Type II.a*** profile, the pressure head decreases from the upstream end with respect to the line, reaches a minimum point ($i_{min}$), and then increases with respect to the line. However, the downstream end pressure head ($H_d$) is still less than the operating inlet pressure ($H_{0I}$). The maximum pressure head is at the inlet ($H_{max} = H_{0I}$); and the minimum pressure head is located at about $i_{min}$ = 0.70, through the downstream section ( $H_{0I} = H_{\max} > \overline{H} > H_d > H_{\min}$ ). In this type of pressure profile, the value of the pressure head roughly intersects the required average pressure head value at about $i = 0.3$ through the ustream section.

As shown in Fig. (2b), the pressure distribution for ***Type-II.b*** profile is demonstrated for efficient-downslope case, $S_0$ = 0.5%. As a typical hydraulic chaacteristic of ***Type II.b*** profile, the operating inlet pressure head is equal to the downstream closed end pressure head ($H_{0I} = H_d$); the maximum pressure is at the inlet ($H_{max} = H_{0I}$) as well as at the closed end of the line ($H_{max} = H_d$). The pressure head is equal to the average pressure head at two points, $i = 0.5$ along upstream and $i = 0.7$ along downstream section. The minimum pressure is located near the middle section of the line, $i_{min}$ = 0.44, for all performed simulations.

As shown in Fig. (3a), the pressure distribution for ***Type-II.c*** profile is presented for nearly-steep downslope situation, $S_0$ = 2%. This type of pressure profile occurs when the line slope is even steeper, so the

pressure at the end of line is higher than the operating inlet pressure. In this condition, the maximum pressure is at the downstream closed end of line ($H_{max} = H_d$), which exponentially decreases along the line, and reaches the minimum pressure, located somewhere along the upstream segment of the line, then inceases toward the upstream end ($H_d = H_{max} > \overline{H} > H_{0l} > H_{min}$ or $H_d = H_{max} > H_{0l} \geq \overline{H} > H_{min}$). In this type of pressure profile, the value of the pressure head roughly intersects the required average pressure head value at two points, $i = 0.6$, near the pipe inlet, and $i = 0.6$ along downstream section for the SBS method, whereas the pressure head is equal to the average pressure head at one point, $i = 0.6$, along downstream segment for the EGR approach. The location of minimum pressure is observed near the upstream end, $i_{min}$ = 0.2, for the EGR approach, whereas $i_{min}$ = 0.3 for the SBS procedure.

As shown in Fig. (3b), the pressure head distribution for ***Type-III*** profile is demostrated for steep-downslope case, $S_0$ = 5% in which the submain line is on a steep downslope, where the total energy gain due to the uniform downslope is larger than the total energy drop due to friction for all sections along the line. In this case, the pressure head increases with respect to the line length. In this condition the maximum pressure is at the downstream closed end of the line (($H_{max} = H_d$), and the minimum pressure head is at the pipe inlet and equal to the operating pressure head ($H_{min} = H_{0l}$) [$H_d = H_{max} > \overline{H} > H_{0l} = H_{min}$]. The value of the pressure head roughly intersects the required average pressure head value at the middle section of the line, $i$ = 0.5, regarding both procedures.

As concluded from Figs, 1, 2 and 3, among all types of pressure profiles, the ***Type-II*** profile is considered as the optimal (or ideal) pressure profile which can produce the minimum pressure head difference when the total energy loss due to friction is just balanced by the total energy gain due to uniform downslope (Profile II-b), as shown in the companion paper (Yıldırım and Singh 2013a).

## CONCLUDING REMARKS

Based on the present EGR approach, the following conclusions can be underlined:

***1.*** Analysis of results obtained from the EGR approach shows that for given values of the uniform pipe slope, $S_0$, the required average outlet pressure head, $\overline{H}$, and the outlet discharge exponent, x, as the operating inlet pressure head, $H_{0I}$ increases the fraction of the required average pressure head, $\delta_H$, and the coefficient of variation of outlet discharge, $C_q$ increase, whereas other uniformity parameters ($U_C$, $D_U$ and $E_U$) decrease, for all types of pressure profiles.

***2.*** To evaluate the influence of different uniform pipe slopes on the $U_C$ values, as the upslope increases the $U_C$ values linearly decrease; hence a large decrease in the $U_C$ values is observed for the highest upslope range, $S_0 = 0.05$ ($U_C = 0.70$). For a given upslope range, the $U_C$ values rapidly decrease as the x value increases. For instance, for $S_0 = 0.05$, the smallest value of $U_C = 0.70$ is observed for the largest value of x = 1.0. For the downhill slope case, the $U_C$ profile has a curve form, even for different *x* values. In this situation, peak points of the $U_C$ profiles approximately occur around the downslope range, $S_0 = 1\%$.

***3.*** To conclude the influence of different uniform pipe slopes on the $H_{0I}$ values; the $H_{0I}$ values increase with increasing upslope whereas decrease with increasing downslope.

***4.*** For all uniform line slope combinations regarded, the water application uniformity gives smaller values with the increase in the outlet discharge exponent, x, generally; for instance for a value of x = 0.2, the uniformity coefficient has highest values, whereas for the laminar flow outlets (x = 1.0), it has smaller values.

***5.*** The pressure head profiles for different uniform line slope situations reveal that the value of the pressure head roughly intersects the required average pressure head value near the middle section of the line. For instance, for ***Type I*** profie ($S_0$ = 0, 2%, 5%), the pressure head is approximately equal to the average value ($H = \overline{H} = 7.2m$) for the dimensionless distance, $i = 0.4$ ~ 0.45; for ***Type II.a*** profile ($S_0$ = 1%), $i = 0.2$ ; for ***Type II. b*** profile (($S_0$ = 0.5%), the pressure head is equal to the average pressure head at two upstream and downstream end points, $i = 0.5$ and $i = 0.7$ ; similarly, for ***Type II.c*** profile ($S_0$ = 2%), $i = 0.6$ and $i = 0.6$ (for SBS) and $i = 0.5$ (for EGR); for ***Type III*** profile ($S_0$ = 5%), $i = 0.6$ .

***6.*** Examination results shows that for the efficient-downslope case (***Type II.b*** profile), the minimum pressure head nearly occurs at the point, $i_{min}$ = 0.44, through the upstream section, for all performed simulations.

**REFERENCES**

Anyoji, H., and Wu, I. P. (1987). "Statistical approach for drip lateral design." Trans. ASAE, 30(1), 187-192.

Barragan, J. and Wu, I.P. (2005). "Simple pressure parameters for micro-irrigation design" Biosystem Eng. 90(4): 463-475.

Christiansen, J. E. (1942). "Irrigation by sprinkling." California Agricultural Experimental Station Bulletin 670, Univ. of California, Davis, California.

Cuenca, R.H. (1989). "Irrigation systems design: an engineering approach". Prentice Hall, New Jersey.

Hathoot, H. M., Al-Amoud, A. I., and Mohammad, F. S. (1993). "Analysis and design of trickle irrigation laterals." J. Irrig. and Drain. Eng., 119(5), 756-767.

Hathoot, H. M., Al-Amoud, A. I., and Mohammad, F. S. (1994). "Analysis and design of sprinkler irrigation laterals." J. Irrig. and Drain. Eng., 120(3), 534-549.

Hathoot, H. M., Al-Amoud, A. I., and Al-Mesned, A. S. (2000). "Design of trickle irrigation laterals considering emitter losses." *ICID Journal,* 49(2): 1-14.

Juana, L., Rodriguez-Sinobas, L., Losada, A. (2002). "Determining minor head losses in drip irrigation laterals. II: experimental study and validation." *J. Irrig. and Drain. Eng.* 128(6): 385-396.

Juana, L., Losada, A., Rodrigoez-Sinobas, L., and Sanchez, R. (2004). "Analytical relationships for designing rectangular drip irrigation units." J. Irrig. and Drain. Eng., 130(1), 47-59.

Kang, Y., and Nishiyama, S. (1996). "Analysis and design of microirrigation laterals." J. Irrig. and Drain. Eng., 122(2), 75-82.

Kang, Y. (2000). "Effect of operating pressures on microirrigation uniformity." Irrig. Sci. 20: 23-27.

Keller, J., and Karmelli, D. (1974). "Trickle irrigation design parameters." Trans. ASAE, 17(4), 678-684.

Keller, J., and Bliesner, r. D. (1990). Sprinkler and trickle irrigation, Van Nostrand Reinhold, New York.

Mahar, P. S., and Singh, R. P. (2003). "Computing inlet pressure head of multioutlet pipeline." J. Irrig. and Drain. Eng., 129(6), 464-467.

Perold, R. P. (1977). "Design of irrigation pipe laterals with multiple outlets." *J. Irrig. and Drain. Eng.,* 103(2): 170-195.

Warrick, A.W. (1983). "Interrelationships of irrigation uniformity terms." J. Irrig. and Drain. Eng., 109(3), 317-332.

Warrick, A.W., and Yitayew, M. (1988). "Trickle lateral hydraulics. I: analytical solution." J. Irrig. and Drain. Eng., 114(2), 281-288.

Wu, I. P. (1992). "Energy gradient line approach for direct hydraulic calculation in drip irrigation design." Irrig. Sci., 13, 21-29.

Wu, I. P. (1997). "An assessment of hydraulic design of micro-irrigation systems." Agric. Water Manage., 32, 275-284.

Wu , I. P., and Yue, R. (1993). "Drip lateral design using energy gradient line approach." Trans. ASAE, 36(2), 389-394.

Valiantzas, J. D. (1998). "Analytical approach for direct drip lateral hydraulic calculation." J. Irrig. and Drain. Eng., 124(6), 300-305.

Wu, I. P., and Gitlin, H. M. (1973). "Hydraulics and uniformity for drip irrigation." J. Irrig. and Drain. Div., ASCE, 99(IR2), Proc. Paper 9786, June, pp. 157-168.

Wu, I. P. and Gitlin, H. M. (1974). "Drip irrigation design based on uniformity." Trans. ASAE, 17(3), 429-432.

Wu, I. P. and Gitlin, H. M. (1975). "Energy gradient line for drip irrigation laterals." J. Irrig. and Drain. Eng., 101(4), 323-326.

Yıldırım, G., and Ağıralioğlu, N. (2004). "Comparative analysis of hydraulic calculation methods in design of micro-irrigation laterals." *J. Irrig. and Drain. Eng.*, 130(3), 201-217.

Yıldırım, G. (2006). "Hydraulic analysis and direct design of multiple outlets pipelines laid on flat and sloping lands." *J. Irrig. Drain .Engrg., ASCE*, 132(6), 537-552.

Yıldırım, G. (2007a). "An Assessment of Hydraulic Design of Trickle Laterals Considering Effect of Minor Losses." *Irrig. and Drain. (ICID Journal)* 56(4), 399-421.

Yıldırım, G. (2007b). "Analytical Relationships for designing multiple outlets pipelines." *J. Irrig. Drain. Engrg., ASCE*, 133(2), 140-154.

Yıldırım, G. (2008). "Determining inlet pressure head incorporating uniformity parameters for multioutlet plastic pipelines." *J. Irrig. Drain .Engrg., ASCE*, 134(3), 341-348.

Yıldırım, G. (2009). "Simplified procedure for hydraulic design of small-diameter plastic pipes." *Irrig. Drain. (ICID J.)* 58(3):209-233.

Yıldırım, G. (2010). "Total energy loss assessment for trickle lateral lines equipped with integrated in-line and on-line emitters" *Irrig. Science,* 28(4): 341-352.

Yıldırım, G. and Singh, V.P. (2013a). "Operating Pressure Assessment for Multi-outlets Submains: Ideal Hydraulic Design" 6th Congress on "International Perspective on Water Research and Environment" by ASCE & EWRI, İzmir, Turkey.

Yıldırım, G. and Singh, V.P. (2013b). "Operating Pressure Assessment for Multi-outlets Submains: Design Applications" 6th Congress on "International Perspective on Water Research and Environment" by ASCE & EWRI, İzmir, Turkey.

Yitayew, M., and Warrick, A. W. (1988). "Trickle lateral hydraulics. *II*: design and examples." *J. Irrig. and Drain. Eng.,* 114(2), 289-300.

**Table 1.** Relationships for the Energy-Grade Line Slope: $S_f$ (%), Fraction of Required Average Pressure Head ($\overline{H}$): $\delta_H$ (%), Multiplication Factors: $\alpha$ and $\beta^*$, to Determine the Operating Inlet Pressure Head ($H_{0l}$) with Related Design Coefficients ($c_1$, $k_1$, $k_2$, $k_3$, $k_4$, $k_5$) for Five Types of Pressure Profiles [***Type-I, Types II.a, II.b, II.c*** and ***Type-III***]

| Energy-Grade Line Slope, $S_f$ (%) | | | | | | Fraction of Required Average Pressure Head: $\delta_H$ (%) | | | | | | Multiplication Factor to the Required Average Pressure Head: $\alpha$ | | | | | | Multiplication Factor to the Potential Energy Head: $\beta^*$ |
|---|---|---|---|---|---|---|---|---|---|---|---|---|---|---|---|---|---|---|
| Type of Pressure Profile(s) | Design Coefficients ($k_1$, $k_2$, $k_3$, $k_4$) | | | | | Type of Pressure Profile(s) | Design Coefficients ($k_1$, $k_2$, $k_3$, $k_4$, $k_5$) | | | | | Type of Pressure Profile(s) | Design Coefficients ($k_1$, $k_2$, $k_3$, $k_4$, $c_1$) | | | | | |
| | $k_1$ | $k_2$ | $k_3$ | $k_4$ | | | $k_1$ | $k_2$ | $k_3$ | $k_4$ | $k_5$ | | $k_1$ | $k_2$ | $k_3$ | $k_4$ | $c_1$ | $\beta^*$ |
| **Type-I** | 4.357 | 3.477 | 2.745 | 2.92 | | **Type-I** and **Type III** | 4.357 | 3.477 | 2.745 | 2.92 | - | **Type-I** | 4.357 | 3.477 | 2.745 | 2.92 | 0.75 ($F_S = 1.0$) | -0.25 ($F_S = 1.0$) |
| | $S_f = k_1 \times \lambda_1 \times \lambda_5 - S_0$<br>$= k_2 \times \lambda_2 \times \lambda_5 - S_0$<br>$= k_3 \times \lambda_3 \times \lambda_5 - S_0$<br>$= k_4 \times \lambda_4 \times \lambda_5 - S_0$ | | | | | | $\delta_H = k_1 \times \lambda_1 = k_2 \times \lambda_2$<br>$= k_3 \times \lambda_3 = k_4 \times \lambda_4$ | | | | | | $\alpha = 1 + c_1 \times k_1 \times \lambda_1 = 1 + c_1 \times k_2 \times \lambda_2$<br>$= 1 + c_1 \times k_3 \times \lambda_3 = 1 + c_1 \times k_4 \times \lambda_4$ | | | | $\frac{0.75}{F_S}$ (Fs ≠ 1.0) | $\frac{1}{2} - \frac{0.75}{F_S}$ (Fs ≠ 1.0) |
| **Type-II.a** | 4.357 | 3.477 | 2.745 | 2.92 | | **Type-II.b** | 0.778 | 0.621 | 0.490 | 0.521 | - | **Type-II.a** | 4.357 | 3.477 | 2.745 | 2.92 | 0.75 ($F_S = 1.0$) | 0.25 ($F_S = 1.0$) |
| | $S_f = S_0 + k_1 \times \lambda_1 \times \lambda_5$<br>$= S_0 + k_2 \times \lambda_2 \times \lambda_5$<br>$= S_0 + k_3 \times \lambda_3 \times \lambda_5$<br>$= S_0 + k_4 \times \lambda_4 \times \lambda_5$ | | | | | | $\delta_H = k_1 \times \lambda_1 = k_2 \times \lambda_2$<br>$= k_3 \times \lambda_3 = k_4 \times \lambda_4$ | | | | | | $\alpha = 1 + c_1 \times k_1 \times \lambda_1 = 1 + c_1 \times k_2 \times \lambda_2$<br>$= 1 + c_1 \times k_3 \times \lambda_3 = 1 + c_1 \times k_4 \times \lambda_4$ | | | | $\frac{0.75}{F_S}$ (Fs ≠ 1.0) | $\frac{1}{2} - \frac{0.75}{F_S}$ (Fs ≠ 1.0) |
| **Type-II.b** | 2.178 | 1.738 | 1.372 | 1.459 | | **Type-II.c** | 4.357 | 3.477 | 2.745 | 2.92 | 0.356 | **Type-II.b** | 0.778 | 0.621 | 0.490 | 0.521 | 0.70 ($F_S = 1.0$) | 0 |
| | $S_0 = S_f = k_1 \times \lambda_1 \times \lambda_5$<br>$= k_2 \times \lambda_2 \times \lambda_5$<br>$= k_3 \times \lambda_3 \times \lambda_5$<br>$= k_4 \times \lambda_4 \times \lambda_5$ | | | | | | $\delta_H = S_0 \times \left(1 - k_1 \times \frac{\lambda_1 \times \lambda_5}{S_0}\right)^{-1/1.75} \times \frac{k_5}{\lambda_5}$<br>$= S_0 \times \left(1 - k_2 \times \frac{\lambda_2 \times \lambda_5}{S_0}\right)^{-1/1.75} \times \frac{k_5}{\lambda_5}$<br>$= S_0 \times \left(1 - k_3 \times \frac{\lambda_3 \times \lambda_5}{S_0}\right)^{-1/1.75} \times \frac{k_5}{\lambda_5}$<br>$= S_0 \times \left(1 - k_4 \times \frac{\lambda_4 \times \lambda_5}{S_0}\right)^{-1/1.75} \times \frac{k_5}{\lambda_5}$ | | | | | | $\alpha = 1 + c_1 \times k_1 \times \lambda_1 = 1 + c_1 \times k_2 \times \lambda_2$<br>$= 1 + c_1 \times k_3 \times \lambda_3 = 1 + c_1 \times k_4 \times \lambda_4$ | | | | $\frac{0.70}{F_S^{-0.57}}$ (Fs ≠ 1.0) | |
| **Type-II.c** and **Type-III** | 4.357 | 3.477 | 2.745 | 2.92 | | | | | | | | **Type-II.c** and **Type-III** | 4.357 | 3.477 | 2.745 | 2.92 | -0.75 ($F_S = 1.0$) | 0.25 ($F_S = 1.0$) |
| | $S_f = S_0 - k_1 \times \lambda_1 \times \lambda_5$<br>$= S_0 - k_2 \times \lambda_2 \times \lambda_5$<br>$= S_0 - k_3 \times \lambda_3 \times \lambda_5$<br>$= S_0 - k_4 \times \lambda_4 \times \lambda_5$ | | | | | | | | | | | | $\alpha = 1 + c_1 \times k_1 \times \lambda_1 = 1 + c_1 \times k_2 \times \lambda_2$<br>$= 1 + c_1 \times k_3 \times \lambda_3 = 1 + c_1 \times k_4 \times \lambda_4$ | | | | $-\frac{0.75}{F_S}$ (Fs ≠ 1.0) | $\frac{0.75}{F_S} - \frac{1}{2}$ (Fs ≠ 1.0) |

***Dimensionless Physical Numbers:*** $\lambda_1 = \frac{(1-U_C)}{x}$, $\lambda_2 = \frac{CV_q}{x}$, $\lambda_3 = \frac{(1-EU)}{x}$, $\lambda_4 = \frac{(1-DU)}{x}$, $\lambda_5 = \frac{\overline{H}}{L}$; and Fs = Enlargemet factor, to take into account the effect of local losses [ $F_S = 1 + (l_e / s)$ ].

**Table 2.** Complete Results from the Comparison Test Between the Proposed EGR Approach, Previous Analytical Development (Yıldırım, 2007) and the SBS Procedure (Hathoot et al. 1993), the Required Hydraulic Characteristics ($S_f$, $h_{f(L)}$, $H_{0l}$, $H_d$, $H_{max}$, $H_{min}$, $\Delta H_{max}$ , $\phi_H$ ) along the Energy-Grade Line (EGL) for Various Uniform Line Uphill and Downhill Slope Situations and three outlet discharge exponents (x = 0.2, 0.5, 1.0), for Five Types of Pressure Head Profiles (***Type-I***, ***Type II.a, Type II.b, Type II.c*** and ***Type III)***

| | | Improved Energy-Gradient Ratio (EGR) Approach (Proposed) | | | | | | | | | Previous Analytical Development (Yıldırım, 2007) | | | | | | | | | Computer-Aided Step-by-Step (SBS) Procedure (Hathoot et al. 1993) | | | | | | | | |
|---|---|---|---|---|---|---|---|---|---|---|---|---|---|---|---|---|---|---|---|---|---|---|---|---|---|---|---|---|
| *x* | ***Type*** | $S_f$ | $K_S$ | $U_C$ | $H_{0l}$ | $H_d$ | $H_{max}$ | $H_{min}$ | $h_{f(L)}$ | $\phi_H$ | $S_f$ | $K_S$ | $U_C$ | $H_{0l}$ | $H_d$ | $H_{max}$ | $H_{min}$ | $h_{f(L)}$ | $\phi_H$ | $S_f$ | $K_S$ | $U_C$ | $H_{0l}$ | $H_d$ | $H_{max}$ | $H_{min}$ | $h_{f(L)}$ | $\phi_H$ |
| - | - | *(%)* | - | *(%)* | *(m)* | *(m)* | *(m)* | *(m)* | *(m)* | - | *(%)* | - | *(%)* | *(m)* | *(m)* | *(m)* | *(m)* | *(m)* | - | *(%)* | - | *(%)* | *(m)* | *(m)* | *(m)* | *(m)* | *(m)* | - |
| .2 | ***I*** | 1.35 | 0 | 98.7 | 8.73 | 6.69 | 8.73 | 6.69 | 2.04 | 1.0 | 1.36 | 0 | 98.7 | 8.70 | 6.66 | 8.70 | 6.66 | 2.05 | 1.0 | 1.30 | 0 | 98.8 | 8.86 | 6.91 | 8.86 | 6.91 | 1.97 | 1.0 |
| .5 | | 1.37 | 0 | 96.7 | 8.75 | 6.68 | 8.75 | 6.68 | 2.07 | 1.0 | 1.38 | 0 | 96.7 | 8.72 | 6.65 | 8.72 | 6.65 | 2.09 | 1.0 | 1.28 | 0 | 96.9 | 8.70 | 6.78 | 8.70 | 6.78 | 1.94 | 1.0 |
| 1 | | 1.43 | 0 | 93.1 | 8.82 | 6.66 | 8.82 | 6.66 | 2.16 | 1.0 | 1.43 | 0 | 93.1 | 8.79 | 6.62 | 8.79 | 6.62 | 2.16 | 1.0 | 1.25 | 0 | 93.4 | 8.57 | 6.69 | 8.57 | 6.69 | 1.89 | 1.0 |
| .2 | | 1.32 | -1.51 | 96.8 | 10.2 | 5.19 | 10.2 | 5.19 | 2.00 | 2.5 | 1.38 | -1.44 | 96.8 | 10.2 | 5.16 | 10.2 | 5.16 | 2.09 | 2.4 | 1.26 | -1.59 | 96.8 | 10.4 | 5.56 | 10.4 | 5.56 | 1.90 | 2.5 |
| .5 | | 1.41 | -1.42 | 91.8 | 10.3 | 5.16 | 10.3 | 5.16 | 2.12 | 2.4 | 1.45 | -1.38 | 91.8 | 10.3 | 5.12 | 10.3 | 5.12 | 2.19 | 2.4 | 1.21 | -1.65 | 92.0 | 10.2 | 5.39 | 10.2 | 5.39 | 1.83 | 2.6 |
| 1 | | 1.55 | -1.29 | 82.9 | 10.5 | 5.10 | 10.5 | 5.10 | 2.34 | 2.3 | 1.57 | -1.27 | 82.9 | 10.4 | 5.06 | 10.4 | 5.06 | 2.37 | 2.2 | 1.53 | -1.31 | 83.2 | 10.6 | 5.33 | 10.6 | 5.33 | 2.31 | 2.3 |
| .2 | | 1.34 | -3.74 | 93.9 | 12.5 | 2.92 | 12.5 | 2.92 | 2.02 | 4.7 | 1.42 | -3.53 | 93.9 | 12.5 | 2.89 | 12.5 | 2.89 | 2.14 | 4.5 | 1.30 | -3.83 | 93.7 | 12.9 | 3.44 | 12.9 | 3.44 | 1.97 | 4.8 |
| .5 | | 1.52 | -3.28 | 84.3 | 12.7 | 2.85 | 12.7 | 2.85 | 2.30 | 4.3 | 1.54 | -3.24 | 84.3 | 12.7 | 2.81 | 12.7 | 2.81 | 2.33 | 4.2 | 1.10 | -4.55 | 84.3 | 12.5 | 3.36 | 12.5 | 3.36 | 1.66 | 5.5 |
| 1 | | 1.84 | -2.72 | 67.1 | 13.1 | 2.73 | 13.1 | 2.73 | 2.77 | 3.7 | 1.81 | -2.76 | 67.1 | 13.0 | 2.69 | 13.0 | 2.69 | 2.74 | 3.8 | 1.58 | -3.17 | 67.4 | 13.0 | 3.08 | 13.0 | 3.08 | 2.38 | 4.2 |
| .2 | ***II.*** | 0.47 | 1.07 | 99.1 | 7.38 | 7.43 | 7.38 | 7.11 | 0.71 | 0.38 | 0.44 | 1.14 | 99.1 | 7.34 | 7.39 | 7.39 | 7.11 | 0.66 | 0.42 | 0.48 | 1.05 | 99.3 | 7.37 | 7.42 | 7.42 | 7.16 | 0.72 | 0.36 |
| .5 | ***b*** | 0.46 | 1.09 | 97.8 | 7.37 | 7.44 | 7.37 | 7.11 | 0.69 | 0.38 | 0.49 | 1.02 | 97.8 | 7.33 | 7.40 | 7.40 | 7.11 | 0.74 | 0.39 | 0.45 | 1.09 | 97.5 | 7.25 | 7.36 | 7.36 | 7.09 | 0.69 | 0.39 |
| 1 | | 0.48 | 1.05 | 95.4 | 7.38 | 7.41 | 7.38 | 7.11 | 0.72 | 0.38 | 0.47 | 1.06 | 95.4 | 7.35 | 7.38 | 7.38 | 7.11 | 0.71 | 0.38 | 0.46 | 1.08 | 95.1 | 7.41 | 7.33 | 7.41 | 7.16 | 0.70 | 0.36 |
| .2 | ***II.*** | 2.77 | 0.36 | 98.3 | 9.58 | 6.91 | 9.58 | 6.54 | 4.18 | 0.73 | 2.87 | 0.35 | 98.3 | 9.51 | 6.84 | 9.51 | 6.54 | 4.33 | 0.69 | 2.81 | 0.35 | 98.0 | 9.57 | 6.95 | 9.57 | 6.71 | 4.25 | 0.67 |
| .5 | ***a*** | 2.66 | 0.38 | 96.0 | 9.46 | 6.95 | 9.46 | 6.58 | 4.02 | 0.72 | 2.77 | 0.36 | 96.0 | 9.39 | 6.88 | 9.39 | 6.58 | 4.18 | 0.67 | 2.62 | 0.38 | 96.2 | 9.53 | 6.97 | 9.53 | 6.79 | 3.96 | 0.69 |
| 1 | | 2.62 | 0.38 | 92.2 | 9.41 | 6.97 | 9.41 | 6.59 | 3.96 | 0.71 | 2.68 | 0.37 | 92.2 | 9.35 | 6.90 | 9.35 | 6.59 | 4.05 | 0.68 | 2.79 | 0.36 | 92.1 | 9.18 | 6.75 | 9.18 | 6.63 | 4.22 | 0.60 |
| .2 | ***II.*** | 1.07 | 1.88 | 99.1 | 6.90 | 8.31 | 8.31 | 6.74 | 1.61 | 0.98 | 1.34 | 1.50 | 99.1 | 6.87 | 8.28 | 8.28 | 6.74 | 2.02 | 0.76 | 1.35 | 1.48 | 99.0 | 7.14 | 8.12 | 8.12 | 6.75 | 2.04 | 0.67 |
| .5 | ***c*** | 1.04 | 1.92 | 97.7 | 6.87 | 8.32 | 8.32 | 6.73 | 1.58 | 1.01 | 1.32 | 1.52 | 97.7 | 6.85 | 8.29 | 8.29 | 6.73 | 1.99 | 0.78 | 1.44 | 1.39 | 97.6 | 7.26 | 8.10 | 8.10 | 6.93 | 2.17 | 0.54 |
| 1 | | 1.04 | 1.92 | 95.4 | 6.87 | 8.32 | 8.32 | 6.73 | 1.58 | 1.01 | 1.29 | 1.54 | 95.4 | 6.85 | 8.29 | 8.29 | 6.73 | 1.96 | 0.79 | 1.47 | 1.36 | 95.7 | 7.24 | 8.04 | 8.04 | 6.87 | 2.22 | 0.53 |
| .2 | ***III*** | 1.2 | 4.32 | 96.3 | 4.73 | 10.5 | 10.5 | 4.71 | 1.75 | 3.34 | 1.29 | 3.87 | 96.3 | 4.71 | 10.5 | 10.5 | 4.71 | 1.95 | 2.97 | 1.34 | 3.72 | 96.4 | 5.17 | 10.7 | 10.7 | 5.17 | 2.03 | 2.72 |
| .5 | | 1.1 | 4.75 | 90.5 | 4.62 | 10.6 | 10.6 | 4.59 | 1.59 | 3.77 | 1.22 | 4.08 | 90.5 | 4.59 | 10.6 | 10.6 | 4.59 | 1.85 | 3.25 | 1.49 | 3.35 | 90.3 | 5.11 | 10.4 | 10.4 | 5.11 | 2.25 | 2.35 |
| 1 | | 0.9 | 5.39 | 80.4 | 4.48 | 10.6 | 10.6 | 4.45 | 1.40 | 4.40 | 1.12 | 4.47 | 80.4 | 4.45 | 10.6 | 10.6 | 4.45 | 1.69 | 3.64 | 1.32 | 3.79 | 80.6 | 5.02 | 10.5 | 10.5 | 5.02 | 1.99 | 2.75 |

# FATALITIES AND INJURIES RELATED TO FALLING FROM A HEIGHT THAT OCCURS DURING AGRICULTURAL ACTIVITIES

*Murat DARÇIN[1], E. Selcen DARÇIN[2], Gürdoğan DOĞRUL[3], Murat ALKAN[3]*

**Abstract:** Despite the frequent occurrence of falls from a height incidents during agricultural activities characterized by poor work health and safety conditions, there is not enough data and work at the national level in our country about the victims, types, causes, prevalence, consequences and other characteristics of the events. The aim of this study, which is considered to contribute to the gap in the literature, is to investigate the agricultural related falls from a height accident and to reveal important factors that affect the falling. In this study; 937 agricultural activities related falls from height accident occurred in selected rural areas were analyzed by data mining method. Approximately one third (35%) of all falling from a height in rural areas and nearly half (47%) of those resulting in death are related to agricultural activities. 17% of falls from a height associated with agriculture activity have resulted in death or serious injury; the mortality rate for non-agricultural activities as a result of falling from a height is 3.7%, while for agriculture activities this rate increases to 6%. 60% of the events are falling from a tree during the fruit picking or pruning. One third of the dead are 70 years old, one in four is over 75 years old. To effectively minimize falls from height; prevention programs that encourage safe working behaviors should be implemented. It is expected that the results of this study will contribute to the information gap in

1 KTO Karatay University, Faculty of Engineering and Natural Science, Konya / Turkey, murat.darcin@karatay.edu.tr, Orcid No: 0000-0002-1553-1002

2 Ankara Hacı Bayram Veli University, Polatlı Faculty of Science and Letters, Ankara / Turkey, emine.darcin@hbv.edu.tr, Orcid No: 0000-0002-1291-5334

3 Ministry of Interior Affairs, Ankara / Turkey

the national scale and to raise awareness about falling from height in agriculture sector.

***Keywords:*** Agriculture, Fall From Height, Accidental Falls, Occupational Health, Occupational Safety

## INTRODUCTION

One of the most prominent features of the agricultural industry, which plays an essential role in the country's culture, social life, environment, economy, and employment policies is one of the most dangerous industries. Besides it has poor occupational health and safety conditions. We cannot record every industrial incident due to the insufficient data reporting system. Accident rates are much higher than in any other industry. Vehicle and agricultural tool/machine-related accidents and poisoning caused by pesticides and falling from a height, which generates hundreds of people each year, are the most common accidents in the agriculture industry. Falls from height frequently occur due to no precautions taken during agricultural activities or the use of defective, inappropriate, or wrong equipment.

Falling from height is an unexpected event that occurs unintentionally. The concept of height refers to places that cannot be reached by taking a step and differs from person to person, which refers to the distance that can cause injury resulting from falling. The primary measure in defining the height point is the second vertebra, the human body center of gravity (balance point). If the work area has a risk of causing death or injury in the event of a fall, whether it is below or above ground level, such works refer to as "working at height."

When a person falls from a height, potential energy (depending on height) is converted into kinetic energy by the effect of gravity. At the moment of impact, the body slows down, and an amount of energy equal to the kinetic energy transferred to the ground is transferred back to the body. In the form of injury, the body absorbs back the lost energy. Fall events, in which the body's damage increases depending on the height, have more severe consequences than other occasions.

In order to be able to analyze fall consequences further and understand better how some factors benefit to the survival of falling from greater heights, there is a need to include more data on persons which fell and explain how it occurred. For example, fall (impact) energy could be calculated through data on fall height and human body mass: E=mgh (J) (Zlatar et al., 2019).

Results on calculations regarding fall energy for four different persons (body mass of 60, 75, 90 and 105kg) were illustrated in Figure 1 (Zlatar et al., 2019).

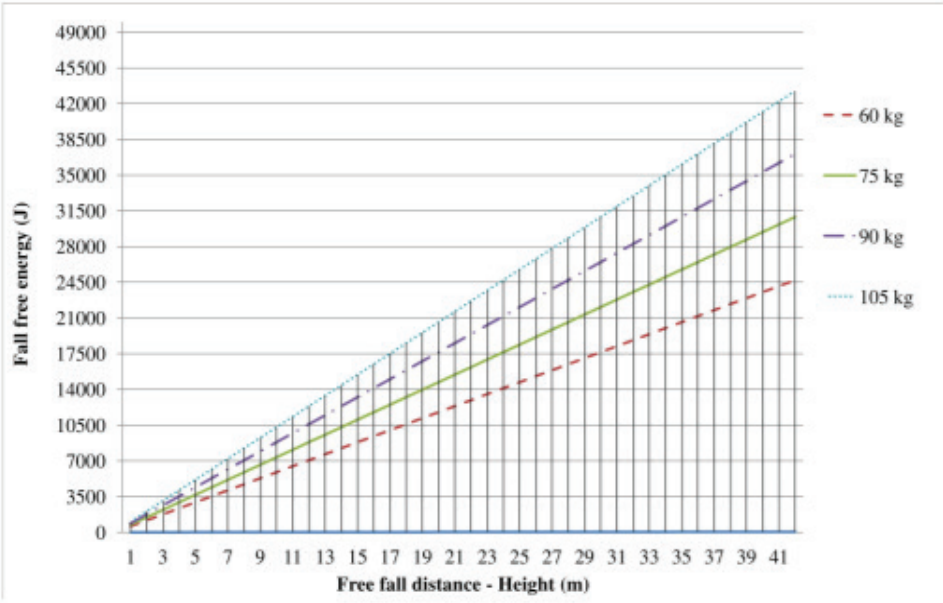


Figure 6. Human body mass an its relation to fall energy and fall height.

**Figure 1. Human Body Mass an its Relations to Fall Energy and Fall Height**

As it is illustrated in Figure 6, the fall energy of 10,500J correspond to fall of a human with a body mass of 105kg from a height of 10m, 90kg from 12m, 75kg from 14m and 60kg from 18m. Therefore, a fall impact from the same height would be much lower for those humans having lower body mass compared with those with higher, representing a heavy person less chance of surviving a fall (Zlatar et al., 2019).

Unfortunately, there is not enough data and studies at the national level in our country about the victims, types, reasons, and other characteristics of the agricultural, industrial incidents, where falling from height occurs at a very high rate. It makes it difficult to precisely determine the events that occurred and reveal their causes and effects.

This study, contributing to the literature gap, analyzes the accidents of falling from height and demonstrates the critical factors that affect the fall. Although this study covers the accidents in the form of falling from a height, it includes slipping, staggering, falling at the same level, falling due to assault, and deliberate self-injury. It excludes falling from a burning building and accidentally falls from the moving vehicle during agricultural activities. This study's concept of agricultural activities includes the agricultural and forestry works specified in Labor Law and the Regulation on Works Considered from Industry, Commerce, Agriculture, and Forestry.

This study reveals some valuable findings of the accident characteristics of the type of fall from height in the agricultural sector at the selected provinces' scale. However, the study has some limitations. We conducted this study in a limited period (2013) in rural areas of 18 selected provinces. Although the selected sample includes the whole rural areas of some provinces in critical agricultural regions, when we consider other geographies including different farming types and characteristics, the study findings need to be supported by other studies to be used in generalization throughout the country.

## MATERIAL and METHODS

In this study, the "falls from a height" related to agricultural activities in rural areas of the provinces selected from a total of 2644 falling from heights on agriculture and non-agricultural were investigated based on the incident reports. We analyzed the agricultural activities (agriculture/forestry/animal husbandry) of these falling accidents for the event type, cause and time, the severity of the accident, age and gender of the victims, and other factors. We employ data mining method to analyze the data of the 937 agriculture-related falls from height incidents

which take place in rural areas of 18 selected provinces (Aydın, Çanakkale, Balıkesir, Burdur, Isparta, Antalya, Bilecik, Afyon, Artvin, Çorum, Amasya, Bingöl, Ağrı, Maraş, Adıyaman, Adana, Hatay, Mersin) in 2013.

***Data Mining***

Data Mining is a technique that has been used in many scientific researches for years, can identify useful examples by analyzing data in large databases (Chang and Wang, 2006; Zhang and Zhang, 2002). One of the data mining models that are useful to find association behaviors among large data sets is association rules (Liao and Perg, 2007; Mirabadi and Sharifian, 2010).

***Association Rules***

Association rules can provide results that will form the basis for decision-making and forecasting about the measures to be taken to reduce accidents by revealing the unknown relationships within the data stacks (Chae et al., 2001; Tsay and Chiang, 2005).

The association rules try to determine the relationship between the two movements by finding the probability that movement B (successor) also occurs when an A move (premise) occurs (Marukatat, 2007). The association rule is shown as A=>B (Agrawal et al., 1993).

The rule support (s) of an association rule is the ratio of the number of transactions covering A∪B to the total number of movements in the database (N) in percentage and formulated as follows (Guillet and Hamilton, 2007):

$$\text{The rule support (s)} = n(A \cup B) \,/\, n(N)$$

Confidence (α), on the other hand, expresses what percentage of the movements that include A includes B and is formulated as follows (Marukatat, 2007);

$$\text{Confidence } (\alpha) = n(A \cup B) / n(A)$$

The higher the rule support (s), the more often the rule repeats; The higher the confidence (α), the less exceptions to the rule.

*Apriori Algorithm*

The Apriori algorithm which is an algorithm that extracts association rules from data sets, was developed by Agrawal and Srikant in 1994 and has become the most widely used algorithm in the history of data mining to extract association rules (Agrawal and Srikant, 1994; Witten and Frank, 2005).

In order to determine the relationships between accident factors, the data were analyzed with the SPSS Clementine Program. In order to determine the dual, triple and quadruple association relationships among accident factors, the Apriori Model was applied to the accident data and the results were interpreted. The support value in the tables showing the Apriori Algorithm used in the analyzes is the percentage of the precursor factor; Confidence value indicates how many of the records containing the precursor factor include the successor factor; The rule support value indicates the percentage of the two factors coexistence.

**RESULTS and DISCUSSION**

During the period, 35% of falls from height in the selected sample are about agricultural activities. Of farm activities, we observe that 83% of casualties were slightly and moderately injured. 11% were seriously injured, and 6% died (Figure 2).

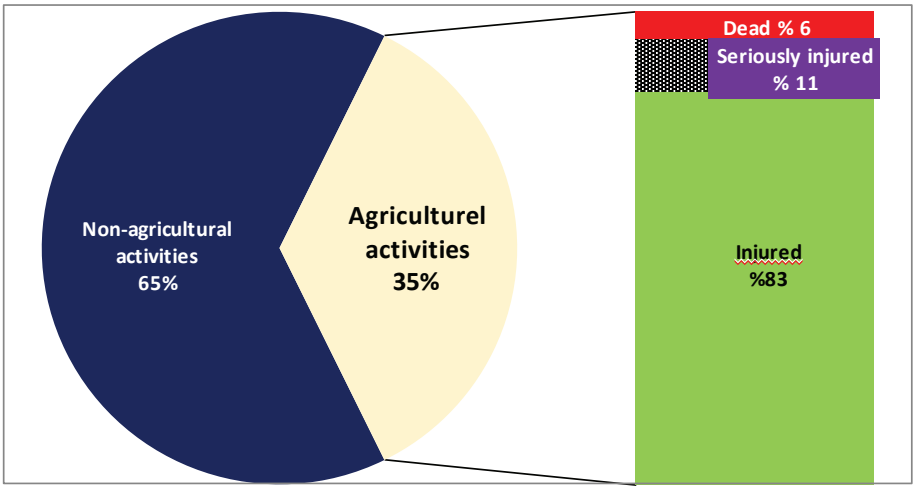


**Figure 2. Share of Agriculture in Falls from Height**

In 2644 fall from height incidents examined both related to agriculture and non-agricultural, 119 people died, 56 of them lost their lives due to agriculture activities. In agricultural activities, falls from heights are more deadly. While the mortality rate resulting from falling from height in non-agricultural activities is 3.7%, this rate increases to 6% in falls from height in agricultural work (Figure 3).

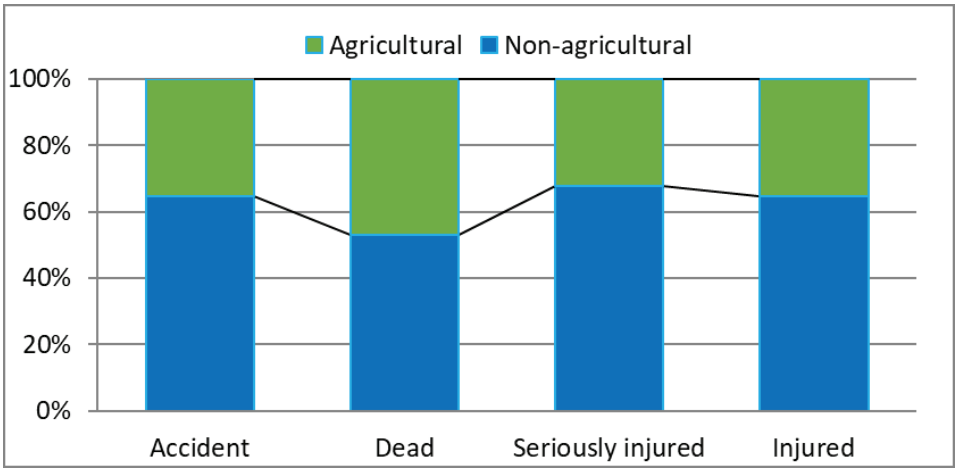


**Figure 3. The Consequences of Falls From Heights**

Per the analysis results, we observe the associations between accident factors in the study. Table 1 illustrates information on the victims' occupation, education, and gender. 77% of the victims are men, 23% are women, approximately 70% are primary school graduates, and 7% are illiterate or literate. When the falls due to agriculture, which result in death only, are examined, we note that 93% of those who died were male, and 17% were illiterate or literate.

37.2% of the victims are farmers, 19% are housewives, 12.3% are self-employed, 9% are students, and the other 9% are workers. Approximately two-thirds (65%) of the victims in fatal accidents are farmers, and 6% are housewives.

**Table 1. Falls from Height Due to Agriculture by Occupation, Education, and Gender**

| Premise | Sequent | Support % | Trust % | Rules Support % |
|---|---|---|---|---|
| Primary school graduate | Male | 69,37 | 76,308 | 52,935 |
| Male | Primary school graduate | 76,841 | 68,889 | 52,935 |
| Farmer | Primary school graduate | 37,247 | 80,516 | 29,989 |
| Primary school graduate | Farmer | 69,37 | 43,231 | 29,989 |
| Primary School Graduate, Male | Farmer | 52,935 | 55,444 | 29,349 |
| Woman | Primary school graduate | 22,946 | 71,628 | 16,435 |
| Female, Primary school graduate | Housewife | 16,435 | 87,013 | 14,301 |

| | | | | |
|---|---|---|---|---|
| Housewife | Primary school graduate | 18,997 | 75,281 | 14,301 |
| High school graduate | Male | 9,605 | 84,444 | 8,111 |
| Worker | Male | 8,858 | 91,566 | 8,111 |
| Self-employed | Primary school graduate | 12,273 | 62,609 | 7,684 |
| Occupation student | Male | 8,965 | 85,714 | 7,684 |
| Primary School Graduate, Male | Self-employed | 52,935 | 14,113 | 7,471 |
| Worker, Male | Primary school graduate | 8,111 | 65,789 | 5,336 |
| Secondary school graduate | Male | 5,87 | 69,091 | 4,055 |
| Literate | Male | 5,016 | 74,468 | 3,735 |
| Retired | Primary school graduate | 5,656 | 49,057 | 2,775 |
| Retired, Male | Primary school graduate | 5,443 | 49,02 | 2,668 |
| Farmer, Male | Literate | 36,499 | 6,14 | 2,241 |

{Primary school graduate => Male} this duo togetherness rule support is 52.9%. In other words, approximately 53% of fall victims are primary school graduates and male. {Primary school graduate => Farmer} the rule support of the duo togetherness is about 30%; {Female => Primary school graduate}, the rule support of the duo is 16.4%; The rule support of the trio {Primary school graduate, Male => Farmer} is 29.3%; {Female, Primary School Graduate => Housewife} The rule support of the trio is 14.3.

**Table 2. The Month, Place, Activity, and Casualty / Injured Status of the Fall From Height**

| Premise | Sequent | Support % | Trust % | Rules Support % |
|---|---|---|---|---|
| Tree | Injured | 60,085 | 83,837 | 50,374 |
| Injured | Tree | 83,244 | 60,513 | 50,374 |
| Harvesting | Tree | 52,295 | 91,02 | 47,599 |
| Tree | Harvesting | 60,085 | 79,218 | 47,599 |
| Harvesting | Injured | 52,295 | 83,673 | 43.757 |
| Harvesting, Tree | Injured | 47,599 | 83,632 | 39,808 |
| Other Activity | Injured | 19,317 | 83,425 | 16.115 |
| September | Tree | 17,182 | 79,503 | 13,661 |
| Harvesting, Tree | September | 47,599 | 25,785 | 12,273 |
| Vehicle | Injured | 13,447 | 88,095 | 11,846 |
| Tree, Injured | September | 50,374 | 22,246 | 11,206 |
| Platform-roof-house-top | Injured | 12,593 | 82,203 | 10,352 |
| September, Tree, Injured | Harvesting | 11,206 | 89,524 | 10,032 |
| Pruning | Tree | 12,166 | 78,947 | 9,605 |
| Tree, Injured | Pruning | 50,374 | 16,525 | 8,324 |
| Loading/unloading: | Vehicle | 9,072 | 90,588 | 8,218 |
| Vehicle, Injured | Loading/unloading: | 11,846 | 57,658 | 6,83 |
| October | Harvesting | 10,993 | 59,223 | 6.51 |
| July | Harvesting | 12,914 | 48.76 | 6,297 |
| Life-threatening | Tree | 10,886 | 57,843 | 6,297 |
| August | Tree | 10,993 | 57,282 | 6,297 |

| | | | | |
|---|---|---|---|---|
| Harvesting | Tree | 6.51 | 95,082 | 6,19 |
| Deceased | Harvesting | 5,87 | 54,545 | 3.202 |
| Harvesting, Tree | Deceased | 47,599 | 5,605 | 2,668 |

Table 2 presents analysis findings per the month of the accident, the location of fall, the activity during the fall, and the result of the fall (dead/injured). The rule support of the duo togetherness {Tree => Injured} is 50.44%; The rule support of the duo togetherness {Picking => Tree} is 47.6%; The rule support of the trio togetherness {harvesting, tree => injured} is 43.8% and the rule support for four of them {September, tree, wounded => harvesting} is 10%.

The accidents of falling from height were mostly due to falling from trees, with 60%. It is followed by falls from the vehicle with 13.4% and falls from the platform-roof-housetop with 12.6% (Figure 4). In falls resulting in death, falling from trees emerges as the main actor at the same rate. While falling from a cliff accounts for 3% of falls from all heights, they account for 7% of fatal falls.

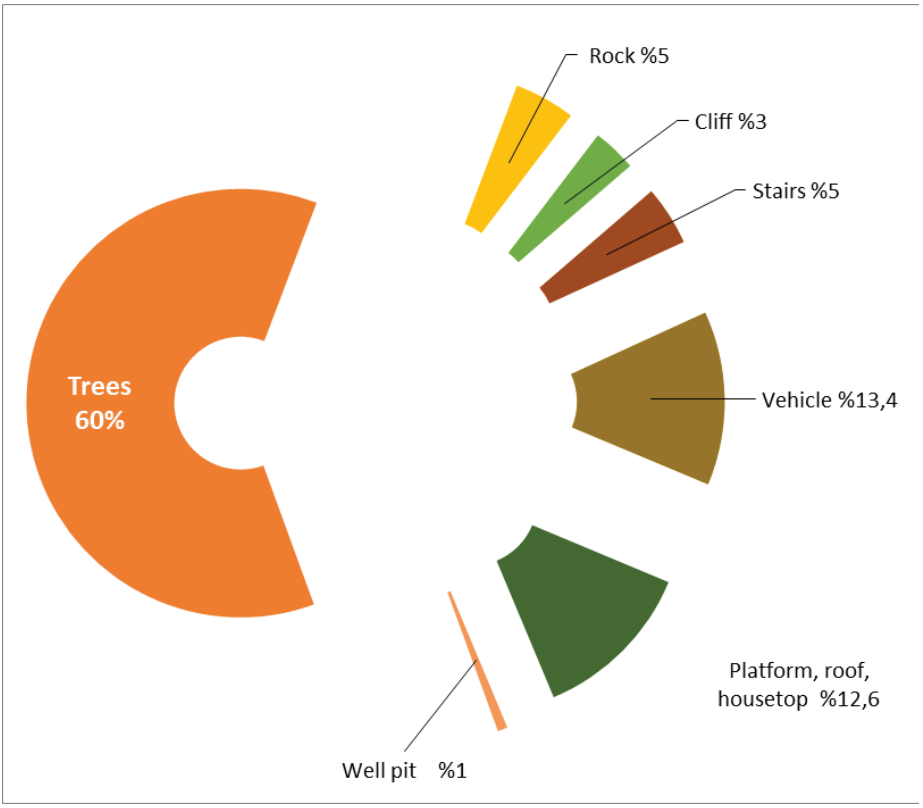


**Figure 4. Places Where Falling from Height Due to Agriculture Occurred**

More than half (52.3%) of falls from height occurred during harvesting activity. It is followed by other activities (irrigation, maintenance, spraying, sowing, so on.) with 19.3%, pruning with 12%, and loading/unloading with 9% (Figure 5). Half of the fatal accidents occurred during harvesting and 19% during pruning.

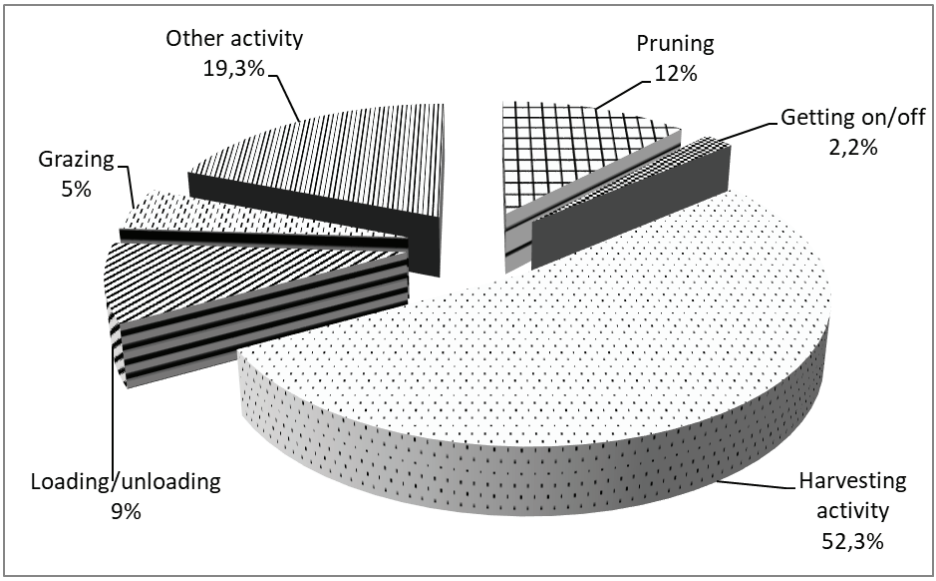


**Figure 5. Agricultural Activity During Falling from a Height**

In terms of the months when the fall accidents occurred, September is when most accidents happen with 17%. 13% of the accidents occurred in July, 11% in August, and 11% in October (Figure 6). About one-third (32%) of falls from heights that resulted in death occurred in September and October.

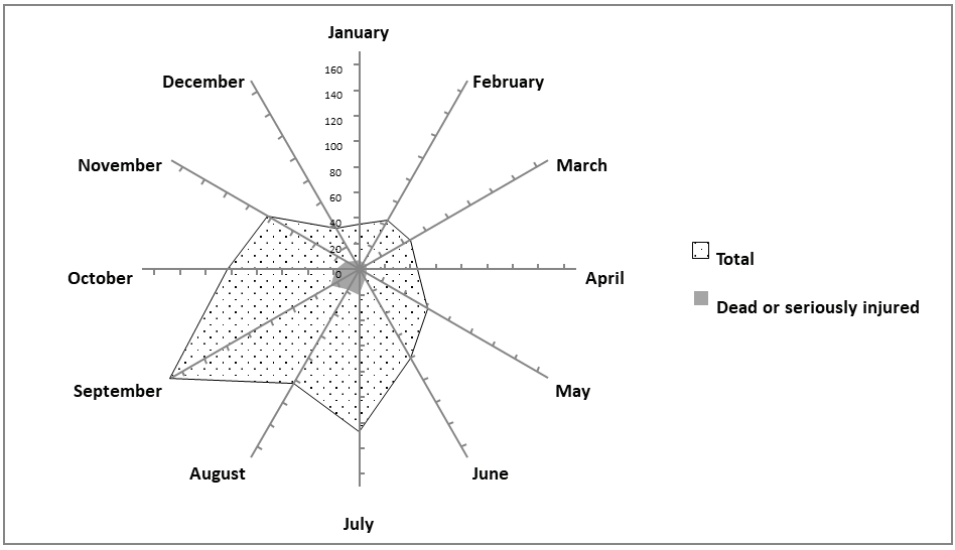


**Figure 6. The Times of Falling from Height During Agricultural Activities (Months)**

Exposure to falls from height in agricultural activities where people of all age groups work is higher in the middle age group, which constitutes an integral part of the agrarian workforce (Figure 7).

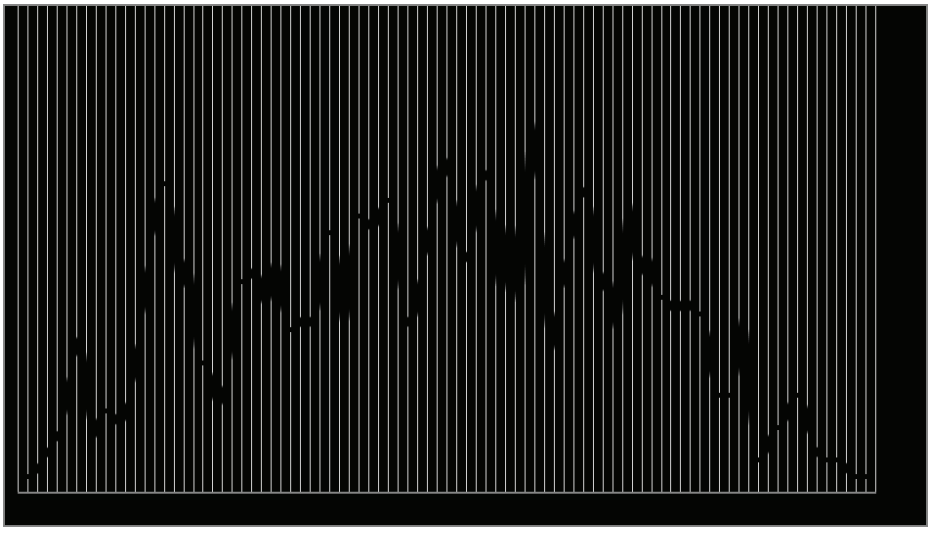

**Figure 7. Falls from Height Due to Agriculture by Age**

When we analyze the accident results per the age categories drawn on a logarithmic scale that considers the percentage change, we see that workers over 60 years of age are the group with the highest rate of fatal falls specific to the agricultural sector (Figure 8). 57% of those who died due to falling from a height during agricultural activities are 60 years old or older. One-third of those who die are over 70 years old, and one-quarter are over 75 years old. This situation shows that; age is a crucial risk factor for falling. Older people are at a too high risk of death or severe injury from falls.

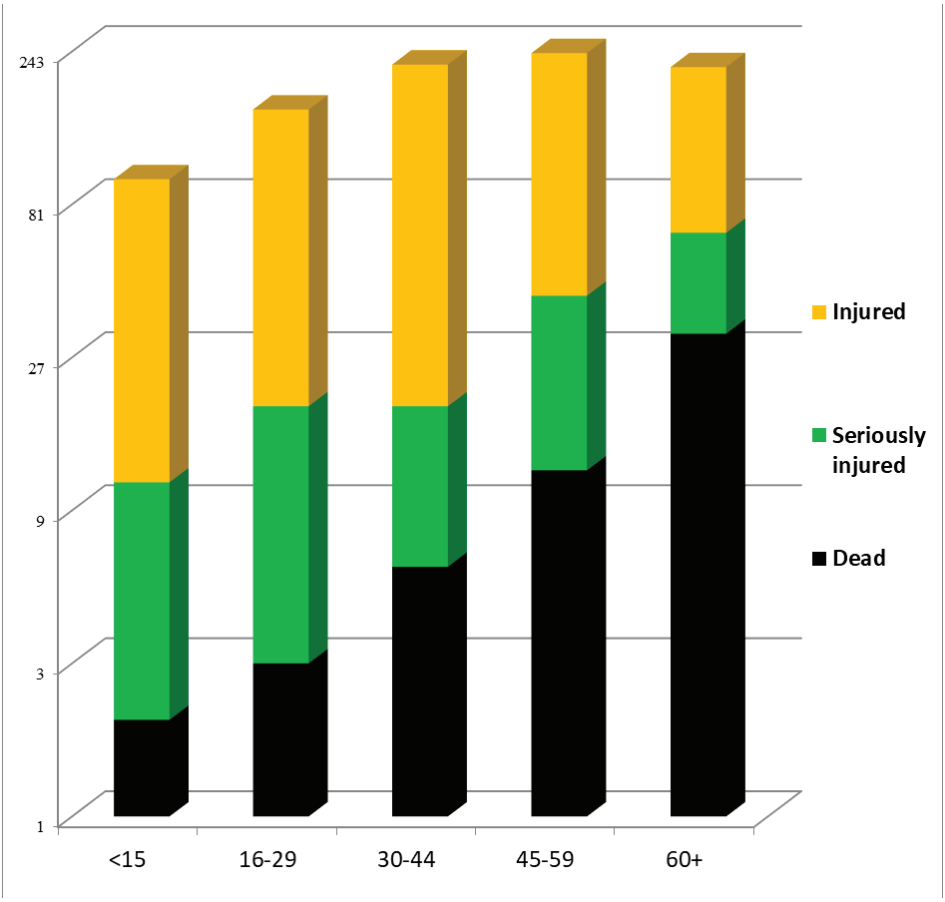


**Figure 8. Falls from Height in Agriculture by Age Categories on a Logarithmic Scale**

Table 3 reveals the accidents' analysis results by age category, gender, and activity during falling from a height. We observe that the age group most exposed to a fall from height is the age group, with 8.6% (41-45). This age group is followed by the age groups, with 8.5% (36-40), 8.4% (46-50), and 8.3% (51-55).

**Table 3. Accidents by Age Category, Gender and Activity**

| Premise | Sequent | Support % | Trust % | Rules Support % |
|---|---|---|---|---|
| (41-45) | Male | 8,645 | 80,247 | 6,937 |
| (16-20) | Male | 6,617 | 83,871 | 5,55 |
| (31-35) | Male | 7,257 | 75,0 | 5,443 |
| (11-15) | Male | 5.763 | 87,037 | 5,016 |
| (66-70) | Male | 6,19 | 77,586 | 4,803 |
| (51-55) | Harvesting | 8,324 | 57,692 | 4,803 |
| (61-65) | Harvesting | 7,471 | 61,429 | 4,589 |
| (56-60) | Harvesting | 8,111 | 56,579 | 4,589 |
| (46-50) | Harvesting | 8,431 | 54,43 | 4,589 |
| (36-40) | Harvesting | 8,538 | 52,5 | 4,482 |
| Grazing | Male | 4,909 | 86,957 | 4,269 |
| (71-75) | Male | 4,376 | 82,927 | 3,629 |
| (16-20) | Harvesting | 6,617 | 53,226 | 3,522 |
| Other Activity | Woman | 19,317 | 17,68 | 3,415 |
| (26-30) | Harvesting | 6,083 | 54,386 | 3,308 |
| (56-60), Harvesting | Male | 4,589 | 69,767 | 3.202 |

| | | | | |
|---|---|---|---|---|
| (56-60), Male | Harvesting | 6,403 | 50,0 | 3.202 |
| (51-55), Male | Harvesting | 5,55 | 55,769 | 3,095 |
| (41-45), Male | Harvesting | 6,937 | 44,615 | 3,095 |
| (6-10) | Male | 3,308 | 83,871 | 2,775 |
| Woman | (51-55) | 22,946 | 12,093 | 2,775 |
| (16-20), Male | Harvesting | 5,55 | 48,077 | 2,668 |

More than half (53%) of falls from agricultural activities occurred between 12:00-6:00 pm. During harvesting, the falls intensify between hours 3:00-6:00 pm (Figure 9). 64% of falls from fatal heights occurred between 12:00 and 6:00 pm.

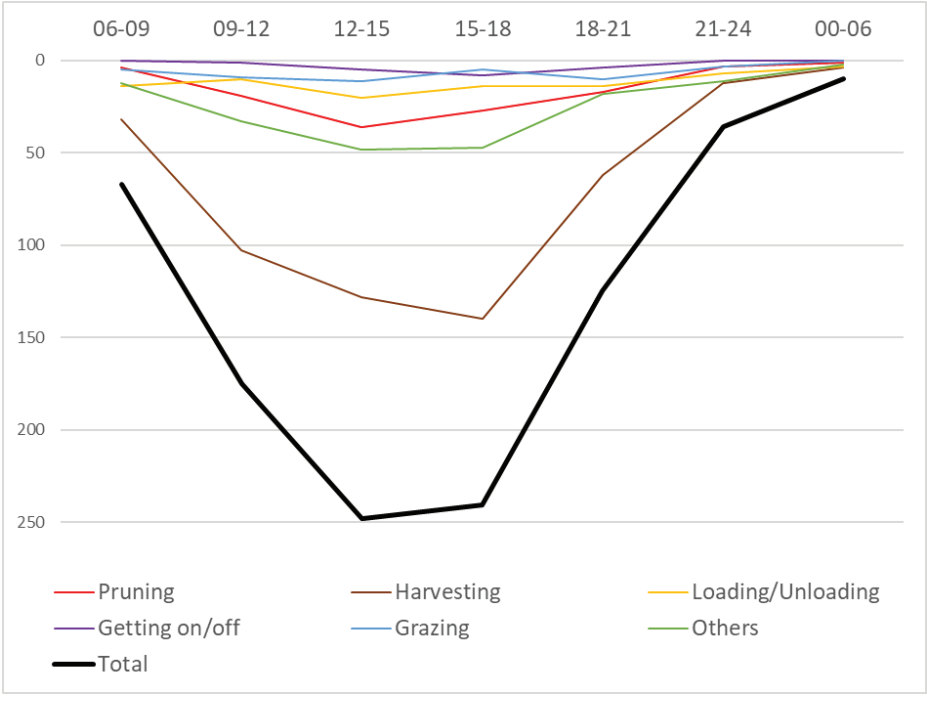


**Figure 9. The Times of Falling From Height During Agricultural Activities (Hours)**

We see accidents in the agricultural industry during the harvest season, July-September (Solomon, 2002) commonly. This study revealed that when pruning and harvesting are more intense in September-October, falls from height are higher than other agricultural accidents. Although both women and men are at risk of falling, as this study reveals, the victims of falls from height are usually men (Al et al., 2009; Gupta & Reeves, 2009; Nabi et al., 2009; Javadi and Naderi, 2013; Negin, 2014). In line with the results of this study, as presented in some country examples, women are exposed to more injuries than fatal accidents in falls during agricultural activities, and men are much more likely to die than women (WHO, 2017; Icer et al., 2013; Majdan and Mauritz, 2015; Darçın and Darçın, 2016). Worldwide, men maintain consistently higher mortality rates (WHO, 2018). The possible explanation for the higher incidence of falls from men is that they are more likely to work at height than women, have high risk-taking behaviors, and work in more dangerous jobs (WHO, 2018).

Falls from tractor/tractor fenders or trees are the leading causes of death due to falls from height in agriculture. The results of this study, likewise other study findings (Yavuz et al., 2004; Ozkan et al., 2010; Içer et al., 2013; Ersoy et al., 2014; Oğuztürk et al., 2016; Darçın & Darçın, 2016) supports that death from trees is one of the leading causes of death in rural areas, as opposed to urban areas (Jagnoor et al., 2011).

Age and specific health problems or medications also increase the risk of falls. Age is one of the critical risk factors for falls. Falls from height are the most common cause of accidental death and hospitalized injuries, especially among elderly farmers. The elderly have the highest risk of death or severe injury from falls compared to other age groups (Darçın & Darçın, 2016; WHO, 2018). As this study shows, workers over 60 years of age are the group with the highest rate of fatal falls specific to the agricultural sector (HSE, 2003). The age and health conditions/reports sought for even less dangerous jobs in other sectors are not pursued in the farming industry, although working at heights is dangerous. In addition to these negativities, people who require special education and have not received any training in working at height can work randomly and uncontrolled in the agricultural sector.

## CONCLUSIONS

By creating safety awareness, we see that simple work safety measures can prevent most agricultural sector accidents. The typical view of those exposed to falls before they fall is: "Nothing will happen to me." Risk assessment is required to determine the appropriate risk control and prevention measures to reduce the risk of falling from height to a reasonably bearable level. There are many approaches to defining a range of potential risk control measures. For the agricultural sector, possible risk control measures could be: We should develop situational awareness/risk perception to be aware of the risks faced by employees and their families. We should establish a safety culture between businesses and employees where safety is a priority. We should improve the availability of safety equipment by increasing the appropriate material ownership rather than fitting existing equipment. To effectively minimize falls from heights, we should apply prevention programs that encourage safe working behaviors and ensure the use of necessary safety devices and equipment, including training, information, and guidance. This study's results expect to raise awareness about falls from heights in agriculture, benefitting the national knowledge gap. The findings will be a valuable reference for researchers working on occupational health and safety in rural areas.

## REFERENCES

Agrawal, R., Imielinski, T., Swami, A. (1993). Mining Association Rules Between Sets of Items in Large Databases. ACM SIGMOD Record, 22(2), 207-216.

Agrawal, R., Srikant, R. (1994). Fast Algorithms for Mining Association Rules. Very Large Data Bases VLDB, 1215, 487-499.

Al, B., Yıldırım, C., Çoban, S. (2009). Falls From Heights in and Around the City of Batman. Turkish Journal of Trauma & Emergency Surgery,15(2), 141-147.

Chae, Y.M., Ho, S.H., Cho, K.W., Lee, D.H., Ji, S.H. (2001). Data Mining Approach to Policy Analysis in a Health Insurance Domain. Int J Med Inform, 62(2), 103–111.

Chang, L.Y., Wang, H.Y. (2006). Analysis of Traffic Injury Severity: An Application of Non-Parametric Classification Tree Techniques. Accid Anal Prev, 38(5), 1019–1027.

Darçın, E.S., Darçın, M. (2016). Falling from a Height Injuries in Agriculture: A 8-year Experience with 173 Samples. Biomedical Research, 27(3), 825-828.

Ersoy, S., Sönmez, B.M., Yılmaz, F., Kavalcı, C., ve diğ. (2014). Analysis and Injury Patterns of Walnut Tree Falls in Central Anatolia of Turkey. World J Emerg Surg, 9(1), 42.

Guillet, F., Hamilton, H.J. (2007). Quality Measures in Data Mining. Springer-Verlag New York, Inc., Secaucus.

Gupta, A., Reeves, B. (2009). Fijian Seasonal Scourge of Mango Tree Falls. ANZ Journal of Surgery, 79(12), 898-900.

İçer, M., Güloğlu, C., Orak, M., Üstündağ, M. (2013). Factors Affecting Mortality Caused by Falls From Height. Turkish Journal of Trauma & Emergency Surgery, 19(6), 529-535.

Jagnoor, J., Suraweera, W., Keay, et.al. (2011). Childhood and Adult Mortality From Unintentional Falls in India. Bulletin of the WHO, 89(10), 733-740.

Javadi, S.A., Naderi, F. (2013). Pattern of Spine Fractures After Falling From Walnut Trees. World Neurosurgery, 80(5), 41-43.

Liao, C.W., Perng, Y.H. (2007). Data Mining for Occupational Injuries in the Taiwan Construction Industry. Safety Science, 46(7), 1091-1102.

Nabi, D.G., TakShafaat, R., Kangoo, K.A., Dar Fiaz, A. (2009). Fracture Patterns Resulting From Falls From Walnut Trees in Kashmir. Injury, 40(6), 591-594.

Negin, J., Vizintin, P., Houasia, P., Martiniuk, A.L. (2014). Barking up the Wrong Tree: Injuries Due to Falls From Trees in Solomon Islands. Med J Aust, 201(11), 698-700.

Majdan, M., & Mauritz, W. (2015). Unintentional fall-related mortality in the elderly: comparing patterns in two countries with different demographic structure. BMJ Open, 5(8), e008672. https://doi.org/10.1136/bmjopen-2015-008672.

Marukatat, R. (2007). Structure-Based Rule Selection Framework for Association Rule Mining of Traffic Accident Data. In Y. Wang, Y. Cheung, and H. Liu (Eds.). Computational Intelligence and Security Lecture Notes in Computer Science, LNAI, 4456, 231-239.

Mirabadi, A., Sharifian, S. (2010). Aplication of Association Rules in Iranian Railways (RAI) Accident Data Analysis. Safety Science, 48(10),1427-1435.

Oğuztürk, H., Turgut, K., Turtay, M.G., Sarıhan, M.E., Gür, A., Beydilli, I., Gürbüz, S. (2016). Apricot Tree Falls: A Study From Malatya, Turkey. Biomed Research, 27(1), 210-213.

Özkan, S., Duman, A., Durukan, P., Avşaroğulları, L., İpekçi, A., Mutlu, A. (2010). Features of Injuries Due to Falls From Walnut Trees. Turkish J of Emerg Med, 10(2), 51-54.

Solomon, C. (2002). Accidental Injuries in Agriculture in the UK. Occup Med, 52(8), 461-466.

The Health and Safety Executive (HSE). (2003). Falls From Height-Prevention and Risk Control Effectiveness (Research Report).

Tsay, Y.J., Chiang, J.Y. (2005). CBAR: An Efficient Method for Mining Association Rules. Knowledge-Based Systems, 18(2):99-105.

WHO. (2021). Falls. https://www.who.int/news-room/fact-sheets/detail/falls

Witten, I.H., Frank, E. (2005). Data Mining: Practical Machine Learning Tools and Techniques, Third Edition. Morgan Kaufmann Publishers. USA.

Yavuz, M.S., Tomruk, O., Baydar, C.L., Küpeli, A. (2004). Evaluation of Accidental Fall From High Cases Who Admitted to Emergency Service. J Forensic Med, 18(3-4): 8-12.

Zhang C, Zhang S 2002. Association Rule Mining: Models and Algorithms. Springer, NY.

Zlatar, T., Lago, E. M. G., Soares, W. A., Baptista, J. S., & Barkokébas Junior, B. (2019). Falls from height: analysis of 114 cases. Production, 29, e20180091. https://doi.org/10.1590/0103-6513.20180091.

# PRODUCTION OF NANOCRYSTALLINE CELLULOSE FROM HEMP

*Ceren EMİR[1], Furkan YAVUZ[2], Cem ÖZEL[3], Sevil YÜCEL[4]*

**Abstract:** Polymers obtained from natural resources with a sustainability approach are widely used in the industrial field. For this reason, polymers obtained from natural resources come to the forefront compared to chemically synthesized polymers, thanks to their environmental, sustainable, and economic nature. Cellulose, a natural polymer, has been one of the polymers used by humanity for all kinds of tools and equipment for centuries. Cellulose, the most important part of plants, is a natural polymer that can be easily obtained from nature. Cellulose is a polymer that can be used alone as a raw material. In addition, it can add different and new features to the materials it is added as an additive. Cellulose is a valuable polymer in the production of industrial commercial composite materials. Functional and innovative properties can be gained by arranging the groups in the chemical structure of cellulose for the purpose of use. In this way, it is also possible to physically produce cellulose in different sizes and with different properties. Micro and nano-sized cellulosic materials are more advantageous in industrial products compared to raw cellulose. The nano-sized crystal form (NCC) of cellulose gives very different properties to the materials to which it is added, such as high strength and electromagnetic response. NCC also changes the permeability,

1 Yıldız Technical University, Faculty of Chemical and Metallurgical Engineering, Department of Bioengineering, İstanbul / Turkey, ckececi@yildiz.edu.tr, Orcid No:0000-0001-9015-3104

2 Yıldız Technical University, Faculty of Chemical and Metallurgical Engineering, Department of Bioengineering, İstanbul / Turkey, furkanyvz1305@gmail.com, Orcid No: 0000-0001-7331-9096

3 Yıldız Technical University, Faculty of Chemical and Metallurgical Engineering, Department of Bioengineering, İstanbul / Turkey, cemozel@yildiz.edu.tr Orcid No:0000-0002-6288-2091

4 Yıldız Technical University, Faculty of Chemical and Metallurgical Engineering, Department of Bioengineering, İstanbul / Turkey, syucel@yildiz.edu.tr, Orcid No:0000-0002-9495-9321

strength, flexibility, and optical properties of composite materials by affecting the surface morphology. Since nano-sized cellulose crystals are new, harmless, and recyclable, they have a high potential for use in the pharmaceutical, food, chemical, agriculture and paint industries. However, studies in the literature show that NCCs are promising in cellular therapies, tissue engineering, and drug delivery systems as a pharmaceutical component. In order to develop nano-sized cellulose, new studies are carried out from different cellulose sources every day. One of the most important of these sources is the cannabis plant. When the structure of the cannabis plant is examined, it is understood that it has a high production potential compared to other NCC sources. Legally promoting local cannabis production is becoming increasingly important in terms of NCC production and expanding the sectors in which NCC can be used. It seems that there are not many international studies on NCC production from cannabis. However, studies show that hemp is an attractive source for the production of NCC due to hemp's high cellulose content. In this study, research on obtaining NCC from cannabis plant are included.

***Keywords:*** Cellulose, Nanocellulose Crystal, Cellulosic composite, Hemp, Cannabis

## INTRODUCTION

Around 4000 BC, the Ancient Egyptians discovered Papyrus, which is considered the ancestor of paper and the first paper-like material as we know it. The name Papyrus comes from the reed variety *Papyrus antiquorum*, which grows on the banks of the Nile River. Papyrus was formed by hammering reed reeds into a hard and thin sheet. The word paper, which means paper in English, is a word derived from papyrus and has survived to the present day. This shows that cellulose was used for the first time in the industrial sense. Cellulose is a very important substance, which is located at the provincial level of the food chain and is the main content material of plants. It was isolated by the French chemist Anselme Payen (1795-1871), who isolated the first enzyme in 1834. While examining different types of wood, he discovered a new substance. He acquired from the cell walls of plants, and he separated into essential glucose units as it does starch and named it "cellulose". After this date,

studies to obtain cellulose have increased and their applications continue rapidly today (Hon, 1994).

**Structure of Cellulose**

Cellulose $(C_6H_{10}O_5)_n$ is a carbohydrate that is formed by the combination of three thousand or more glucose, forms a large part of the cell structure in plants and is used in the production of paper, artificial silk, and explosive materials (Fortunati et al, 2012). Cellulose makes the plant hard and solid. Herbivorous animals can digest cellulose because of the cellulase enzyme secreted by symbiont bacteria, protozoa species and some wood-eating insect species living in their intestines. Cellulose is preferably used in ceramics under the name CMC in the industry, and it is economical in paint production thanks to its superior film-forming feature (Fortunati et al, 2012). According to the most generally accepted approach today, the cellulose structure consists of two different parts: the crystalline region, where the microfibrils are arranged in an order and in the form of bundles with dense hydrogen bonds, and the amorphous region, which is in a looser arrangement. Although the ratio of crystalline and amorphous regions varies according to the source, in general, cellulose; It consists of 60-70% crystalline and 40-30% amorphous regions (Luzi et al, 2014).

Cellulose, the main component of the cell wall, is a large molecule, structurally complex and difficult to analyze compound. It forms the skeleton of the cell wall. Cellulose consists of cellulose molecules in the form of chains composed of glucose anhydride units $(C_6H_{10}O_5)$. A cellulose molecule contains an average of 10,000 glucose units. Cellulose molecules are joined to each other in the form of bundles. The smallest bundle is called the elementary fibril. The diameter of the elementary fibril is 3.5 mμ and consists of 40 cellulose molecules extending in the same direction (Belgacem, & Pizzi, 2016). Our daily diet contains approximately 10-15 grams of cellulose. 43% of the cellulose taken orally is excreted in the feces. The human body cannot digest cellulose, but by increasing bowel movements, it ensures regular bowel movement. It is recommended in slimming regimens, as it provides a feeling of fullness in the stomach and intestines, to prevent constipation. Raw and edible

fruits and vegetables, as well as whole grain products, are foods rich in cellulose (Feldman, 1985).

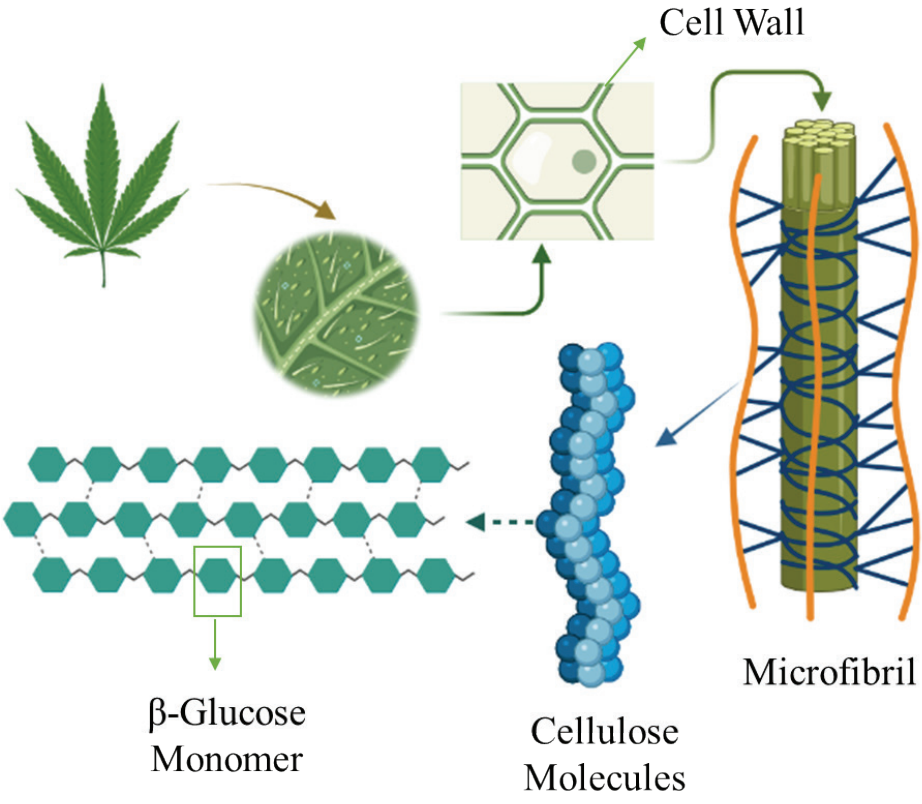


**Figure 1. Structure of Plant Cellulose**

**Cellulose Sources**

Cellulose is the fundamental material of the cell mass of hemp, wood, flax, bamboo, cotton and other plant materials and covers 40-60% of the cell mass of plant. Besides cellulose, minor components, for example cellulose acetic acid derivative and cellulose nitrate, are additionally used in the creation of materials such as rayon, explosives, plastics, visual films, cellulosic stains. It is a microscopically flat polymer and consists of chain-molded atoms. The building block consists of glucose anhydride units. These units are connected to each other by 1-4 ~ glu-

cosidic bonds. As a result of acidic hydrolysis, only glucose as reaction product, cellobiose, cellotriose etc. as intermediate product (Abraham et al., 2016).

**Physicochemical Properties of Cellulose**

Cellulose is immiscible in water, sodium hydroxide solution (75.5%) and organic solvents such as benzene, alcohol, acetone, chloroform. Regenerated cellulose or various cellulose derivatives called "alpha cellulose" are widely used in industrial production. For example, mercerized cotton is processed to disperse cellulose in dilute sodium hydroxide solution. In this way, mixtures of copper-II-hydroxide and concentrated ammonium hydroxide, called "Schweitzer solution", are prepared to dissolve the cellulose used in industrial production. When the solution is passed through an acid bath in this way, regenerated cellulose is obtained and regenerated cellulose is called "viscose rayon" in the market (Tao et al., 2019).

Cellulose makes the plant hard and strong, herbivorous animals can digest it because of the cellulase enzyme secreted by symbiosis bacteria living in their intestines, protozoa species and some wood-eating insect species. Cellulose is preferred in the industry, under the name of CMC, in the production of ceramics, in paint production, and because it is economical thanks to its superior film formation. They are formed because of glucose molecules' reverse bonds. Humans and animals cannot use cellulose as an energy source. Cellulose is insoluble in water and does not react with iodine (Szymańska-Chargot et al., 2019). It has been revealed as a result of long research that all the building blocks in the cellulose molecule are connected to each other by 1-4-β-glycosidic bonds. Therefore, only glucose emerges as a reaction product because of applied acidic hydrolysis. β-glycosidic glucose polymers are formed as intermediates (Tayeb et al., 2018).

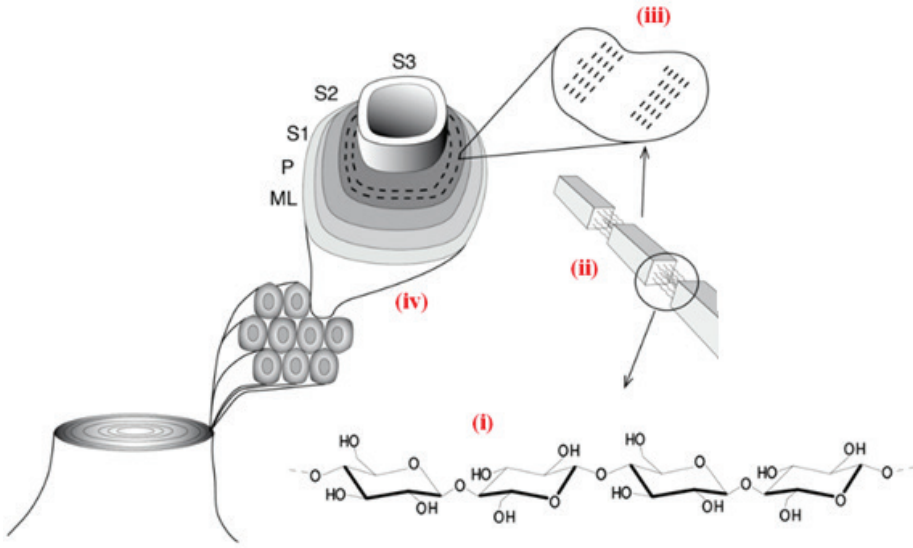


**Figure 2. (i) Cellulose's The Molecular Structure, (Ii) Polymer Fractions as Microfilaments with Crystalline/Non-Crystalline Regions, (Iii) A Macrofibril Form of Microfilaments, (Iv) Layers of Plant Cell Wall (García Vogel, 2017)**

The stabilization and regular structure of long chain polymers such as cellulose is related to the presence of functional groups that can bond with each other There are three hydroxyl (-OH) groups in the cellulose chain that hold the glucose units together and are responsible for revealing the chemical and physical properties of cellulose (Tayeb et al., 2018; García Vogel, 2017).

## Cellulose Derivatives

By using different compounds or molecules together with cellulose, structures with desired properties can be obtained.

### *Ethyl Cellulose*

It is an ether derivative of cellulose and is obtained by treating cellulose fibers with sodium hydroxide and ethyl chloride. Ethyl cellulose plastics are resistant to a wide temperature range. In addition, these plastics are highly resistant to water, strong bases and oils, and their

surfaces are bright. They are used in some automobile parts and packaging (Godakanda et al.,2019).

***Cellulose Acetate***

It is a thermoplastic resin obtained from cellulose. Cellulose acetate is an odorless, white powder or flake that softens at 60-97 °C and melts at 260 °C. It is obtained by treating wood or cotton cellulose with acetic acid and acetic anhydride with sulfuric acid. The resulting product is partially hydrolyzed. Each glucose unit in cellulose contains an average of 2-2.5 acetate groups. Cellulose acetate is used in the production of resin varnishes, artificial leather, transparent papers known as acetate in the market, some plastics and product coating. When cellulose acetate is used as a plastic, it is combined with plasticizers and dyes. These plastics are quite durable and do not catch fire easily. It can be used in toys, forks, knives, tool handles, radio etc. used in tools. Cellulose acetate fibers are used in the manufacture of products that are similar to silk, strong, easily dyed and good to wear. These fibers are obtained by passing a solution of cellulose acetate in acetone through fine slits, through a stream of hot air. Thus, the acetone evaporates and leaves the fibers. When the cellulose acetate film is to be obtained, the solution is spread in one layer. When the solvent evaporates, a cellulose acetate film remains. Cellulose acetate films are also used in photographic films, magnetic tapes for sound recordings, packaging, etc. used (Tamilselvi, 2019).

***Cellulose Nitrate***

Cellulose nitrate, also known as “Nitrocellulose”, is a flammable substance used in explosives and protective films, formed as a result of the reaction of cellulose with nitric acid (Szymańska-Chargot et al., 2019). The solubility of cellulose nitrate in organic solvents and mixtures in different ratios vary, these ratios are given in Table 1.

**Table 1. Solubility of Cellulose Nitrates at in Organic Solvents (Kırcı et al., 2001)**

| Nitrate (%) | Degree of Substitution | Solvent | Application |
|---|---|---|---|
| 10.5-11.1 | 1.8-2.0 | Ethanol | Plastics, Varnishes |
| 11.2-12.2 | 2.0-2.3 | Methanol Esther Acetone | Vernicle Adhesives |
| 12.0-13.7 | 2.2-2.8 | Acetone | Explosives |

***Cellulose Esters***

Cellulose esters, defined as the most important technical derivatives of cellulose, are the leading compounds of cellulose chemistry (Hoppe, 1998). Esters of cellulose cannot be thermoplastically processed but can produce materials suitable for processing using derivatization methods. Cellulose esters such as cellulose acetate, cellulose acetate propionate and cellulose acetate butyrate are thermoplastic materials produced by esterification of cellulose (Gao et al., 2018).

Various raw materials such as recycled paper, wood, cotton and sugarcane can be used in the preparation of powdered cellulose ester biopolymers. Powdered cellulose esters prepared with plasticizers and additives can be extruded to produce plastics from long-chain aliphatic acid esters of commercial biodegradable cellulose to varying degrees in pelleted form (Rudnik, 2012). Cellulose esters are characterized by their stiffness, moderate heat resistance, high moisture vapor transmission, oil resistance, clarity, appearance and moderate impact resistance. Some properties of commercial cellulose esters are given in Table 2 (Fortunati et al. 2012).

**Table 2. Cellulose Derivatives and Application Areas (Kırcı et al. 2001)**

| Cellulose Derivatives | Application |
|---|---|
| Tire Fibers | Wire And Reinforced Belts |
| High Wet Fiber Modules | Apparel, Furniture |
| Normal Flame | Clothing |
| Cellopone | Packaging |
| Seamless Flame | Clothes |
| Esters | |
| Acetate | Film |
| Flament | Apparel, Furniture Equipment |
| Tow | Cigarette Filter |
| Plastics | Film Sheet, Pressed Goods |
| Mixed Esters | Sheet, Pressed Goods |
| Nitrates | Varnish, Lacquer, Explosives |
| Ethers | |
| Cmc(Carboxymethyl Cellulose) | Detergent, Cosmetics, Food, Textile, Paper Bonding |
| Hec(Hydroxyethylcellulose) | Rubber, Paints, Polymerization Emulsions |
| Mc(Methylcellulose) | Food, Dyes, Pharmaceutical Industry |
| Ec(Ethylcellulose) | Coating, Inks |
| Hpc(Hydroxypropylcellulose) | Food, Pharmaceutical Industry |

Among the esters, the most important commercially and technologically are cellulose nitrate, cellulose xanthate and cellulose acetate. Cellulose sulfate, nitrate, phosphate, tricarbonylate and some esters with higher carbonic acid have also gained importance (Rudnik, 2012).

### Main Components of Cellulose Source Plants

Woody plants are structurally composed of 3 different cellulosic components. These; lignin, alpha cellulose and hemicellulose. In addition, some plants contain pectin, which provides resistance.

***Lignin***

It is a non-carbohydrate complex compound. "Lignin" is found 25%-35% in coniferous woods and 17-25% in leafy woods. The building block is the phenyl propane unit. Lignin, a water-repellent substance, binds cellulose to hemicelluloses, revealing the woody structure. For this reason, wood has a composite structure consisting of cellulose, hemicellulose and lignin. As such, lignin can be viewed as a natural polymer or cement. It has a structure with aromatic and aliphatic functions. It is also said to have a chaotic structure. They are optically passive (Chio et al.,2019).

***Alpha Cellulose***

The group with the most stable and highest degree of polymerization of cellulose is the alpha cellulose group. It is used in light colored thermoset resins. It is obtained as a result of processing wood pulp with alkali. It can be used as a coating to limit the water absorption of alpha cellulose materials (Gooch, 2010).

***Hemicellulose***

The polymeric amorphous hydrocarbons in the cell wall are called hemicellulose (beta cellulose and gamma cellulose). Hemicellulose constitutes 20-30% of the dry weight of all tree species and consists of branched molecular chains. Hemicelluloses are included in the group of heteropolysaccharides. It is soluble in alkaline aqueous solutions (such as 17.5% NaOH solution) and can be partially hydrolyzed in acid solutions (Chio et al.,2019).

***Pectin***

Pectin is a polymer composed of polysaccharide galacturonic acid and rhamnose. Pectin is located in the cell walls and intercellular spaces of plants, it retains water and gives elasticity to the structure. Since it can be used as a gel, it is used for drug delivery systems in the food industry and pharmaceutical industry (Antunes et al., 2021; Flutto, 2003).

**Table 3. Chemical Analysis of Some Plants (Klemm et al., 2011)**

| Raw Material | Cellulose (total %) | Alfa Cellulose | Lignin | Silisium | Referances |
|---|---|---|---|---|---|
| Hemp | 71,4 | 63,2 | 6,6 | - | (Gümüşkaya et al., 2002) |
| Tobacco Stalk | 46,5 | 37,5 | 17,5 | - | (Eroğlu et al., 1985) |
| Sunflower Stalk | 47,6 | 37,5 | 18,2 | - | (Bostancı et al., 1980) |
| Cotton Stalk | 46,5 | 38,9 | 19,5 | 0,1 | (Atchson et al., 1897) |
| Corn Stalk | 45,6 | 35,6 | 17,4 | 3,5 | (Usta et al., 1990) |
| Wheat Straw | 48,0 | 38,9 | 15,7 | 2,6 | (Deniz et al., 1994) |
| Rye Straw | 51,5 | 44,4 | 15,4 | 1,5 | (Usta et al., 1985) |
| Lake Cane | 50,3 | 47,5 | 18,7 | 3,4 | (Kırcı et al.,1996) |

**Cellulosic Nanocrystals**

Cellulosic crystals can be classified into three categories according to their production sources and preparation methods: nanofibrillated cellulose (NFC) or microfibrillated cellulose (MFC), nanocrystalline cellulose (NCC), and bacterial nanocellulose (BNC). However, the terminology of cellulose nanomaterials has not yet been standardized. Crystals have different uses according to their size.

**Table 4. Cellulosic Nanocrystalline Types (Klemm et al., 2011)**

| Nanocellulose Type | Names in Literature | Resource Obtained | Average Dimensions |
|---|---|---|---|
| **NFC** | Microfibrillated Cellulose<br>Cellulose Nanofibrils | Wood<br>Sugar Beet<br>Hemp<br>Linen | Mechanical Disintegration of Dough<br>Chemical or Enzymatic Treatment<br>Diameter:5-60 nm<br>Length: A Few µm |
| **BC** | Microbial Cellulose<br>Bacterial Cellulose | Low Molecular<br>Sugar Alcohols | Bacterial Synthesis<br>Diameter: 20-100 nm |
| **NCC** | Cellulose Nanocrystals<br>Cellulose Nanocrystallites | Wood<br>Cotton<br>Hemp<br>Linen<br>Wheat Straw<br>Mulberry Bark | Acid Hydrolysis of Cellulose<br>Diameter: 5-7 nm<br>Length: 10-500 nm (Vegetable Cellulose)<br>100 nm-few µm (Bacterial/Algae-Based Cellulose) |

*Microcrystalline Cellulose*

Microcrystalline cellulose (MCC) is one of the crystalline forms of fibrous microparticular, water-insoluble cellulose. It is a pure product of the depolymerization of cellulose. It is in the form of odorless and tasteless powder. As an excipient in the pharmaceutical industry, in the tableting phase, and also it is used as a plasticizer, filler, disintegrant, anti-adhesive and diluent (Luzi, 2014). MCC can be easily degraded, after being metabolized in the body, its by-products are harmless and absorbed by the body. Aqueous suspensions of MCC have stable viscosities over a wide temperature range, are heat stable. Since it does not react with carrier materials, it can be safely used in drug delivery systems (Battista and Smith, 1962). MCC is also added in the food industry as an excipient in functional foods thanks to its similar properties. In the cosmetics and paint industry, it is used to adjust the consistency of coat-

ings thanks to the thixotropic and thickening properties of MCC. It is also added to oil-based products due to its emulsification feature (Luzi, 2014; Ravit, et al. 2019). Aside from all its advantages, its high cost for production is an important disadvantage.

***Nanocellulose***

Nanocelluloses are the new form of cellulose. These new biobased nanomaterials with excellent properties have attracted much attention in recent years. Nanocelluloses are cellulose-based materials that have one or more dimensions at the nanoscale, that is, between 1 and 100 nm. Nanocelluloses can be classified into three categories according to their production sources and preparation methods: nanofibrillated cellulose (NFC) or microfibrillated cellulose (MFC), nanocrystalline cellulose (NCC), and bacterial nanocellulose (BNC). In this thesis, nanocellulose production is aimed (Tayeb et al., 2018; Ravit et al., 2019).

**Table 5. The Analysis of Some Natural Cellulose Sources (Jones et al. 2019)**

| Source | Degree of Crystallinity (%) | Microfibril Length |
|---|---|---|
| Algal Cellulose | >80 | 10 nm |
| Bacterial Cellulose | 65-79 | 5 nm |
| Cotton Fibers | 56-65 | 5 nm |
| Hemp | 60 | 3-5 nm |
| Linen | 56 | 4-5 nm |

***Nanocrystalline Cellulose***

Nanocrystalline cellulose (NCC) is a nano-sized crystal form extracted from cellulose. The fact that NCC provides many important properties such as high strength, hardness and electromagnetic properties to the materials to which it is added makes it advantageous to be used in different sectors such as medicine, chemistry, electronics, membranes, especially in the field of nanotechnology (Klemm et al. 2011; AI-Jawhari, 2020). By changing the surface properties of NCC composite membranes, it changes the permeability, strength, flexibility and optical properties of the material. It has been seen those composite films with NCC added

look brighter, thus making them suitable for use in decorative products, optical films and special packaging. In addition, since NCC is affected by magnetic and electric fields, its use in magnetic paper, electronic memory cards and readers and other electronic products may be beneficial. Not only the food and pharmaceutical industries, but also the aerospace and automotive industries use NCC as an additive for lightweight and high-strength composite materials. What makes NCC so advantageous today is that it can be produced from renewable and recyclable natural resources. Testing to date for NCC shows that it is non-toxic and its production does not pose serious environmental risks. NCC is biodegradable and renewable in nature and therefore sustainable and environmentally friendly for most applications (George and Sabapathi, 2015; Tozluoğlu, 2015). Essentially hydrophilic in nature; however, they can be surface functionalized to meet a variety of stringent requirements, such as the development of high-performance nanocomposites using hydrophobic polymer matrices. Work is being done on the fabrication of NCCs using different methods, such as powder, gel, suspension, filament, and films.

Usage Areas of Nanocrystalline Cellulose:

- Oil and Liquid: NCC gives fluids a controllable nature to meet the harsh heat, pressure and formation conditions (Svensson et al., 2005; Habibi et al., 2010).
- Glue: NCC increases the wet and dry strength of wood adhesives such as phenol formaldehyde and urea/melamine formaldehyde, strengthens the bonding feature, and improves production performance (Svensson et al., 2005; Habibi et al., 2010).
- Paper and Non-Woven Fabrics: It has been observed that the white water and product quality in the paper machine are improved with the addition of NCC in paper production. When integrated into superabsorbent materials, NCC has been shown to increase absorption, improving the material's structural integrity. High performance super absorbent materials have been developed using less material. The use of NCCs in products such as sanitary napkins or diapers is promising (Habibi et al., 2010).

- Cement: It was observed that the flexural strength, homogeneity and uniformity of the bubble size were improved with the addition of NCC to the cement (Habibi et al., 2010).
- Plastics and Composites: There are studies on adding NCC to the materials in order to make the materials used in the plastic and composite industry harder and lighter, as well as structurally and mechanically strong. For example, NCC has been shown to increase the toughness of epoxy resins used in composite applications by more than 150% (Habibi et al., 2010).
- Paints and Coatings: The paint and coating industry seeks sustainable and high-performance materials. NCCs used with paints contribute to the following properties; right resistance, drying time, spill, Volatile Organic Compounds (VOC) emissions, scratch resistance, durability (Habibi et al., 2010).
- Personal Care: NCC is an ingredient that improves the touch feeling of the cosmetic product. In addition to its antioxidant properties, NCC particle size and shape lead the development of new high-value products (Habibi et al., 2010).

Some of the advantages of NCC in use are as follows (Xu et al., 2020).:

- It is used in materials such as steel vest and carbon fiber due to its high strength in the defense industry.
- It has lightness and high temperature stability.
- It can be used as hydrophilic and hydrophobic depending on the intended use.
- It is used to strengthen the composites.
- Forms stable foams, aerogels and transparent films.
- Obtained from biomass.
- Sustainable.
- Renewable.
- Biodegradable

**Cannabis Plant**

It is a plant species that is the oldest source of vegetable raw materials in human history, and is used in yarn, weaving and fabric making, and the pulpy part is used in paper making, thanks to the fibers found in its stems. It is the first plant on earth used to make rope. In 3000 BC, the Chinese used it to make cloth. The name "Şah Tohumu" (Şah Danaç), which was transferred from Persian to Arabic and used for cannabis, also shows the importance given to this plant (Akgul and Yilmaz, 2015). In a work written in China in B.C. 2737, the physical and spiritual effects of cannabis were mentioned and it was said that it was suitable for use in the treatment of some diseases. The famous Venetian traveler Marco Polo (1254-1324) transported hemp from east to west. Ibni Sina (980-1037) named cannabis "kinnap" and studied this plant. It is known that there are many nations such as the Sumerians, Assyrians, Egyptians, Romans, who grow cannabis and poppy and use them in treatment. This plant was grown for various purposes in the Greeks and the Islamic world. Evliya Çelebi mentioned that there were cannabis shops in Istanbul called tradesmen-ı benkçiyan. In the 19th century, one dirham of cannabis was sold for one cent in Istanbul and was widely used among both the rich and the poor. Despite its prohibition of production and consumption, cannabis has been one of the most common drugs traded secretly around the world (Demirhan, 1975).

Cannabis is a one-year plant that is produced in certain provinces in Turkey, especially in Kastamonu. The first investments made by the public for the evaluation of cannabis production were made in Kastamonu. The first of these investments is the Taşköprü cannabis factory, which was established by Sümerbank in 1946 in order to use the cannabis produced in the region by pooling and peeling. The factory, which has a processing capacity of 4 thousand tons of cannabis sticks, was able to purchase half of its capacity due to various reasons, although there is a production of 16 thousand-24 thousand tons in the region. Due to the factory's inability to operate at full capacity and making losses, Sümerbank decided to close the hemp pooling and peeling facility at the end of 1949 and ended its operations in mid-1951. Another facility established in Kastamonu is Kendir Sanayii Müessesi. It was immediately included

in the industry plan in 1945 for the production of twine and cross-stitch from hemp fiber and its construction started in 1949. The factory, which meets the sack needs of the Turkish Grain Board, started to import jute, which is much cheaper than India, after 1953, due to the low efficiency and profitability of hemp used as raw material. This situation, which negatively affected hemp production, was compensated by purchasing hemp to be used in paper production at the factory of Turkey Cellulose and Paper Factories Inc. (SEKA) established in Izmit. In 1976, it was decided to establish a paper factory belonging to SEKA in Taşköprü and the factory started operating in 1984. The factory, which was included in the scope of privatization in 1998, was privatized and sold in 2004. Since the hemp need of the factory was cheaper after privatization, the way of supplying from abroad brought hemp production to the point of extinction (Akgul and Yilmaz, 2015).

***Taxonomy of Cannabis***

The cannabis plant is a genus of Cannabis from the Cannabinacease family of the Urticales order. The cannabis plant is divided into 4 different types according to the components in its structure and their ratios (Figure 3.). Some subspecies of cannabis;

- *Cannabis sativa vulgaris* L. (Cultured cannabis)
- *Cannabis indica* Lam. (Cannabis)
- *Cannabis sub gigantica* (Giant cannabis)
- *Cannabis sativa ruderaris* (Wild hemp)

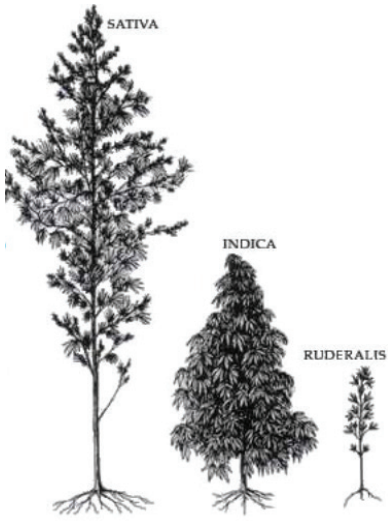


**Figure 3. Cannabis Types**

Cannabis is grown as an annual seed grown in temperate regions and can reach up to 5 meters. Crops grow best in well-drained sandy soils and require an average of at least 65 mm of rainfall per month during the season. Plants cultivated for fiber are densely planted. Plants grown for oilseeds are planted far from each other. It is shorter and more branched. Slight stems are empty aside from the tip and base. The leaves are palmately compound and the blossoms are little and greenish yellow. The seed-creating blossoms structure since quite a while ago, pointed groups that develop on pistillate or female plants. Dust creating blossoms structure exceptionally fanned bunches on staminate or male plants. Most extreme yield and quality are accomplished by gathering plants following they arrive at development, stamping them in full sprout, and free shedding of dust from male plants. Plants are most often cut to about 2.5 cm (1 inch) above the ground, although it is sometimes pulled up by hand. Generally, 30-35% male plants and 65-70% female plants are formed from the seed sown of cannabis. When planting seeds in the field, the producer does not have a choice of male or female plant seeds. The long and straight fibers are obtained by soaking the stems in water, followed by a series of processing methods that include drying,

crushing and agitation. The fibers, usually 1.8 meters long, consist of individual cylindrical cells with an irregular surface as seen in Figure 4. Longer and less flexible than linen, but stronger and more durable, the fibers are usually yellow, green, dark brown or gray. Since it is not easily bleached, it is rarely used by dyeing on cord and artificial sponges such as yarn, rope, cable and twine, and thick fabrics such as burlap and canvas (Väisänen et al., 2019; Brunet and Mura, 2014).

**Figure 4. Cannabis Sativa and Its Fibers**

***Cannabis Seeds***

Cannabis seeds are egg-shaped, hard and brown-green in color as seen in Figure 5. Hemp seeds contain 30-32% fat, 22-23% protein and 21% carbohydrates. Edible seeds are a source of protein, fiber and magnesium. Edible hulled hemp seeds, also called the heart of hemp, are healthy and nutritious. It can be added to meals or sprinkled on cold salads. Hemp seed milk can be used as an alternative to dairy products in drinks and recipes. The oil obtained from hemp seeds can be used in low-smoke paints, varnishes, soaps, and can also be used as cooking oil (Frassinetti et al., 2018; Brunet and Mura, 2014).

**Figure 5. Cannabis Seeds**

There are Tetra-hydra-cannabinol and Cannabidiol compounds in the hemp plant structure and these are psychoactive components.

Tetra-hydra-cannabinol (THC): Cannabis contains THC at varying rates (0.2% - 0.3%) depending on the subspecies, cultivation technique and variety. THC is the main psychoactive component of the cannabis plant. In other words, THC is the substance directly related to recreational cannabis use. This compound works in part by mimicking the effects of anandamide and 2-AG (2-arachidonoyl glyceride). These neurotransmitters are produced naturally by the human body and help regulate sleep and eating habits, pain perception, and countless other bodily functions. THC can have effects such as relaxation, changed vision, sense of smell and hearing, fatigue, hunger, reduced aggression. Literature studies show that THC can be used as an adjuvant in Chemotherapy side effects, Multiple sclerosis, HIV/AIDS, spinal injury: reducing tremor, nausea and vomiting, chronic pain, inflammation, digestive health (Akgul, and Yilmaz, 2015).

Cannabidiol (CBD): Like THC, it is more abundant in the flowering plant parts of cannabis. Cannabidiol is one of the most critical cannabinoids found in the cannabis plant. It is found in both agricultural can-

nabis and medical marijuana. While cannabinoids are found in a variety of plants in nature, the only herb known to contain CBD is hemp. CBD has the same chemical formula as THC and the atoms are in a different arrangement. This slight difference causes THC to have a psychoactive effect, while CBD does not. This fact means that when you take CBD for medicinal purposes, you will experience relief from your unwanted ailments with little or no noticeable effect on your cognitive abilities. Studies continue as a pharmaceutical raw material and there are also patented drugs (Premoli et al., 2019).

**Products from Hemp**

It is known that hemp has been used in textiles and apparel since ancient times. Well-made hemp garments have been found to last for years. Fabrics derived from hemp are known to be naturally resistant to UV rays and mildew, and resistant to salt water if treated. This discovery was made possible by the centuries-old use of hemp in sailor clothing working on sailboats and ocean liners. At the same time, due to its fibrous structure, fabric types that breathe easily can be produced. It is naturally comfortable due to its mechanical and physical properties. Compared to cotton, hemp is stronger. Since it requires fewer toxic chemicals and fresh water for its production, it is more environmentally friendly and natural, making the use of hemp sustainable. In recent years it has become a popular practice to mix hemp with other fabrics, especially organic cotton. The addition of hemp increases the strength of the fabric and gives the fabric a pleasant softness. Hemp can also be easily confused with flax. Hemp fabrics and apparel are found in casual wear such as hats, shirts, trousers and sweaters, as well as designer apparel specially selected for the extraordinary applications of hemp. Hemp fabric can meet the needs of manufacturers if made with care and quality (Demirhan, 1975).

The increase in the need for food and personal care products in direct proportion to the increase in population has turned to increase R&D activities to improve agricultural processing capabilities and genetics of new crops in order to obtain higher yields and better product quality. Companies in the market are working on fiber processing technology

for the production of water-repellent, fire-resistant, absorbent and super-soft material, which is expected to bring demand. The addition of hemp and cellulosic products derived from hemp to all these processes has had a positive effect on the production of industrial products (Özşeker et al., 2017).

**Table 6. Substances in the Structure of Natural Cellulosic Fibers (González-García et al., 2010)**

| Fiber Type | Cellulose (%) | Hemicellulose (%) | Lignin (%) | Pectin (%) |
|---|---|---|---|---|
| Cotton | 92 | 6 | - | 0-1 |
| Jute | 72 | 13 | 13 | - |
| linen | 81 | 14 | 3 | 4 |
| Sisal | 73 | 13 | 11 | 2 |
| Hemp | 74 | 18 | 4 | 1 |
| Kapok | 13 | - | - | - |

## RESULTS

Industrial applications of NCC, a natural cellulosic product with high economic value, have started with a new approach today. NCC can be obtained from many cellulose sources, but the use of cellulose sources rich in by-products such as pectin, lignin and hemicellulose increase the cost and slows the process. For this reason, hemp is a very advantageous source for obtaining NCC compared to other cellulose sources. To obtain NCC from hemp, it is only necessary to subject the fibers to a three-step chemical pretreatment, enzymatic pretreatment, and acid treatment. The physicochemical characterization of NCC extracted from cannabis is known to show good local purity and high crystallinity. Literature-based information has proven that NCC particles obtained from the cannabis plant can be used to produce value-added products in industry.

**REFERENCES**

Abraham, R. E., Wong, C. S., & Puri, M. (2016). Enrichment Of Cellulosic Waste Hemp (Cannabis Sativa) Hurd into Non-Toxic Microfibres. Materials, 9(7), 562.

AI-Jawhari, I. F. H. (2020). Nanocellulose For Sustainable Future Applications. Handbook Of Nanomaterials and Nanocomposites for Energy and Environmental Applications, 1-12.

Akgul, A., & Yilmaz, K. (2015). Ramifications Of Recent Developments in Turkey's Southeast on Cannabis Cultivation. International Journal of Drug Policy, 26(3), 330-331.

Antunes, F. A. F., Rocha, T. M., Philippini, R. R., Martiniano, S. E., Prado, C. A., Mier-Alba, E., & Da Silva, S. S. (2021). The Potential of Vegetal Biomass for Biomolecules Production.

Battista, O. A., & Smith, P. A. (1962). Microcrystalline Cellulose. Industrial & Engineering Chemistry, 54(9), 20-29.

Belgacem, M. N., & Pizzi, A. (2016). Lignocellulosic Fibers and Wood Handbook: Renewable Materials for Today's Environment. John Wiley & Sons.

Brunet, B., & Mura, P. (2014). Cannabis And Drug-Facilitated Crimes. In Toxicological Aspects of Drug-Facilitated Crimes (Pp. 139-157). Academic Press.

Chio, C., Sain, M., & Qin, W. (2019). Lignin Utilization: A Review of Lignin Depolymerization from Various Aspects. Renewable And Sustainable Energy Reviews, 107, 232-249.

DEMİRHAN,A. (1975).Tıp Fakültesi And T. Tarihi Ve Deontoloji Kürsüsü Asistanı, "Geçmişten Günümüze Esrar Ve Halk Arasında Kullanımı. FABAD J. Pharm. Sci., (2):5, 36-40

Feldman, D. (1985). Wood—Chemistry, Ultrastructure, Reactions, By D. Fengel and G. Wegener, Walter De Gruyter, Berlin And New York, 1984, 613 Pp. Price: 245 DM. Journal of Polymer Science: Polymer Letters Edition, 23(11), 601-602.

Fortunati, E., Armentano, I., Zhou, Q., Iannoni, A., Saino, E., Visai, L., ... & Kenny, J. M. (2012). Multifunctional Bionanocomposite Films

of Poly (Lactic Acid), Cellulose Nanocrystals and Silver Nanoparticles. Carbohydrate Polymers, 87(2), 1596-1605.

Frassinetti, S., Moccia, E., Caltavuturo, L., Gabriele, M., Longo, V., Bellani, L., ... & Giorgetti, L. (2018). Nutraceutical Potential of Hemp (Cannabis Sativa L.) Seeds and Sprouts. Food Chemistry, 262, 56-66.

Gao, C., Liu, S., & Edgar, K. J. (2018). Regioselective Chlorination Of Cellulose Esters By Methanesulfonyl Chloride. Carbohydrate Polymers, 193, 108-118.

García Vogel, A. (2017). Production Of Regenerated Nanocomposite Fibers Based on Cellulose and Their Use In All-Cellulose Composites.

George, J., & Sabapathi, S. N. (2015). Cellulose Nanocrystals: Synthesis, Functional Properties, And Applications. Nanotechnology, Science and Applications, 8, 45.

Godakanda, V. U., Li, H., Alquezar, L., Zhao, L., Zhu, L. M., De Silva, R., ... & Williams, G. R. (2019). Tunable Drug Release from Blend Poly (Vinyl Pyrrolidone)-Ethyl Cellulose Nanofibers. International Journal of Pharmaceutics, 562, 172-179.

González-García, S., Hospido, A., Feijoo, G., & Moreira, M. T. (2010). Life Cycle Assessment of Raw Materials for Non-Wood Pulp Mills: Hemp and Flax. Resources, Conservation and Recycling, 54(11), 923-930.

Gooch, J. W. (Ed.). (2010). Encyclopedic Dictionary of Polymers (Vol. 1). Springer Science & Business Media.

Habibi, Y., Lucia, L. A., & Rojas, O. J. (2010). Cellulose Nanocrystals: Chemistry, Self-Assembly, And Applications. Chemical Reviews, 110(6), 3479-3500.

Hon, D. N. S. (1994). Cellulose: A Random Walk Along Its Historical Path. Cellulose, 1(1), 1-25.

Hoppe, R. H. (1998). Wilhelm Klemm 1896-1985. Journal Of Fluorine Chemistry, 90(2), 177-179.

J. Thuvander And A.-S. Jönsson, "Influence Of Air And Nitrogen Sparging On Flux During Ultrafiltration Of Hemicelluloses Extracted From Wheat Bran," Sep. Purif. Technol., Vol. 212, Pp. 84–88, Apr. 2019.

Jones, A. O., Resel, R., Schrode, B., Machado-Charry, E., Röthel, C., Kunert, B., ... & Spirk, S. (2019). Structural Order in Cellulose Thin Films Prepared from A Trimethylsilyl Precursor. Biomacromolecules, 21(2), 653-659.

Kirci, H., Ateş,S., Akgül, M. (2001). Selüloz Türevleri Ve Kullanim Yerleri. Fen ve Mühendislik Dergisi, Cilt 4, Sayı 2, 119-130.

Klemm, D., Kramer, F., Moritz, S., Lindström, T., Ankerfors, M., Gray, D., & Dorris, A. (2011). Nanocelluloses: A New Family of Nature-Based Materials. Angewandte Chemie International Edition, 50(24), 5438-5466.

L. Flutto, (2003). "PECTIN | Properties And Determination," Encycl. Food Sci. Nutr., Pp. 4440–4449.

Lavoine, N., Desloges, I., Dufresne, A., & Bras, J. (2012). Microfibrillated Cellulose–Its Barrier Properties and Applications in Cellulosic Materials: A Review. Carbohydrate Polymers, 90(2), 735-764.

Luzi, F., Fortunati, E., Puglia, D., Lavorgna, M., Santulli, C., Kenny, J. M., & Torre, L. (2014). Optimized Extraction of Cellulose Nanocrystals from Pristine and Carded Hemp Fibres. Industrial Crops and Products, 56, 175-186.

Özşeker, P. E., Dip, A., Dağlıoğlu, N., & Gülmen, M. K. (2017). Sentetik Kannabinoidler: Yeni Nesil Esrar. Türk Aile Hekimleri Dergisi, 21(1), 34-40.

Premoli, M., Aria, F., Bonini, S. A., Maccarinelli, G., Gianoncelli, A., Della Pina, S., ... & Mastinu, A. (2019). Cannabidiol: Recent Advances and New Insights for Neuropsychiatric Disorders Treatment. Life Sciences, 224, 120-127.

Ravit, R., Abdullah, J., Ahmad, I., & Sulaiman, Y. (2019). Electrochemical Performance of Poly (3,4-Ethylenedioxythipohene)/Nanocrystalline Cellulose (PEDOT/NCC) Film for Supercapacitor. Carbohydrate Polymers, 203, 128-138.

Rudnik, E. (2012). 10—Compostable Polymer Materials: Definitions, Structures, And Methods of Preparation. Handbook Of Biopolymers and Biodegradable Plastics, 10, 189-211.

Svensson, A., Nicklasson, E., Harrah, T., Panilaitis, B., Kaplan, D. L., Brittberg, M., & Gatenholm, P. (2005). Bacterial Cellulose as A Potential Scaffold for Tissue Engineering Of Cartilage. Biomaterials, 26(4), 419-431.

Szymańska-Chargot, M., Chylińska, M., Pieczywek, P. M., & Zdunek, A. (2019). Tailored Nanocellulose Structure Depending on The Origin. Example Of Apple Parenchyma and Carrot Root Celluloses. Carbohydrate Polymers, 210, 186-195.

Tamilselvi, A., Jayakumar, G. C., Charan, K. S., Sahu, B., Deepa, P. R., Kanth, S. V., & Kanagaraj, J. (2019). Extraction Of Cellulose from Renewable Resources and Its Application In Leather Finishing. Journal Of Cleaner Production, 230, 694-699.

Tao, P., Zhang, Y., Wu, Z., Liao, X., & Nie, S. (2019). Enzymatic Pretreatment for Cellulose Nanofibrils Isolation from Bagasse Pulp: Transition Of Cellulose Crystal Structure. Carbohydrate Polymers, 214, 1-7.

Tayeb, A. H., Amini, E., Ghasemi, S., & Tajvidi, M. (2018). Cellulose Nanomaterials—Binding Properties and Applications: A Review. Molecules, 23(10), 2684.

Tozluoğlu, A., Çöpür, Y., Özyürek, Ö., & Çıtlak, S. (2015). Nanoselüloz Üretim Teknolojisi. Turkish Journal of Forestry, 16(2), 203-219.

Väisänen, T., Kilpeläinen, P., Kitunen, V., Lappalainen, R., & Tomppo, L. (2019). Effect Of Steam Treatment on The Chemical Composition of Hemp (Cannabis Sativa L.) And Identification of The Extracted Carbohydrates and Other Compounds. Industrial Crops and Products, 131, 224-233.

Xu, Y., Atrens, A., & Stokes, J. R. (2020). A Review of Nanocrystalline Cellulose Suspensions: Rheology, Liquid Crystal Ordering and Colloidal Phase Behaviour. Advances In Colloid and Interface Science, 275, 102076.

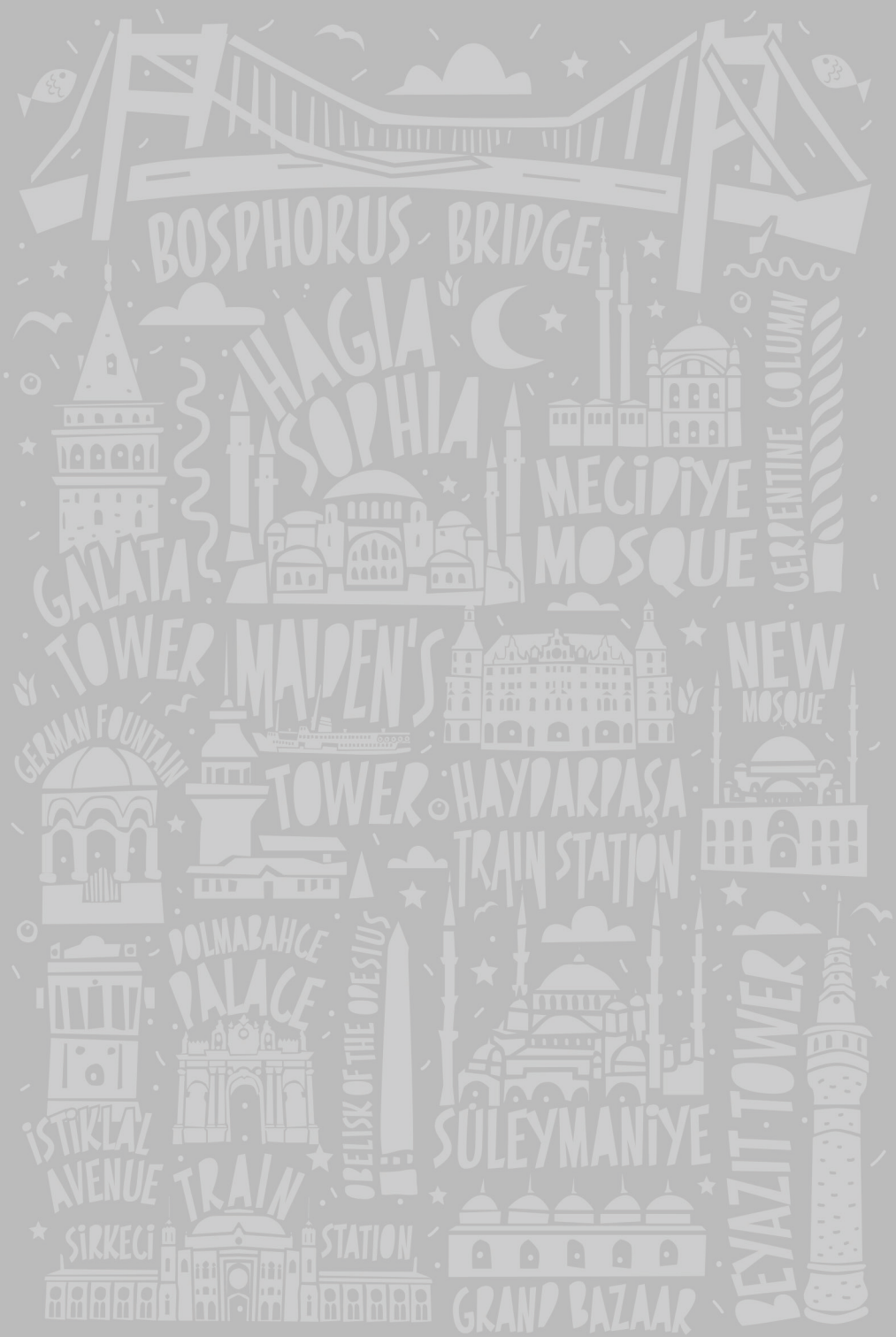


9 786257 367028

GÜVEN PLUS GRUP A.Ş.

GPGD

ORP